

ABSTRACT

ADHIKARI, PRAJESH. Developing New Multicomponent Systems: From Coatings, Gels to Nanofiller Composites. (Under the direction of Dr. Saad A. Khan and Dr. Orlando Rojas).

The design of new materials with advanced functionality necessitates the use of systems consisting of two or more components, referred to as multicomponent systems. To fulfill demands in the industry, polymers have been used either as homopolymers or as copolymers, blends and composites to manufacture engineered products with improved performance. In this dissertation, we focus on multicomponent systems consisting of a random copolymer for protein capture, and nanofillers for polymer composites.

The first research topic focuses on surface modification of inert polybutylene terephthalate (PBT) using a facile method that installs surface reactive groups, followed by copolymer adsorption that dramatically enhances non-specific biomacromolecule binding. PBT films and nonwoven fabrics are modified upon acid-hydrolysis of pre-adsorbed trimethylsilylcellulose (TMSC), which facilitates attachment of a bromine-terminated initiator. Random hydrophilic copolymers of poly (sodium vinyl benzene sulfonate-co-hydroxyethyl methacrylate) (poly(SVBS-co-HEMA)) are then grafted from the surface using activator re-generated by electron transfer (ARGET) atom-transfer radical polymerization (ATRP). The copolymer architecture was studied for enhanced protein capture and release of adsorbed model proteins, with maximum binding observed for a copolymer with dominant HEMA composition. Such system was regenerated after protein adsorption by introducing electrolyte solutions. The modified polyester represents an attractive alternative for imparting protein-adsorption functionality toward advanced separations.

The second research topic focuses on modulating the crosslinking dynamics and enhancing mechanical performance of aqueous photoactive poly(vinyl alcohol) derivative

(PVA-SbQ) via network formation using cellulose nanocrystals (CNC). The resulting changes in the rheological behavior of PVA-SbQ show that inclusion of CNC's above a critical threshold concentration between 1-1.5 wt.% results in a percolated CNC network before UV-exposure, corroborated using Van Gorp-Palmen and Cole-Cole plots used as signatures for percolation. The structure build-up after UV exposure studied using in-situ dynamic photo-crosslinking experiments reveals alterations in gelation kinetics and mechanical strength of the neat system. A steep jump in the storage modulus of fully-crosslinked networks representative of percolation with critical threshold concentration (~1.4 wt. %) as well as ~131% increase in storage modulus (G') at 2.5 wt. % CNC is observed. The results point to the existence of favorable polymer-CNC interactions that induce a percolated microstructure that allows efficient stress transfer. The findings of this work can be utilized in the design of photocrosslinkable systems for applications requiring mechanical reinforcement.

The third research topic focuses on understanding the interfacial aspects of multicomponent systems consisting of nanodiamonds (ND) in semi-crystalline and amorphous polymers to understand structure-property-function relationships. Macroscopic property reinforcements using ND in polymer-nanodiamond composites have been extensively studied. However, not much is known about the relationship between polymer-ND interfacial energy parameters, polymer-ND interactions and final mechanical properties in ND-reinforced electrospun fibers. In this work, surface-energy dependent parameters such as wettability, work of spreading, and work of dispersion-aggregation transition of ND's were used to derive a criterion for dispersion (D_c) as a hypothesized predictor of polymer-ND interactions and final tensile strength in electrospun poly (vinyl) alcohol (PVA),

polyacrylonitrile (PAN), and polystyrene (PS). The results show that shifts in glass transition temperature (ΔT_g), used as a measure of polymer-ND interactions, show a direct correlation with D_c in the order of PVA > PS > PAN regardless of amorphous or semi-crystalline nature of the polymer. However, the final tensile strength showed a direct correlation with D_c and ΔT_g for semi-crystalline polymers only, with amorphous polystyrene showing maximum reinforcement contrary to predictions made by ΔT_g , suggesting the additional role of polymer morphology to final tensile strength. The findings of this study could offer additional insight into the design of interfaces for polymer-ND fiber composites.

© Copyright 2018 Prajesh Adhikari

All Rights Reserved

Developing New Multicomponent Systems: From Coatings, Gels to Nanofiller Composites

by
Prajesh Adhikari

A dissertation submitted to the Graduate Faculty of
North Carolina State University
in partial fulfillment of the
requirements for the degree of
Doctor of Philosophy

Chemical Engineering

Raleigh, North Carolina

2018

APPROVED BY:

Dr. Saad A. Khan
Committee Co-Chair

Dr. Orlando J. Rojas
Committee Co-Chair

Dr. Jan Genzer

Dr. Behnam Pourdeyhimi

DEDICATION

To my parents for their endless sacrifice, patience and support

BIOGRAPHY

Prajesh Adhikari was born in Kathmandu, Nepal to his parents Kamal and Kalpana Adhikari, and has two elder brothers Prabin and Prabal Adhikari. He spent most of his childhood in Kathmandu and went to national boarding school for 7 years. Growing up, he was very interested in sports (soccer, tennis, table tennis, cricket) and later became fascinated with aircrafts that led to his interest in the field of engineering. In 2008, he decided to pursue higher education in the US and accepted admissions for undergraduate education in Lafayette College, Easton, PA, where he received his Bachelor of Science in Chemical Engineering with honors under the direction of Professor Joshua A. Levinson. Following graduation in 2012, he joined North Carolina State University where he pursued his doctorate degree in Chemical Engineering under the direction of Dr. Saad A. Khan and Dr. Orlando J. Rojas. Outside of work, he loves reading books on behavioral psychology and finance, playing and watching sports, traveling, exploring new cultures and aircrafts/flight simulators. Post-completion of his Ph.D. degree in January 2018, he will join Intel Corporation in Hillsboro, Oregon, where he will be working as a back-end CMP process engineer.

ACKNOWLEDGMENTS

The past 5+ years in graduate school would not have been a rewarding experience without the help of many people. First of all, I would like to thank my advisor Dr. Saad A. Khan for his immense support, encouragement, mentorship as well as continuous financial support throughout my time in graduate school. I would not have been able to get this far without your help, so I am very grateful for everything you have provided me over the past 5+ years. Also, I would like to thank all the members of my thesis committee - Dr. Rojas for his incredible congeniality and work ethics that I tried to emulate, Dr. Genzer for sharing his enormous amount of knowledge and resources, inspiring me to constantly think about new ideas, and Dr. Pourdeyhimi for his continuous support on all my projects funded through the Nonwovens Institute. I duly acknowledge all the support I received which was immensely helpful at different steps in the process.

I would also like to thank all the active and former graduate students and post-docs of Khan research group, for their invaluable support over the years. It was great fun working with this group and learned a lot in the process. Also, a big thank you to all the members of Rojas and Genzer research groups for providing me access to all the resources I needed to complete my work. In addition, I thank all the members of staff in the Department of Chemical and Biomolecular Engineering, Department of Forest Biomaterials, Nonwovens Institute (NWI) and Analytical Instrumentation Facility (AIF) for their constant support.

During my educational journey in the U.S that began 9+ years ago, I have been very lucky to share some great friendships that started very early in college. I want to acknowledge all my friends from Lafayette - Ankit Chandra, Ashutosh Tamrakar, Bidur Dahal, Kirtika Challa, Kruti Suchde, Nripesh Parajuli, and Rupesh Gajurel - for their

incredible support over the years, as well as sharing the closest vantage point of my life in graduate school. The friendships that have evolved for over a decade have been instrumental in putting this together. In addition, I would also like to thank Anurodh Tripathi, Ishan Joshipura, and Rohan Patil for their camaraderie and many memorable moments at the *Firth of Tay Way*.

During the past decade of my academic journey, I have been back to my hometown in Nepal only once. I am so very grateful to my parents for their endless sacrifice they have made over the years to send me abroad for quality education. Their constant commitment to our education has been remarkably inspiring and without their vision and support, I would not be where I am today. I have also been very fortunate to have two elder brothers, Prabin and Prabal who have been inspirational starting very early on in my life. Their intellectual and thought-provoking discussions, passion for physics and simulators have always inspired me, so I am very grateful to have them as my role models. Finally, a big thank you to my sister-in-law, Clare, for everything she has done for me over the years.

TABLE OF CONTENTS

LIST OF TABLES	ix
LIST OF FIGURES	xi
Chapter 1 Introduction and Organization.....	1
1.1 Introduction and Motivation	1
1.2 Background	3
1.2.1 Protein Adsorption on Solid Substrates	4
1.2.1.1 Polymer Brushes: Grafting ‘From’ vs. Grafting ‘To’	5
1.2.1.2 Synthesis of Polymer Brushes Using Polymerization Techniques	7
1.2.1.3 Factors Affecting Protein Adsorption	9
1.2.1.4 Thermodynamics of Protein Adsorption.....	10
1.2.1.5 Nonwoven Fabrics	11
1.2.1.6 Research Goals.....	13
1.2.2 Synthesis of Cellulose Nanocrystals and Interactions with Polymers	14
1.2.2.1 Interaction of CNC’s with Polymers.....	15
1.2.2.2 Rheology of Cellulose Nanocrystals and Polymer-CNC Composites	17
1.2.2.3 Research Goals.....	18
1.2.3 Fundamentals of Polymer Nanocomposites.....	18
1.2.3.1 Synthesis, Purification and Applications of Nanodiamonds.....	22
1.2.3.2 Nanodiamond Deaggregation	24
1.2.3.3 Nanodiamond-Based Polymer Nanocomposites.....	25
1.2.3.4 Research Goals.....	27
1.3 Organization of Dissertation.....	27
1.4 References.....	35
Chapter 2 Polyester Modification with Random Copolymers via Surface-Initiated Atom Transfer Radical Polymerization: Engineering the Surface Architecture for Protein Capture and Release	50
2.1 Abstract.....	50
2.2 Introduction.....	51
2.3 Materials and Methods.....	53
2.3.1 Materials.....	53
2.3.2 Preparation of PBT Thin Films by Spin Coating.....	54
2.3.3 Preparation of Hydroxyl-Terminated PBT Surfaces.....	55
2.3.4 Synthesis of Initiator-Functionalized Surfaces	55
2.3.5 ARGET-ATRP using SVBS and HEMA.....	55
2.3.6 Protein Adsorption	56
2.3.7 Surface Characterization	57

2.4 Results and Discussion	58
2.4.1 Preparation and Characterization of Polyester and PP Thin Films and Surfaces Grafted with poly(SVBS-co-HEMA).....	58
2.4.2 Effect of Copolymer Composition on Lysozyme Adsorption	63
2.4.3 Regeneration of Lysozyme Adsorbed on poly(SVBS-co-HEMA)-modified Surfaces.....	66
2.4.4 Effects of pH on Protein Adsorption.....	68
2.4.5 Protein Adsorption on Nonwoven Fabrics.....	74
2.5 Conclusions	76
2.6 Acknowledgment	77
2.7 References	88
Chapter 3 Modulating Gelation Kinetics and Mechanical Properties of Photocurable Poly(vinyl alcohol) Derivative through Network Formation Using Cellulose Nanocrystals	94
3.1 Abstract	94
3.2 Introduction	95
3.3 Materials and Methods	98
3.3.1 Materials.....	98
3.3.2 Preparation of PVA-SbQ/CNC Solutions.....	98
3.3.3 Rheological Measurements and Characterization.....	99
3.4 Results and Discussion	101
3.5 Conclusions	114
3.6 References	128
Chapter 4 Nanodiamond-Reinforced Electrospun Fibers: Understanding the Role of Interfacial Interactions on Mechanical Properties	136
4.1 Abstract	136
4.2 Introduction	137
4.3 Materials and Methods	140
4.3.1 Materials.....	140
4.3.2 Nanodiamond Dispersion and Ultrasonic Deaggregation.....	141
4.3.3 Electrospinning Polymers with Nanodiamonds.....	141
4.3.4 Characterization	142
4.4 Results and Discussion	144
4.4.1 Dispersion of Nanodiamond in Different Solvents.....	144
4.4.2 Characterization of c-ND (as is) vs. SAUD c-ND	145
4.4.3 Nanodiamond Surface Energy	147
4.4.4 Theoretical Basis.....	151

4.4.4.1	Compatibility of Nanodiamond with Polymer.....	152
4.4.4.2	Wettability.....	152
4.4.4.3	Work of Spreading Polymer on Nanodiamonds	153
4.4.4.4	Work Associated with Dispersion-Aggregation Transition ($\Delta W_{\text{DIS-AGG}}$)..	153
4.4.4.5	Criterion for Dispersion of Nanodiamonds in Polymers	155
4.4.5	Effect of Nanodiamond on Glass Transition Temperature of Polymer Fiber Composites.....	159
4.4.6	Correlation between Glass Transition Temperature and Tensile Strength	162
4.5	Conclusions.....	166
4.6	Acknowledgement.....	167
4.7	References.....	178
Chapter 5	Conclusions and Future Outlook.....	188
5.1	Conclusions.....	188
5.2	Future Work and Recommendations.....	191
5.2.1	Photoinduced Grafting of Copolymer on Nonwoven Fabrics	191
5.2.1.1	Materials and Methods.....	193
5.2.1.2	Results and Discussion	196
5.2.2	Modulating Gelation Kinetics and Mechanical Strength of PVA-SbQ	212
5.2.3	Nanodiamond-Reinforced Electrospun Fibers.....	213
5.3	References.....	215
APPENDICES.....		216
Appendix A	Supplemental Information for Chapter 2.....	217
Appendix B	Supplemental Information for Chapter 3.....	225
Appendix C	Supplemental Information for Chapter 4.....	229

LIST OF TABLES

Table 2-1	Adsorption parameters of lysozyme (5 mg/ml in 10 mM PBS at pH 7.4) on control PBT thin films, and poly(SVBS-co-HEMA) 8:2 grafted on PBT using method 1 (with TMSC) and method 2 (without TMSC).....	80
Table 2-2	Adsorption parameters of lysozyme (1 mg/ml in 10 mM PBS at pH 7.4) on PBT for various copolymer ratio (SVBS: HEMA) in poly(SVBS-co-HEMA)....	82
Table 3-1	Hydrodynamic size, zeta potential and conductivity of 0.1 wt.% and 0.5 wt.% CNC suspension in water and 100 μ m PVA-SbQ Solution. Dispersions were prepared using bath sonication for 1 hour.....	118
Table 3-2	Herschel-Bulkley parameters (yield stress, consistency index and flow-behavior index) of PVA-SbQ (6 wt. %) containing different amounts of CNC.	120
Table 3-3	Slopes of G' and complex viscosity and relaxation exponent for neat PVA-SbQ and PVA-SbQ with CNC's at different concentrations.	122
Table 4-1	Summary of relevant adhesion parameters in understanding dispersion-aggregation behavior of ND's in different polymers extracted from data shown in Figure 4.2 and 4.3.....	171
Table 4-2	Glass transition temperature (T_g) and relative shift in glass transition temperature (ΔT_g) of electrospun polymer fibers with varying c-ND loadings..	173
Table 4-3	Tensile strength (σ) and elongation at break (ϵ) of polymer nanofibers with different c-ND loadings, obtained using stress-strain data shown in Figures C.7-C.9.....	176
Table 4-4	Shifts in glass transition temperature (ΔT_g), normalized tensile strength and Pukanszky interaction parameter of polymer nanofibers with different c-ND loadings.	177
Table 5-1	Free-radical polymerization synthesis conditions for homopolymers and copolymers of poly (butylmethacrylate) (PBMA) and poly (dimethylaminoethyl) methacrylate (PDMAEMA) at 75°C.....	203
Table 5-2	Theoretical and experimental atomic content (%) for homopolymers of PBMA and PDMAEMA, and copolymers with 1:1 and 3:1 P(BMA-co-DMAEMA).	207
Table 5-3	Element content (%) of carbon, nitrogen and oxygen for PBT nonwoven fabric (as is) and nonwoven fabrics grated with PBMA and 1:1 P(BMA-co-DMAEMA).	209
Table C-1	Solubility parameters of different solvents used to disperse nanodiamonds	229
Table C-2	Dispersive and polar components of total surface energy of polymers	235
Table C-3	Electrospinning conditions for PVA (MW 10-98, 15 wt.%) in water, PAN (8 wt.%) in DMF and PS (30 wt.%) in DMF and with different SAUD c-ND loadings (0.1 wt.%, 0.5 wt.%, 1.0 wt.% and 2.0 wt.%)	236

Table C-4 Parameters extracted from TGA graph of polymer-ND fiber composites showing decomposition temperature (T_d) and temperatures of maximum weight loss (T_{max}).....	253
--	-----

LIST OF FIGURES

Figure 1.1 Grafting “From” vs. Grafting “To” Approach to Surface Modification for Protein Adsorption / Desorption. ¹⁵⁴	28
Figure 1.2 Aqueous ATRP route for polymer synthesis using grafting-from approach. (Adapted from Matyjaszewski Polymer Group, Carnegie Mellon University, 2016)	29
Figure 1.3 Schematic of meltblowing process consisting of extruder, metering pump and die assembly used to manufacture nonwovens. ¹⁵⁵	30
Figure 1.4 Cellulose nanocrystals extracted from forest products using acid hydrolysis. (Adapted from Substance, Scientific News and Innovation from ETS – New Class of Biomaterials: Cellulose Nanocrystals, 2014).....	31
Figure 1.5 DHR-3 rheometer accessory to study in-situ UV crosslinking of photoactive poly(vinyl) alcohol derivative incorporating cellulose nanocrystals. (Adapted from TA Instruments Brochure, DE, 2015).....	32
Figure 1.6 Structure of nanodiamonds showing presence of sp^2 carbons on the surface and sp^3 carbon in the inner core. ¹⁵⁶	33
Figure 1.7 Schematic of electrospinning set up used to make polymer fibers with nanodiamonds. (Adapted from Oxolutia, 2014)	34
Figure 2.1 Schematic illustration of preparation of poly(SVBS-co-HEMA) on PBT using two different methods: Method 1 employs TMSC as an anchoring layer before initiator immobilization and Method 2 immobilizes initiator directly on PBT substrates.	78
Figure 2.2 (a) Changes in wettability of PBT on Si-wafer upon surface modification, and (b) real-time adsorption of lysozyme (5 mg/ml in 10 mM PBS (with 150 mM Na^+) at pH 7.4) on three different surfaces – PBT, PBT-g-poly(SVBS-co-HEMA) (8:2) (Method 1) and PBT-g-poly(SVBS-co-HEMA) (8:2) (Method 2). At 10 minutes, lysozyme solution in PBS (10 mM with 150 mM Na^+) was injected into the system and at 60 minutes the system was rinsed with same buffer.	79
Figure 2.3 (a) The effect of SVBS:HEMA copolymer ratio on the wettability of grafted surfaces, (b) Real-time adsorption of lysozyme (1 mg/ml in 10 mM PBS at pH 7.4) on surfaces with different ratios of SVBS: HEMA.	81
Figure 2.4 (a) Lysozyme adsorption on 8:2 poly (SVBS-co-HEMA) from bulk concentration of 1 mg/ml in 10 mM PB and PBS at pH 7.4. Desorption of lysozyme was achieved using respective buffers, and (b) lysozyme adsorption on 2:8 poly (SVBS-co-HEMA) from bulk concentration of 1 mg/ml in 10 mM PB, followed by desorption using PB and PBS showing surface regeneration capability.	83
Figure 2.5 Effect of pH on adsorption of BSA, fibrinogen and lysozyme (1 mg/ml in 10 mM PB): (a) adsorption of BSA, fibrinogen and lysozyme at pH 7.0 and (b)	

at pH 4.0. Adsorption experiments were performed on 2:8 poly(SVBS-co-HEMA) surfaces grafted for 2 h.	84
Figure 2.6 (a) XPS scans for PBT nonwoven fabric (reference) and PBT grafted with 2:8 poly(SVBS-co-HEMA) for different times (2 and 8 hours), and (b) elemental composition showing presence of sodium and sulfur after grafting PBT with 2:8 poly(SVBS-co-HEMA), confirming the presence of the copolymer.	85
Figure 2.7 (a) Morphology of PBT nonwoven fabric (A), PBT nonwoven fabric after treatment with TMSC followed by hydrolysis (B) and PBT nonwoven fabric after grafting 2:8 poly(SVBS-co-HEMA) (C).	86
Figure 2.8 Effect of ATRP grafting and immersion time on adsorption of lysozyme (0.3 mg/ml in 10 mM PBS at pH 7.4) on PBT nonwoven fabric modified with 2:8 poly(SVBS-co-HEMA).	87
Figure 3.1 (a) Steady shear viscosity of neat PVA-SbQ at different concentrations, and (b) specific viscosity of PVA-SbQ at different concentrations used to estimate entanglement concentration.	116
Figure 3.2 (a) Huggins plot showing specific viscosity vs. CNC concentration to determine aspect ratio of cellulose nanocrystals (using this method the aspect ratio of CNC is ~24), and (b) steady shear viscosity of cellulose nanocrystals at different concentrations.	117
Figure 3.3 Shear stress as a function of shear rate for PVA-SbQ (6 wt. %) with different CNC concentration between 0 wt. % and 2.1 wt. % (for 0.3 wt. % increments).	119
Figure 3.4 (a) Storage and loss modulus (G' and G'') and (b) complex viscosity vs. frequency, for neat PVA-SbQ and PVA-SbQ containing CNC's up to 3 wt.% using stress of 1 Pa.	121
Figure 3.5 (a) van Gurp-Palmen plot (δ vs. $ G^* $), and (b) Cole-Cole plot (G' vs. G'') for aqueous PVA-SbQ with varying CNC's used to observe percolation behavior.	123
Figure 3.6 The design principle used to modulate mechanical strength via network formation using cellulose nanocrystals. Percolated network was first achieved by adding negatively charged CNC and further crosslinked using UV exposure to obtain densely interconnected structure.	124
Figure 3.7 (a) Frequency sweep for PVA-SbQ (6 wt. %) using UV intensity of 10 W/cm ² , and (b) changes in slope (G' vs. G'') and complex viscosity as a function of frequency after different exposure times (t = 0 seconds, t = 900 seconds and t = 3600 seconds).	125
Figure 3.8 (a) Time sweeps for PVA-SbQ (6 wt. %) using UV intensity of 10 W/cm ² , and (b) G' , G'' crossover for different CNC concentrations.	126

Figure 3.9 (a) Average storage modulus of PVA-SbQ (6 wt. %) for different CNC concentrations (wt. %), and (b) frequency sweep of PVA-SbQ (6 wt. %) with different CNC contents after UV exposure for 1 h at 10 mW/cm ²	127
Figure 4.1 (a) FTIR spectrum and (b) XPS scan for c-ND and SAUD c-ND showing changes in surface composition after deaggregation. SAUD c-ND shows minor amounts of sodium (Na) and nitrogen (N).	168
Figure 4.2 (a) Owens-Wendt plot used to calculate the surface energy of c-ND, and (b) ΔG_{mix} , work of adhesion ($W_{P/ND}$), and work of cohesion ($W_{ND/ND}$) for c-ND mixed in two semi-crystalline polymers (PVA, PAN) and amorphous polymer (PS).	169
Figure 4.3 (a) Work of spreading, work of dispersion-aggregation transition, and (b) dispersion criterion for c-ND in PVA, PAN and PS derived using surface energies.	170
Figure 4.4 (a) The effect of c-ND loadings on glass transition temperature (T_g) of PVA, PAN and PS electrospun fibers, and (b) the change in glass transition temperature (ΔT_g) post c-ND addition relative to nanofibers without c-ND.....	172
Figure 4.5 Plot showing maximum change in glass transition temperature of electrospun fibers containing c-ND as a function of criteria for dispersion (D_c). Higher values of (D_c) result in greater shifts in T_g ($^{\circ}C$) in the order PVA > PS > PAN.....	174
Figure 4.6 (a) Normalized tensile strength as a function of SAUD c-ND loadings (vol. %) and (b) adhesion parameter (B) as a function of SAUD c-ND loadings derived by fitting experimental data to Pukanszky model.....	175
Figure 5.1 (a) Proposed chemistry for development of PBT nonwovens with high non-specific protein capture efficiency consisting of poly (2-dimethylaminoethyl methacrylate) (PDMAEMA), poly(butyl) methacrylate (PBMA) and poly(3-sulfopropyl) methacrylate, and (b) positively charged segment obtained after quaternization of PDMAEMA, which allows capture of proteins with negative charges.....	201
Figure 5.2 (a) Free-radical polymerization synthesis route for the fabrication of P(BMA-co-DMAEMA) copolymer using AIBN and suitable solvent at 75 $^{\circ}C$, (b) strategy for attachment of copolymer to nonwoven substrate using UV-induced crosslinking in the presence of benzophenone, and (c) mechanism of crosslinking in the presence of benzophenone, showing hydrogen abstraction from polymer and attachment to the substrate.....	202
Figure 5.3 FTIR-spectra of homopolymers of PBMA, PDMAEMA and 1:1 P (BMA-co-DMAEMA) synthesized using free-radical copolymerization.	204
Figure 5.4 Comparison of NMR spectra of homopolymer of PBMA, PDMAEMA and 1:1 (theoretical ratio) P (BMA-co-DMAEMA) synthesized using free-radical copolymerization.....	205
Figure 5.5 XPS-spectra of homopolymer of PBMA, PDMAEMA, 1:1 and 3:1 P(BMA-co-DMAEMA) synthesized using free-radical copolymerization.	206

Figure 5.6 XPS-spectra of neat PBT nonwoven fabric (20 g/m ² basis weight) and fabric grafted with PBMA and 1:1 P(BMA-co-DMAEMA) showing successful attachment of copolymer using UV crosslinking in the presence of benzophenone.	208
Figure 5.7 SEM images showing morphology of (A) neat PBT nonwoven fabrics, (B) grafted with PBMA using UV intensity of 3 J/cm ² , (C) grafted with PBMA using UV intensity of 9 J/cm ² , and (D) grafted with 1:1 P(BMA-co-DMAEMA) using UV intensity of 9 J/cm ²	210
Figure 5.8 Degree of grafting of PBMA and 1:1 P(BMA-co-DMAEMA) on PBT nonwoven fabric. PBT nonwoven fabric (20 g/m ²) was immersed in THF containing 100 mg/ml of polymer of interest and 10 wt.% benzophenone, and samples exposed to UV 10-30 mW/cm ² for 5 minutes. Samples were then rinsed in THF overnight to dissolve unreacted polymer and benzophenone, followed by rinsing in water and drying in oven to constant weight.....	211
Figure A.1 Spin-coating PBT thin films onto silicon substrate using different PBT concentrations (0.10 wt.% and 0.16 wt.%) in 1,1,1,3,3,3-hexafluoro-2-propanol (HFIP) - (left) thickness and corresponding contact angles for the PBT-coated surfaces, and (right) AFM images of spin-coated surface.	217
Figure A.2 AFM images of PP thin films on silicon substrate and corresponding changes in contact angle upon using TMSC as an anchoring layer and subsequent acid hydrolysis.	218
Figure A.3 (a) The effect of surface modification on apparent contact angle for different nonwoven fabrics (PBT, PET and PP). Grafting of pure poly (HEMA) creates super hydrophilic nonwovens that are stable for 3 months in water.	219
Figure A.4 FTIR spectra of polypropylene nonwoven fabric after different surface modification steps. The grafting of pure poly (HEMA) was confirmed by peak at ~1730 cm ⁻¹ indicative of strong C=O stretching vibration.....	220
Figure A.5 First derivative of frequency changes for different surfaces showing rate of lysozyme adsorption on different poly (SVBS-co-HEMA) surfaces.	221
Figure A.6 Thickness of protein layer (1 mg/ml in PB at pH 7.0) adsorbed on the surface of 2:8 poly (SVBS-co-HEMA) calculated using Voigt model.....	222
Figure A.7 Thickness of protein layer (1 mg/ml in PB at pH 4.0) adsorbed on the surface of 2:8 poly (SVBS-co-HEMA) calculated using Voigt model.....	223
Figure A.8 Changes in apparent wettability of PBT nonwoven fabric in different steps of surface modification. Grafting of 2:8 poly (SVBS-co-HEMA) completely wicks the surface.....	224
Figure B.1 Representative digital images of (A) CNC (0.1 wt.%) and CNC (0.1 wt.%) with PVA-SbQ (100 μM), (B) CNC (0.1 wt.%) with NaCl (100 mM, 5.84 mg/ml) and CNC (0.1 wt.%) with PVA-SbQ (100 μM) / NaCl (100 mM, 5.84 mg/ml); (C) CNC (0.5 wt.%) and CNC (0.5 wt.%) with PVA-SbQ (100 μM) and (D) CNC (0.5 wt.%) with NaCl (100 mM, 5.84 mg/ml) and CNC	

(0.5 wt.%) with PVA-SbQ (100 μ M) / NaCl (100 mM, 5.84 mg/ml). All CNC suspensions shown above were prepared using bath sonication for 1 hour. CNC dispersion turns cloudy upon addition of PVA-SbQ as well as sodium chloride. CNC dispersions containing PVA-SbQ show some aggregation whereas dispersions containing both PVA-SbQ and sodium chloride show intense aggregation..... 225

Figure B.2 Representative digital images of CNC's at different weight percent dispersed in water after sonication for 4 hours (Branson 1510). Concentrations below 6 wt. % show solution-like behavior whereas concentrations above 6 wt. % show gel-like behavior..... 226

Figure B.3 Cole-Cole plot showing the relationship between real (η') and imaginary parts of complex viscosity (η'') for PVA-SbQ with different CNC concentrations. The inset shows data for neat PVA-SbQ, and PVA-SbQ with 0.5 wt. % and 1 wt. % CNC not visible in the original plot. 227

Figure B.4 Determination of gel-point concentration using frequency independence of $\tan \delta$ based on Winter-Chambon criterion. 228

Figure C.1 Dispersion of carboxylated nanodiamonds (c-ND) in 18 different solvents immediately post-sonication, after 1 day and 10 days. Dispersion stability was labeled stable, moderately stable, less stable and unstable based on the visual differences in color of colloidal solution - most stable in water, DMF, and DMAc; moderately stable in acetone, methanol, and ethanol; less stable in acrylonitrile and acetonitrile; and unstable in DMSO. 230

Figure C.2 Dispersion map for c-ND dispersed in different solvents, showing stable dispersions (triangles), moderately stable dispersions (squares), less stable dispersions (light squares) and unstable dispersions (circles) - (a) dispersive solubility parameter vs. polar solubility parameter (b) hydrogen bonding solubility parameter vs. polar solubility parameter and (c) hydrogen bonding solubility vs. dispersive solubility parameter..... 231

Figure C.3 Particle size distribution for (a) ND-COOH (0.1 wt. %) and (b) ND-COOH (1.0 wt. %) post sonication and after 1 day, 7 days and 10 days. Digital images show ND-COOH at different times after initial sonication. Inset shows particle settling at the bottom of the vial. 232

Figure C.4 Salt-Assisted Ultrasonic Deaggregation (SAUD) technique was employed to obtain c-ND (labeled ND-COOH in the plot) with smaller particle size. Branson Sonifier S-450 with a flat tip (a) and micro tip (b) was used for ultrasonic deaggregation. DLS measurements were obtained for c-ND (as-received) and SAUD c-ND for 0.1 wt. % and 1.0 wt. % using refractive index of 1.427 and viscosity of 0.899 mPa-s. The data shown above are an average of 5 measurements. 233

Figure C.5 Conductometric titration curves for c-ND and SAUD c-ND showing similar amounts of surface carboxylic acid groups, confirming no significant functionality changes upon deaggregation..... 234

Figure C.6 Electrospinning solution containing (a) polyvinyl alcohol (MW 10-98, 15 wt. %), and (b) polyvinyl alcohol (MW 10-98, 15 wt. %) with SAUD c-ND (2 wt. %) showing the effect of SAUD c-ND on appearance of solution. Electrospun fiber mats are shown in (c) showing the effect of c-ND on color of electrospun mats indicative of aggregation.	237
Figure C.7 (a) Stress-strain plot for poly(vinyl alcohol) (PVA) nanofibers with different SAUD c-ND loadings between 0.1 wt.% to 2 wt.% and (b) tensile strength and elongation at break at different SAUD c-ND extracted from data in (a).	238
Figure C.8 The effect of ND's on crystallinity of PVA nanofibers calculated using DSC. .	239
Figure C.9 (a) Stress-strain plot for polyacrylonitrile (PAN) nanofibers with different SAUD c-ND loadings between 0.1 wt.% to 2 wt.% and (b) tensile strength and elongation at break at different SAUD c-ND extracted from data in (a).	240
Figure C.10 Stress-strain plot for polystyrene (PS) nanofibers with different SAUD c-ND loadings between 0.1 wt.% to 2 wt.% and (b) tensile strength and elongation at break at different SAUD c-ND extracted from data in (a).	241
Figure C.11 (a-f) SEM images of electrospun fibers containing ND: (a) PVA (15 wt. %) and (b) PVA (15 wt.%) with SAUD c-ND (2 wt.%); (c) PS (30 wt.%) and (d) PS (30 wt.%) with SAUD c-ND (2 wt.%); (e) PAN (8 wt.%) and (f) PAN (8 wt.%) with SAUD c-ND (2 wt.%). Uniform nanofibers were produced at different polymer concentrations. Electrospinning conditions are shown in Table C.3.	244
Figure C.12 (a-f) Cross-section images of electrospun fiber composites containing SAUD c-ND: (a) PVA (15 wt.%) and (b) PVA (15 wt.%) with SAUD c-ND (2 wt.%); (c) PS (30 wt.%) and (d) PS (30 wt.%) with SAUD c-ND (2 wt.%); (e) PAN (8 wt.%) and (f) PAN (8 wt.%) with SAUD c-ND (2 wt.%). Uniform nanofibers were produced at these polymer concentrations.	245
Figure C.13 Morphology of electrospun fibers showing aggregation behavior of ND's in (a) PVA, (b) PAN and (c) PS. Figures (a', b',c') and (a'', b'', c'') shown images at different magnifications.	246
Figure C.14 (a) Weight loss (%) and (b) derivative weight loss of PVA nanofibers with different SAUD c-ND loadings between 0.1 wt.% and 2.0 wt.%.	250
Figure C.15 (a) Weight loss (%) and (b) derivative weight loss of PAN nanofibers with different SAUD c-ND loadings between 0.1 wt.% and 2.0 wt.%.	251
Figure C.16 (a) Weight loss (%) and (b) derivative weight loss of PS nanofibers with different SAUD c-ND loadings between 0.1 wt.% and 2.0 wt.%.	252

Chapter 1 Introduction and Organization

1.1 Introduction and Motivation

The design of new materials with advanced functionality necessitates the use of polymer systems consisting of two or more components, often referred to as multicomponent polymeric systems. To fulfill demands in the industry, polymers have been used either as homopolymers or as copolymers, blends, and composites to manufacture engineered products with improved performance that would otherwise not be realizable with individual components alone. Successful implementations of multicomponent systems have been shown in the design of coatings, adhesives, nanostructured gels, elastomers, additives and nanocomposites for diverse applications ranging from but not limited to marine and implants biofouling, protective and maintenance technology, electronics, optics, sensing, drug delivery, enzyme entrapments, and high-strength materials.¹⁻³ As such, multicomponent systems have been at the forefront of surface and composite engineering research for decades. Such advances in engineered products using multicomponent systems have been possible in part due to revolutionary breakthroughs in polymer science, most specifically in the field of polymer synthesis. The discovery of ‘living’ polymerization techniques such as nitroxide-mediated polymerization and atom-transfer radical polymerization have enabled well-controlled designs of complex architectures such as block copolymers, molecular brushes, gradients and functional colloidal structure, with well controlled composition (homopolymer, block, statistical, periodic, random, gradient copolymer), topology (linear, branched, network, star, cyclic), and functionality (side and end functional, multifunctional,

telechelic) on either flat, spherical or cylindrical surfaces, allowing appropriate selection and design of architectures suited for desired applications.^{4,5}

The first class of multicomponent systems consists of copolymers, which are prepared using polymerization of two or more different monomers, combining different properties that are simultaneously desirable. The most common commercially available copolymer known for its impact resistance and high toughness is acrylonitrile-butadiene-styrene (ABS), which combines heat resistance of acrylonitrile, rigidity of styrene, and impact strength of butadiene often used in applications in automotive, construction and electronics.⁶ Block copolymers synthesized through sequential addition of monomers using ‘living’ polymerization techniques, show self-assembly properties that have enabled possibilities of generating new morphologies for applications in lithography, photovoltaic, electronics and targeted drug delivery systems.⁷ Similarly, random copolymers grown from surfaces using surface-initiated polymerization have been used in the design of responsive materials for drug delivery, diagnostics, and tissue engineering, smart coatings and textiles.⁸ In addition to copolymers, polymer blends, in which two different polymers are blended together with or without compatibilization, are unique examples of multicomponent polymeric systems. For instance, the commercially available high-impact polystyrene (HIPS) is an immiscible blend of polystyrene and polybutadiene that gives brittle polystyrene more flexibility.⁹ The immiscible blend of polyvinyl alcohol (PVA) in polyethylene terephthalate (PET), which generates lamellar morphology, combines barrier properties of PVA with the strength of PET for use as plastic bottles for carbonated beverages.¹⁹ Finally, multicomponent polymeric systems that have received significant attention include polymer composites, which combine

particulates,¹⁰ fibers,¹¹ nanotubes,¹² graphene,¹³ and nanocrystals¹⁴ in polymers to achieve property reinforcements. The use of carbon fiber-reinforced polymers to achieve low weight and high strength properties to improve environmental performance and cost efficiency in the airline industry represents one of the most successful implementations of such multicomponent systems.¹¹

The challenge in the current field of multicomponent systems, however, lies in the creation or use of existing fundamental knowledge in designing new multicomponent systems in the form of coatings, gels, and composites suited for particular application of interest. **Chapter 2** in this dissertation focuses on using existing principles of surface-initiated polymerization to design protein adsorption coatings with regeneration capabilities using facile surface chemistry on model polyester thin films and nonwovens for applications in protein capture systems such as biofluid filtration and wastewater treatment. **Chapter 3** focuses on reinforcing mechanical properties of a photocrosslinkable polymer using rod-shaped cellulose nanocrystals and using rheological measurements to probe microstructural changes and moduli reinforcements. **Chapter 4** focuses on understanding the interfacial aspects of multicomponent systems consisting of nanodiamonds in either semi-crystalline or amorphous polymers with different surface energies to create fundamental knowledge on structure-property-function relationships in nanodiamond-based composite materials.

1.2 Background

The following sections in this Chapter provide a brief overview of some of the definitions and key concepts important in the design of coatings for protein adsorption, networks for cellulose nanocrystals-based composites, and composites using nanodiamonds,

with the intent of providing a broad knowledge base on key areas of research and general context of the major contribution of this work. The dissertation chapters, however, can be read independently.

1.2.1 Protein Adsorption on Solid Substrates

Protein adsorption is a ubiquitous and complex phenomenon, detrimental in numerous applications ranging from biosensors, cell adhesion, drug delivery, medical implants, marine biofouling, and tissue regeneration, but highly desirable in applications involving protein separation and purification, biofluid filtration, and wastewater treatment.¹⁵ In case of protein adsorption systems with high protein loadings for waste-water treatment, controlled protein capture is beset with problems such as low capture efficiency and surface saturation, further manifesting in the form of higher manufacturing and operating costs attributed to interruptions in production cycles, clean and exchange of filter surfaces, and re-entrainment into process streams. Similarly, the accumulation of biological organisms as surface deposits in marine environments results in biofouling, increasing energy consumptions and cleaning costs.^{16,17} As such, generating surfaces for either protein adsorption or protein passivation rests heavily on designing systems that tackle problems associated with cost, durability and regeneration capabilities. In addition, highly sensitive techniques such as quartz-crystal microbalance and surface plasmon resonance available for real-time monitoring of protein accumulation on flat surfaces allow for the study of capacity and kinetics of adsorption.

The notoriety of proteins to stick to different substrates can be understood based on its fundamental structure. Proteins are amphiphilic macromolecules, consisting of a

hydrophobic core with hydrophilic and charged amino groups extending out of the backbone with multiple structure levels.^{18,19} The primary structure of proteins is comprised of positively charged (lysine), negatively charged (aspartic acid), polar (serine) and non-polar (alanine) amino acid residues. The combinations of these primary amino acid residues form secondary structures consisting of either α -helices stabilized by intramolecular hydrogen bonding between C=O and –NH residues, which comprises ~25% in globular proteins, or β -sheets stabilized by intermolecular hydrogen bonding between C=O and –NH of adjacent chains. The folding of secondary structures forms tertiary structures, and organization of multiple tertiary units form quaternary structures.¹⁹ Some examples of blood plasma proteins include albumins, globulins, and fibrinogen, which have different size, molecular weights, and isoelectric points, resulting in different levels of molecular interactions. In fact, these molecular interaction forces generated during protein adsorption include ionic or electrostatic interactions, hydrogen bonding, entropically driven hydrophobic associations and hydrogen bonding. Protein adsorption studies have been conducted in several polymeric systems such as anionic (polystyrene sulfonate, poly(3-sulfopropyl) methacrylate), cationic (quaternized poly(dimethylaminoethyl) methacrylate), hydrophilic (poly(hydroxyethyl) methacrylate, polyethylene oxide), hydrophobic (polystyrene, poly(butyl)methacrylate) and zwitterionic polymers (poly(methacryloyloxyethyl) phosphorylcholine, poly(sulfobetaine methacrylate)).²⁰

1.2.1.1 Polymer Brushes: Grafting ‘From’ vs. Grafting ‘To’

The two most versatile approaches used to alter surface properties to create hydrophilic, hydrophobic, gradient or switchable surfaces include ‘grafting from’ and

‘grafting to’ as shown in Figure 1.1.^{21,22} In sharp contrast to the ‘grafting from’ approach in which polymerization initiating moieties called initiators are first deposited on either planar substrates such as silicon, highly curved surface such as nanoparticles, or cylindrical substrates, and monomers are added using living radical polymerization techniques such as nitroxide-mediated radical polymerization (NMP),²³ atom-transfer radical polymerization (ATRP),²⁴ reversible addition-fragmentation chain-transfer polymerization (RAFT),²⁵ ‘grafting to’ approach relies on attachment of pre-made polymers to the substrate. In the ‘grafting from’ approach, the nanoscale properties such as chemical composition, chain lengths, thickness, molecular weight, surface coverage, and conformation of the grafted polymers can be precisely controlled using living polymerization techniques. Such polymerization techniques have been the subject of numerous experimental and theoretical investigations, as its versatility offers a wide array of possibilities of well-controlled designs of complex architectures for different applications. In particular, different conformations of grafted polymers can be obtained by tuning the grafting density, which is a simple function of thickness and molecular weight of the polymer attached to the surface.²⁶ At low grafting densities, tethered chains are weakly interacting in the ‘mushroom’ regime, whereas at very high grafting densities, tether chains ‘stretch’ away from the interface to prevent overlapping, forming polymer brushes.²⁶ In particular, the potential of polymer brushes in the development of advanced polymer surface coatings has largely been explored since the introduction of the theory of polymer brushes.²⁷ Since then numerous studies with well-controlled polymer brushes have been used to study the effect of thickness, molecular weight, grafting density, swelling, surface roughness, chain flexibility, and interfacial water

on adsorption of different proteins such as bovine serum albumin, lysozyme, and fibrinogen to name a few.

1.2.1.2 Synthesis of Polymer Brushes Using Polymerization Techniques

With the introduction of the term ‘living polymerization’ for the first time in 1956 by Michael Szwarc, controlling the precise structure of polymers became possible.²⁸ The first breakthrough came in 1985 when Australian chemists Rizzardo and Solomon revolutionized polymerization synthesis by introducing nitroxide-mediated polymerization (NMP),²⁹ which offers living polymer chains that can be elaborated into complex architectures. Since then several living radical polymerization techniques that allow the growth of well-controlled macromolecules with precise nanoscale physical and chemical properties have been discovered, namely atom-transfer radical polymerization (ATRP) developed in 1995 by Sawamoto and Matyjaszewski and reversible addition-fragmentation chain-transfer (RAFT) developed by Moad, Rizzardo and Thang at CSIRO in 1998.^{24,30–32} Out of these living controlled polymerization techniques, ATRP is most relevant to this work and preferred method for systems requiring surface-initiated polymerization. Matyjaszewski successfully tackled the problem of very fast radical propagation rates of conventional radical polymerization (monomer adds to the chain length with frequency ~ 1 ms equivalent to 1000 monomer additions each second), by extending lifetime of propagating chain in radical polymerization techniques from less than a second to greater than an hour, by establishing equilibrium between radicals and dormant species. This technique is a versatile technique for polymer grafting, which utilizes transition metal complexes to mediate a dynamic equilibrium between dormant and active species. Metal catalysts, such as copper, in its lower

oxidation state abstract halogen atom from the initiator, creating active radicals that can participate in propagation as shown in Figure 1.2.²⁴ The steps typically include activation of the initiator using copper and ligand, monomer addition and deactivation of thousand of chains. ATRP allows tremendous control of polymer architecture chain length, molecular weight, polydispersity index (PDI), composition and functionality and has been utilized to synthesize complex architectures such as gradient, block and star copolymers, micro-gels, organic-inorganic hybrids, nanostructures carbons and polymer brushes from variety of substrates including gold, silicon, cellulose fibers, and porous membranes. However, two major drawbacks associated with ‘normal’ ATRP involving the use of large quantities of copper catalyst and extreme sensitivity to oxygen, necessitating steps for costly purification steps and demanding stringent inert conditions, make normal ATRP less desirable. Since radical polymerizations are sensitive to oxygen and always include terminations, the concentration of catalysts exceeds 1000 ppm in normal. To overcome these drawbacks, Matyjaszewski developed a new approach called activators regenerated by electron transfer or ARGET-ATRP in which Cu (II) is constantly reduced to Cu (I) using affordable reducing agent such as ascorbic acid, phenol, sugar, hydrazine, amine, thereby limiting amount of copper required for polymerization from 1000’s of ppm to tens of ppm levels.³³⁻³⁶ In addition, this approach showed increased tolerance to limited amounts of oxygen and is applicable to diverse monomers such as styrene, methacrylate, and acrylamides, making ARGET-ATRP a preferred method of grafting in this work. Since its discovery, ATRP catalytic systems have evolved to ppm Cu (ARGET and initiators for continuous activator regeneration (ICAR) in 2006 and supplemental activator and reducing agent (SARA) ATRP

in 2013).^{37,38} Irrespective of the techniques, engineering macromolecules using controllable techniques into complex architectures using environmentally friendly means remains at the forefront of the discoveries, thus enabling nanotechnology and development of new functional materials. In this work, we will utilize surface-initiated ATRP where the selected hydrophilic, hydrophobic, cationic, anionic, or zwitterion monomers are polymerized uniformly from the initiators immobilized on the substrate of choice to form homogenous polymer layers.

1.2.1.3 Factors Affecting Protein Adsorption

Several different parameters related to the surface, types of protein as well as the solution influence the extent, the kinetics, and energetics of protein adsorption on a surface. As such, the fundamentals of protein adsorption have been studied using bare substrates such as glass, metals, mica, quartz as well with modifications using self-assembled monolayers, silane chemistry, and polymer-grafting techniques.^{39,40} The amount of adsorbed proteins depends on the physicochemical properties of the surfaces such as surface wettability as hydrophobic domains preferentially add to hydrophobic sites, binding more proteins compared to a hydrated hydrophilic surface that generally resists protein adsorption. The composition of the brush chemistry, as well as its surface potential, dictates charge distribution of ions in solutions and proteins, influencing the type of intermolecular forces governing substrate-protein interactions. Surface inhomogeneity often increases protein binding as non-uniform surfaces provide more domains for protein interactions, and the characteristics of the grafted polymer such as thickness, molecular weight, grafting density, chain flexibility, swelling influence the modes of protein adsorption. In addition to surface

properties, protein characteristics such as protein structure and stability of intramolecular bonds which dictates rates of protein unfolding, size of protein as large molecules provide more active sites, molecular weight, surface charge as well as protein conformation play an important role in adsorption behavior. Stable proteins cannot unfold to a greater extent and form more contact relative to unstable ones, and proteins that can unfold rapidly can form more surface contact quickly. In addition, crucial phenomena such as dehydration of surface as well as protein, structural rearrangement and conformation changes of protein as well as redistribution of surface charged groups upon adsorption significantly affect protein adsorption phenomena. For systems regulated by charged species, solution properties such as pH, ionic strength, buffer composition, temperature and the amount of interfacial water regulates protein-surface interactions.⁴¹ To understand the influence of substrate-protein-solution characteristics on protein adsorption several experimental techniques are available including ellipsometry, quartz-crystal microbalance (QCM), surface plasmon resonance (SPR), dual polarization interferometry (DPI), neutron and X-ray reflectivity, atomic force microscopy (AFM), surface force apparatus (SFA), solution-depletion technique, differential scanning calorimeter (DSC), and nuclear magnetic resonance (NMR).⁴²

1.2.1.4 Thermodynamics of Protein Adsorption

The interactions that occur concurrently between proteins, surface and solvent near the adsorption surface dictate the amount of adsorbed proteins. As such, protein adsorption occurs spontaneously when the change in Gibbs free energy (ΔG_{ads}) of a system is negative, and is energetically favorable through processes causing a decrease in enthalpy (ΔH_{ads}) or an increase in entropy of the system (ΔS_{ads}) or when slight increase in enthalpy can be

compensated by a large decrease in entropy. The highly structured or compact nature of protein due to the presence of hydrophobic interactions as well as hydrogen bonding reduces its mobility as well as conformation entropy.⁴³ However, a typical protein adsorption event on a hydrophobic surface process involves diffusion of protein towards the substrate and dehydration of the solvated layer around the protein near the substrate-polymer interface, which results in an increase in entropy that acts as a driving force for adsorption of protein on non-polar surfaces. In addition, the molecular interactions and surface forces present between proteins and surfaces serve as driving forces for protein adsorption mediated by secondary bond formation such as electrostatics, hydrogen bonding and dispersive interactions in the order of decreasing bond energy.⁴⁴ However in hydrophilic substrates, there is no significant contribution of entropy to drive off the solvated layer around the protein, thereby impeding protein adsorption. Finally, adsorption can take place through various modes – adsorption at the top layer of the brush for protein sizes higher than inter-brush distance, adsorption due to polymer brush compression due to the large protein size and strong adsorption, interpenetration of the protein into the polymer brush and subsequent protein-polymer complexation, and the adsorption of protein on the surface of the material post interpenetration without any disturbance to the polymer brushes for proteins with radii much smaller than inter-layer distance.⁴⁵

1.2.1.5 Nonwoven Fabrics

Nonwoven fabrics are flat, porous, web-like structures made of individual short and long fibers of natural or synthetic materials bound together by either chemical, thermal or mechanical means.⁴⁶ Using different manufacturing processes, nonwoven fabrics are

engineered to have unique characteristics such as large surface to volume ratio, fiber diameter, density, porosity, pore size distribution, and thickness, providing specific functionality such as absorbency, elasticity, filtration properties, liquid repellency, strength, flame retardancy, shock adsorption, making them useful in numerous applications in filtration, geotextiles medical and hygiene industry.^{46,47} These nonwovens can be manufactured economically at very high throughputs greater than 1000 ft. per min, and are very inexpensive making them cost effective as single-use products, as well as products requiring long-term durability. Typically in a manufacturing process, nonwoven fabrics start as loose webs and are carded into position either mechanically in the dry laid process, using controlled air stream in the air laid process or transported by water in the wet laid process, after which fibers are fused together using resins, heat, punched with needles (needle punching) or meshed with high velocity water (hydro entangling) to form nonwoven fabrics with carefully engineered properties. Alternatively, in the meltblown and the spun bond process, polymer pellets are melted and extruded through a die to form filaments, which after extenuation using hot air forms fibers that are driven to the collector plate.⁴⁷ A typical meltblowing process consists of an extruder that extrudes pre-heated polymer, metering pump that maintains desired pressure for uniform delivery of polymer to the die, and the die assembly consisting of air manifolds that sets the temperature of air as shown in Figure 1.3. The hot air stream draws the polymer starting at the die tip, fractures the polymer stream and creates entangled microfiber, which are subsequently cooled by secondary air. The fibers manufactured using this process have very high entanglements that contribute to the strength of the fiber and forms fine, low porosity, low orientation (isotropic) and soft fibers with

broad fiber diameter distribution compared to spun bond process that forms fibers with higher diameter, strength to weight ratio and higher degree of orientation. By systematically varying polymer parameters such as polymer type (polyethylene, polypropylene polyesters, polycarbonates, polystyrene, polyamides and polyurethanes), molecular weight, viscosity; extruder conditions such as temperature and shear; hot air conditions such as temperature and velocity; die conditions such as temperature and air flow rate profiles; die-to-collector distance, ambient air and laydown conditions, nonwoven fabrics with desired fiber diameter, porosities and basis weight can be obtained. The intrinsic benefit associated with these fibers such as high surface area and high porosities that results in low-pressure drops makes them suitable choice for protein adsorption applications.⁴⁶⁻⁴⁹

1.2.1.6 Research Goals

The absence of reactive functional groups on polyester fibers limits their possibility for protein binding, desirable in applications such as wastewater purification and bio-filtration. The main research goal in **Chapter 2** is to modify polybutylene terephthalate (PBT) with surface-active groups that facilitate attachment of initiators to graft random hydrophilic copolymers using surface initiated polymerization techniques. The copolymer architecture will be studied for enhanced capture and release of model lysozyme protein, and the effects of pH on adsorption of lysozyme, fibrinogen and bovine serum albumin (BSA) will be studied. The adsorption behavior will then be interpreted in terms of the balance of protein-surface and protein-protein interactions.

1.2.2 Synthesis of Cellulose Nanocrystals and Interactions with Polymers

Cellulose nanocrystals are cellulose-based derivatives obtained from different raw materials such as algae, bacteria, cotton, wood pulp, and tunicates using purification techniques to remove non-cellulosic biomass and modifications such as acid hydrolysis using sulfuric acid and hydrochloric acid to dissolve the amorphous regions, leaving behind highly crystalline and ordered domains called cellulose nanocrystals (see Figure 1.4). The length and width of resulting nanocrystals varies between 50-500 nm and 1-20 nm respectively, and properties such as morphology, chemistry and degree of crystallinity vary significantly depending on source of cellulose and purification techniques. Nonetheless, its unique properties such as biocompatibility, low density (1.6 g/cm^3), high aspect ratio, high stiffness (110-220 GPa in axial direction and 10-50 GPa in transverse direction), high tensile strength (7.5-7.7 GPa), high thermal stability and low expansion coefficient, liquid crystalline properties, rheological modifiers, versatile surface functionality, combined with low environmental and production costs, makes CNC's unique for applications as rheological modifiers, optical and barrier coatings, sensors and catalysis, textile development, and lightweight packaging.^{50,51} Since its discovery primarily in the 1990s, this material has been used as a valuable biocompatible commodity, and several research areas utilizing CNC has focused on its synthesis and isolation,^{50,51} interactions with different solvents,⁵² adsorption of polyelectrolytes and neutral polymers,⁵³ rheological properties,⁵⁴ self-assembly of CNC suspensions,^{55,56} surface functionalization,⁵⁷ fabrication of CNC-based films,⁵⁸ CNC-based fibers composites,⁵⁹ and 3-D structures such hydrogels and aerogels.^{58,60} We briefly review

some previous work done on the rheological properties of CNC based systems to establish where Chapter 3 sits in the research spectrum.

1.2.2.1 Interaction of CNC's with Polymers

Cellulose nanocrystals are unique materials which depending on the amount and presence of adsorbing or non-adsorbing polymers can form gels. For instance, the interaction of rod-shaped nanocrystalline cellulose with two water-soluble polymers, non-ionic hydroxyethyl cellulose (HEC) and ionic carboxymethyl cellulose (CMC) investigated using viscoelastic rheological measurements and isothermal titration calorimetry revealed gel formation with yield stresses, which was attributed to depletion flocculation due to the presence of non-adsorbing polymers.⁶¹ The gelation concentration was reduced after addition of small amounts of adsorbing polymers such as non-ionic polysaccharides which increased the effective volume fraction of CNC dispersions, causing gelation at much lower concentration.⁶² The interaction of two water-soluble polymers, anionic sodium polyacrylate (PAAS) and non-ionic polyethylene glycol (PEG) on self-assembly of commercial CNC suspension, studied using quartz-crystal microbalance revealed adsorption of PEG onto CNC most likely due to steric stabilization and hydrogen bonding between CNC's and PEG, but absence of adsorption of PAAS onto CNC due to unfavorable electrostatic interactions.⁶³ However, studies have demonstrated that hydrogen bonding does not play an important role because the cellulose surface hydroxyl groups are not sufficiently acidic to form hydrogen bonding with oxygen in PEG dissolved in water, and the adsorption is rather entropically driven.⁶⁴ Depletion flocculation was the primary reason for gelation behavior of semi-dilute CNC's in semi-dilute un-entangled carboxymethyl cellulose solutions, whereas weak

depletion interactions occurred in systems with PEO after surfaces were saturated with PEO adsorption.⁵³ These interactions between water-soluble polymers and cellulose nanocrystals can be used in the design of new systems that require mechanical reinforcement via favorable polymer-CNC interactions. The gelation properties can be studied using dynamic oscillatory rheological methods.

Dynamic oscillatory rheological experiments can be used to study the viscoelastic behavior of polymeric systems. In a typical oscillatory experiment, a sinusoidal strain (γ) is applied with amplitude (γ_0) and frequency (ω), to a sample placed between plates of either parallel, cone or serrated geometries as shown in equation (1), and the resulting response of the material in the form of steady sinusoidal stress (σ) is measured using the rheometer as shown in equation (2).

$$\gamma = \gamma_0 \sin \omega t \quad (1)$$

$$\sigma = \sigma_0 (\sin \omega t + \delta) \quad (2)$$

Based on the changes in phase angle (δ), rheological behavior of a sample can be classified as either elastic ($\delta = 0$), viscous ($\delta = 90$) or viscoelastic ($0 < \delta < 90$). The resulting response of the material can be represented using equation (3), where G' is the storage modulus which measures the elasticity of the sample, and G'' is the viscous modulus which measures the

$$\sigma = \sigma_0 (G'(\omega) \sin(\omega t) + G''(\omega) \cos(\omega t)) \quad (3)$$

$$G' = \frac{\sigma_0}{\gamma_0} \cos \delta \quad (4)$$

$$G'' = \frac{\sigma_0}{\gamma_0} \sin \delta \quad (5)$$

This region can be established using stress sweep experiments by applying increasing oscillatory strains or stresses to the sample at constant frequency, and measuring the response of the material is measured which shows distinct regions where moduli is independent of strain often referred to as the linear viscoelastic regime (LVE) and the strain at which the microstructure. Rheological measurements will be obtained using UV accessory on DHR-3 as shown in Figure 1.5.

1.2.2.2 Rheology of Cellulose Nanocrystals and Polymer-CNC Composites

Aqueous suspensions of CNC's show unique concentration dependent phase behavior and interesting rheological properties. It is well established that CNC's show four distinct phases depending on the concentration – isotropic, mixture of isotropic and liquid crystals (biphasic), liquid crystals and gels.^{54,65–68} At very dilute concentrations in the isotropic regime, a Newtonian plateau at low shear rates and shear thinning at high shear rates is observed. As the concentration increases, the dispersion consists of mixtures of isotropic and liquid crystal domains, resulting in a gradual increase in viscosity. Further increases in concentration beyond phases containing isotropic and liquid crystal domains results in pure liquid crystal phase identified as chiral nematic or cholesteric, and the critical concentration of this biphasic to liquid crystalline transition is seen as a sharp increase in low shear viscosity versus concentration plots.^{54,67} Typically shear rheology of CNC's in the liquid crystal regime show a three-region viscosity profile – low shear rate regions where pronounced shear thinning is observed, a semi-plateau region where shear thinning is less pronounced, and a high shear regions where shear thinning behavior is observed but much less pronounced than at low shear rates. At much higher concentration, the three region-shear

thinning disappears and the suspension behaves like a rheological gel showing a single shear thinning behavior.⁶⁹⁻⁷³ The concentration dependent phase behavior of CNC's can also be observed using polarized optical microscopy, as isotropic phase appears dark and liquid crystalline phase is birefringent in cross-polarized images. The relative composition of the isotropic and anisotropic (liquid crystalline) phases can be quantified by measuring the height of respective compositions. The phase behavior, however, is dependent on factors such as source of nanocrystals, aspect ratio,⁷⁴ surface characteristics,⁷⁵ degree of sulfation⁶⁷ and amount of salt.⁷⁶

1.2.2.3 Research Goals

The absence of control over crosslinking kinetics and mechanical integrity of photocrosslinkable polymers limits their use in several applications. The main research goal in **Chapter 3** is to utilize cellulose nanocrystals (CNC) to modulate crosslinking kinetics as well as enhance mechanical performance of aqueous photoactive polyvinyl alcohol derivative, poly (vinyl alcohol), N-methyl-4 (4'-formylstyryl) pyridinium methosulfate acetal (PVA-SbQ). Most specifically, the interactions between PVA-SbQ and CNC present in dispersions prepared using simple solution mixing will be studied using rheological measurements. The changes in rheological behavior of PVA-SbQ before and after exposure to UV will be studied, and the precise mechanism to explain any observed changes will be proposed.

1.2.3 Fundamentals of Polymer Nanocomposites

The advances in polymer composite materials over many decades have been realized through the use of nanoscale fillers, often referred to as polymer nanocomposites (PNC),

replacing their micron-sized counterparts to enhance physical (scratch resistance, barrier properties, solvent transport), thermo-mechanical (stiffness, bulk modulus, toughness, crystallization, thermal stability), electrical (conductivity), optical (transparency) and rheological properties.^{1,77,78} In contrast to micron-size fillers that require significantly high loadings for property reinforcement, resulting in issues of high viscosity during polymer processing, nanofillers can achieve desirable properties at significantly lower loadings. This remarkable ability of nanofillers to reinforce polymer matrices even at low contents arises due to its length scale, which is typically between 0.1 to 100 nm, comparable to length scales of polymer, giving rise to unique nanoscale interactions that influence macroscopic properties.⁷⁷ The concomitant increase in surface area with the reduction in particle size offers high volume of the interphase, regions between bulk polymer and the particle, often considered to be the origin of reinforcement of macroscopic properties. In fact, the properties of PNC's are dominated mostly by the interphase compared to the bulk polymer at very high nanofiller loadings, making the interphase very significant in dictating the interactions between the polymer and nanofiller. However, a key challenge arises when initially well-dispersed nanofillers start to aggregate due to strong filler-filler interactions, significantly altering the distribution and the amount of interface available in the nanocomposite and negating the benefits of nanoscale fillers.^{79,80} The driving force for such re-agglomeration has enthalpic origins primarily in the form of van der Waal's attraction, but can be controlled through interfacial modifications via polymer grafting to modulate both enthalpic and entropic interactions.⁸¹ Nonetheless, any surface chemistry used for interface modification should promote high polymer wetting and interfacial adhesion to create very strong interfaces

that can effectively transfer load from fillers to the matrix, thereby reinforcing the properties of the bulk polymer. The presence of well-dispersed homogenous nanofillers is a necessary condition; however, it is not sufficient for the accurate prediction of macroscopic behavior of PNC's, since the observed macroscopic properties is a complex function of nanofiller surface area, aspect ratio, loading, alignment, interface chemistry, volume of interphase, interfacial adhesion between particle-polymer, morphology of the host polymer as well as processing methods such as solvent blending, in-situ polymerization and melt-mixing.⁸²

While unifying theories and experimental observations to establish direct correlation between nanoscale properties with macroscopic reinforcement remains elusive, glass transition temperature (T_g) of the polymer offers insight into the nature of polymer-filler interactions.⁸³ The relative shifts in T_g after nanofiller inclusions capture the effect of nanofillers on the polymer dynamics at the interface. The extent of favorable polymer-nanofiller interactions dictates the direction of this shift, with attractive interfaces showing upward shifts in T_g and repulsive interfaces showing downward shifts in T_g , allowing for the possibility of correlating such shifts with aggregation behavior and polymer-filler interactions. These ideas tested in thin polymer films have demonstrated that T_g is a function of film thickness and the magnitude as well as the direction of the shift depends on the polymer-substrate interactions. The absence and presence of interactions were mimicked using free standing films, films supported on a substrate and films capped between two rigid walls. Interestingly, the trends in T_g shifts for model homopolymer polystyrene (PS) system containing untreated silica (non-wetting to PS) resembled that of free standing films, whereas the trends for PS containing PS-grafted silica (wetting to PS) resembled that of capped-

surfaces, successfully establishing quantitative equivalence between thin films and nanocomposites.⁸⁴ Similarly, measurements in both bulk and in thin films in PS-carbon nanotube systems showed an increase in T_g of 3°C, and similar dependence on thickness with T_g reduction with decreasing thickness below 45 nm.⁸⁵ For systems containing particles grafted with polymer brushes to increase compatibility with the matrix, the wetting properties can be tuned by appropriately controlling the grafting density and molecular weight of brushes relative to that of the matrix. For PS-grafted silica particles, low molecular weight PS melt matrix wets the PS-grafted silica accompanied by increase in T_g , in sharp contrast to high molecular weight PS melt matrix that does not wet the surface of PS-grafted silica.^{86,87} The reductions in T_g of 25°C attributed to non-adhering nanoparticles in poly(methyl methacrylate (PMMA)-alumina composites were suppressed using PMMA-coated alumina.^{88,89} Several examples exist that establish a correlation between polymer wetting nanofillers surface and shifts in T_g . For example, a shift of 30°C ad 40°C was reported for functionalized graphene sheets in PMMA and PAN respectively at very low loadings.⁹⁰ An increase in T_g was observed for atactic-PMMA systems containing thermally reduced graphene in nanocomposites processed via in-situ polymerization.⁹¹

Previous work in the field of PNC's have used numerous types of nanoscale fillers such as silica, aluminum oxide, titanium dioxide, polyhedral oligomeric silsesquioxane (POSS),⁹² layered-silicates,⁹³ graphene,¹³ carbon nanotubes,¹² and cellulose nanocrystals.¹⁴ The subject of Chapter 4, however, pertains to fiber-based composite fabrication using a new type of carbon-based nanofiller called nanodiamonds.

1.2.3.1 Synthesis, Purification and Applications of Nanodiamonds

The observation of single crystals of cubic diamond particles made by scientists from the Soviet Union in 1960's in soot formed by explosion of TNT and hexogen mixtures under oxygen deficient conditions marked the discovery of a novel carbon-based material known as nanodiamonds (ND) shown in Figure 1.6. However, it was not until early 1990's when ND's emerged with great potential for wide-ranging applications in areas such as bioimaging,⁹⁴⁻⁹⁹ chromatography,¹⁰⁰⁻¹⁰² coatings and composites,¹⁰³ drug delivery,¹⁰⁴⁻¹⁰⁸ electrochemistry,¹⁰⁹⁻¹¹³ and tribology.¹¹⁴⁻¹¹⁷ The delayed introduction was in part due to lack of suitable techniques to disintegrate nanodiamonds with tight core into primary particles. However, since then the growth in ND application areas, as well as interests in scientific community and industries alike, is fueled by the emergence of cheaper commercial scale production strategies. With advances in ND-based research, the process called detonation synthesis involving explosion of trinitrotoluene (TNT) and hexogen (RDX) mixture in a negative oxygen condition is often used in large scale and low-cost production of commercial ND's.¹¹⁸ The resulting product of a detonation event is a diamond core containing graphitic carbon and soot that require further purification. Acid-based oxidizing systems and air-based oxidizing treatments have shown to efficiently oxidize non-diamond or graphitic carbon, resulting in ultrafine particles with a diamond core containing carbon-oxygen functionality in its outer periphery.¹¹⁹⁻¹²³ This method of detonation synthesis produces ND's with particle size of roughly 4-10 nm, with narrow size distribution, spherical surface morphology, and strong agglomeration potential, in sharp contrast to methods employing high-pressure and high-temperature which yields ND's less than 100 nm with broad size distribution, faceted

morphology and low agglomeration potential.^{124,125} The purification treatments remove the graphitic layers (sp^2 carbon), exposing the inner domains containing sp^3 hybridized carbon with crystalline structure with interlayer spacing of ~ 0.21 nm corresponding to the diamond phase. Nonetheless, these particles have excellent properties such as high surface area, thermal conductivity, diamond-like hardness, biocompatibility and low cytotoxicity, and are attractive to enhance a variety of commercial products. As a result, the addition of trace amounts of nanodiamonds to alter the thermo mechanical properties of different polymers has been a subject of key interest to researchers in the nanodiamond community.

After decades of work dedicated toward synthesis, purification and isolation of ND's, researches have implemented them in numerous applications. Moreover, emerging studies pointing toward low cytotoxicity of ND's, in addition to their properties such as small particle size and dispersibility in water, have spurred their use as drug delivery vehicles, presenting itself as a viable alternative to other carbon-based materials with known toxicity.¹²⁶ Simple and cheap ways to produce continuously and homogeneously fluorescent ND's, combined with the stability of N-V defect on ND surface, has opened new avenues for ND's as biomarkers for use in biomedicine, replacing traditional markers beset with problems of photoblinking and photobleaching.⁹⁴⁻⁹⁹ ND's have also been used as anti-friction agents or lubricant additives and has shown to impart resistance to wear and tear of sliding surfaces.¹¹⁵⁻¹¹⁷ In addition, the exceptional diamond-like hardness, combined with its small particle size, has instigated research in ND based polymer fibers and coatings.¹⁰³

1.2.3.2 Nanodiamond Deaggregation

Despite these useful properties, however, ND's are composed of core aggregates consisting of bridging interparticle bonds that are very difficult to disintegrate. For applications requiring well-controlled single digit particle size such as in the fabrication of composites using ND's as reinforcing agents, the subject of Chapter 4 in this thesis, such aggregates pose significant difficulties during processing. Realizing the need to find ways to overcome this problem, researchers have come up with different de-aggregation strategies to disintegrate these tight cores including graphitization-oxidation, ultrasound and high-dynamic pressure pulse, stirred-media milling, bead-assisted milling, bead-assisted ultrasonic deaggregation (BASD) and salt-assisted ultrasonic deaggregation (SAUD). The graphitization-oxidation method reported by Xu *et al.* showed for the first time the possibility of breaking these extraordinarily tight aggregates by graphitizing the interlayers using heat treatment and oxidizing the confined graphitic layers.^{127,128} In this method, nanodiamonds are heat-treated in nitrogen and in air at high temperature, resulting in 50% particles with size less than 50 nm and ~1000-2000 nm. Another embodiment of the process yielded a range of particle sizes 5-10 nm (43%), 10-18 nm (25.2%), 1-5 nm (20.1 %), 36-60 nm (7%) and 18-36 nm (4.7%) and requires no post-processing. Using ultrasound and high pressure pulse on a pyrolytic graphite surface, Vul *et al.* obtained ND's with clusters between 2-3 nm and lateral dimensions of 10 nm on atomically smooth highly oriented pyrolytic graphite (HOPG) using atomic force microscopy.¹²⁹ Much more practical method, however, relies on use of bead-assisted milling techniques using ceramic, zirconia or silica based beads as milling agents.^{124,125,130-132} Krueger *et al.* and Edelman *et al.* were able to obtain particles sizes <10

nm using this approach; however, compromised purity due to contamination issues imparted by milling agents.^{133,134} Ozawa *et al.* similarly employed zirconia beads and strong acids used to avoid contamination. The resulting issues of contamination and generation of graphitic layer reported in bead-milling system was overcome by dry media assisted attrition milling, a milling method utilizing water soluble compounds, allowing easy removal through water rinsing.¹³⁵ Most recently, a very attractive method called salt-assisted ultrasonic deaggregation (SAUD) was reported in literature, wherein deaggregation of commercially available carboxylated nanodiamonds is achieved using combinations of salt, water and nanodiamonds in a specific ratio, resulting in reduced particle sizes, and avoiding issues associated with contamination and intricate post-processing. A simple water rinse was able to remove all the de-aggregation products, thereby offering cheap, easy, accessible and contamination-free approach to ND de-aggregation, opening up new avenues that require smaller particle size such as in the fabrication of polymer-ND based composites.¹³⁶

1.2.3.3 Nanodiamond-Based Polymer Nanocomposites

Several implementations of ND-based composites processed in various polymers such as poly (vinyl) alcohol (PVA),¹³⁷⁻¹³⁹ poly (methyl) methacrylate (PMMA),^{140,141} poly (L-lactic) acid (PLLA),¹⁴²⁻¹⁴⁴ polyacrylonitrile (PAN),¹⁴⁵ polyethylene (PE),^{146,147} and epoxy¹⁴⁸⁻¹⁵³ using solution casting, in-situ polymerization, melt compounding, compression molding, and electrospinning have reported remarkable increase in properties such as elastic modulus, tensile strength, elongation at break, toughness, hardness and glass transition temperature. Morimune *et al.* reported the success of ND-reinforcement in films of PVA, a biodegradable polymer, showing 186% increase in elastic modulus and 30% tensile strength

at 5 wt.% loading.¹³⁹ In another study by Maitra *et al.*, ND loadings at 0.6 wt.% improved elastic modulus and hardness of PVA films by 98% and 79% respectively.¹³⁸ Kurkin *et al.* reported PVA-ND fiber composites with increments of ~200% in longitudinal modulus at 7 wt.% loading.¹³⁷ Similar results were reported for another biodegradable thermoplastic polymer, PLLA. Across different studies, the effect ND's was to increase elastic modulus as well as tensile strength primarily due to increase in crystallization in PLLA. Additional studies of ND incorporation in polar polymers such as PMMA and PAN reveal property reinforcements upon addition of ND's. In addition to polar polymers, ND's have also been incorporated in non-polar, low cost polymer like PE to increase its mechanical properties. Incorporation of ND's functionalized using alkylation by Jee *et al.* and using silanization by Roumeli *et al.* in PE show enhancement in hardness of ~458% using 11 wt.% ethylhexyl functionalized ND, and 17.3 % increase in toughness at 0.5 wt.% loadings respectively.^{146,147} In addition, significant deviations in glass transition temperature (T_g) relative to bulk polymer in ND-based polymer composites have been reported. Morimune *et al.* reported 24°C increase in T_g in solution-casted films of PVA-ND,¹³⁹ Protopapa *et al.* reported 21°C shifts in T_g in ND-based PMMA resins,¹⁴⁰ Neitzel *et al.* and Roy *et al.* reported positive shifts of 14°C and 37 °C in T_g in epoxy-ND matrix cured using hardening agent respectively.^{149,152} These examples showing increments in mechanical properties as well as glass transition temperatures is indicative of ND's potential as reinforcing agents in polymer matrix. This work will investigate the reinforcing effects of ND's in fibers formed using electrospinning process as shown in Figure 1.7.

1.2.3.4 Research Goals

While numerous studies have provided direct evidence of nanodiamonds ability to reinforce bulk polymer matrices, precise understanding of structure-property-function relationships in relation to nanoscale aggregation, polymer-nanodiamond interactions as well as nanodiamond-nanodiamond interactions is non-existent. The main goal in **Chapter 4** is to investigate the interfacial aspects of multicomponent systems consisting of nanodiamonds in electrospun fibers of either semi-crystalline or amorphous polymers with different surface energies to create fundamental knowledge on their structure-property-function relationships.

1.3 Organization of Dissertation

In this dissertation, we present our findings on three different types of multicomponent systems consisting of copolymers, composite gels, and nanodiamond-filled composites. **Chapter 2** demonstrates successful surface modification of inert polyester thin films and nonwovens using atom-transfer radical polymerization (ATRP), and tests the efficacy of attached copolymers for capture and release of model lysozyme protein for applications such as wastewater treatment and bio fluid filtration of relevance to industry. **Chapter 3** focuses on modulating gelation kinetics and mechanical strength of photocurable poly(vinyl alcohol) derivative through network formation using cellulose nanocrystals, and studies microstructural changes using rheological techniques. **Chapter 4** seeks to establish fundamental knowledge on design principles important in the fabrication of nanodiamond-based composite electrospun fibers made from semi-crystalline and amorphous polymers. Finally, **Chapter 5** summarizes key results of each chapter and discusses experimental research that can be done in the future.

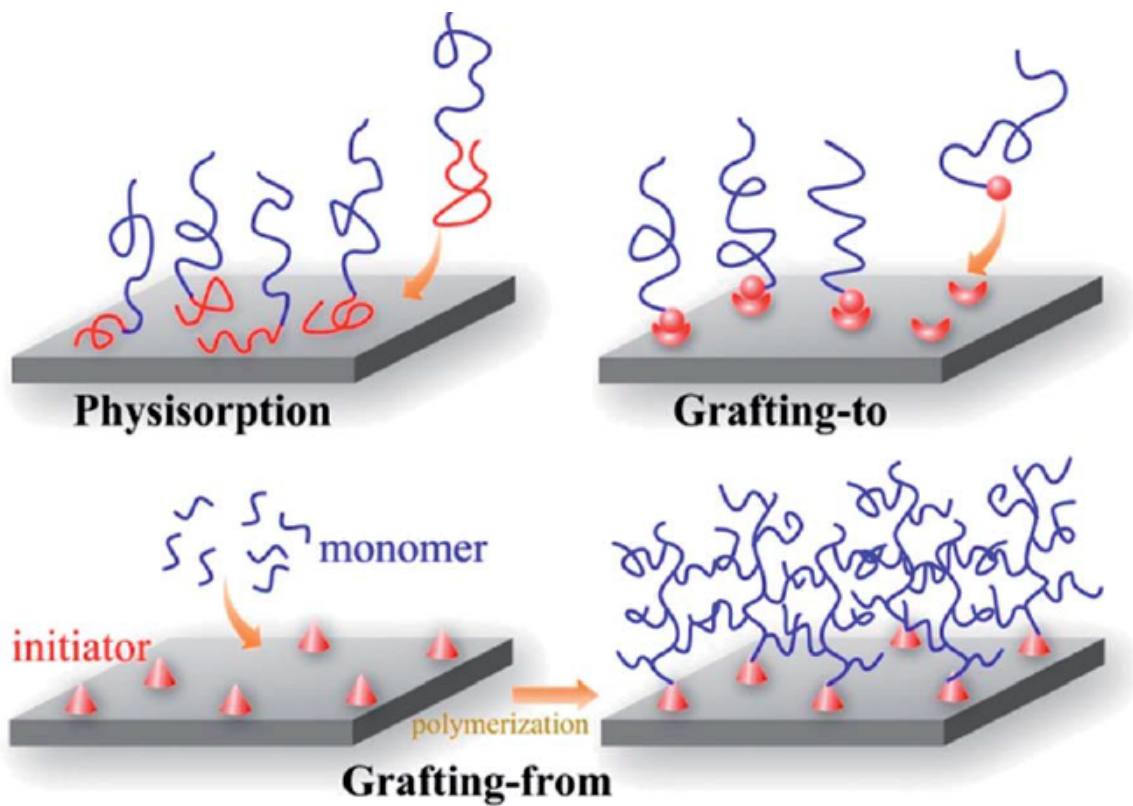


Figure 1.1 Grafting “From” vs. Grafting “To” Approach to Surface Modification for Protein Adsorption / Desorption.¹⁵⁴

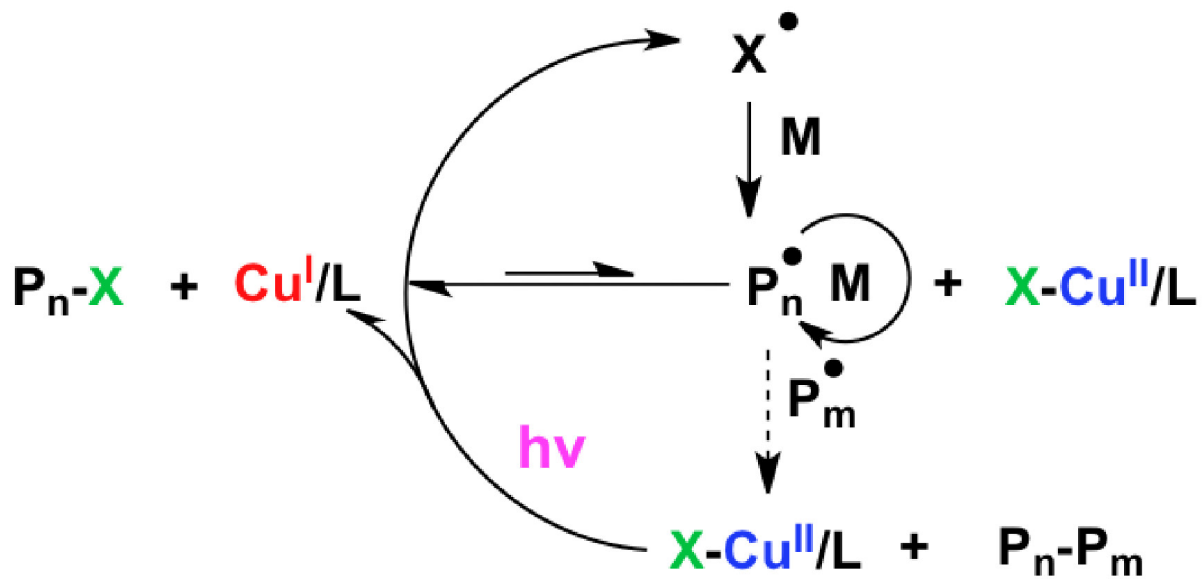


Figure 1.2 Aqueous ATRP route for polymer synthesis using grafting-from approach. (Adapted from Matyjaszewski Polymer Group, Carnegie Mellon University, 2016)

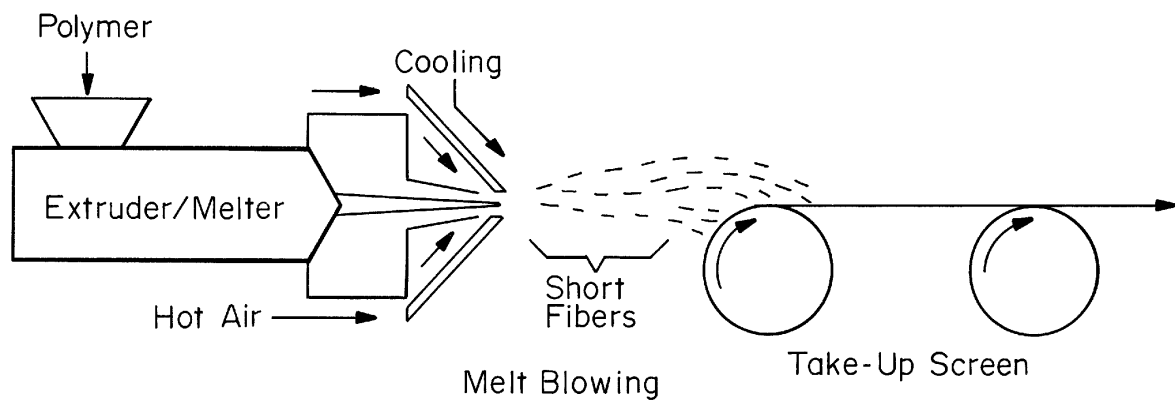


Figure 1.3 Schematic of meltblowing process consisting of extruder, metering pump and die assembly used to manufacture nonwovens.¹⁵⁵

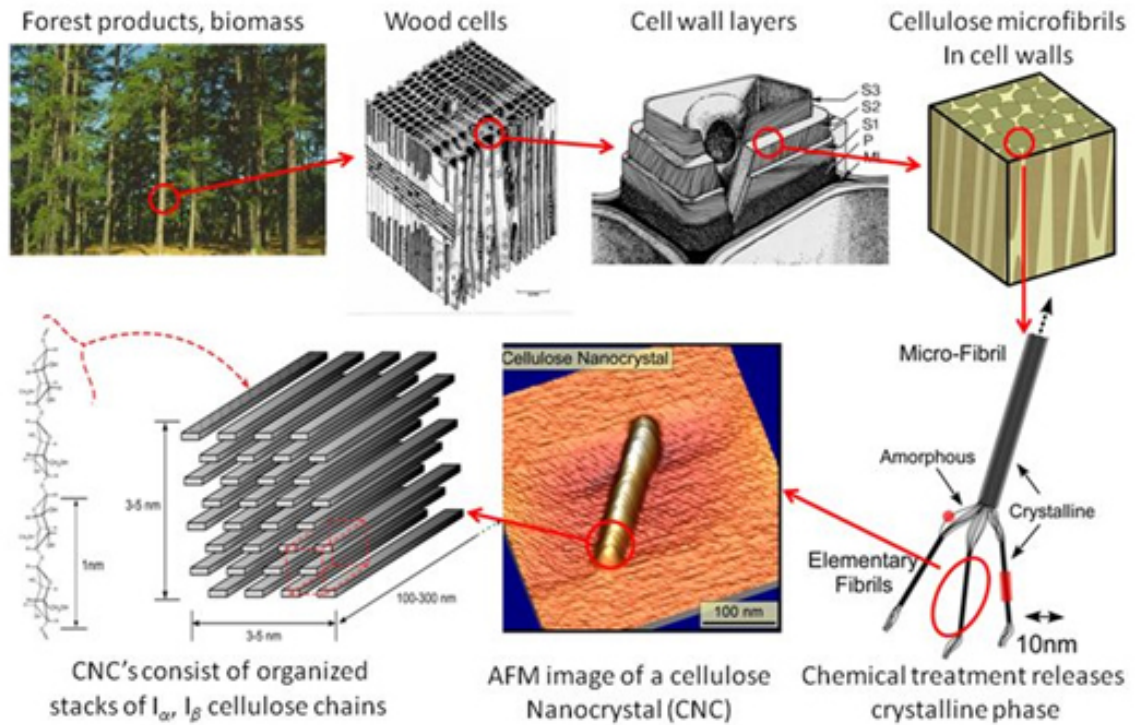


Figure 1.4 Cellulose nanocrystals extracted from forest products using acid hydrolysis. (Adapted from Substance, Scientific News and Innovation from ETS – New Class of Biomaterials: Cellulose Nanocrystals, 2014)

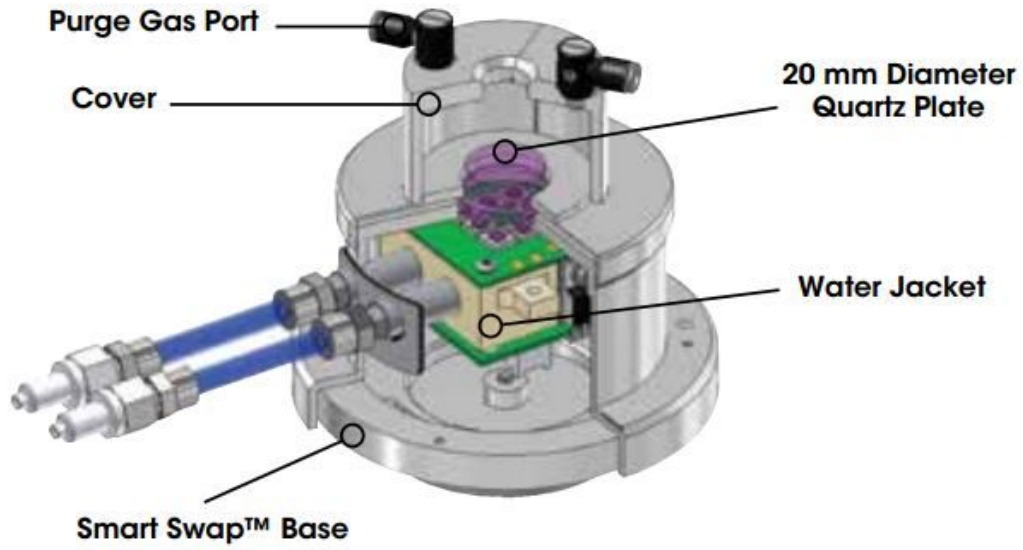


Figure 1.5 DHR-3 rheometer accessory to study in-situ UV crosslinking of photoactive poly(vinyl) alcohol derivative incorporating cellulose nanocrystals. (Adapted from TA Instruments Brochure, DE, 2015).

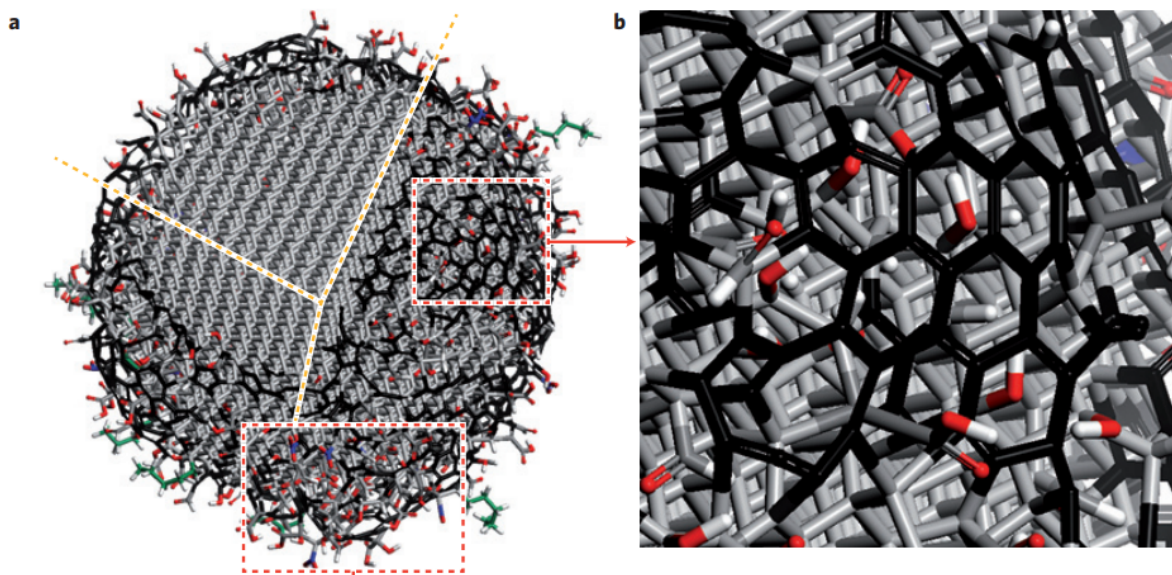


Figure 1.6 Structure of nanodiamonds showing presence of sp^2 carbons on the surface and sp^3 carbon in the inner core.¹⁵⁶

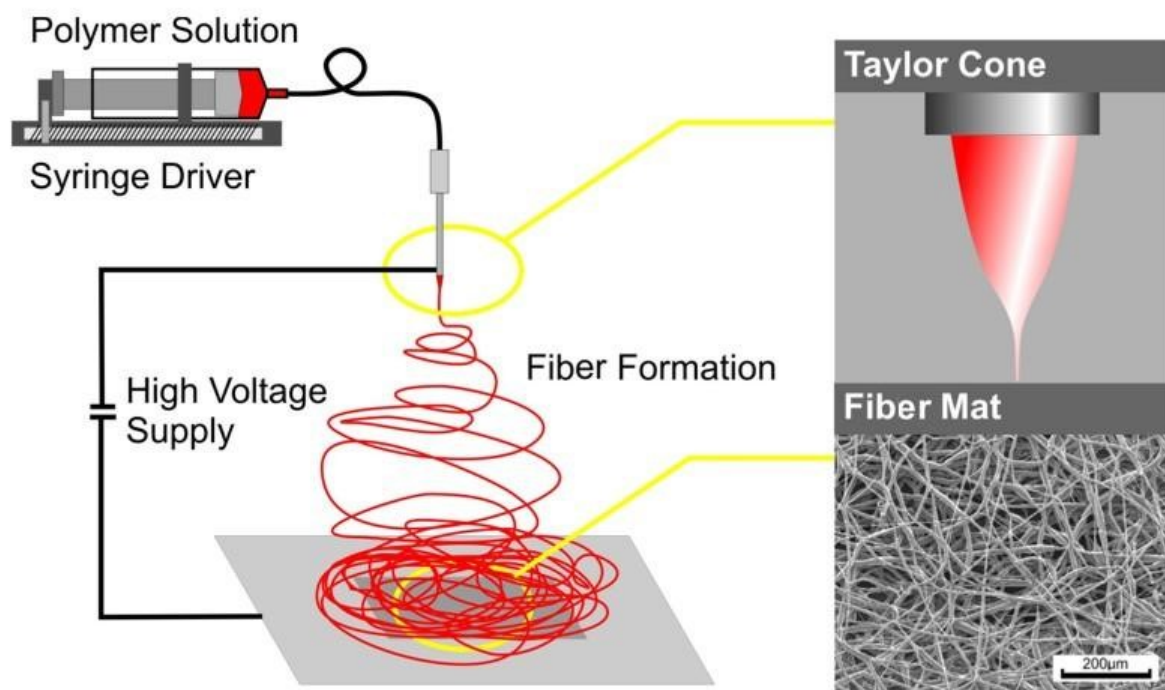


Figure 1.7 Schematic of electrospinning set up used to make polymer fibers with nanodiamonds. (Adapted from Oxolutia, 2014)

1.4 References

1. Jordan, J., Jacob, K. I., Tannenbaum, R., Sharaf, M. A. & Jasiuk, I. Experimental trends in polymer nanocomposites - A review. *Mater. Sci. Eng. A* **393**, 1–11 (2005).
2. Krishnamoorthy, M., Hakobyan, S., Ramstedt, M. & Gautrot, J. E. Surface-initiated polymer brushes in the biomedical field: Applications in membrane science, biosensing, cell culture, regenerative medicine and antibacterial coatings. *Chem. Rev.* **114**, 10976–11026 (2014).
3. Ahmed, E. M. Hydrogel: Preparation, characterization, and applications: A review. *J. Adv. Res.* **6**, 105–121 (2015).
4. Matyjaszewski, K. & Spanswick, J. Controlled/living radical polymerization. *Mater. Today* **8**, 26–33 (2005).
5. Grubbs, R. B. Nitroxide-mediated radical polymerization: Limitations and versatility. *Polym. Rev.* **51**, 104–137 (2011).
6. Kulshreshtha, A. K. A review of commercial polyblends based on PVS, ABS, and PC. *Polym. Plast. Technol. Eng.* **32**, 551–578 (1993).
7. Fasolka, M. J. & Mayes, A. M. Block Copolymer Thin Films: Physics and Applications. *Annu. Rev. Mater.* **31**, 323–355 (2001).
8. Edmondson, S., Osborne, V. L. & Huck, W. T. S. Polymer brushes via surface-initiated polymerizations. *Chem. Soc. Rev.* **33**, 14 (2004).
9. Katime, I., Quintana, J. R. & Price, C. Influence of the microstructural morphology on the mechanical properties of high-impact polystyrene. *Mater. Lett.* **22**, 297–301 (1995).
10. Fu, S. Y., Feng, X. Q., Lauke, B. & Mai, Y. W. Effects of particle size, particle/matrix interface adhesion and particle loading on mechanical properties of particulate-polymer composites. *Compos. Part B Eng.* **39**, 933–961 (2008).
11. Chand, S. Carbon fibers for composites. *J. Mater. Sci.* **35**, 1303–1313 (2000).

12. Moniruzzaman, M. & Winey, K. I. Polymer nanocomposites containing carbon nanotubes. *Macromolecules* **39**, 5194–5205 (2006).
13. Chee, W. K., Lim, H. N., Huang, N. M. & Harrison, I. Nanocomposites of graphene/polymers: a review. *RSC Adv.* **5**, 68014–68051 (2015).
14. Miao, C. & Hamad, W. Y. Cellulose reinforced polymer composites and nanocomposites: A critical review. *Cellulose* **20**, 2221–2262 (2013).
15. Wei, Q. *et al.* Protein interactions with polymer coatings and biomaterials. *Angew. Chemie - Int. Ed.* **53**, 8004–8031 (2014).
16. Krishnan, S., Weinman, C. J. & Ober, C. K. Advances in polymers for anti-biofouling surfaces. *J. Mater. Chem.* **18**, 3405 (2008).
17. Banerjee, I., Pangule, R. C. & Kane, R. S. Antifouling coatings: Recent developments in the design of surfaces that prevent fouling by proteins, bacteria, and marine organisms. *Adv. Mater.* **23**, 690–718 (2011).
18. Latour, R. Biomaterials: protein-surface interactions. ... *Biomater. Biomed. Eng.* 1–15 (2005). doi:10.1081/E-EBBE-120041856
19. Andrade, J. D. & Hlady, V. Protein adsorption and materials biocompatibility: A tutorial review and suggested hypotheses. 1–63 (1986). doi:10.1007/3-540-16422-7_6
20. Fristrup, C. J., Jankova, K. & Hvilsted, S. Surface-initiated atom transfer radical polymerization—a technique to develop biofunctional coatings. *Soft Matter* **5**, 4623 (2009).
21. Bhattacharya, A. & Misra, B. N. Grafting: A versatile means to modify polymers: Techniques, factors and applications. *Prog. Polym. Sci.* **29**, 767–814 (2004).
22. Azzaroni, O. Polymer brushes here, there, and everywhere: Recent advances in their practical applications and emerging opportunities in multiple research fields. *J. Polym. Sci. Part A Polym. Chem.* **50**, 3225–3258 (2012).
23. Blas, H., Save, M., Boissière, C., Sanchez, C. & Charleux, B. Surface-initiated

- nitroxide-mediated polymerization from ordered mesoporous silica. *Macromolecules* **44**, 2577–2588 (2011).
24. Matyjaszewski, K. Atom Transfer Radical Polymerization. *Chem. Rev.* **101**, 2921–2990 (2001).
 25. Ohno, K. *et al.* Surface-initiated reversible addition-fragmentation chain transfer (RAFT) polymerization from fine particles functionalized with trithiocarbonates. *Macromolecules* **44**, 8944–8953 (2011).
 26. Brittain, W. J. & Minko, S. A structural definition of polymer brushes. *J. Polym. Sci. Part A Polym. Chem.* **45**, 3505–3512 (2007).
 27. Milner, S. T., Witten, T. A. & Cates, M. E. Theory of the Grafted Polymer Brush. *Macromolecules* **21**, 2610–2619 (1988).
 28. Smid, J., Van Beylen, M. & Hogen-Esch, T. E. Perspectives on the contributions of Michael Szwarc to living polymerization. *Prog. Polym. Sci.* **31**, 1041–1067 (2006).
 29. Rizzardo, E. & Solomon, D. H. On the origins of nitroxide mediated polymerization (NMP) and reversible addition fragmentation chain transfer (RAFT). *Aust. J. Chem.* **65**, 945–969 (2012).
 30. Matyjaszewski, K. Atom Transfer Radical Polymerization (ATRP): Current Status and Future Perspectives. *Macromolecules* **45**, 4015–4039 (2012).
 31. Tang, H. *et al.* Highly active copper-based catalyst for atom transfer radical polymerization. *J. Am. Chem. Soc.* **128**, 16277–85 (2006).
 32. Horn, M. & Matyjaszewski, K. Solvent Effects on the Activation Rate Constant in Atom Transfer Radical Polymerization. (2013).
 33. Matyjaszewski, K., Dong, H., Jakubowski, W., Pietrasik, J. & Kusumo, A. Grafting from surfaces for ‘everyone’: ARGET ATRP in the presence of air. *Langmuir* **23**, 4528–31 (2007).
 34. Hansson, S., Östmark, E., Carlmark, A. & Malmström, E. ARGET ATRP for Versatile

- Grafting of Cellulose Using Various Monomers. *ACS Appl. Mater. Interfaces* **1**, 2651–2659 (2009).
35. Simakova, A., Averick, S. E., Konkolewicz, D. & Matyjaszewski, K. Aqueous ARGET ATRP. *Macromolecules* **45**, 6371–6379 (2012).
 36. Paterson, S. M. *et al.* The synthesis of water-soluble PHEMA via ARGET ATRP in protic media. *J. Polym. Sci. Part A Polym. Chem.* **48**, 4084–4092 (2010).
 37. Konkolewicz, D. *et al.* ICAR ATRP with ppm Cu catalyst in water. *Macromolecules* **45**, 4461–4468 (2012).
 38. Kryś, P., Wang, Y., Matyjaszewski, K. & Harrison, S. Radical Generation and Termination in SARA ATRP of Methyl Acrylate: Effect of Solvent, Ligand, and Chain Length. *Macromolecules* **49**, 2977–2984 (2016).
 39. Minko, S. Responsive Polymer Brushes. *J. Macromol. Sci. Part C Polym. Rev.* **46**, 397–420 (2006).
 40. Uyama, Y., Kato, K. & Ikada, Y. Surface Modification of Polymers by Grafting. *Grafting/Characterization Tech. Model.* **137**, 1–39 (1998).
 41. Rabe, M., Verdes, D. & Seeger, S. Understanding protein adsorption phenomena at solid surfaces. *Adv. Colloid Interface Sci.* **162**, 87–106 (2011).
 42. Nakanishi, K., Sakiyama, T. & Imamura, K. On the adsorption of proteins on solid surfaces, a common but very complicated phenomenon. *Biosci. Bioeng.* **91**, 233–244 (2001).
 43. Norde, W. Driving forces for protein adsorption at solid surfaces. *Macromol. Symp.* **103**, 5–18 (1996).
 44. Sakata, S., Inoue, Y. & Ishihara, K. Molecular Interaction Forces Generated during Protein Adsorption to Well-Defined Polymer Brush Surfaces. *Langmuir* **31**, 3108–3114 (2015).
 45. Taylor, W., Ebbens, S., Skoda, M. W. A., Webster, J. R. P. & Jones, R. A. L. Mode of

- lysozyme protein adsorption at end-tethered polyethylene oxide brushes on gold surfaces determined by neutron reflectivity. *Eur. Phys. J. E. Soft Matter* **38**, 14 (2015).
46. Dutton, K. C. Overview and Analysis of the Meltblown Process and Parameters. *J. Text. Apparel, Technol. Manag.* **6**, 1–24 (2008).
 47. Bresee, R. R. & Ko, W. Fiber Formation During Melt Blowing. *INJ* 21–28 (2003).
 48. Bo, Z. Production of polypropylene melt blown nonwoven fabrics: Part II -Effect of process parameters. *Indian J. Fibre Text. Res.* **37**, 326–330 (2012).
 49. Ellison, C. J., Phatak, A., Giles, D. W., Macosko, C. W. & Bates, F. S. Melt blown nanofibers: Fiber diameter distributions and onset of fiber breakup. *Polymer.* **48**, 3306–3316 (2007).
 50. Habibi, Y., Lucia, L. A. & Rojas, O. J. Cellulose Nanocrystals: Chemistry, Self-Assembly, and Applications. **d**, 3479–3500 (2010).
 51. Trache, D., Hussin, M. H., Haafiz, M. K. M. & Thakur, V. K. Recent progress in cellulose nanocrystals: sources and production. *Nanoscale* **9**, 1763–1786 (2017).
 52. Reid, M. S., Villalobos, M. & Cranston, E. D. Cellulose nanocrystal interactions probed by thin film swelling to predict dispersibility. *Nanoscale* **8**, 12247–12257 (2016).
 53. Oguzlu, H. & Boluk, Y. Interactions between cellulose nanocrystals and anionic and neutral polymers in aqueous solutions. *Cellulose* **24**, 131–146 (2017).
 54. Shafiei-Sabet, S., Hamad, W. Y. & Hatzikiriakos, S. G. Rheology of nanocrystalline cellulose aqueous suspensions. *Langmuir* **28**, 17124–17133 (2012).
 55. Lagerwall, J. P. F. *et al.* Cellulose nanocrystal-based materials: From liquid crystal self-assembly and glass formation to multifunctional thin films. *NPG Asia Mater.* **6**, 1–12 (2014).
 56. Bruckner, J. R., Kuhnhold, A., Honorato-Rios, C., Schilling, T. & Lagerwall, J. P. F. Enhancing self-assembly in cellulose nanocrystal suspensions using high-permittivity

- solvents. *Langmuir* **32**, 9854–9862 (2016).
57. Tang, J., Sisler, J., Grishkewich, N. & Tam, K. C. Functionalization of cellulose nanocrystals for advanced applications. *J. Colloid Interface Sci.* **494**, 397–409 (2017).
 58. Yang, J., Han, C., Xu, F. & Sun, R. Simple approach to reinforce hydrogels with cellulose nanocrystals. *Nanoscale* **6**, 5934 (2014).
 59. Ching, Y. C. *et al.* Rheological properties of cellulose nanocrystal-embedded polymer composites: a review. *Cellulose* **23**, 1011–1030 (2016).
 60. De France, K. J., Hoare, T. & Cranston, E. D. Review of Hydrogels and Aerogels Containing Nanocellulose. *Chem. Mater.* **29**, 4609–4631 (2017).
 61. Boluk, Y., Zhao, L. & Incani, V. Dispersions of nanocrystalline cellulose in aqueous polymer solutions: Structure formation of colloidal rods. *Langmuir* **28**, 6114–6123 (2012).
 62. Hu, Z., Cranston, E. D., Ng, R. & Pelton, R. Tuning cellulose nanocrystal gelation with polysaccharides and surfactants. *Langmuir* **30**, 2684–2692 (2014).
 63. Bardet, R., Belgacem, N. & Bras, J. Flexibility and color monitoring of cellulose nanocrystal iridescent solid films using anionic or neutral polymers. *ACS Appl. Mater. Interfaces* **7**, 4010–4018 (2015).
 64. Reid, M. S., Villalobos, M. & Cranston, E. D. The role of hydrogen bonding in non-ionic polymer adsorption to cellulose nanocrystals and silica colloids. *Curr. Opin. Colloid Interface Sci.* **29**, 76–82 (2017).
 65. Hirai, A., Inui, O., Horii, F. & Tsuji, M. Phase separation behavior in aqueous suspensions of bacterial cellulose nanocrystals prepared by sulfuric acid treatment. *Langmuir* **25**, 497–502 (2009).
 66. Ureña-Benavides, E. E., Ao, G., Davis, V. A. & Kitchens, C. L. Rheology and phase behavior of lyotropic cellulose nanocrystal suspensions. *Macromolecules* **44**, 8990–8998 (2011).

67. Shafeieei-Sabet, S., Hamad, W. Y. & Hatzikiriakos, S. G. Influence of degree of sulfation on the rheology of cellulose nanocrystal suspensions. *Rheol. Acta* **52**, 741–751 (2013).
68. Liu, D., Chen, X., Yue, Y., Chen, M. & Wu, Q. Structure and rheology of nanocrystalline cellulose. *Carbohydr. Polym.* **84**, 316–322 (2011).
69. Chen, Y., Xu, C., Huang, J., Wu, D. & Lv, Q. Rheological properties of nanocrystalline cellulose suspensions. *Carbohydr. Polym.* **157**, 303–310 (2017).
70. Qiao, C., Chen, G., Zhang, J. & Yao, J. Structure and rheological properties of cellulose nanocrystals suspension. *Food Hydrocoll.* **55**, 19–25 (2016).
71. Li, M.-C. *et al.* Cellulose Nanoparticles: Structure–Morphology–Rheology Relationships. *ACS Sustain. Chem. Eng.* **3**, 821–832 (2015).
72. Lu, A., Hemraz, U., Khalili, Z. & Boluk, Y. Unique viscoelastic behaviors of colloidal nanocrystalline cellulose aqueous suspensions. *Cellulose* **21**, 1239–1250 (2014).
73. Jia, X. *et al.* Rheological properties of an amorphous cellulose suspension. *Food Hydrocoll.* **39**, 27–33 (2014).
74. Wu, Q. *et al.* Rheological behavior of cellulose nanocrystal suspension: Influence of concentration and aspect ratio. *J. Appl. Polym. Sci.* **131**, 1–8 (2014).
75. Moberg, T. *et al.* Rheological properties of nanocellulose suspensions: effects of fibril/particle dimensions and surface characteristics. *Cellulose* **24**, 2499–2510 (2017).
76. Lenfant, G., Heuzey, M. C., van de Ven, T. G. M. & Carreau, P. J. A comparative study of ECNC and CNC suspensions: effect of salt on rheological properties. *Rheol. Acta* **56**, 51–62 (2017).
77. Jancar, J. *et al.* Current issues in research on structure-property relationships in polymer nanocomposites. *Polymer.* **51**, 3321–3343 (2010).
78. Crosby, A. J. & Lee, J. Y. Polymer nanocomposites: The ‘nano’ effect on mechanical properties. *Polym. Rev.* **47**, 217–229 (2007).

79. Wagner, H. D. & Vaia, R. A. Nanocomposites: Issues at the interface. *Mater. Today* **7**, 38–42 (2004).
80. Rittigstein, P., Priestley, R. D., Broadbelt, L. J. & Torkelson, J. M. Model polymer nanocomposites provide an understanding of confinement effects in real nanocomposites. *Nat. Mater.* **6**, 278–282 (2007).
81. Schadler, L. S., Kumar, S. K., Benicewicz, B. C., Lewis, S. L. & Harton, S. E. Designed Interfaces in Polymer Nanocomposites: A Fundamental Viewpoint. *MRS Bull.* **32**, 335–340 (2007).
82. Balazs, A. C., Emrick, T. & Russell, T. P. Nanoparticle Polymer Composites : Where Two Small Worlds Meet. *Science (80-.).* **314**, 1107–1110 (2006).
83. Serenko, O. A. *et al.* The effect of size and concentration of nanoparticles on the glass transition temperature of polymer nanocomposites. *RSC Adv.* **7**, 50113–50120 (2017).
84. Bansal, A. *et al.* Quantitative equivalence between polymer nanocomposites and thin polymer films. *Nat. Mater.* **4**, 693–698 (2005).
85. Pham, J. Q. *et al.* Glass transition of polymer/single-walled carbon nanotube composite films. *J. Polym. Sci. Part B-Polymer Phys.* **41**, 3339–3345 (2003).
86. Bansal, A. *et al.* Controlling the Thermomechanical Properties of Polymer Nanocomposites by Tailoring the Polymer-Particle Interface. *J. Polym. Sci. Part B-Polymer Phys.* **44**, 2944–2950 (2006).
87. Chen, F. *et al.* Glass transition temperature of polymer-nanoparticle composites: Effect of polymer-particle interfacial energy. *Macromolecules* **46**, 4663–4669 (2013).
88. Ash, B. J., Schadler, L. S. & Siegel, R. W. Glass transition behavior of alumina/polymethylmethacrylate nanocomposites. *Mater. Lett.* **55**, 83–87 (2002).
89. Ash, B. J., Siegel, R. W. & Schadler, L. S. Glass-transition temperature behavior of alumina/PMMA nanocomposites. *J. Polym. Sci. Part B Polym. Phys.* **42**, 4371–4383 (2004).

90. Ramanathan, T. *et al.* Functionalized graphene sheets for polymer nanocomposites. *Nat. Nanotechnol.* **3**, 327–331 (2008).
91. Liao, K. H., Aoyama, S., Abdala, A. A. & Macosko, C. Does graphene change Tg of nanocomposites? *Macromolecules* **47**, 8311–8319 (2014).
92. Kuo, S. W. & Chang, F. C. POSS related polymer nanocomposites. *Prog. Polym. Sci.* **36**, 1649–1696 (2011).
93. Pavlidou, S. & Papaspyrides, C. D. A review on polymer-layered silicate nanocomposites. *Prog. Polym. Sci.* **33**, 1119–1198 (2008).
94. Hsiao, W. W. W., Hui, Y. Y., Tsai, P. C. & Chang, H. C. Fluorescent Nanodiamond: A Versatile Tool for Long-Term Cell Tracking, Super-Resolution Imaging, and Nanoscale Temperature Sensing. *Acc. Chem. Res.* **49**, 400–407 (2016).
95. Hui, Y. Y., Cheng, C.-L. & Chang, H.-C. Nanodiamonds for optical bioimaging. *J. Phys. D. Appl. Phys.* **43**, 374021 (2010).
96. Boudou, J.-P. *et al.* High yield fabrication of fluorescent nanodiamonds. *Nanotechnology* **20**, 235602 (2009).
97. Chang, Y.-R. *et al.* Mass production and dynamic imaging of fluorescent nanodiamonds. *Nat. Nanotechnol.* **3**, 284–288 (2008).
98. Fu, C.-C. *et al.* Characterization and application of single fluorescent nanodiamonds as cellular biomarkers. *Proc. Natl. Acad. Sci. U. S. A.* **104**, 727–32 (2007).
99. Yu, S.-J., Kang, M.-W., Chang, H.-C., Kuan-Ming Chen, A. & Yu, Y.-C. Bright Fluorescent Nanodiamonds: No Photobleaching and Low Cytotoxicity. *JACS Commun.* **127**, 17604–17605 (2005).
100. Xue, Z., Vinci, J. C. & Colón, L. A. Nanodiamond-Decorated Silica Spheres as a Chromatographic Material. *ACS Appl. Mater. Interfaces* **8**, 4149–4157 (2016).
101. Saini, G. *et al.* Core - Shell Diamond as a Support for Solid-Phase Extraction and High-Performance Liquid Chromatography. **82**, 4448–4456 (2010).

102. Spitsyn, B. V. *et al.* The physical-chemical study of detonation nanodiamond application in adsorption and chromatography. *Diam. Relat. Mater.* **19**, 123–127 (2010).
103. Behler, K. D. *et al.* Nanodiamond-polymer composite fibers and coatings. *ACS Nano* **3**, 363–369 (2009).
104. Mochalin, V. N., Pentecost, A., Li, X. & Neitzel, I. Adsorption of Drugs on Nanodiamond: Towards Development of a Drug Delivery Platform Adsorption of Drugs on Nanodiamond: Towards Development of a Drug Delivery Platform. (2013). doi:10.1021/mp400213z
105. Chow, E. K. *et al.* Nanodiamond Therapeutic Delivery Agents Mediate Enhanced Chemoresistant Tumor Treatment. *Sci. Transl. Med.* **3**, 73ra21-73ra21 (2011).
106. Zhang, X. Q. *et al.* Multimodal nanodiamond drug delivery carriers for selective targeting, imaging, and enhanced chemotherapeutic efficacy. *Adv. Mater.* **23**, 4770–4775 (2011).
107. Liu, K.-K. *et al.* Covalent linkage of nanodiamond-paclitaxel for drug delivery and cancer therapy. *Nanotechnology* **21**, 315106 (2010).
108. Huang, H., Pierstorff, E., Osawa, E. & Ho, D. Active nanodiamond hydrogels for chemotherapeutic delivery. *Nano Lett.* **7**, 3305–3314 (2007).
109. Kausar, A., Ashraf, R. & Siddiq, M. Polymer/Nanodiamond Composites in Li-Ion Batteries: A Review. *Polym. Plast. Technol. Eng.* **53**, 550–563 (2014).
110. Kovalenko, I., Bucknall, D. G. & Yushin, G. Detonation nanodiamond and onion-like-carbon-embedded polyaniline for supercapacitors. *Adv. Funct. Mater.* **20**, 3979–3986 (2010).
111. Zang, J. B., Wang, Y. H., Zhao, S. Z., Bian, L. Y. & Lu, J. Electrochemical properties of nanodiamond powder electrodes. *Diam. Relat. Mater.* **16**, 16–20 (2007).
112. Portet, C., Yushin, G. & Gogotsi, Y. Electrochemical performance of carbon onions,

- nanodiamonds, carbon black and multiwalled nanotubes in electrical double layer capacitors. *Carbon N. Y.* **45**, 2511–2518 (2007).
113. Ferreira, N. G. *et al.* Nanodiamond films growth on porous silicon substrates for electrochemical applications. *Diam. Relat. Mater.* **14**, 441–445 (2005).
 114. Ivanov, M. & Shenderova, O. Nanodiamond-based nanolubricants for motor oils. *Curr. Opin. Solid State Mater. Sci.* **21**, 17–24 (2017).
 115. Elomaa, O., Oksanen, J., Hakala, T. J., Shenderova, O. & Koskinen, J. A comparison of tribological properties of evenly distributed and agglomerated diamond nanoparticles in lubricated high-load steel-steel contact. *Tribol. Int.* **71**, 62–68 (2014).
 116. Elomaa, O. *et al.* Diamond nanoparticles in ethylene glycol lubrication on steel-steel high load contact. *Diam. Relat. Mater.* **34**, 89–94 (2013).
 117. Chou, C. C. & Lee, S. H. Tribological behavior of nanodiamond-dispersed lubricants on carbon steels and aluminum alloy. *Wear* **269**, 757–762 (2010).
 118. Dolmatov, V. Y., Veretennikova, M. V., Marchukov, V. A. & Sushchev, V. G. Currently available methods of industrial nanodiamond synthesis. *Phys. Solid State* **46**, 611–615 (2004).
 119. Shenderova, O. *et al.* Surface chemistry and properties of ozone-purified detonation nanodiamonds. *J. Phys. Chem. C* **115**, 9827–9837 (2011).
 120. Pichot, V. *et al.* An efficient purification method for detonation nanodiamonds. *Diam. Relat. Mater.* **17**, 13–22 (2008).
 121. Petrov, I. *et al.* Detonation nanodiamonds simultaneously purified and modified by gas treatment. *Diam. Relat. Mater.* **16**, 2098–2103 (2007).
 122. Osswald, S., Yushin, G., Mochalin, V., Kucheyev, S. O. & Gogotsi, Y. Control of sp²/sp³ carbon ratio and surface chemistry of nanodiamond powders by selective oxidation in air. *J. Am. Chem. Soc.* **128**, 11635–11642 (2006).
 123. Kulakova, I. I. Surface chemistry of nanodiamonds. *Phys. Solid State* **46**, 636–643

- (2004).
124. Krueger, A. & Boedeker, T. Deagglomeration and functionalisation of detonation nanodiamond with long alkyl chains. *Diam. Relat. Mater.* **17**, 1367–1370 (2008).
 125. Krueger, A. *et al.* Deagglomeration and functionalisation of detonation diamond. *Phys. Status Solidi Appl. Mater. Sci.* **204**, 2881–2887 (2007).
 126. Mochalin, V. N., Shenderova, O., Ho, D. & Gogotsi, Y. The properties and applications of nanodiamonds. *Nat. Nanotechnol.* **7**, 11–23 (2012).
 127. Xu, X., Yu, Z., Zhu, Y. & Wang, B. Influence of surface modification adopting thermal treatments on dispersion of detonation nanodiamond. *J. Solid State Chem.* **178**, 688–693 (2005).
 128. Xu, K. & Xue, Q. A New Method for Deaggregation of Nanodiamond from Explosive Detonation : Graphitization – Oxidation Method 1. *Phys. Solid State* **46**, 633–634 (2004).
 129. Vul, A. Y. *et al.* Direct observation of isolated ultrananodimensional diamond clusters using atomic force microscopy. *Tech. Phys. Lett.* **32**, 561–563 (2006).
 130. Osawa, E. Recent progress and perspectives in single-digit nanodiamond. *Diam. Relat. Mater.* **16**, 2018–2022 (2007).
 131. Ozawa, M. *et al.* Preparation and behavior of brownish, clear nanodiamond colloids. *Adv. Mater.* **19**, 1201–1206 (2007).
 132. Liang, Y., Ozawa, M. & Krueger, A. A general procedure to functionalize agglomerating nanoparticles demonstrated on nanodiamond. *ACS Nano* **3**, 2288–2296 (2009).
 133. Eidelman, E. D. *et al.* A stable suspension of single ultrananocrystalline diamond particles. *Diam. Relat. Mater.* **14**, 1765–1769 (2005).
 134. Krüger, A. *et al.* Unusually tight aggregation in detonation nanodiamond: Identification and disintegration. *Carbon N. Y.* **43**, 1722–1730 (2005).

135. Pentecost, A., Gour, S., Mochalin, V., Knoke, I. & Gogotsi, Y. Deaggregation of nanodiamond powders using salt- and sugar-assisted milling. *ACS Appl. Mater. Interfaces* **2**, 3289–3294 (2010).
136. Turcheniuk, K., Trecuzzi, C., Deelepojananan, C. & Mochalin, V. N. Salt-Assisted Ultrasonic Deaggregation of Nanodiamond. *ACS Appl. Mater. Interfaces* **8**, 25461–25468 (2016).
137. Kurkin, T. S. *et al.* Structure of oriented fibers based on poly(vinyl alcohol) modified by detonation nanodiamonds. *Polym. Sci. - Ser. A* **50**, 43–50 (2008).
138. Maitra, U., Prasad, K. E., Ramamurty, U. & Rao, C. N. R. Mechanical properties of nanodiamond-reinforced polymer-matrix composites. *Solid State Commun.* **149**, 1693–1697 (2009).
139. Morimune, S., Kotera, M., Nishino, T., Goto, K. & Hata, K. Poly (vinyl alcohol) Nanocomposites with Nanodiamond. 4415–4421 (2011).
140. Protopapa, P., Kontonasaki, E., Bikiaris, D., Paraskevopoulos, K. M. & Koidis, P. Reinforcement of a PMMA resin for fixed interim prostheses with nanodiamonds. *Dent. Mater. J.* **30**, 222–231 (2011).
141. Jee, A. Y. & Lee, M. Mechanical properties of Polycarbonate and Poly(Methyl Methacrylate) Films Reinforced with Surface-Functionalized Nanodiamonds.pdf. (2011).
142. Zhao, Y. Q. *et al.* Nanodiamond/poly (lactic acid) nanocomposites: Effect of nanodiamond on structure and properties of poly (lactic acid). *Compos. Part B Eng.* **41**, 646–653 (2010).
143. Zhang, Q. *et al.* Fluorescent PLLA-nanodiamond composites for bone tissue engineering. *Biomaterials* **32**, 87–94 (2011).
144. Zhang, Q. *et al.* Mechanical properties and biomineralization of multifunctional nanodiamond-PLLA composites for bone tissue engineering. *Biomaterials* **33**, 5067–

5075 (2012).

145. Branson, B. T., Seif, M. A., Davidson, J. L. & Lukehart, C. M. Fabrication and macro/nanoscale characterization of aggregated and highly de-aggregated nanodiamond/polyacrylonitrile composite thick films. *J. Mater. Chem.* **21**, 18832 (2011).
146. Jee, A. Y. & Lee, M. Thermal and mechanical properties of alkyl-functionalized nanodiamond composites. *Curr. Appl. Phys.* **11**, 1183–1187 (2011).
147. Roumeli, E. *et al.* Factors controlling the enhanced mechanical and thermal properties of nanodiamond-reinforced cross-linked high density polyethylene. *J. Phys. Chem. B* **118**, 11341–52 (2014).
148. Ayatollahi, M. R., Alishahi, E. & Shadlou, S. Mechanical Behavior of Nanodiamond/Epoxy Nanocomposites. *Int. J. Fract.* **170**, 95–100 (2011).
149. Neitzel, I., Mochalin, V., Knoke, I., Palmese, G. R. & Gogotsi, Y. Mechanical properties of epoxy composites with high contents of nanodiamond. *Compos. Sci. Technol.* **71**, 710–716 (2011).
150. Ayatollahi, M. R., Alishahi, E., Doagou-R, S. & Shadlou, S. Tribological and mechanical properties of low content nanodiamond/epoxy nanocomposites. *Compos. Part B Eng.* **43**, 3425–3430 (2012).
151. Neitzel, I. *et al.* Maximizing Young's modulus of aminated nanodiamond-epoxy composites measured in compression. *Polymer.* **53**, 5965–5971 (2012).
152. Roy, S. Detonation Nanodiamonds and Carbon Nanotubes as Reinforcements in Epoxy Composites — A Comparative Study. *J. Nanotechnol. Eng. Med.* **4**, 1–7 (2013).
153. Zdeno, S. *et al.* Effect of Nanodiamond Particles on Properties of Epoxy Composites.
154. Li, D., Zheng, Q., Wang, Y. & Chen, H. Combining surface topography with polymer chemistry: exploring new interfacial biological phenomena. *Polym. Chem.* **5**, 14–24

(2014).

155. Martin, D. P., Rizk, S., Ho, K. & Williams, S. F. Medical Devices Containing Melt-blown Nonwovens of poly(4-hydroxybutyrate) and Copolymers Thereof. (2009).
156. Mochalin, V. N., Shenderova, O., Ho, D. & Gogotsi, Y. The properties and applications of nanodiamonds. *Nat. Nanotechnol.* **7**, 11–23 (2012).

Chapter 2 Polyester Modification with Random Copolymers via Surface-Initiated Atom Transfer Radical Polymerization: Engineering the Surface Architecture for Protein Capture and Release

2.1 Abstract

The absence of reactive functional groups on polyester fibers limits their possibility for protein binding, desirable in applications such as wastewater purification and bio-filtration. We report a facile method that installs surface reactive groups on polybutylene terephthalate (PBT) followed by copolymer adsorption that dramatically enhanced non-specific biomacromolecule binding. PBT nonwoven fabrics and films, the latter of which were used as model substrates, were modified upon acid-hydrolysis of pre-adsorbed trimethylsilylcellulose (TMSC), which facilitated attachment of a bromine-terminated initiator. Random hydrophilic copolymers of poly (sodium vinyl benzene sulfonate-co-hydroxyethyl methacrylate) (poly(SVBS-co-HEMA)) were then grafted from the surface, using activator re-generated by electron transfer (ARGET) atom-transfer radical polymerization (ATRP). The copolymer architecture was studied for enhanced protein capture and release. It was found that PBT surfaces modified with the poly(SVBS-co-HEMA) adsorbed significant amounts of model proteins and a maximum binding was found for a copolymer with dominant HEMA composition (20% SVBS and 80% HEMA or 2:8 poly(SVBS-co-HEMA)). Such system was regenerated after protein adsorption by introducing electrolyte solutions, as shown in quartz-crystal microgravimetry experiments that also unveiled details about the dynamics of adsorption (capture) and regeneration (protein release). The adsorption of representative proteins – lysozyme, fibrinogen and

bovine serum albumin (BSA) – depended on the pH of the aqueous matrix, with fibrinogen and BSA adsorbing on the ‘wrong side’ of the isoelectric point under electrostatically repulsive conditions. Such adsorption behavior was interpreted in terms of the balance of protein-surface and protein-protein interactions. The modified polyester represents an attractive alternative for imparting protein-adsorption functionality toward advanced separations.

2.2 Introduction

The observation of instantaneous protein adsorption on biomaterials in different biological systems has triggered research, mostly to create biocompatible and protein-resistant materials for several applications such as medical implants,¹ marine fouling,^{2,3} affinity chromatography,⁴ and biosensors.^{5,6} While fouling is a concern in such systems, thus requiring protein-passivation to reduce non-specific protein adsorption, the opposite, namely, controlled protein binding or capture is desirable for applications related to wastewater purification and bio-fluid filtration. Moreover, in cases of high protein loading, surface saturation results in protein build-up, making it necessary to incorporate surface regeneration capabilities without compromising time and cost.

During the past decade, a significant progress has been made in the field of nonwovens for bio-filtration media because of their unique properties such as pore size, high permeability, and low-pressure drop.⁷ Several nonwoven filtration applications have been demonstrated to capture metals,⁸ proteins,⁹ and affinity ligands.¹⁰ Achieving protein adsorption functionality on polyester surfaces, however, remains a challenge primarily due to the absence of reactive surface functional groups that are otherwise needed for

immobilization. Some of the well-established physical methods for pre-activation of inert surfaces include plasma,^{11,12} corona discharge^{13,14} and ultraviolet (UV) irradiation.^{15,16} However, such techniques oxidize polymer surfaces, resulting in modification of bulk properties, thereby affecting properties such as processability and mechanical strength of the parent material. Several alternative modification strategies utilizing the ester functionality such as hydrolysis,^{17,18} aminolysis,¹⁹ and enzymatic hydrolysis²⁰ have been previously reported. While these approaches induce reactive functionality (-OH, -NH₂, -COOH), which facilitates polymer grafting, they often result in polymer degradation.

A versatile technique for polymer grafting, atom transfer radical polymerization (ATRP), utilizes transition metal complexes to mediate a dynamic equilibrium between dormant and active species.²¹⁻²³ Metal catalysts, such as copper, in its lower oxidation state abstract halogen atom from the initiator, creating active radicals that can participate in propagation.²³ ATRP allows tremendous control of chain length, molecular weight, polydispersity index (PDI) and has been utilized to graft polymers from a variety of substrates including gold,²⁴ silicon,²⁴ cellulose fibers,^{25,26,27} and porous membranes.²⁸ However, two major drawbacks associated with ATRP involve the use of large quantities of copper catalyst and extreme sensitivity to oxygen, necessitating steps for costly purification steps and demanding stringent inert conditions. To overcome these drawbacks, activators regenerated by electron transfer or ARGET-ATRP have been used in which Cu (II) is constantly reduced to Cu (I) by using a reducing agent such as ascorbic acid, thereby limiting the amount of copper required for polymerization to ppm levels.²⁹⁻³¹ In addition, this approach showed increased tolerance to limited amounts of oxygen and is applicable to

diverse monomers such as styrene, methacrylate, and acrylamides, making ARGET-ATRP a preferred method of grafting in this work.³²

In this study, the design principle focuses on invoking a simple strategy to induce reactive functionality on a polyester surface, such as polybutylene terephthalate (PBT), utilizing trimethylsilylcellulose (TMSC), followed by ARGET-ATRP to graft a hydrophilic random copolymer poly (sodium vinyl benzene sulfonate-co-hydroxyethyl methacrylate) (poly(SVBS-co-HEMA)) for protein capture and release. The system takes advantage of protein adsorption capability of negatively charged poly(SVBS) segment, combined with excellent protein-repelling properties of poly(HEMA). Investigation of protein-adsorption treatments incorporates thin film deposition and modification on a gold-coated piezoelectric sensor to monitor mass adsorption (via quartz-crystal microgravimetry) using model proteins such as lysozyme, fibrinogen and bovine serum albumin (BSA). The effectiveness of the proposed surface modification approach for protein capture, optimum copolymer composition, surface regeneration capabilities, effects of pH on protein adsorption and the translation of the proposed method to nonwovens are revealed in this study.

2.3 Materials and Methods

2.3.1 Materials

Polybutylene terephthalate (PBT) and polypropylene (PP) pellets were obtained from Sigma Aldrich (Allentown, PA). PBT, PP and polyethylene terephthalate (PET) nonwoven fabrics, manufactured in Reicofil pilot plant, were provided by the Nonwovens Institute (NWI, Raleigh), Silicon wafer, sulfuric acid (99.99%), hydrogen peroxide (ACS reagent, 29.0-32.0 wt.%), hexafluoroisopropanol (HFIP, >99%), m-xylene (anhydrous, > 99%)

toluene (>99%), hydrochloric acid (HCl, 37%), α -bromoisobutyryl bromide (BIBB, 98%), triethylamine (TEA, >99%), 4-dimethylaminopyridine (DMAP, >99%). Sodium 4-vinylbenzene sulfonate (SVBS, >90%), 2-hydroxyethylmethacrylate (HEMA, < 50ppm monomethyl ether hydroquinone inhibitor, > 99%), copper (II) bromide (CuBr₂, 99%), L-ascorbic acid (99%), methanol (99.8%) was purchased from Sigma Aldrich (Allentown, USA) and used without further purification. Trimethylsilylcellulose (TMSC) was provided by Aalto University, Espoo, Finland. Lysozyme (lyophilized powder, protein >90%), fibrinogen from human plasma (50-70% protein) and bovine serum albumin (BSA, BioReagent for molecular biology), phosphate buffer powder, phosphate buffer saline powder (pH 7.4 for preparing 1L solutions), and sodium chloride (99%, ACS reagent) were purchased from Sigma Aldrich and used as received. Gold-coated sensors (5MHz) were used as received from Q-Sense.

2.3.2 Preparation of PBT Thin Films by Spin Coating

Initially, gold-coated sensors were immersed in Piranha solution (sulfuric acid/hydrogen peroxide = 7:3 (v/v)) (**Caution:** Piranha solution reacts violently with organic materials and should be handled carefully) for 2-5 minutes at room temperature. Thereafter, the sensors were thoroughly rinsed with Milli-Q water and dried completely under flow of nitrogen. Once the substrates were cleaned, they were placed under UV irradiation for 30 minutes just before use. PBT (0.16 wt.%) in hexafluoroisopropanol was spun coated (3000 rpm, 20 seconds) on the gold-coated quartz crystal. The solution was prepared by mixing 10 mg of PBT pellets in 6 mg HFIP in a small vial and allowing it to dissolve for 24 hours³³. Once dissolution was complete, 50 μ L of the solution was dispensed on the substrate placed

on the spin coater. Infrared lamp was used to maintain the temperature of the rotor head at 25°C. The spin-coated quartz crystals were then placed in an oven at 80°C for 2 hours to remove the residual solvent.

2.3.3 Preparation of Hydroxyl-Terminated PBT Surfaces

Trimethylsilylcellulose, a non-polar derivative of cellulose, was deposited on spin-coated substrates by adsorption of 1mg/mL solution of TMSC in toluene. The substrates were incubated in a vial containing TMSC for three hours and were placed in an oven at 80°C for 30 minutes to remove the residual solvent. After deposition, the substrates were subjected to vapor phase hydrolysis in which 10% hydrochloric acid was placed at the bottom of a desiccator and samples were exposed to acid vapor for 15 minutes under vacuum. The samples were then ready for use in further steps.

2.3.4 Synthesis of Initiator-Functionalized Surfaces

ATRP initiator was immobilized by reaction of BIBB with hydroxyl groups on the surface obtained after acid hydrolysis. Substrates were placed in a flask thoroughly degassed using nitrogen for 15 minutes before solution containing BIBB (60 μ L), TEA (76.4 μ L), and a catalytic amount of DMAP in THF (20 mL) was added. The reaction was allowed to proceed for 1 h in ice, and was allowed to proceed further for 15 h at room temperature. Thereafter, the immobilized substrate was thoroughly washed in THF and placed in THF for 5 min. This was followed by thorough DI water rinse to remove residual reactants and side products. The samples were then thoroughly dried using nitrogen flow.

2.3.5 ARGET-ATRP using SVBS and HEMA

The poly(SVBS-co-HEMA) modified surfaces were prepared via surface initiated

ARGET-ATRP of SVBS and HEMA grafted from bromine-terminated surface. The reaction solution was prepared by dissolving SVBS (0.45 g, 2.2 mmol), HEMA (1.15 g, 8.8 mmol), bipyridine (7.7 mg), CuBr₂ (1.6 mg), and ascorbic acid (0.02 g) into a mixture of methanol (7 mL) and water (6 mL). Bromine-terminated surfaces were immersed into the reaction solution for 2 h at room temperature. Finally, the surfaces were removed from the solution, rinsed with abundant Milli-Q water and anhydrous methanol to remove unreacted monomers and physically adsorbed polymers, and then dried under a nitrogen flow to achieve poly(SVBS-co-HEMA) surfaces. For nonwoven fabrics, PBT with a basis weight of 100 g/cm² were cut into 2cm-by-2cm grid and were cleaned by sonication in acetone for 10 minutes, followed by rinsing in copious amounts of water, and subsequently placed in oven at 50°C for 30 minutes. After pre-treatment, the surface modification was performed using the same procedure for thin films).

2.3.6 Protein Adsorption

Real-time QCM measurements were performed using Q-sense E4 system (Gothenburg, Sweden) using gold-coated sensors of 1cm² area. Sensors were mounted in the chamber and calibrated using air. A stable baseline signal was obtained after running water (Milli Q) and buffer solutions at 25 °C. Adsorption experiments were conducted by running protein solutions at a flow rate of 50 µL/min until saturation. Finally, protein solution was exchanged with buffer to remove any unbound or loosely bound proteins. Change in resonant frequency (Δf) with time was recorded. The Sauerbrey equation was used to calculate the solvated protein mass using the corresponding frequency shifts, which assumes adsorption as a rigid layer:

$$\Delta m = -C \frac{\Delta f}{n} \quad (1)$$

Where m is the solvated protein mass, C is the mass sensitivity constant (17.7 ng cm⁻² Hz⁻¹ for 5 MHz crystals), and n is the overtone number. For studies on pH effects, the Voigt model was used to fit raw data using QTools which allowed the calculation of the layer mass and thickness. Fluid density and viscosity was assumed at 1000 kg/m³ and 0.001 kg/m-s respectively and layer density was assumed to be 1300 g/cm³ for all proteins. Protein adsorption on nonwoven fabrics was obtained using UV-VIS spectrophotometer. 2 cm by 2 cm nonwoven samples were immersed in a fixed concentration of protein/buffer solution for different times. The amount of protein captured on the surface was calculated using the absorbance of protein in the residual solution (Equation 2).

$$\Delta m_{ads} = \frac{C_i - C_f}{m_n} \quad (2)$$

where Δm_{ads} is the mass of adsorbed protein (mg/g), C_i is the initial protein concentration (mg/ml), C_f is the final protein concentration (mg/ml), and m_n is the mass of nonwoven fabric (g).

2.3.7 Surface Characterization

The thickness of spin-coated PBT layer on silica substrate was measured using spectroscopic ellipsometry (J.A. Woollam Co., Inc., model M-2000V) at an incidence angle of 60° and wavelength varying between 400 nm to 700 nm. The thickness of PBT on silica was extracted using Cauchy model. The reported values and error are averages taken over three measurements at different regions within the sample. Changes in the wettability of modified surfaces were measured using static water contact angles (WCA) using a contact

angle goniometer (SEO Phoenix 300) at room temperature. Milli-Q water with approximately 50 μ L drop volume was used. All measurements for static WCA were obtained after the drop stabilized on the surface. Reported values of WCA were obtained using average of five independent measurements. The characterization of grafting on PBT nonwovens was performed by X-ray photoelectron spectroscopy. Data was obtained on Specs XPS using Mg source with energy of 1253.6 eV. Casa-XPS was used to calibrate C1s spectrum to 285.0 eV, to determine peak areas and to calculate the elemental composition. The surface morphology of thin films was studied using atomic force microscopy and PBT nonwoven was studied using scanning electron microscopy (SEM, Phenom G2 system). Nonwovens were mounted on stubs by means of a double-sided adhesive carbon tape. A thin layer gold was sputtered onto the sample prior to SEM analysis.

2.4 Results and Discussion

2.4.1 Preparation and Characterization of Polyester and PP Thin Films and Surfaces

Grafted with poly(SVBS-co-HEMA).

Polybutylene terephthalate (PBT) was chosen as model polyester for surface modification. However, the versatility of the surface modification chemistry allows its application to other substrates such as polyethylene terephthalate (PET) and polypropylene (PP). PBT thin films were prepared using spin coating procedure reported in literature.³³ The ellipsometry thickness of spin-coated PBT and wettability measured using static water contact angle (WCA) are shown in Figure A.1. The thickness of PBT layer on Si-surface ranged from approximately 17 ± 2 nm to 25 ± 5 nm for 0.10 wt.% and 0.16 wt.% PBT respectively. The change in surface wettability was evident since the contact angles increased

from $40^\circ \pm 3^\circ$ for bare Si to $55^\circ \pm 1^\circ$ for 0.10% solution to $64^\circ \pm 7^\circ$ after coating from a 0.16% solution. The surface morphology of PBT-spin coated surfaces examined using AFM revealed a homogeneous surface with RMS roughness of 1.4 ± 0.4 nm. PBT flat surfaces prepared using 0.16 wt.% solution were used for subsequent experiments.

Direct modification of polyester surfaces presents a unique challenge due to the lack of reactive groups on the surface. Therefore, two different approaches to graft copolymer of SVBS and HEMA, capable of enhancing non-specific protein capture using a ‘grafting from’ technique, were considered as illustrated in Figure 2.1. The first approach (Method 1) relied on an anchoring layer containing TMSC on which the initiator is immobilized, whereas the second approach (Method 2) employed direct immobilization of initiator on the surface of PBT. For both approaches, the immobilized initiator served as the anchoring point for covalent linkage of poly(SVBS-co-HEMA). Successful surface modification of PBT thin films using Method 1 was confirmed using static WCA, shown in Figure 2.2a. TMSC layer on top of spin-coated PBT layer obtained after immersion in TMSC/toluene solution (1 mg/ml) for three hours increased the static WCA from $72^\circ \pm 2^\circ$ for neat PBT to $87^\circ \pm 4^\circ$, resulting in a surface with lower wettability due to methyl groups on TMSC, relative to PBT.

Upon acid hydrolysis, TMSC coated surface turned hydrophilic with WCA of $39^\circ \pm 3^\circ$. This is attributed to the regeneration of cellulose surface after exposure to acid vapor. Furthermore, attachment of the bromine-terminated initiator increased the wettability of the multilayer substrate, decreasing the contact angle from $39^\circ \pm 3^\circ$ to $29^\circ \pm 3^\circ$. The versatility of this technique in rendering hydrophobic surfaces hydrophilic was successfully

demonstrated by using PP surfaces (Figure A.2). PP thin films fabricated using methods reported previously³³ with average roughness of 1.27 nm and WCA of ca. 116° showed substantial changes in wettability. After TMSC adsorption, the WCA decreased to ca. 92° and subsequent hydrolysis decreased the WCA further to ca. 57°. The reduction in hydrophobicity, combined with the presence of hydroxyl-terminated surfaces, facilitated attachment of initiator and grafting of copolymers. Furthermore, the effectiveness of this approach was extended to PP, PET and PBT nonwoven fabrics using WCA measurements. WCA reported for nonwoven fabrics, however, can be only taken as a qualitative assessment of the wettability since it is influenced by the surface roughness and other factors. As shown in Figure A.3, the adsorption of TMSC layer results in a slight increase in WCA for all nonwovens, i.e. WCA changed from 122° to 124° for PBT, 108° to 137° for PET and 133° to 140° for PP. After acid hydrolysis, the WCA changed significantly for PBT and PET from 124° and 137° to less than 20° and wicking respectively. For the PP nonwoven, however, the acid hydrolysis resulted in a minor decrease in WCA, from 140° to 128°, which is due to extremely inert nature of PP nonwoven fabrics. However, upon grafting pure poly (HEMA) on the surface of nonwovens, all samples showed wicking behavior, suggesting the expected effect of poly (HEMA). This was further validated using ATR-FTIR (Figure A.4). Pure PP shows asymmetric -CH_2 stretches at 2870 cm^{-1} and symmetric -CH_2 stretches at 2840 cm^{-1} . The signals at 2970 cm^{-1} and 2910 cm^{-1} correspond to asymmetric and symmetric stretches of methyl groups (-CH_3), whereas the signals at 1370 cm^{-1} and 1460 cm^{-1} correspond to bending vibrations of -CH_3 and -CH_2 respectively. After grafting of poly (HEMA), signature of C=O appear close to 1730 cm^{-1} , showing the possibility of grafting

poly (HEMA) on nonwoven fabrics. Since hydrophobicity is useful for protein capture due to hydrophobic interactions and hydrophilic nature of hydroxyl-terminated surface is a key requirement to graft poly(SVBS-co-HEMA), we chose PBT as the most ideal substrate for subsequent work. The design principle of this work is based on combining the protein affinity properties of (poly(SVBS)), together with protein-repellant function of (poly (HEMA)). Thus, PBT was decorated on the surface with copolymers of SVBS and HEMA for non-specific protein capture and surface regeneration (protein release). PBT films on QCM-D quartz crystals were used to understand the effects of the grafting method, copolymer composition, pH and ionic strength on adsorption of lysozyme, BSA and fibrinogen and the optimized platform was replicated for PBT nonwovens to demonstrate capture of lysozyme.

The two approaches were compared using spin coated PBT (from 0.16 wt.% solution) on 5 MHz QCM-D crystal grafted with 8:2 poly(SVBS-co-HEMA). The adsorption of lysozyme resulted in frequency shifts corresponding to increase in ‘solvated mass’ dictated by Sauerbrey equation for a rigid layer (Equation 1). The solvated protein mass measured by QCM accounts the contributions from hydration shell around protein, solvent trapped within protein and solvent residing at the protein-substrate interface.²⁶ Figure 2.2b shows QCM adsorption profiles for three distinct surfaces – control PBT, PBT grafted with 8:2 poly(SVBS-co-HEMA), using Method 1 (with TMSC), and PBT grafted with 8:2 poly(SVBS-co-HEMA) grafted with Method 2 (without TMSC). Sauerbrey mass extracted from QCM adsorption profile is tabulated in Table 2.1. Accordingly, PBT adsorbed the least amount of solvated lysozyme at 230 ng/cm² compared to PBT modified with Method 1,

which adsorbed 661 ng/cm². PBT modified with Method 2 absorbed 260 ng/cm² solvated that is slightly higher than the value for the control PBT. The low values of adsorption obtained using Method 2, relative to Method 1, is attributed to the absence of an anchoring layer, which resulted in initiators deposited on the PBT substrate. The amount of solvated lysozyme adsorbed on bare PBT (230 ng/cm²) is within the range of lysozyme monolayer on a flat surface at sufficiently high surface coverage.³⁴ In addition, the concentration in the solution was sufficiently high to observe mass above that estimated for a monolayer coverage. However, this mass incorporates contributions from the solvent, suggesting that PBT adsorbed less than a monolayer of lysozyme. For hydrophilic polymers such as PEO and PAA, approximately 40-50% comprised of water¹. Assuming similar values for solvation for PBT, the amount of protein bound on PBT is ~138 ng/cm², significantly lower than a monolayer. The surface coverage of lysozyme on PBT, calculated using a density of 0.65 mg/ml reported in literature, corresponded to approximately 3.5 nm.

The results further indicate two distinct kinetic regimes – fast adsorption upon protein injection ($t < 10$ minutes) followed by slow adsorption ($10 \text{ min} < t < 60 \text{ min}$). The initial rapid adsorption takes place in ~3 minutes, followed by slow adsorption until ~60 minutes, as the adsorption approaches equilibrium. The removal of unbound or loosely bound proteins after buffer rinse is a direct evidence of reversible binding, suggesting weak binding affinity with grafted poly(SVBS-co-HEMA). For pure PBT, 77 ng/cm² (~33%) of adsorbed lysozyme was desorbed, whereas for PBT modified with Method 1, 277 ng/cm² (~42%) was desorbed. About 65 ng/cm² (~25%) was desorbed when buffer was passed through PBT modified with Method 2. The larger desorption for 8:2 SVBS:HEMA surfaces can be explained by the fact

that 20% HEMA is a protein repellent. Despite the large desorption, however, PBT modified with Method 1 absorbed 384 ng/cm^2 of solvated lysozyme, significantly higher than bare PBT (153 ng/cm^2) or PBT modified with Method 2 (195 ng/cm^2). Combined together, the results suggest that the proposed approach for surface modification induces much larger protein adsorption compared to unmodified PBT, providing a new platform to enhance protein capture. We further proceed by modifying PBT using Method 1 in subsequent experiments.

2.4.2 Effect of Copolymer Composition on Lysozyme Adsorption

The copolymer ratio in poly(SVBS-co-HEMA) is expected to play a significant role in the extent of lysozyme adsorption. SVBS segments aid in protein adsorption via electrostatic interactions, while HEMA segment should hinder protein adsorption, offering capabilities of protein adsorption and surface regeneration through SVBS and HEMA segments, respectively. In addition to copolymer composition, grafting density, thickness and conformation of polymer brushes dictate the final adsorption properties. For instance, proteins can penetrate grafted copolymers at low grafting density, whereas protein stays on the surface for densely grafted copolymers. In this study, we assumed a constant grafting density and polymer brush thickness using the same initiator-to-monomer ratio and a constant reaction time of two hours. Therefore, poly(SVBS-co-HEMA) of varying compositions were synthesized using ARGET-ATRP with a constant initiator to monomer ratio and grafting time of two hours. The total monomer in the reaction solution was fixed at 11 mmol and each monomer concentration was varied to achieve copolymers with SVBS:HEMA ratios of 10:0 (homopolymer of SVBS), 8:2 (20% HEMA), 5:5 (50% HEMA), 2:8

(80% HEMA) and 0:10 (homopolymer of HEMA). The grafting of copolymers with different ratios onto PBT thin films induced different changes in wettability of the substrate. Surfaces with SVBS homopolymer and copolymer containing 20% and 50% HEMA completely wicked the surface, suggesting a highly hydrophilic surface. When HEMA composition in the copolymer was increased to 80%, the surface registered a WCA of $18^\circ \pm 3^\circ$, which further increased to $36^\circ \pm 4^\circ$ for the case of HEMA homopolymer (Figure 2.3a). Pure SVBS is highly polar and hydrophilic relative to pure HEMA; therefore, SVBS homopolymer completely wicks the surface. The increase in HEMA segment, which is less hydrophilic than SVBS, lowered the wettability and increased the WCA. Nonetheless, the distinct changes in wettability of the substrate are expected to play a key role in determining protein-binding capacity.

Figure 2.3b shows the adsorption profiles of poly(SVBS-co-HEMA) of varying ratios grafted on gold-coated QCM sensors. The profiles were obtained by injecting lysozyme with a bulk solution concentration of 1 mg/ml in PBS at pH 7.4. Different parameters extracted from raw isotherm are tabulated in Table 2.2. The adsorption profiles revealed a fast initial adsorption, which accounted for over half the absorbed solvated lysozyme, followed by a slow adsorption over 60 minutes. The adsorption of lysozyme on pure SVBS surface induced the lowest frequency shift, 62.4 Hz, corresponding to solvated lysozyme of 368 ng/cm^2 (Table 2.2). Upon increasing HEMA content to 20%, the frequency change increased to 94 Hz which is equivalent to 556 ng/cm^2 of solvated lysozyme. Further increase in HEMA content to 50% showed a similar trend in higher frequency change (162.3 Hz), equivalent to solvated lysozyme of 957 ng/cm^2 . The maximum change in frequency (443.5 Hz) and

corresponding solvated lysozyme mass of 2617 ng/cm² was induced upon increasing HEMA content to 80%. This particular observation of increased lysozyme binding with increasing HEMA content could be explained using combination of electrostatic interactions, which reduced with increased HEMA content, and changes in surface wettability. The presence of more HEMA makes the surface relatively less hydrophilic. Furthermore, prior to rinsing with buffer at 60 minutes, lysozyme adsorption reached near equilibrium for surfaces with 0%, 20% and 50% HEMA, whereas for surface with 80% HEMA, lysozyme adsorption exhibited a slow kinetics and took much longer to reach equilibrium. After 60 minutes, the adsorption of lysozyme on 80% HEMA surfaces was still increasing.

The raw adsorption isotherms also revealed the binding kinetics and strength for lysozyme onto different poly(SVBS-co-HEMA) surfaces. The change in the first derivative of the QCM frequency during lysozyme adsorption ($\delta(\Delta f)/\delta t$) revealed the initial adsorption kinetics. Figure A.5 shows a plot of $\delta(\Delta f)/\delta t$ which primarily reveals two stages in the process: a rapid stage taking place in less than 6 minutes, followed by a slower dynamics stage saturation or buffer rinse, depending on the composition of the copolymer. SVBS homopolymer showed the fastest kinetics, with initial adsorption taking place in ca. 4.6 min. For 8:2, 5:5 and 2:8 surfaces, the peak adsorption took place at 5.1 min, 5.6 min and 5.8 min, respectively. For all surfaces, a steep profile in protein adsorption occurred within 6 minutes after injection and slowed down thereafter, until the buffer was introduced at 60 min. This can take as the possible contribution of multi-layer adsorption or re-conformation. We speculate that at the initial stage the positively charged lysozyme bound very quickly because

of the large number of available proteins and sites available in the copolymer. The saturation of binding sites caused then slowed lysozyme uptake rates due to fewer sites availability.

The binding affinity of lysozyme to different copolymer surfaces could be established by rinsing the system with buffer after 60 min. The resulting desorption isotherms revealed reversible lysozyme binding occurring in two distinct stages. The first stage of desorption displayed a fast kinetics relative to the second stage; it was most prominent in the surface containing 80% HEMA. This can be explained by the loss of weakly bound proteins from the top of the adsorbed layer. After desorption of the topmost adsorbed molecules, the exposed inner proteins began to desorb, at a slower rates. The total amount of bound protein, as measured at the end of the desorption process, varied with composition. For surfaces containing 0, 20, 50 and 80% HEMA, the total bound protein that remained was 305, 435, 453, and 556 ng/cm², respectively. These results point to the possibility of using the weak binding strength of lysozyme on 2:8 SVBS: HEMA surfaces for the purpose of regeneration of coating on PBT films, as discussed in the next section.

2.4.3 Regeneration of Lysozyme Adsorbed on poly(SVBS-co-HEMA)-modified Surfaces

In order to decouple the effect of electrostatic contributions in lysozyme adsorption, the adsorption dynamics of this protein at bulk concentration of 1 mg/ml and pH 7.4 was further tested in 10 mM phosphate buffer (PB) (without Na⁺) and PBS (150 mM Na⁺ present). The electrostatic contribution in lysozyme binding could be probed by changing the background solution used. This would allow reversible protein binding simply by introducing a salt-containing solution. Figure 2.4a shows real-time lysozyme adsorption on 8:2 poly(SVBS-co-HEMA) surfaces in PB and PBS. The kinetics of lysozyme adsorption on

PBS showed two distinct time scales, as noted in the earlier section – a fast adsorption at short times (Δf of -30 Hz in ~10 min), followed by slow adsorption (total Δf of -60 Hz after ~60 min). It can be assumed that the positively charged protein the negatively charged (sulfonated) surface rapidly, and the existing adsorbed protein further limited the driving force for adsorption, due to electrostatically repulsive patches within lysozyme. However, for adsorption in PB at early times, lysozyme adsorbed instantaneously and the frequency shift accounted for nearly 90% of adsorbed protein (Δf of -130 Hz in ~10 min). Compared to the case of PBS background solution, the sulfonated segments attached to the substrate in the presence of PB had fewer Na^+ counterions around them to neutralize the negative domains that show high affinity to lysozyme, which contains additional Na^+ . The adsorption rate slowed down eventually, comparable to that in PBS with negligible additions to the existing layer. This is primarily due to the lack of Na^+ ions impeding the interaction of protein in solution with both the surface as well as the pre-adsorbed protein layer. Furthermore, exchanging protein solution with respective buffers at 60 min resulted in relatively higher desorption in PBS compared to PB. The presence of Na^+ counter ions resulted in a more (electrostatically) repulsive condition, allowing easier desorption of the bound proteins. This provided a direct evidence of the role of electrostatics in lysozyme binding.

One of the most important implications of desorption upon exposure to PB and PBS is the potential for regenerating the poly(SVBS-co-HEMA) surface by exposure to these buffers. By introducing combinations of PB and PBS at the end of lysozyme adsorption from PB, the original surface, without any protein, was successfully regenerated. As shown in Figure 2.4b, adsorption of lysozyme on 2:8 poly(SVBS-co-HEMA) surfaces in PB showed a

rapid adsorption similar to that in PBS (Δf of -700 Hz in ~10 min), but much higher mass adsorbed (approximately five times more in frequency change). QCM-D mass gives contributions of solvent, and the presence of larger amount of HEMA leads to higher water coupling and thus larger sensed mass. The effects of water, however, cannot be decoupled. Adsorption of lysozyme tested for PB for a layer of the pure, antifouling poly(HEMA), showed minor frequency changes. If water swelling contributed to frequency change, pure poly(HEMA) should have adsorbed significant amounts of water. This suggests that a tailored composition of the pre-adsorbed layer, in terms of sulfonated and HEMA monomers, may result in systems with the right balance of protein adsorption (capture) and repellency (regeneration).

2.4.4 Effects of pH on Protein Adsorption

In addition to polymer composition, solution properties such as pH,³⁴⁻³⁷ ionic strength, buffer type³⁸ as well as type of proteins, significantly influence protein-substrate and protein-protein interactions.³⁹⁻⁴¹ Adsorption studies using 2:8 poly(SVBS-co-HEMA) surfaces prepared using fixed initiator-to-monomer ratio and reaction time can be useful to inquire into the effects of pH on the adsorption lysozyme (14 kDa, pI = 11.1, 4 nm x 3 nm x 3 nm), fibrinogen (340 kDa, pI = 5.5, 47 nm x 5 nm x 5 nm) and BSA (66 kDa, pI = 4.8, 7 nm x 4 nm x 4 nm).⁴² Figure 2.5 shows QCM-D adsorption profiles for these proteins on 2:8 poly(SVBS-co-HEMA) at pH 7 and pH 4 in 10 mM PB (without salt). Figures A.6 and A.7 show corresponding changes in mass and thickness calculated using the Voigt model. For each protein, the normalized frequency changes showed significant dependence on overtone number ($n = 3, 5$ and 7), validating the utility of the Voigt approximation for soft, highly

dissipative films. The pH-dependent adsorption for the three proteins (lysozyme, fibrinogen and BSA) on poly(SVBS-co-HEMA) is discussed individually using the Sauerbrey QCM mass plotted in Figure 2.5 c and d.

The adsorption isotherm of lysozyme on 2:8 poly(SVBS-co-HEMA) at pH 7.0 and pH 4.0 showed two steps: an fast adsorption followed by slowed dynamics, as shown in Figure 2.5 a and b. For adsorption at pH 7.0, fast adsorption happened between $0 < t < 20$ min followed by a slower kinetics or even an increase in frequency, occurring from ($20 < t < 140$ min). This second stage took much longer, suggesting water expulsion from the interface and conformational changes of the adsorbed proteins. For adsorption at pH 4.0, the initial, fast adsorption stage took place in less than 2 min and the slower stage with increased frequency took place between ($5 < t < 70$ min). The smaller amount of solvated lysozyme (~ 980 ng/cm²) captured at pH 4.0, compared to ~ 1900 ng/cm² at pH 7.0, accounts for differences in equilibration time, since lower adsorption at lower pH drives the system much faster relative to that at high pH. Rinsing with buffer revealed information on the binding strength of lysozyme. At pH 7, the introduction of buffer resulted in desorption of ~ 1400 ng/cm² lysozyme, which corresponds to the release of $\sim 74\%$ of the initial, solvated mass. The permanent solvated mass on the surface after desorption was ~ 500 ng/cm². This is in sharp contrast to desorption of ~ 160 ng/cm² lysozyme at pH 4.0, which accounts for desorption of only $\sim 16\%$ of the initial proteins, leaving ~ 820 ng/cm² of solvated lysozyme on the surface. These results clearly reveal the effect of pH on lysozyme adsorption and desorption on poly(SVBS-co-HEMA) surfaces and in a manner consistent with findings for other systems in the literature.^{35,36}

The initial higher adsorption of lysozyme (1900 ng/cm^2) at pH 7.0 compared to $\sim 980 \text{ ng/cm}^2$ at pH 4.0 can be rationalized by considering the role of protein-protein electrostatic interactions. At both pH values, lysozyme is positively charged (pI of 11.1) and adsorption takes place due to favorable protein-substrate electrostatic interactions. SVBS segments are charged and form quenched brushes, with negative charges across all pH.⁴³ Assuming that the charged SVBS shows weak dependence on pH, the adsorption should be more favorable at a pH further away from the pI such that like charges interact. Lysozyme has a higher net positive charge at pH 4.0 compared to pH 7.0. Should protein-substrate interactions become the dominant mode of protein adsorption, adsorption at pH 4.0 should be higher than at pH 7.0, yet the adsorption profiles revealed lower capacity and faster equilibration at pH 4.0. An explanation for this observation includes two possibilities: first, the surface charge on the brushes decrease as pH is decreased, thereby compensating for the increased protein charge and leading to a less adsorption. This would imply that protein-substrate interactions are dominant. However, desorption profiles revealed that binding strength of lysozyme at pH 7.0 was much lower. This could be explained if protein-protein interactions were dominant. As more and more lysozyme is reversibly bound to the surface, multilayers could be formed, which are held together by weak electrostatic or hydrophobic effects, with some repulsive interactions existing between neighboring lysozyme molecules. If one assumes that the copolymer attached to the substrate prevents lysozyme molecules to penetrate, the initial and final adsorption at pH 7.0, for side-on configuration, correspond, to 8 and 3 close-pack layers, respectively.³⁴⁻³⁷ Similarly, the initial and final adsorption at pH 4.0 corresponds to 5 and 4 layers, respectively. However, desorption at pH 4.0 revealed only 18% wet mass loss,

corresponding to a loss of a single monolayer and suggesting that lysozyme was adsorbed not only on the surface, but also within the polymer brushes. Similar conclusion could be achieved if one assumes 50% solvated water mass for lysozyme.^{44,45} Finally, after desorption, which eliminates contributions of protein-protein interactions in a multilayer adsorption, the remaining wet mass of lysozyme adsorbed was higher at pH 4.0 compared to pH 7.0. By isolating contributions of protein-substrate interactions, the differences in adsorption amounts reveal a favorable electrostatically interaction between lysozyme and poly(SVBS-co-HEMA).

Figure 2.5 a and b shows the frequency changes when poly(SVBS-co-HEMA) surface was exposed to fibrinogen. The introduction of fibrinogen solution resulted in an immediate frequency shift for pH 7.0 ($0 \text{ min} < t < 20 \text{ min}$), followed by slow adsorption between ($20 \text{ min} < t < 130 \text{ min}$). The second stage adsorption process took much longer and the system did not reach equilibrium, even after 130 min. The initial adsorption accounted for $\sim 4131 \text{ ng/cm}^2$ solvated mass of fibrinogen. Upon exchanging the protein solution with PB, gradual desorption of 674 ng/cm^2 , corresponding to $\sim 16\%$, took place. This left behind $3,458 \text{ ng/cm}^2$ as calculated by using Sauerbrey equation, which underestimates the adsorbed mass. Using the adsorption profile, information on mass and thickness variations was extracted using Voigt viscoelastic modeling. Using this model, the initial adsorption of fibrinogen was significant, $\sim 13,000 \text{ ng/cm}^2$, much higher than that predicted by Sauerbrey approximation, but showed a mass loss of $\sim 14\%$, very similar to that predicted by Sauerbrey. The initial rapid adsorption event resulted in adsorption of $\sim 60 \text{ nm}$ fibrinogen, which gradually increased until $\sim 90 \text{ nm}$. Most interestingly, the adsorption of fibrinogen at pH 7.0 took place even at the

wrong side of pI (pI = 5.5). At this pH, fibrinogen has a net negative charge, which offers electrostatically repulsive conditions for adsorption on sulfonated surfaces. This observation has been reported in prior literature.⁴⁶⁻⁵⁰ The adsorbed fibrinogen mass was significantly higher than that calculated from a closed-pack protein monolayer, which corresponds to 240 ng/cm² for a side-on orientation and to 2260 ng/cm² for an end-on orientation.⁵¹⁻⁵³

In contrast to adsorption events at pH 7.0, adsorption mass, time scales of adsorption as well as desorption events differed significantly. The initial drop in frequency leveled off between 20-30 min followed by further decrease in frequency although at a much slower rate. While the adsorption of fibrinogen at pH 7.0 did not reach equilibrium after 130 min, the adsorption at pH 4.0 was close to equilibrium around 60 min. This is primarily because at pH 7.0 the wet mass of adsorbed fibrinogen was ~4131 ng/cm² compared to 2988 ng/cm² adsorbed for pH 4.0. The smaller amount of fibrinogen captured at lower pH accounts for differences in equilibration time, since lower adsorption at lower pH drove the system much faster relative to higher pH. The exposure of poly(SVBS-co-HEMA) surfaces to PB after fibrinogen adsorption resulted in desorption of ~80 mg (~2.67%) with net irreversible fibrinogen binding of ~2908 ng/cm².

QCM-D analysis for adsorption of BSA on poly(SVBS-co-HEMA) surfaces showed negligible frequency changes upon injection of 1 mg/ml BSA solution at pH 7.0. This is in sharp contrast to results of adsorption at pH 4.0, where frequency changes showed a rapid decrease at early times of the experiment. A temporary desorption event occurred after early saturation, followed by further adsorption of BSA at a much slower time scale. Further exchanging the protein solution with PB at the end of 65 min, resulted in negligible

desorption. The solvated mass calculated using Voigt model after 65 min adsorption and that after rinsing with buffer corresponded to 3300 ng/cm² and 2990 ng/cm², respectively, which accounts for 9% protein desorption. However, the solvated mass after adsorption and rinsing corresponded to 79 ng/cm² and 0.24 ng/cm², respectively, suggesting ~100% desorption of BSA at pH 7. Clearly, pH dependence of BSA adsorption on poly(SVBS-co-HEMA) is corroborated by two key trends: higher adsorption and higher retention of BSA at pH 4 relative to pH 7. This is because changing pH further away from the isoelectric point of BSA (pI 4.7), where zero net-charge condition exists, induced higher charges in BSA. This promoted protein-protein repulsive interactions in the adsorption process. This particular observation of reduced protein adsorption at pH values away from the isoelectric point was apparent for lysozyme as well as fibrinogen. This is further corroborated by desorption events, which were more pronounced at pH 7 (~100% loss) compared to pH 4 (12% loss). Due to the presence of high protein-protein repulsive interactions at pH 7, BSA can be assumed to be loosely held within the adsorbed layer. Introducing buffer resulted in loss of these loosely held proteins at pH 7.0, whereas the loss was negligible at pH 4.0, due to relatively less electrostatically repulsive conditions within the adsorbed layer. This trend was reported previously for BSA adsorption on hydrophilic silica substrate, which was highest at pH 5.0 compared to pH 3 and 7.⁵⁴ Compared to lysozyme and fibrinogen, the affinity of the surfaces to BSA was minimal. Using Voigt thickness model and the dimensions of BSA (14 nm in major axis and 4 nm in minor axis, cross-section area of ~56 nm²)^{54,55} and assuming a densely grafted copolymer surface, quantitative information about the size scale of adsorbed BSA can be determined. For a layer density of 1.3 g/cm³, the thickness of adsorbed BSA

layer at pH 4.0 (3330 ng/cm² to 2990 ng/cm²) and pH 7.0 (79 ng/cm² to 0.24 ng/cm²) are ~26 to 23 nm and less than 1 nm, respectively. The representative thickness of ~24 nm is above each of the two axial dimensions of BSA, confirming the ability of poly(SVBS-co-HEMA) to adsorb BSA.

2.4.5 Protein Adsorption on Nonwoven Fabrics

Polybutylene terephthalate nonwoven fabrics (PBT-NF) were prepared using meltblowing technology at different air flow rates, resulting in different average fiber diameter and basis weight. Fabrics with basis weight of 18 grams per m² were chosen for this work. The chemical composition of poly(SVBS-co-HEMA) copolymer grafted from the surface of PBT was assessed by XPS, which probes a depth of ~10 nm. Figure 2.6a shows survey scans for PBT-NF and PBT-NF grafted with poly(SVBS-co-HEMA) copolymer for different reaction times (2 and 8 h). For the reference PBT-NF, the scans revealed two distinct signals, corresponding to carbon at 285 eV and oxygen at 532 eV. The calculation of the area under the curves indicated surface concentrations of 73% carbon and 27 % oxygen, very close to theoretical concentration of 75% carbon and 25% oxygen calculated from the number of atoms present in the repeat unit of the polymer. The growth of poly(SVBS-co-HEMA) resulted in signals at 1072.2 eV and 168.7 eV, corresponding to sodium and sulfur, respectively, providing strong evidence for the presence of the copolymer on the surface. However, the concentrations of sodium and sulfur on the surface showed very weak dependence on the reaction time. For PBT-NF grafted for 2 h, sodium and sulfur contents were 2.6 % and 2.2 %, respectively, compared to PBT-NF grafted for 8 h, which showed sodium and sulfur contents of 3.4% and 2.6 %, respectively (Figure 2.6b). The increase in

O/C ratios from 0.36 for PBT-NF to 0.49 and 0.52 for PBT-NF grafted for 2 and 8 h corroborates successful grafting of the copolymer. Qualitative changes in surface hydrophilicity of PBT-NF were tested using sessile drop experiments. A drop of water on the surface of PBT-NF sat atop with a water contact angle (WCA) of $\sim 102^\circ$ and rolled off the surface, revealing its hydrophobic nature. Deposition of TMSC made the PBT-NF more hydrophobic, with WCA of $\sim 112^\circ$, and subsequent hydrolysis rendered the PBT-NF hydrophilic, with significant reduction in WCA to $\sim 43^\circ$. After immobilization of 2:8 poly(SVBS-co-HEMA), the modified PBT-NF showed a wicking behavior further showing its hydrophilicity (Figure A.8). The morphology of the fabrics shown in Figure 2.7 reveal no significant changes in average fiber diameter, from $\sim 10 \mu\text{m}$ for PBT nonwoven fabric to $\sim 11 \mu\text{m}$ for PBT post hydrolysis, which further increases to $\sim 22 \mu\text{m}$ for PBT grafted with 2:8 poly(SVBS-co-HEMA).

Static binding of lysozyme on the reference and grafted nonwoven fabric were studied by incubating the fabrics in lysozyme solution (0.3 mg/ml in 10 mM PBS at pH 7.4) for times ranging between 2 to 22 h as shown in Figure 2.8. The copolymer was grafted on the fabric using three different grafting times, namely, 2, 6 and 8 hours. For all fabrics, protein adsorption took place rapidly, on very short time scales, and adsorption reached saturation after 22 h. The reference, unmodified fabric immersed for 2, 6 and 22 h showed adsorption amounts equivalent to 1.2 ± 0.8 , 1.1 ± 0.45 and 1.2 ± 0.32 mg lysozyme per gram of fabric, respectively. The results indicate negligible dependence on immersion time. Similar trends were observed for fabrics grafted with poly(SVBS-co-HEMA) for different reaction times. While longer immersion times did not improve protein capture, longer

grafting times resulted in higher lysozyme adsorbed mass. For grafting times of 2, 6 and 8 hours, the amount of lysozyme adsorbed increased from 1.2 ± 0.8 (reference fabric) to 7 mg, 7.5 mg and $8.9 \text{ mg} \pm 0.7 \text{ mg}$ lysozyme per gram of fabric, respectively. Therefore, lysozyme adsorption on PBT nonwoven fabrics was clearly enhanced by modification with 2:8 poly(SVBS-co-HEMA).

2.5 Conclusions

Modification of inert polyester substrates for protein immobilization presents challenges and existing physical and chemical methods are harsh or result in degradation. In this work, polyester was successfully modified by activating the surface with trimethyl cellulose followed by vapor-phase acid-hydrolysis, which generated reactive hydroxyl groups. This facilitated copolymer grafting via ARGET-ATRP. We found that PBT, became hydrophilic after activation and, upon copolymer attachment, it adsorbed higher amounts of lysozyme compared to unmodified PBT. The grafted copolymer containing 20% SVBS and 80% HEMA (2:8 poly(SVBS-co-HEMA)) displayed a maximum adsorption capacity. The 2:8 poly(SVBS-co-HEMA) surfaces were regenerated after lysozyme adsorption by introducing combinations of different electrolyte solutions at pH 7.4, as shown by experiments with quartz-crystal microgravimetry. The adsorption of various proteins – lysozyme, fibrinogen and bovine serum albumin – showed strong pH dependence, with fibrinogen and BSA adsorbing on the ‘wrong side’ of the isoelectric point under electrostatically repulsive conditions. The pH-dependent behavior is due to repulsive protein-protein interactions, which is more pronounced further away from the isoelectric point. The proposed surface modification was translated to PBT nonwoven fabrics, which showed

lysozyme binding capacity of up to ~9 mg/g fabric, remarkably higher compared to unmodified PBT nonwovens. The proposed approach is an attractive alternative for imparting protein-adsorption functionality on polyesters.

2.6 Acknowledgment

Financial support for this project was provided by Groz-Beckert through Nonwovens Institute (NWI), Raleigh, North Carolina, Project A-4 (2014-15)

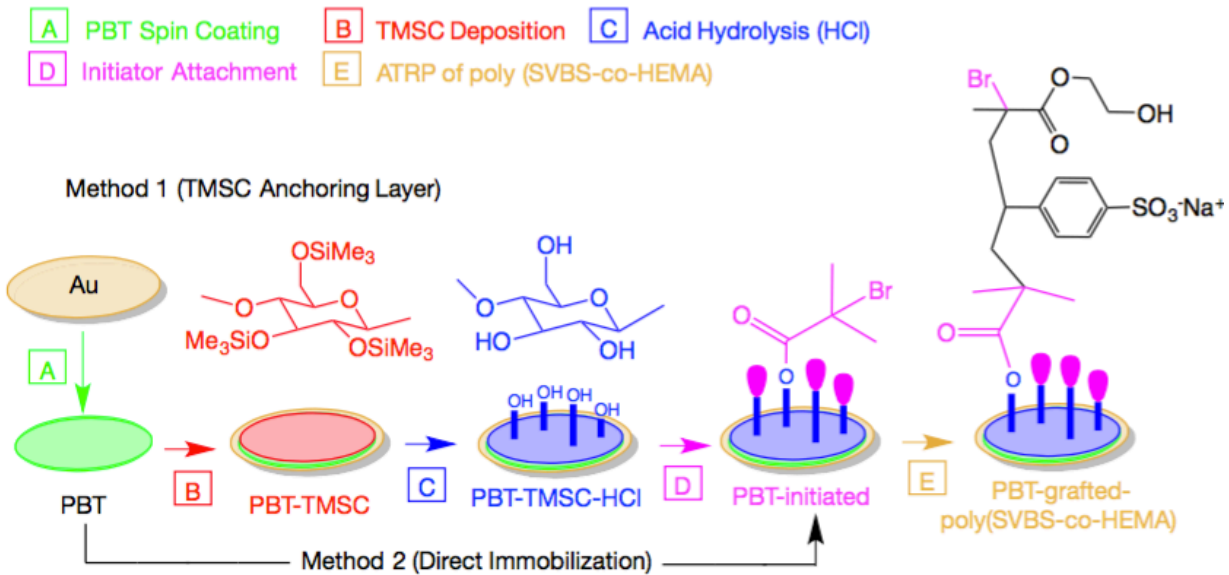


Figure 2.1 Schematic illustration of preparation of poly(SVBS-co-HEMA) on PBT using two different methods: Method 1 employs TMSiC as an anchoring layer before initiator immobilization and Method 2 immobilizes initiator directly on PBT substrates.

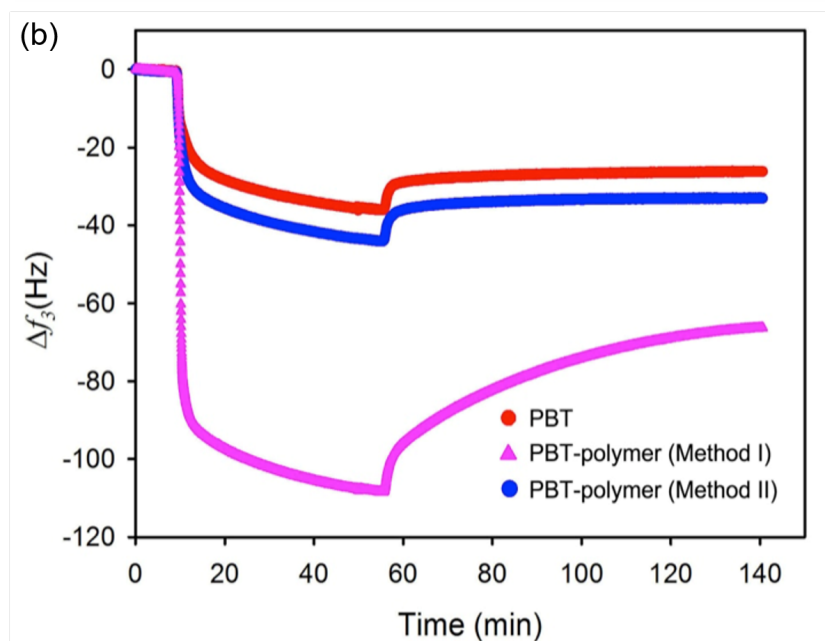
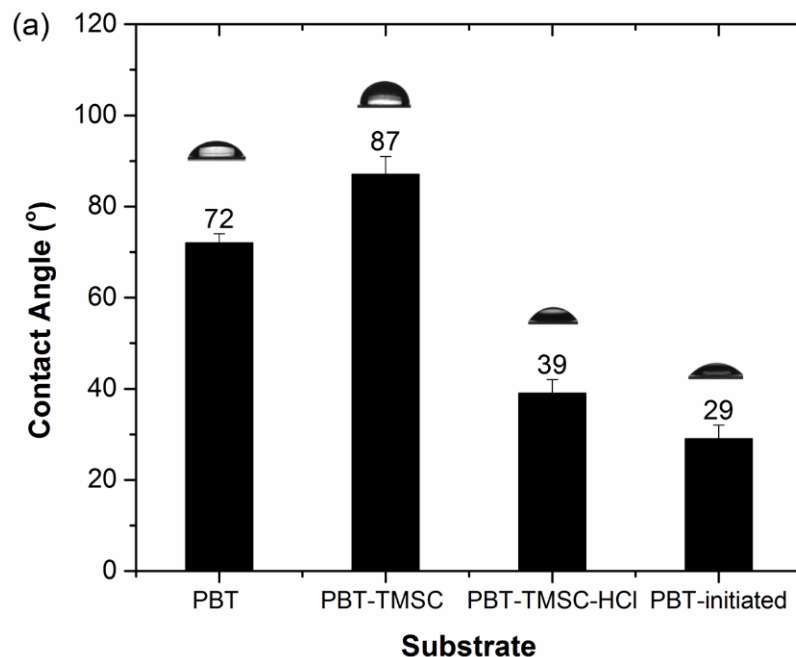


Figure 2.2 (a) Changes in wettability of PBT on Si-wafer upon surface modification, and (b) real-time adsorption of lysozyme (5 mg/ml in 10 mM PBS (with 150 mM Na⁺) at pH 7.4) on three different surfaces – PBT, PBT-g-poly(SVBS-co-HEMA) (8:2) (Method 1) and PBT-g-poly(SVBS-co-HEMA) (8:2) (Method 2). At 10 minutes, lysozyme solution in PBS (10 mM with 150 mM Na⁺) was injected into the system and at 60 minutes the system was rinsed with same buffer.

Table 2-1 Adsorption parameters of lysozyme (5 mg/ml in 10 mM PBS at pH 7.4) on control PBT thin films, and poly(SVBS-co-HEMA) 8:2 grafted on PBT using method 1 (with TMSC) and method 2 (without TMSC)

Method	$-\Delta f_{\text{ads}}$ (Hz)	$^* \Delta m_{\text{ads}}$ (ng/cm²)	$-\Delta f_{\text{des}}$ (Hz)	Δm_{des} (ng/cm²)	$-\Delta f_{\text{total}}$ (Hz)	Δm_{total} (ng/cm²)	Desorption (%)
-	39	230	13	77	26	153	33
TMSC	112	661	47	277	65	384	42
no TMSC	44	260	11	65	33	195	25

*All masses correspond to Sauerbrey mass for rigid layer derived using third overtone

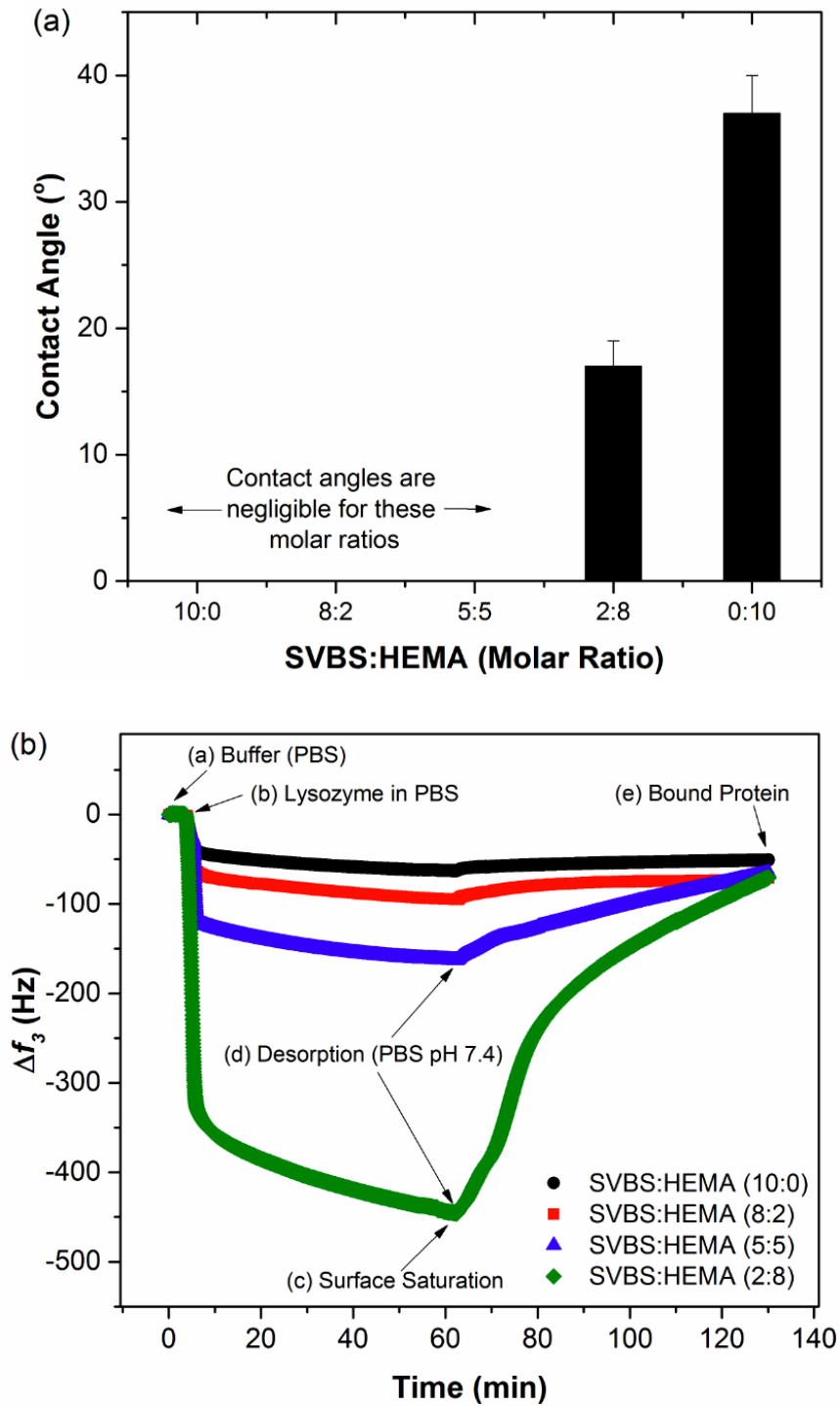


Figure 2.3 (a) The effect of SVBS:HEMA copolymer ratio on the wettability of grafted surfaces, (b) Real-time adsorption of lysozyme (1 mg/ml in 10 mM PBS at pH 7.4) on surfaces with different ratios of SVBS: HEMA.

Table 2-2 Adsorption parameters of lysozyme (1 mg/ml in 10 mM PBS at pH 7.4) on PBT for various copolymer ratio (SVBS: HEMA) in poly(SVBS-co-HEMA)

(SVBS: HEMA)	$-\Delta f_{\text{ads}}$ (Hz)	Δm_{ads} (ng/cm²)	$-\Delta f_{\text{des}}$ (Hz)	Δm_{des} (ng/cm²)	$-\Delta f_{\text{total}}$ (Hz)	Δm_{total} (ng/cm²)	Desorption (%)
10:0 (0 % HEMA)	62.41	368	10.77	64	51.64	305	17
8:2 (20% HEMA)	94.29	556	20.6	122	73.69	435	22
5:5 (50% HEMA)	162.28	957	85.52	505	76.76	453	53
2:8 (80% HEMA)	443.5	2617	349.2	2061	94.27	556	79

*All masses correspond to Sauerbrey mass for rigid layer derived using third overtone

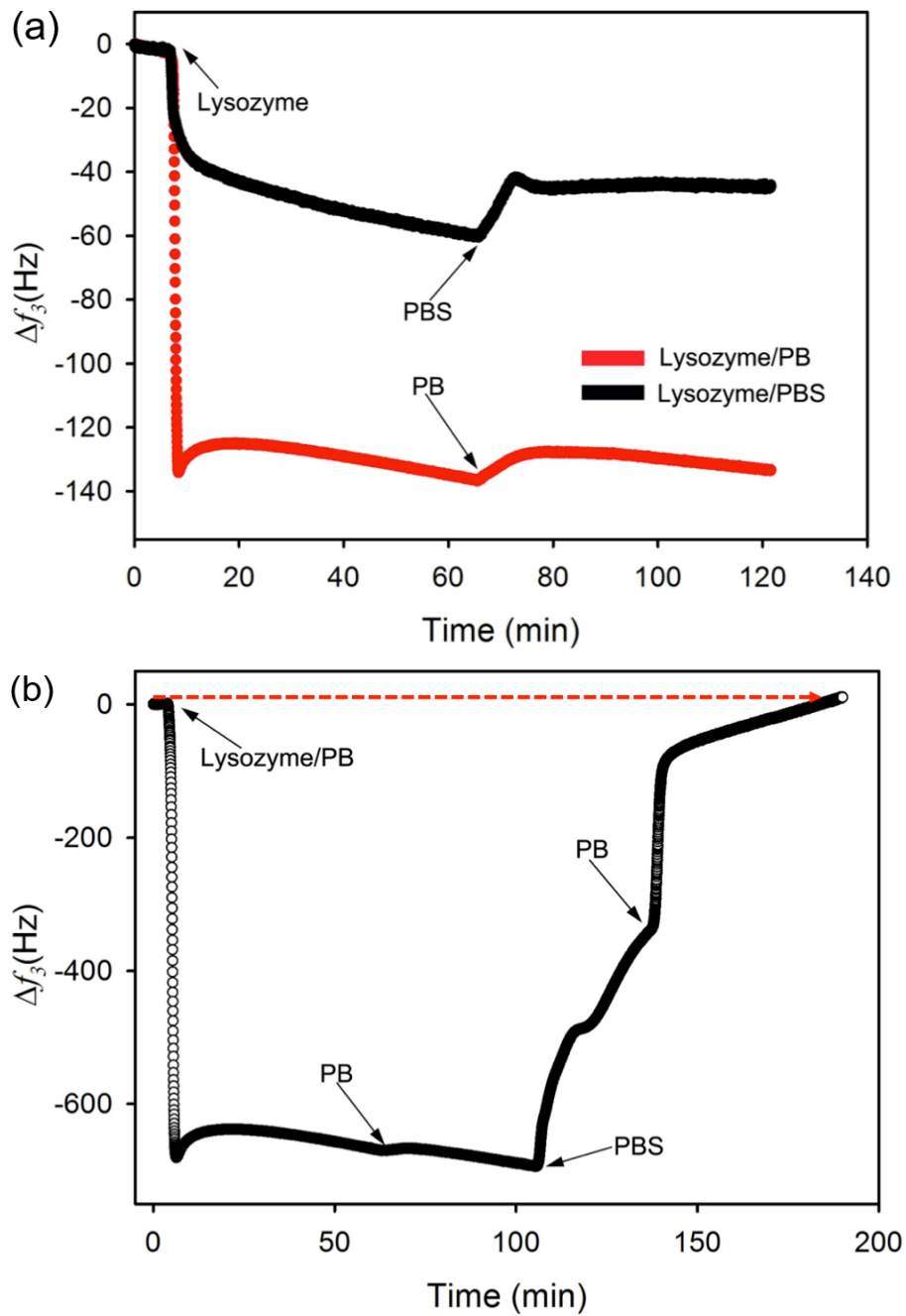


Figure 2.4 (a) Lysozyme adsorption on 8:2 poly (SVBS-co-HEMA) from bulk concentration of 1 mg/ml in 10 mM PB and PBS at pH 7.4. Desorption of lysozyme was achieved using respective buffers, and (b) lysozyme adsorption on 2:8 poly (SVBS-co-HEMA) from bulk concentration of 1 mg/ml in 10 mM PB, followed by desorption using PB and PBS showing surface regeneration capability.

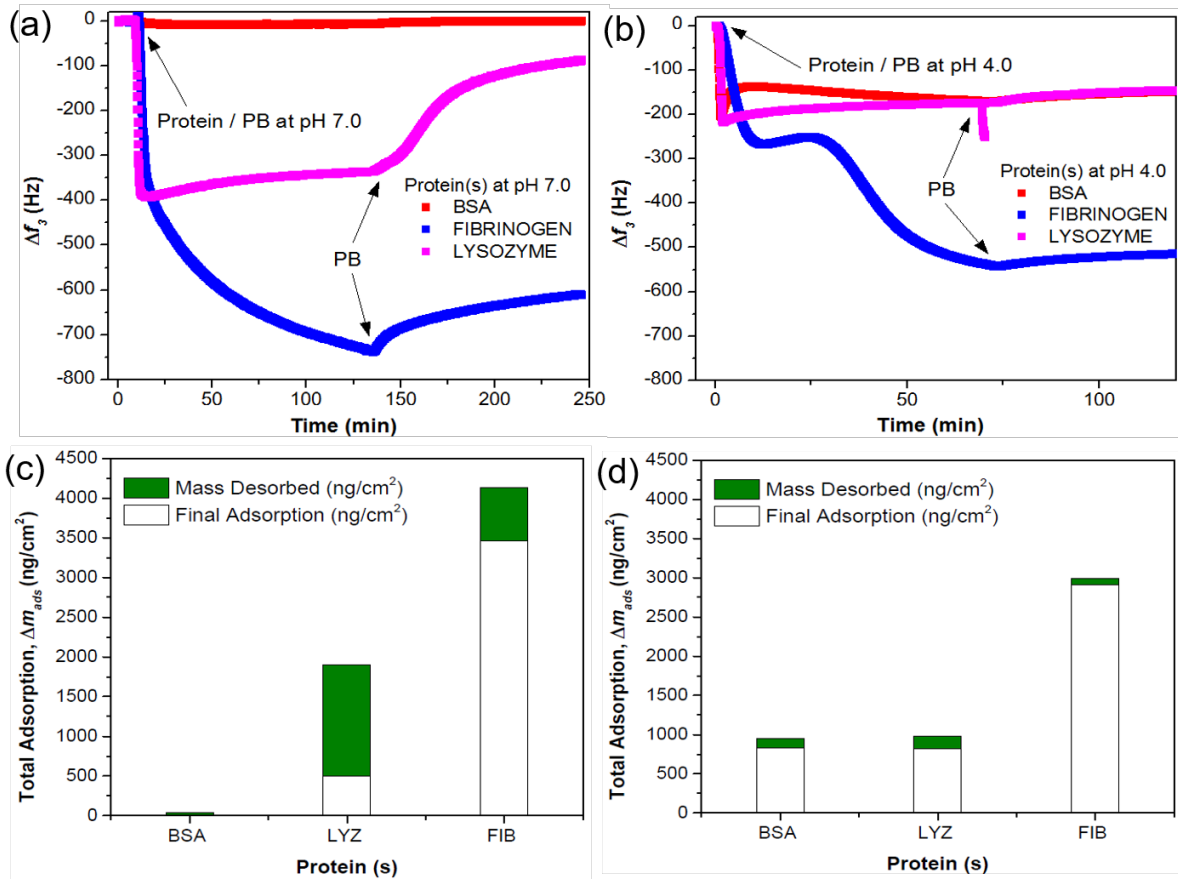


Figure 2.5 Effect of pH on adsorption of BSA, fibrinogen and lysozyme (1 mg/ml in 10 mM PB): (a) adsorption of BSA, fibrinogen and lysozyme at pH 7.0 and (b) at pH 4.0. Adsorption experiments were performed on 2:8 poly(SVBS-co-HEMA) surfaces grafted for 2 h.

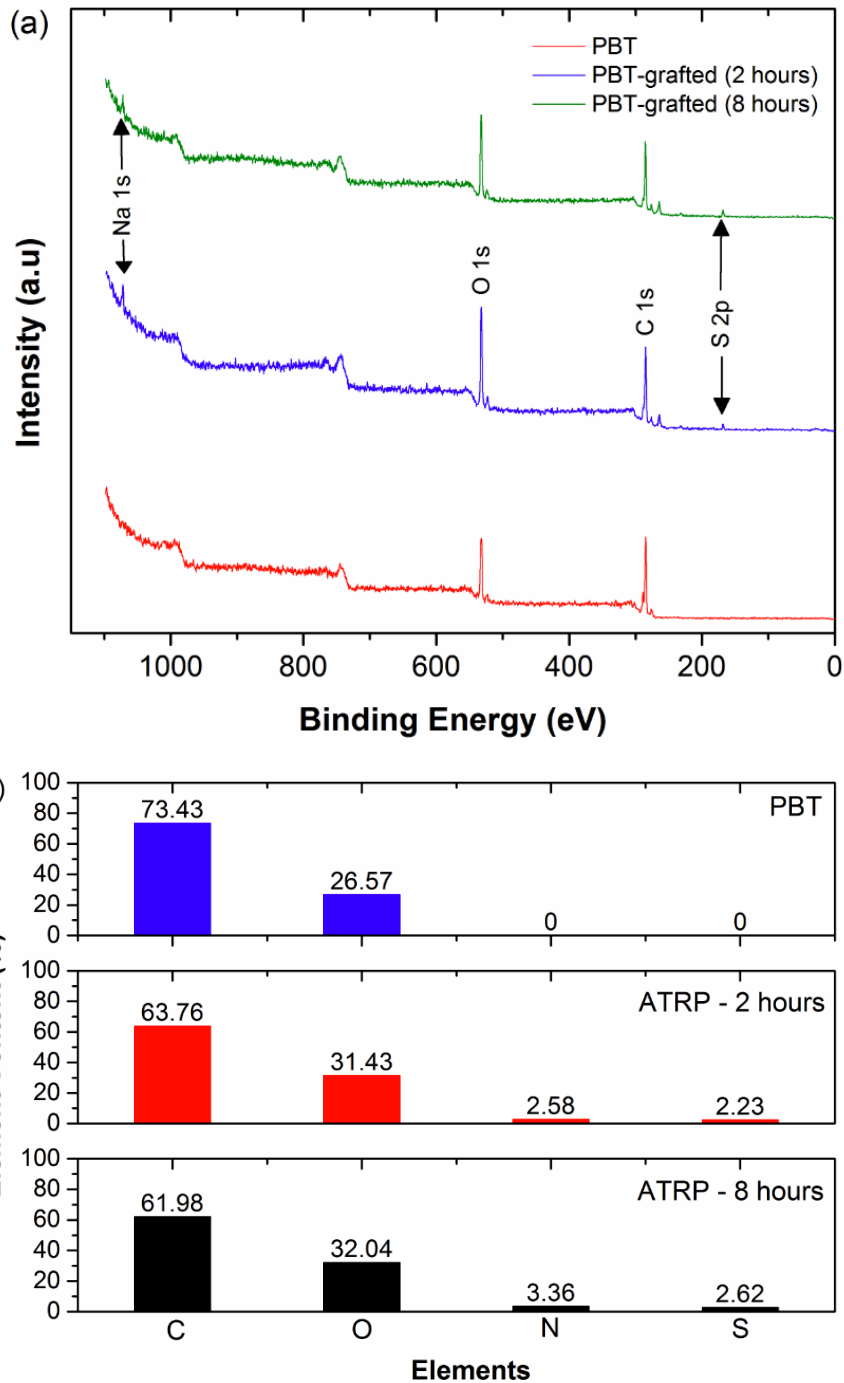


Figure 2.6 (a) XPS scans for PBT nonwoven fabric (reference) and PBT grafted with 2:8 poly(SVBS-co-HEMA) for different times (2 and 8 hours), and (b) elemental composition showing presence of sodium and sulfur after grafting PBT with 2:8 poly(SVBS-co-HEMA), confirming the presence of the copolymer.

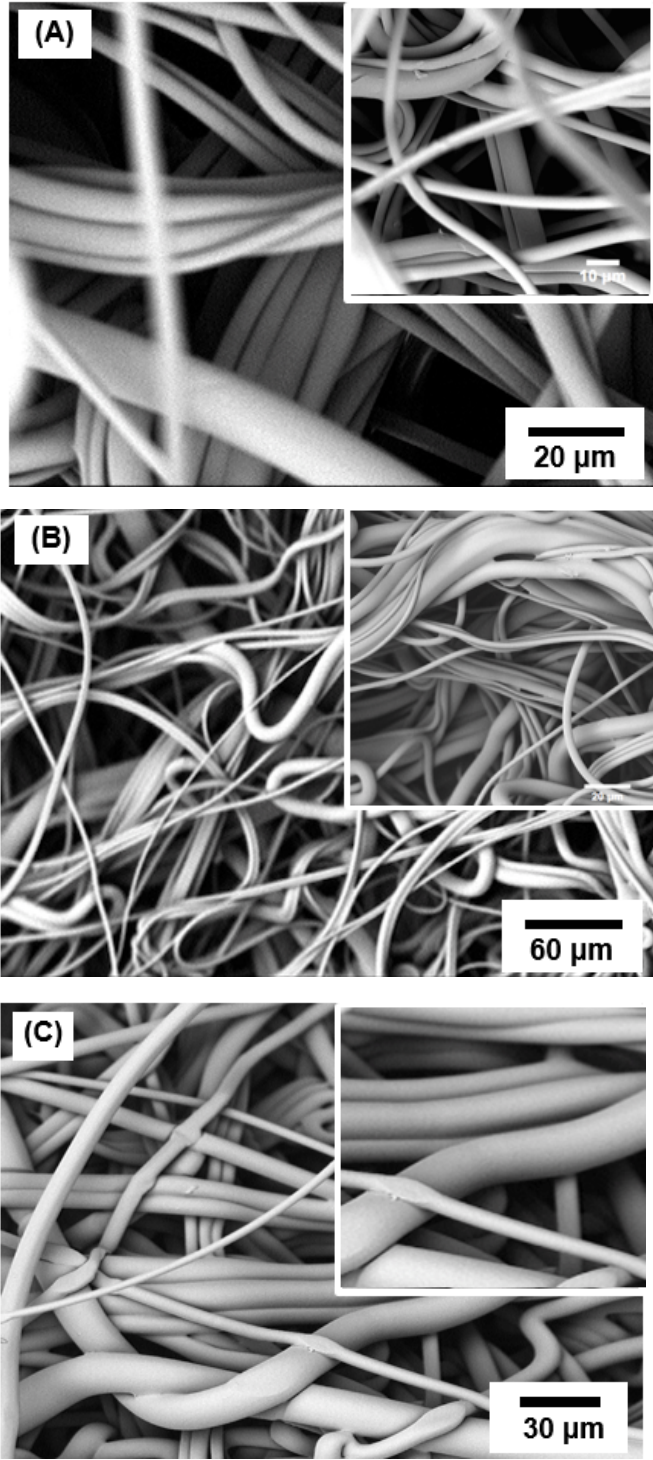


Figure 2.7 (a) Morphology of PBT nonwoven fabric (A), PBT nonwoven fabric after treatment with TMSC followed by hydrolysis (B) and PBT nonwoven fabric after grafting 2:8 poly(SVBS-co-HEMA) (C).

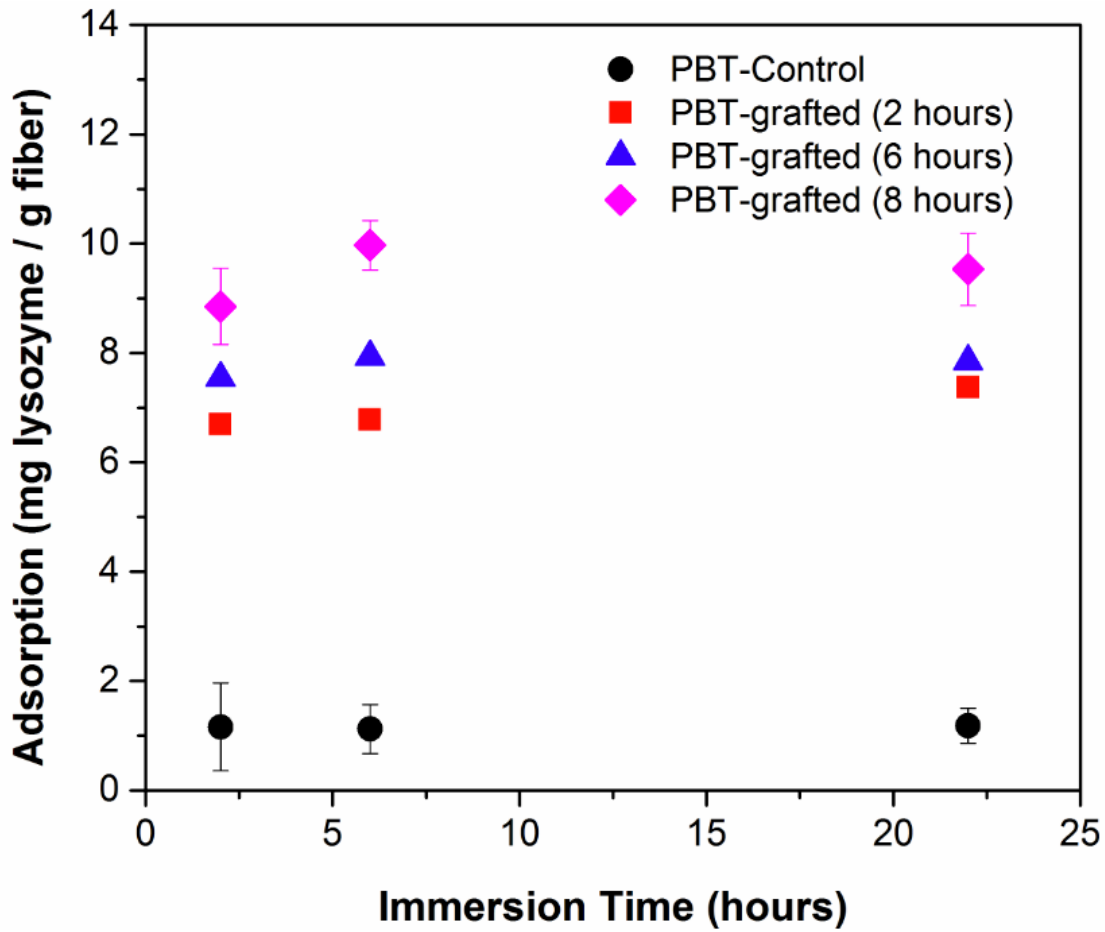


Figure 2.8 Effect of ATRP grafting and immersion time on adsorption of lysozyme (0.3 mg/ml in 10 mM PBS at pH 7.4) on PBT nonwoven fabric modified with 2:8 poly(SVBS-co-HEMA).

2.7 References

1. Langer, R. & Tirrell, D. A. Designing materials for biology and medicine. *Nature* **428**, 487–492 (2004).
2. Krishnan, S., Weinman, C. J. & Ober, C. K. Advances in polymers for anti-biofouling surfaces. *J. Mater. Chem.* **18**, 3405 (2008).
3. Banerjee, I., Pangule, R. C. & Kane, R. S. Antifouling coatings: Recent developments in the design of surfaces that prevent fouling by proteins, bacteria, and marine organisms. *Adv. Mater.* **23**, 690–718 (2011).
4. Burnouf, T. & Radosevich, M. Affinity chromatography in the industrial purification of plasma proteins for therapeutic use. *J. Biochem. Biophys. Methods* **49**, 575–586 (2001).
5. Bhakta, S. A., Evans, E., Benavidez, T. E. & Garcia, C. D. Protein adsorption onto nanomaterials for the development of biosensors and analytical devices: A review. *Anal. Chim. Acta* **872**, 7–25 (2015).
6. Vuoriluoto, M., Orelma, H., Zhu, B., Johansson, L. S. & Rojas, O. J. Control of Protein Affinity of Bioactive Nanocellulose and Passivation Using Engineered Block and Random Copolymers. *ACS Appl. Mater. Interfaces* **8**, 5668–5678 (2016).
7. Chang, M. C., Horng, R. Y., Shao, H. & Hu, Y. J. Performance and filtration characteristics of non-woven membranes used in a submerged membrane bioreactor for synthetic wastewater treatment. *Desalination* **191**, 8–15 (2006).
8. Kavakli, P. A. & Guven, O. Removal of concentrated heavy metal ions from aqueous solutions using polymers with enriched amidoxime groups. *J. Appl. Polym. Sci.* **93**, 1705–1710 (2004).
9. Klomp, A. J. A., Engbers, G. H. M., Mol, J., Terlingen, J. G. A. & Feijen, J. Adsorption of proteins from plasma at polyester non-wovens. *Biomaterials* **20**, 1203–1211 (1999).

10. Zheng, Y., Liu, H., Gurgel, P. V. & Carbonell, R. G. Polypropylene nonwoven fabrics with conformal grafting of poly(glycidyl methacrylate) for bioseparations. *J. Memb. Sci.* **364**, 362–371 (2010).
11. Gupta, B. *et al.* Surface modification of polyester films by RF plasma. *J. Appl. Polym. Sci.* **78**, 1083–1091 (2000).
12. Vesel, A., Junkar, I., Cvelbar, U., Kovac, J. & Mozetic, M. Surface modification of polyester by oxygen- And nitrogen-plasma treatment. *Surf. Interface Anal.* **40**, 1444–1453 (2008).
13. Goresek, M. *et al.* Functionalization of PET Fabrics by Corona and Nano Silver. *Text. Res. J.* **80**, 253–262 (2010).
14. Xu, W. & Liu, X. Surface modification of polyester fabric by corona discharge irradiation. *Eur. Polym. J.* **39**, 199–202 (2003).
15. Srinivasan, R. & Lazare, S. Modification of Polymer Surfaces By UV. **26**, 1297–1300 (1985).
16. Wang, C. X., Ren, Y. & Qiu, Y. P. Penetration depth of atmospheric pressure plasma surface modification into multiple layers of polyester fabrics. *Surf. Coatings Technol.* **202**, 77–83 (2007).
17. Chen, W. & McCarthy, T. J. Chemical Surface Modification of Poly(ethylene terephthalate). *Macromolecules* **31**, 3648–3655 (1998).
18. Fadeev, A. Y. & McCarthy, T. J. Surface Modification of Poly (ethylene terephthalate) To Prepare Surfaces with Silica-Like Reactivity. *Langmuir* **14**, 5586–5593 (1998).
19. Bech, L. *et al.* Atom transfer radical polymerization of styrene from different poly(ethylene terephthalate) surfaces: Films, fibers and fabrics. *Eur. Polym. J.* **45**, 246–255 (2009).
20. Hsieh, Y.-L. & Cram, L. A. Enzymatic Hydrolysis to Improve Wetting and Absorbency of Polyester Fabrics. *Text. Res. J.* **68**, 311–319 (1998).

21. Horn, M. & Matyjaszewski, K. Solvent Effects on the Activation Rate Constant in Atom Transfer Radical Polymerization. *Macromolecules* **46**, 3350–3357 (2013).
22. Matyjaszewski, K. Atom Transfer Radical Polymerization (ATRP): Current Status and Future Perspectives. *Macromolecules* **45**, 4015–4039 (2012).
23. Matyjaszewski, K. Atom Transfer Radical Polymerization. *Chem. Rev.* **101**, 2921–2990 (2001).
24. Rakhmatullina, E. *et al.* Functionalization of gold and silicon surfaces by copolymer brushes using surface-initiated ATRP. *Macromol. Chem. Phys.* **208**, 1283–1293 (2007).
25. Carlmark, A. & Malmström, E. Atom transfer radical polymerization from cellulose fibers at ambient temperature. *J. Am. Chem. Soc.* **124**, 900–901 (2002).
26. Carlmark, A. & Malmström, E. E. ATRP grafting from cellulose fibers to create block-copolymer grafts. *Biomacromolecules* **4**, 1740–1745 (2003).
27. Zoppe, J. O. *et al.* Poly(N -isopropylacrylamide) brushes grafted from cellulose nanocrystals via surface-initiated single-electron transfer living radical polymerization. *Biomacromolecules* **11**, 2683–2691 (2010).
28. Yue, W. W. *et al.* Grafting of zwitterion from polysulfone membrane via surface-initiated ATRP with enhanced antifouling property and biocompatibility. *J. Memb. Sci.* **446**, 79–91 (2013).
29. Matyjaszewski, K., Dong, H., Jakubowski, W., Pietrasik, J. & Kusumo, A. Grafting from surfaces for ‘everyone’: ARGET ATRP in the presence of air. *Langmuir* **23**, 4528–31 (2007).
30. Paterson, S. M. *et al.* The synthesis of water-soluble PHEMA via ARGET ATRP in protic media. *J. Polym. Sci. Part A Polym. Chem.* **48**, 4084–4092 (2010).
31. Simakova, A., Averick, S. E., Konkolewicz, D. & Matyjaszewski, K. Aqueous ARGET ATRP. *Macromolecules* **45**, 6371–6379 (2012).

32. Hansson, S., Östmark, E., Carlmark, A. & Malmström, E. ARGET ATRP for Versatile Grafting of Cellulose Using Various Monomers. *ACS Appl. Mater. Interfaces* **1**, 2651–2659 (2009).
33. Song, J. *et al.* Development and characterization of thin polymer films relevant to fiber processing. *Thin Solid Films* **517**, 4348–4354 (2009).
34. Kim, D. T., Blan, H. W. & Radke, J. Direct Imaging of Lysozyme Adsorption onto Mica by Atomic Force Microscopy. *Langmuir* **18**, 5841–5850 (2002).
35. Su, T. J., Lu, J. R., Cui, Z. F. & Penfold, J. The Effect of Solution pH on the Structure of Lysozyme Layers Adsorbed at the Silica-Water Interface Studied by Neutron Reflection. *Langmuir* **14**, 438–445 (1998).
36. Lu, J. R., Swann, J., Peel, L. L. & Freeman, N. J. Lysozyme Adsorption Studies at the Silica/Water Interface Using Dual Polarization Interferometry. *Langmuir* **20**, 1827–1832 (2004).
37. Su, T. J., Lu, J. R., Thomas, R. K., Cui, Z. F. & Penfold, J. The Adsorption of Lysozyme at the Silica-Water Interface: A Neutron Reflection Study. *J. Col* **203**, 419–429 (1998).
38. Wei, T., Kaewtathip, S. & Shing, K. Buffer Effect on Protein Adsorption at Liquid/Solid Interface. *J. Phys. Chem. C* **113**, 2053–2062 (2009).
39. Arima, Y. & Iwata, H. Effect of wettability and surface functional groups on protein adsorption and cell adhesion using well-defined mixed self-assembled monolayers. *Biomaterials* **28**, 3074–3082 (2007).
40. Arima, Y. & Iwata, H. Effects of surface functional groups on protein adsorption and subsequent cell adhesion using self-assembled monolayers. *J. Mater. Chem.* **17**, 4079 (2007).
41. Bellion, M. *et al.* Protein adsorption on tailored substrates: long-range forces and conformational changes. *J. Phys. Condens. Matter* **20**, 404226 (2008).

42. Kim, J. & Somorjai, G. A. Molecular Packing of Lysozyme , Fibrinogen , and Bovine Serum Albumin on Hydrophilic and Hydrophobic Surfaces Studied by Infrared - Visible Sum Frequency Generation and Fluorescence Microscopy. *JACS* 3150–3158 (2003).
43. Yu, J. *et al.* Structure of Polyelectrolyte Brushes in the Presence of Multivalent Counterions. *Macromolecules* **49**, 5609–5617 (2016).
44. Xu, K., Ouberai, M. M. & Welland, M. E. A comprehensive study of lysozyme adsorption using dual polarization interferometry and quartz crystal microbalance with dissipation. *Biomaterials* **34**, 1461–1470 (2013).
45. Ouberai, M. M., Xu, K. & Welland, M. E. Effect of the interplay between protein and surface on the properties of adsorbed protein layers. *Biomaterials* **35**, 6157–6163 (2014).
46. De Vos, W. M., Biesheuvel, P. M., De Keizer, A., Kleijn, J. M. & Stuart, M. A. C. Adsorption of the protein bovine serum albumin in a planar poly(acrylic acid) brush layer as measured by optical reflectometry. *Langmuir* **24**, 6575–6584 (2008).
47. Hollmann, O., Gutberlet, T. & Czeslik, C. Structure and protein binding capacity of a planar PAA brush. *Langmuir* **23**, 1347–1353 (2007).
48. Hollmann, O. & Czeslik, C. Characterization of a planar poly(acrylic acid) brush as a materials coating for controlled protein immobilization. *Langmuir* **22**, 3300–3305 (2006).
49. Wittemann, A. & Ballauff, M. Interaction of proteins with linear polyelectrolytes and spherical polyelectrolyte brushes in aqueous solution. *Phys. Chem. Chem. Phys.* **8**, 5269 (2006).
50. Ballauff, A. W. B. H. M. Polyelectrolyte-mediated Protein Adsorption. *Prog. Polym. Sci.* **133**, 58–64 (2006).
51. Hu, Y. *et al.* Study of fibrinogen adsorption on poly(ethylene glycol)-modified

surfaces using a quartz crystal microbalance with dissipation and a dual polarization interferometry. *RSC Adv.* **4**, 7716 (2014).

52. Tsapikouni, T. S. & Missirlis, Y. F. pH and ionic strength effect on single fibrinogen molecule adsorption on mica studied with AFM. *Colloids Surfaces B Biointerfaces* **57**, 89–96 (2007).
53. Hu, Y. *et al.* pH Dependence of Adsorbed Fibrinogen Conformation and Its Effect on Platelet Adhesion. *Langmuir* **32**, 4086–4094 (2016).
54. Su, T. J., Lu, J. R., Thomas, R. K. & Cui, Z. F. Effect of pH on the Adsorption of Bovine Serum Albumin at the Silica/Water Interface Studied by Neutron Reflection. *J. Phys. Chem. B* **103**, 3727–3736 (1999).
55. Su, T. J., Thomas, R. K., Cui, Z. F. & Penfold, J. The Conformational Structure of Bovine Serum Albumin Layers Adsorbed at the Silica–Water Interface. *J. Phys. Chem. B* **102**, 8100–8108 (1998).

Chapter 3 Modulating Gelation Kinetics and Mechanical Properties of Photocurable Poly(vinyl alcohol) Derivative through Network Formation Using Cellulose Nanocrystals

3.1 Abstract

The absence of control over crosslinking kinetics and mechanical integrity of photocrosslinkable polymers limits their use in several applications. We report a simple technique utilizing cellulose nanocrystals (CNC) to modulate crosslinking kinetics as well as enhance mechanical performance of aqueous photoactive polyvinyl alcohol derivative, poly(vinyl alcohol), N-methyl-4 (4'-formylstyryl) pyridinium methosulfate acetal (PVA-SbQ). The interactions between PVA-SbQ and CNC present in dispersions prepared using simple solution mixing facilitated network formation. The resulting changes in rheological behavior of PVA-SbQ were studied before and after exposure to UV at a fixed intensity of 10 mW/cm². We found that inclusion of CNC's above a critical threshold concentration between 1-1.5 wt.% results in a percolated CNC network before UV-exposure, further corroborated using Van Gurp Palmen and Cole-Cole plots as signatures for percolation. The structure build-up after UV exposure studied using in-situ dynamic photo-crosslinking experiments reveals alterations in gelation kinetics and mechanical strength of neat systems. The crossover times of storage (G') and loss moduli (G'') increased with CNC content less than 1.5 wt.% but dramatically reduced above 1.5 wt.%. A steep jump in the storage modulus of fully-crosslinked networks representative of percolation with critical threshold concentration (~1.4 wt.%) as well as ~131% increase in storage modulus (G') at 2.5 wt.% CNC was observed. The results point to the existence of microstructural changes wherein the polymer-

CNC interactions induce a percolated microstructure that allows efficient stress transfer. The induced percolation mechanism can be utilized in the design of photocrosslinkable systems for applications requiring mechanical reinforcement.

3.2 Introduction

The formation of three-dimensional networks of crosslinked polymers for applications such as coatings,¹ adhesives,² tissue engineering,^{3,4} and 3-D printing⁵⁻⁹ has been realized through the use of synthetic polymers such as polyvinyl (alcohol) (PVA),^{10,11} poly (ethylene oxide) (PEO)¹² and poly (acrylic acid) (PAA)¹³⁻¹⁵ as well as natural biopolymers such as cellulose,^{16,17} chitosan¹⁸ and alginates.¹⁹ These networks are typically formed using physical crosslinking via the use of ionic interactions and hydrogen bonding, and chemical crosslinking approaches using free radical and photo-polymerization techniques.²⁰ Typically, photocrosslinkable systems consist of monomers, oligomers, and photoinitiators that undergo series of radical generation and monomer addition in the presence of UV light to form highly insoluble and infusible interconnected 3-D architectures.^{21,22} However, polymers with inherent photosensitivity are attractive additions to the library of photocrosslinkable polymers. These possess light-sensitive photocrosslinkable moieties that undergo intermolecular crosslinking upon exposure to light, forming interconnected networks in the process.. One such commercially available, water-soluble, photocrosslinkable polymer of interest to us is PVA-SbQ, synthesized via substitution of pendant hydroxyl groups on the PVA backbone with photoactive styrylpyridinium (SbQ) moiety, which is sensitive to UV emitting light, acting as crosslinkable domains.²³⁻²⁵ While negating the need for external photoinitiators, oligomers and monomers, the addition of modest amounts of SbQ ranging

between 0.1 to 4 mol% to the PVA backbone offers very high photosensitivity relative to conventional photoresists,^{23–25} simultaneously maintaining physical and chemical characteristics of PVA such as biocompatibility and water resistance.²⁶ The precise mechanism of crosslinking was contested until high-resolution spectral analyses undertaken to probe precise nature of photo crosslinking mechanism revealed a blue shift in the absorption spectra to ~325 nm, referred to as the H-band, arising due to intramolecular H-aggregation even in dilute solutions.^{27–29} The photo dimerization of the double bonds in the presence of UV emitting light at ~365 nm produces a three-dimensional structure that partially swells but does not disassociate in aqueous solutions. PVA-SbQ has been used for immobilization of enzymes,^{30,31} cell entrapment,³² crosslinkers in systems containing hyaluronic acid to enhance mechanical properties,³³ photopolymer emulsions for screen-printing, and bio printable ink formulation.²⁷ However, these systems are often limited by weak mechanical performance, and further require implementations of strategies to reinforce their mechanical properties.

Several strategies have been utilized to increase the strength of crosslinked networks, including the inclusion of nanoparticles,^{34–37} double-network formation³⁸ and use of interpenetrating networks.^{39,40} Herein, we report use of biodegradable, rod-like cellulose nanocrystals (CNC) to achieve mechanical reinforcement via percolation mechanism. Cellulose nanocrystals are unique materials, which can form gels depending on the amount and presence of adsorbing or non-adsorbing polymers. **For instance**, the interaction of rod-shaped nanocrystalline cellulose with two water-soluble polymers, non-ionic hydroxyethyl cellulose (HEC) and ionic carboxymethyl cellulose (CMC) investigated using viscoelastic

rheological measurements and isothermal titration calorimetry revealed gel-like structures with yield stresses, which was attributed to depletion flocculation due to the presence of non-adsorbing polymers.⁴¹ The gelation concentration was reduced after addition of small amounts of adsorbing polymers such as non-ionic polysaccharides which increased the effective volume fraction of CNC dispersions, causing gelation at much lower concentration.⁴² The interaction of two water-soluble polymers, anionic sodium polyacrylate (PAAS) and non-ionic polyethylene glycol (PEG) on self-assembly of commercial CNC suspension, studied using quartz-crystal microbalance revealed adsorption of PEG onto CNC most likely due to steric stabilization and hydrogen bonding between CNC's and PEG, but no adsorption of PAAS onto CNC due to unfavorable electrostatic interactions.⁴³ However, studies have demonstrated that hydrogen bonding does not play an important role because the cellulose surface hydroxyl groups are not sufficiently acidic to form hydrogen bonds with oxygen in aqueous PEG, and the adsorption is rather entropically driven.⁴⁴ Depletion flocculation was the primary reason for gelation behavior of semi-dilute CNC's in semi-dilute un-entangled carboxymethyl cellulose solutions, whereas weak depletion interactions occurred in systems with PEO after surfaces were saturated with PEO adsorption.⁴⁵ These interactions between water-soluble polymers and cellulose nanocrystals can be used in the design of new systems that require mechanical reinforcement via favorable polymer-CNC interactions.

To improve the weak mechanical performance associated with traditional photopolymer crosslinking, we utilize rigid, rod-like cellulose nanocrystals that form sample spanning networks above a critical concentration. By combining negatively charged CNC

with positively charged PVA-SbQ, networks with high elastic moduli can be obtained. The presence of negatively charged CNC in salt-free aqueous solutions of positively charged PVA-SbQ induces favorable electrostatics, forming percolated microstructures beyond a critical concentration, above which the host polymer no longer dominates rheological properties, and improves systems that are limited by weak mechanical performance. This study aids in the development of photo-curable polymers, simultaneously exhibiting controllable kinetics and mechanical properties, for potential applications in hydrogels, UV-based gel spinning, and 3D printing.

3.3 Materials and Methods

3.3.1 Materials

Poly (vinyl alcohol), N-methyl-4 (4'-formylstyryl) pyridinium methosulfate acetal ((PVA-SbQ), MW ~ 45,000 g/mol and 4.1 mol % SbQ content, 13.3 wt.% in water, Polysciences Inc., Warrington, PA) and cellulose nanocrystals ((CNC), length of 100 nm, width of 5 nm, University of Maine Process Development Center, U.S.A) were used as received. Prior to preparing solutions, CNC powder was dried in a vacuum oven for 2 days at 120°C.

3.3.2 Preparation of PVA-SbQ/CNC Solutions

5 wt.% homogeneous stock solution of well dispersed CNC's in deionized water was prepared by adding deionized water to the CNC's, and vortex mixing for 1-2 minutes to break down large aggregates. After vortex mixing the aqueous CNC solution was sonicated in a bath sonicator (8510 Branson, U.S.A) for 4 hours. Following sonication, which produced a homogeneous dispersion of CNC's, the solution was further vortex mixed to ensure a

homogenous suspension which was stored in a refrigerator at 4 °C to hinder particle settling. After 30 days, there was no evidence of CNC's settling in the stock solution. Aqueous solutions of PVA-SbQ with well-dispersed CNC's were made by diluting the stock concentrations of aqueous CNC and PVA-SbQ to the desired levels. The PVA-SbQ/CNC solutions were then vortex-mixed for 30 seconds. Afterwards, the vials were wrapped in aluminum foil to prevent trace UV light exposure and placed on a stir plate for 6 hours. Following stirring, the PVA-SbQ/CNC solutions were sonicated for 1 hour. All solutions were stored in a refrigerator at 4 °C. Samples were taken out of the refrigerator and stirred for 40 minutes prior to any experiments. All experiments were completed within 7 days after sample preparation. To prevent temperature-induced artifacts such as aggregation, heating and reverse esterification, sonication was performed using an ice-bath.

3.3.3 Rheological Measurements and Characterization

All rheological experiments were performed on a stress-controlled Discovery Hybrid Rheometer-2 manufactured by TA Instruments (New Castle, DE). A 20 mm aluminum parallel-plate was selected as the top geometry. A UV photo-curing attachment with a transparent, acrylic bottom plate was used to administer controlled dosages of UV light ($\lambda=365$ nm) to each sample and collect *in-situ* data during photo-crosslinking. UV radiometer (Silver Line) was used to calibrate the intensity of UV light before each experiment. Samples were exposed to UV light with an intensity of 10 mW/cm² at the beginning of each time sweep, and the UV light was turned off at the end of each time sweep. The frequency of dynamic oscillation fixed (10 rad/s) throughout each time sweep. The photo-crosslinking reaction was found to proceed much faster at lower intensities with a smaller gap, which can

be attributed to the exponential decay of observed intensity through the sample¹ (i.e. $I(x) = I_0 e^{-\alpha x}$ where I is the observed intensity, I_0 is the applied intensity, α is the decay factor and x is the material thickness). A gap of 500 microns was set for all experiments because it is the lower limit of the acceptable gap range (specified by TA instruments) for 20 mm parallel plate geometry. Before conducting dynamic experiments, stress sweeps were performed to ensure that the parameters selected for each solution would be within their corresponding linear viscoelastic regimes. To ensure consistency across samples, measurements were performed after pre-shearing samples at 10 rad/s for 10 s and equilibration time of 10 s. Particle size and zeta potential of cellulose nanocrystals with and without PVA-SbQ were obtained using a zeta potential analyzer (Zeta2000, Malvern Instruments, U.S.A.) equipped with a 4.0 mW He-Ne laser ($\lambda=633$ nm). Reported values are average of six independent measurements. Entanglement concentration regime of PVA-SbQ was confirmed by electrospinning solutions of PVA-SbQ ranging between 1-10 wt.%. The solutions in a syringe were loaded in a syringe pump (Model No. 2345) that set the flow rate at 0.5 ml/h. A high voltage power supply (Model No. 1721) was used to impart voltage of 15 kV at the needle tip. The fibers were collected on aluminum foil-wrapped grounded stationary collector plate 10-15 cm away from the needle tip. The experiments were carried out at room temperature (20-25°C) and relative humidity 20-30%. The morphology of resulting nanofibers was investigated under scanning electron microscope (FEI Verios 460L). Nanofibers were pressed on a carbon tape fixed to the sample holder, sputtered coated with ~ 7 nm layer of Pd before imaging.

3.4 Results and Discussion

Understanding of precise mechanism by which CNC's alter rheological behavior of PVA-SbQ relies first on the determination of whether salt-free aqueous solutions of PVA-SbQ behaves rheologically as a neutral polymer or as a polyelectrolyte, and then on the determination of its entanglement regime using simple steady shear rheology combined with scaling principles based on neutral polymers and polyelectrolytes. In semi-dilute unentangled and semi-dilute entangled regime for neutral polymer, viscosity scales with concentration to the 2 and 4.7 power respectively, in sharp contrast to polyelectrolytes for which viscosity scales with concentration to 0.5 and 1.5 power, suggesting weak concentration dependence on viscosity for polyelectrolytes compared to neutral polymer.⁴⁶⁻⁵⁰ Figure 3.1a shows the concentration effect of salt-free aqueous solutions of PVA-SbQ on the shear rheology across three decades of shear rate (10^0 - 10^3 s⁻¹), often used to find entanglement concentration. At low concentration (< 2 wt.%), the viscosity of PVA-SbQ resembles that close to water (10^{-3} Pa-s) and the effect of increasing concentration to 10 wt.% is to increase the viscosity by three decades (close to 0.5 Pa-s). However, the viscosity curves, despite the addition of PVA-SbQ, maintain their Newtonian behavior irrespective of polymer concentration.

Typically, shear thinning of polymer solutions is more pronounced in highly concentrated systems or melts compared to dilute solution; however, PVA-SbQ is rheologically unique because, at shear rates lower than 1 s⁻¹, there is evidence of a lack of or minor shear thinning and a plateau at higher shears rates. Since measurements at low shear rates to obtain zero-shear rate viscosity were experimentally inaccessible due to inadequate signals from the sample, the viscosity at higher accessible shear rates was used to obtain

specific viscosity. The log-log plot of specific viscosity versus polymer concentration to determine the entanglement concentration (Figure 3.1b) reveals slopes of 2.2 and 4.9 in excellent agreement with scaling relationships proposed by Doi and Edwards for neutral polymers, as opposed to those for polyelectrolytes, in semi-dilute unentangled and semi-dilute entangled regime⁵¹. The neutral polymer type behavior could be explained by the low amount (4.1 mol%) of charged N-methyl-4(4'-formylstyryl) pyridinium methosulfate acetal group, which is not sufficient to impart a polyelectrolyte character. The entanglement concentration (C_e) for PVA-SbQ is determined at 4.8 wt.%, and corroborated using electrospinning, showing beaded fibers for concentrations less than 5 wt.% compared to smooth, uniform, bead-free fibers obtained at concentrations above critical entanglement concentration (6 wt.%).

The physical properties and surface characteristics of CNC used in this work have been characterized thoroughly in the previous literature.⁴³ Atomic force microscopy measurements reveal an aspect ratio of 41 ± 14 nm, very close to manufacturers values between 30-40 nm.⁴³ Bath sonication, which breaks the aggregates, is used to prepare dilute dispersions of these rod-like particles (< 1 wt.%) to understand its aggregation state and contributions to viscosity. At low concentrations (<1 wt.%), sonication was able to make a homogeneous dispersion. The hydrodynamic characteristics of 0.1 wt.% CNC's obtained using dynamic light scattering measurements shown in Table 3.1 reveal hydrodynamic size ~ 91 nm and a zeta potential of -42.8 due to negative charges on the surface. The theoretical hydrodynamic radius, calculated using combinations of Stokes-Einstein and Kirkwood and Riseman,⁵² for CNC's of length 150-200 nm and aspect ratio of 30-40 is between 22.1 and 27.1 nm, suggesting that CNC's are not individually dispersed but shows appreciable

aggregation. In addition, dispersions of 0.5 wt.% CNC's reveal hydrodynamic size of ~70 nm and much a higher zeta potential of -53.6, suggesting that addition of CNC's did not increase the extent of flocculation, instead added additional negative charges facilitating further stabilization due to electrostatic repulsion. This addition increases the conductivity from 0.04 mS/cm to 0.08 mS/cm and from 0.08 mS/cm to 0.13 mS/cm for dispersions containing 0.1 wt.% and 0.5 wt.% CNC's respectively.

Furthermore, contributions of CNC's to viscosity in the dilute regime can be used to determine their aspect ratio, which otherwise is typically determined using microscopy techniques. The steady-shear rheological behavior of dispersions containing rod-like structures such as CNC's is predominantly influenced by stresses related to the suspending medium as well as the particle. In very dilute dispersions, where colloidal interactions can be neglected, the contribution to viscosity is a consequence of the balance between Brownian and hydrodynamic forces, and additional particle properties such as particle size, particle shape, particle size distribution, particle stiffness and particle deformability - its tendency to align into ordered phase under shear flow. Assuming dispersions contain homogeneous, cylindrical, stiff rod-like structures, the intrinsic viscosity of CNC's, which is approximately ~40 ml/g determined using Huggins plot shown in Figure 3.2a, is predominantly due to extra energy dissipation arising from non-spherical nature of particles.⁵³ Simha's equation, which captures the effect of particle shape on intrinsic viscosity, combined with the experimental value of intrinsic viscosity reveals an axial ratio of the ellipsoid (aspect ratio) of ~25 nm.^{54,55}

The interaction between dilute CNC's and PVA-SbQ was further studied using scattering experiments and visual representative images. The hydrodynamic size and zeta

potential of the initial dispersion of 0.1 wt.% CNC increased from ~ 91 nm and -42.8 mV respectively to ~ 349 nm and 22.2 mV upon addition of $100 \mu\text{M}$ aqueous solutions containing PVA-SbQ. The increase in hydrodynamic size and a positive zeta potential implies the presence of excess PVA-SbQ forming attractive electrostatics resulting in an aggregated structure, confirmed visually in representative images shown in Figure B.1. The influence of 100 mM NaCl was much milder than $100 \mu\text{M}$ PVA-SbQ, resulting in zeta potential of -17.9 mV indicating much higher stability in NaCl compared to PVA-SbQ as shown in representative images, with NaCl systems showing less aggregation (Note: size measurements could not be calculated due to excess aggregation). The addition of 100 mM NaCl followed by $100 \mu\text{M}$ PVA-SbQ results in unstable dispersions, appearing as dense white opaque dispersion indicative of larger particle size. Similarly, for dispersions containing $0.5 \text{ wt.}\%$ CNC, the initial hydrodynamic size and zeta potential of increased from ~ 70 nm and -53.6 mV to ~ 150 nm and -33.5 mV respectively after addition of $100 \mu\text{M}$ PVA-SbQ as shown in Table 3.1. The addition of 100 mM NaCl resulted in reduced destabilization relative to PVA-SbQ, resulting in zeta potential of -26.7 very similar to observations made for $0.1 \text{ wt.}\%$. These quantitative observations are further verified qualitatively using representing images, which show subsequent destabilization after addition of NaCl followed by PVA-SbQ.

We further proceed to examine the rheological behavior of CNC's as an extension of previous work done by several researchers. Representative images of dispersions of CNC's between $0.1 \text{ wt.}\%$ and $10 \text{ wt.}\%$ are shown in Figure B.2, with dispersions less than $6 \text{ wt.}\%$ showing liquid-like characteristics, and gel-like characteristics at concentrations higher than

6.7 wt.%. Figure 3.2b shows aspects of the concentration effect of CNC's on the shear rheology across five decades of shear rate (10^{-2} - 10^2 s $^{-1}$). The most prominent features for 1-3 wt.% CNC include a small Newtonian plateau for 1 wt.%, which disappears at higher concentrations, steep shear-thinning region at low shear rates, with a short plateau at medium shear rate (~ 1 s $^{-1}$), and further shear-thinning region at higher shear rates, but less steeper, commonly attributed to lyotropic polymer liquid crystals. The appearance of plateau region at medium shear rates, however, becomes less pronounced for 6.7 wt.% and slopes of shear thinning regions at low and high shear rates become similar. This behavior has been the subject of many previous rheological studies and has been attributed to gel formation, which impedes the formation of chiral-nematic ordered phases.^{53,56,57} The precise nature of the plateau region and its dependence on experimental parameters is beyond the scope of this paper. The concentration of CNC's to form PVA-SbQ composites will be limited to less than 3 wt.% where it exhibits solution-like behavior.

With the entanglement concentration of PVA-SbQ established at 4.8 wt.%, and solution-like behavior observed for CNC at less than 3 wt.%, rheological measurements with varying amounts of CNC's less than 3 wt.% were used to study the influence of CNC on the microstructure and later on the photo-crosslinking dynamics of salt-free aqueous solutions of PVA-SbQ (6 wt.%). The effect of CNC's on microstructure can be first understood via simple shear rheology by measuring stresses in response to imposed shear rates. As shown in Figure 3.3, the presence of low concentration CNC in aqueous solution of PVA-SbQ (6 wt.%) shows a Newtonian behavior, with visible deviations arising at concentrations around 1.5 wt.%, showing non-linear behavior. This non-linear behavior is fitted using Herschel-

Bulkley model containing three adjustable parameters including yield stress (τ_0), the consistency index parameter (K), and flow behavior index (n). The fitting results, tabulated in Table 3.2, reveal an absence of apparent yield stress for concentrations below 1.5 wt.%, with yield stresses varying between 0.01 Pa to 0.06 Pa. Similarly, across the CNC concentration range below 1.5 wt.%, the consistency index varies between 0.04 – 0.36 Pa-sⁿ, and flow behavior index varies between 0.998 to 0.771 suggestive of initial Newtonian behavior followed by shear thinning behavior in the presence of CNC's. Above 1.5 wt.% CNC, however, a measurable increase in yield stress of 1.14 Pa for 1.8 wt.% CNC is observed, which further increases to 8.61 Pa for systems containing 2.1 wt.% CNC. Therefore, at a threshold concentration of 1.5 wt.%, the system showed high shear thinning behavior (n = 0.572 and 0.455) with measurable yield stresses. Furthermore, shear stress measurements as a function of concentration also reveal the presence of transition concentration (~1.5 wt.%), at which the initial lack of dependence of shear stress on concentration changes drastically, as shear stresses in the material rise exponentially.

The storage modulus (G') and loss modulus (G''), as well as complex viscosity, as functions of frequency for neat PVA-SbQ and PVA-SbQ containing varying amounts of CNC's, are shown in Figure 3.4. The viscoelastic behavior of salt-free aqueous solutions of 6 wt.% PVA-SbQ shown in Figure 3.4a reveals a response typical of polymers in the terminal regime with $G' \sim \omega^2$ and $G'' \sim \omega$. Liquid-like behavior is observed at low frequencies as G'' is greater than G' , with the transition from liquid-like to solid-like occurring at ~1.5 rad/s corresponding to a relaxation time of ~0.7 seconds, followed by solid-like behavior at higher frequencies as G' is greater than G'' . The addition of 1 wt.% CNC changes the slope of G' in

the terminal regime from 2 to 1.43, suggesting a much smaller frequency dependence due to the formation of solid microstructure that imparts resistance to deformation at low frequencies. The slope shows remarkable decrease to 0.50 for systems containing 1.5 wt.% CNC, and a further increase in CNC's causes progressive decrease in slopes, eventually scaling with $G' \sim \omega^{0.21}$ for maximum CNC loading of 3 wt.%. The addition of CNC's results in favorable polymer-CNC interactions forming gel-like interconnected structures, and absence of G' and G'' crossover indicative of structures with infinite relaxation times. In addition, the complex viscosity plots shown in Figure 3.4b reveals a long plateau at low frequencies for neat PVA-SbQ with minor shear thinning occurring at higher frequencies. Addition of 1 wt.% CNC results in an order of magnitude increase in complex viscosity from $\sim 10^{-1}$ Pa-s to ~ 1 Pa-s, while still showing a zero shear plateau at lower frequencies and minor shear thinning at higher frequencies.

The complex viscosity of CNC incorporated systems also corroborate the frequency sweep results - a relatively flat Newtonian behavior exhibited by PVA-SbQ shows dramatic shear-thinning behavior after addition of CNC's at and above 1.5 wt.% as the viscosity is no longer dominated by the host polymer alone, but by the presence of attractive polymer-CNC and CNC-CNC interactions. At low shear rates, viscosity increases across 2 decades, relative to neat systems, to ~ 20 Pa-s after incorporation of 1.5 wt.% CNC, which further increases to greater than ~ 1000 Pa-s at 0.1 rad/s for maximum loading of 3 wt.% CNC. The shear thinning behavior in the presence of CNC's, which is attributed to the alignment of CNC's at higher frequencies, becomes more pronounced as evident from the increase in the slope of shear-thinning region from -0.14 for neat PVA-SbQ up to -0.79 for CNC-loaded PVA-SbQ.

As $\eta^* \sim \omega^{n-1}$, the relaxation exponent extracted from the slope is consistent with values obtained from frequency sweeps near the gel point as shown in Table 3.3. The combined results suggest a transformation in the liquid-like structure of PVA-SbQ to interconnected networks, often seen in filled polymer nanocomposites containing carbon nanotubes,⁵⁸⁻⁶¹ further explaining the presence of a yield stress observed under steady-shear experiments.

While the presence of yield stress during liquid-solid transition points to the existence of interconnected structures, further analysis is necessary to confirm the precise nature of microstructure. The effect of nanofillers such as CNC's on the polymer dynamics and the extent of network formation can be studied by probing changes in rheological parameters such as G' , G'' and phase angles (δ) at low frequencies or frequency equivalent parameter such as complex modulus (G^*). Two important plots, very sensitive to the formation of interconnected structures in systems containing nanofillers in both polymeric solutions and melts and obtained using dynamic viscoelastic measurements, are often used as signatures for identification of a rheological percolation threshold, namely, van Gurp-Palmen plot and Cole-Cole. The van Gurp-Palmen plot shows the dependence of phase angle on complex modulus ($|G^*|$), with a decrease in phase angle below 45° used as the criteria for percolation, which is the threshold filler concentration at which transition from liquid-like to solid-like microstructure takes place. The Cole-Cole plot shows the dependence of storage modulus (G') on loss modulus (G''), with deviations from the original slope of systems without nanofillers representative of formation of interconnected networks. This technique has been used in prior literature, most notably in polymer melts systems of PLA/CNC,^{62,63} HDPE/Octamethyl-POSS,⁶⁴ and carbon nanotube-based composites.⁶⁵ Using these plots

together, rheological percolation threshold of CNC's, i.e. critical concentration that results in a percolated network, can be estimated. Figure 5a shows van-Gurp Palmen plots for the systems with varying amounts of CNC. It is clear that for aqueous PVA-SbQ without and with 1 wt.% CNC's, the phase angle starts out at $\sim 90^\circ$ indicating the dominance of viscous behavior at low frequencies and approaches $\sim 60^\circ$ at high frequencies, much higher than 45° , which is the threshold phase angle for percolation, suggesting lack of percolated network. The high phase angles demonstrate a liquid-like structure, which corroborates previous observations made through frequency sweep data. However, upon addition of 1.5 wt.% CNC, a clear difference in microstructure relative to neat polymer is noted due to a drastic reduction in phase angle, which stays below 45° and shows a steep decline from 40° to 35° , with decreasing complex moduli from 35 Pa to 10 Pa before rising again up to 40° below 6 Pa, indicating that CNC particles are percolated in aqueous PVA-SbQ solutions with a threshold value between 1 and 1.5 wt.%. The presence of yield stress of 1.14 Pa observed for 1.8 wt.% CNC loading discussed earlier could be attributed to the resulting percolated network. This percolation range, however, is higher than those reported in previous literature for CNC-based systems, suggesting some aggregation. The percolation concentration of 0.88 wt.% was reported for systems containing microcrystalline cellulose with aspect ratio of 10-15 mixed in polyurethane.⁶⁶ Similarly, percolation was observed at 0.68 wt.% for CNC with aspect ratio of 6 ± 2 nm, and at 3 wt.% for spray freeze-dried CNC's with aspect ratio of 11 ± 5 nm for PLA-CNC based composites.^{62,63}

The percolation threshold range was further verified using Cole-Cole plot which plots G' as a function of G'' . In the case of a homogenous polymer system, the logarithmic plot of

G' vs. G'' at low frequencies should yield a slope of 2, since at low frequencies $G' \sim \omega^2$ and $G'' \sim \omega$ and ratio of the exponents at low frequencies equals 2. The extent of deviation from the standard slope, with decrease in slopes representative of heterogeneity in the system, often used as a measure of network formation. Figure 5b shows Cole-Cole plot for various concentrations of CNC's added to neat PVA-SbQ. For neat PVA-SbQ, the plot yields a slope of 2, and G' is lower than G'' at low frequencies in agreement with viscoelastic behavior of polymer solutions. The addition of 1 wt.% CNC shifts the curve toward higher G'' indicating the dominance of viscous behavior, but G' is significantly lower than G'' , consistent with frequency sweep and van Gurp-Palmen plots. However, at loadings of 1.5 wt.% CNC and higher, G' is higher than G'' which is accompanied by changes in the slopes, pointing to the existence of a percolated network. The slope (which corresponds to the ratio of G' and G'') decreases to 1.3 for 1.5 wt.% CNC, and to 1.04 for loadings of 2 wt.%. Further additions of CNC's result in higher slopes corresponding to 1.24 and 1.23 for 2.5 wt.% and 3 wt.% CNC respectively, still large deviations from aqueous polymer behavior. This behavior is further corroborated using Cole-Cole plot of imaginary viscosity (η'') versus real viscosity (η'), which should reveal a smooth, semi-circular shape for homogeneous systems, with any upward inflections indicating immiscibility or yield behavior.^{64,65} As shown in Figure B.3 (inset), neat PVA-SbQ and PVA-SbQ with 1 wt.% CNC shows an arc typical for homogeneous systems. However, further increases to 1.5 wt.% and higher show an upward inflection suggesting yield behavior possibly due to a percolated structure. In addition, the critical concentration of gelation can be further calculated using Winter-Chambon's criterion, which states that $\tan(\delta)$ as a function of gelation parameters such as time, temperature and

concentration are frequency independent at the gel point.^{21,22,67,68} Accordingly, the critical gelation concentration close to 1.5 wt.% was determined based on the frequency independence of $\tan \delta$ at the gel point as shown in Figure B.4.

After formation of percolated network using CNC's above a threshold concentration, PVA-SbQ was crosslinked using UV light of fixed intensity at 10 mW/cm^2 as shown in Figure 3.6. The crosslinking kinetics of PVA-SbQ in the presence of CNC's was studied using small amplitude dynamic oscillatory experiment. Initially, stress sweep was used to determine the linear viscoelastic region, and material responses to small stress (1 Pa) were measured in this regime. The variations in the microstructure of neat polymer after UV exposure at different times were first studied using frequency sweeps using stress (1 Pa) in the LVE to preserve the microstructure. Figure 3.7a shows the elastic (G') and viscous moduli (G'') as a function of frequency for two different exposure times. Prior to UV exposure, frequency sweep of neat PVA-SbQ reveals a response typical to polymers in the terminal regime with both storage and loss moduli showing frequency dependence as $G' \sim \omega^{2.08}$ and $G'' \sim \omega^{1.03}$, and G'' much higher than G' at low frequencies indicating solution-like characteristics. After 900 s of UV exposure, elastic and viscous moduli scaled as $G' \sim \omega^{1.26}$ and $G'' \sim \omega^{0.9}$, showing a much smaller dependence on frequency and reduced relaxation time from ~ 0.5 s before UV-exposure to ~ 0.1 s. However, G' is still lower than G'' suggesting solution-like characteristics, but the initial slope of G' relative to G'' of 1.99 decreases to 1.42 after 900 s, suggesting incipient structure formation (Figure 3.7b). Since elastic and viscous moduli exhibit different power-law behavior with respect to frequency, the microstructure formed after 900 s is well below the critical instant of gelation, referred to as the gel point.

When the sample was exposed to UV for 3600 s, however, frequency sweep reveals a response typical to a material past its gel point – the transition from a viscous liquid to a system containing gel resulting due to clusters which connect into sample-spanning network. While frequency sweeps reveal the presence of highly-crosslinked gel-like microstructure after 3600 s, they are inadequate to determine the critical instant of gelation, which occurs between 900 s and 3600 s. In addition, the strength of the network after 60 minutes of UV exposure as indicated by G' which exceeds 10^3 Pa. As shown in Figure 3.7b', the increment across three decades of moduli is due to the crosslinking reaction between the hydrophobes in PVA-SbQ, which forms a gel after 3600 s of UV exposure. In addition, with the increasing exposure time, the initial Newtonian behavior with viscosity ~ 0.04 Pa-s increases by an order of magnitude to ~ 0.4 Pa-s after 900 s, and eventually exceeds 10^4 Pa-s at low frequencies after 3600 s exposure. At low frequencies, the gel also shows a shear thinning behavior with a slope of -0.99 which corresponds to relaxation exponent (n) ~ 0.01 , which is consistent with the slope of 0.006 from frequency sweeps at 3600 s. The precise mechanism of crosslinking has been the subject of numerous prior studies.

Alternatively, the kinetics of the sol-gel transition as well as the time at which the crossover takes place can be studied by following elastic and viscous moduli as a function of UV exposure time at a constant frequency. Figure 3.8a shows the time evolution of G' and G'' at a frequency of 10 rad/s for PVA-SbQ systems containing CNC's up to 2.1 wt.% exposed to UV for 3600 s. For neat PVA-SbQ, the liquid-like behavior dominates the initial microstructure as G'' is higher than G' at the onset of UV exposure. During UV exposure, both moduli start to increase, with G' increasing at a faster rate relative to G'' , eventually

crossing over at around $\sim 909 \pm 84$ s, beyond which G' is higher than G'' for ~ 2000 seconds. Similar trends are visible at the onset of UV exposure for systems containing CNC's less than 1.5 wt.% (raw data not shown) with no significant changes in the crossover time as shown in Figure 3.8b. In fact, the crossover times between 1200 s to 1400 s for CNC's below 1.5 wt.% was higher than that relative to neat PVA-SbQ.

The addition of 1.8 wt.% CNC shows similar trends, with G'' higher than G' initially, eventually crossing over before G' builds up and exceeds G'' ; however, the crossover time is significantly reduced (~ 151 s at 1.8 wt.% relative to neat ~ 900 s for PVA-SbQ). Finally, the addition of 2.1 wt.% results in G' much higher than G'' and lack of a cross-over. While the crossover G' and G'' does not reveal the gel point, the effects of CNC's on the microstructure is evident. As the system is exposed to continuous UV past the gel point, the microstructure starts to build up with G' several orders of magnitude higher than G'' . The presence of yield stress, as well as percolation mechanism, after addition of CNC's implies a potential effect on the final mechanical strength of composites relative to PVA-SbQ. As shown in Figure 3.9, the elastic moduli after UV exposure for 3600 s are fairly independent of CNC concentration below 1.5 wt.%, fluctuating between 3500 Pa to 4500 Pa with no visible trends. However, a sharp increase in moduli is observed at CNC concentration higher than 1.5 wt.%. The moduli increases to ~ 6389 Pa for systems containing 1.8 wt.% CNC, followed by subsequent increases to ~ 7181 Pa and 8607 Pa for loadings of 2.1 wt.% and 2.5 wt.% CNC respectively. At maximum loading, the increase corresponds to approximately 131% suggesting the reinforcing effect of CNC's.

The sharp transition occurs when finite CNC's transitions to a new state, driven by

particle-particle interactions upon increasing volume fraction of these rod-like particles, resulting in a new state where the clusters span the entire network. The growing interconnected network adds to the elasticity and ability to transmit stresses across the system, showing up as a sharp increase in shear modulus. The microstructure formed, therefore, resembles a percolated network that forms at a critical concentration, which can be calculated by fitting the experimental data for storage modulus of CNC-filled PVA-SbQ after UV exposure using a percolation model shown in Equation (1), where, m is the mass of cellulose nanocrystals, m_c is the percolation mass fraction and β is an exponent at percolation.^{66, 69,70}

$$G' \propto (m - m_c)^\beta \quad (1)$$

As shown in Figure 3.9a inset, critical percolation concentration occurs at 1.41 wt.% very similar to the threshold for systems without UV. Finally, the presence of dense crosslinked network via percolation and photo-crosslinking was verified using frequency sweeps shown in Figure 3.9b. For neat as well as filled systems, G' and G'' show frequency independence, suggesting that the final microstructure is a fully crosslinked gel.

3.5 Conclusions

Weak mechanical performance associated with photocrosslinkable polymer necessitates strategies to reinforce their mechanical properties. In this work, we report a simple technique using cellulose nanocrystals (CNC's) that induce favorable electrostatic interactions to modulate crosslinking kinetics as well as to enhance mechanical performance of aqueous photoactive polyvinyl alcohol derivative, poly (vinyl alcohol), N-methyl-4 (4'-formylstyryl) pyridinium methosulfate acetal (PVA-SbQ). Steady-shear rheological

measurements of PVA-SbQ shows characteristics similar to neutral polymers and entanglement at ~4.8 wt.%. Low concentration CNC rheology, combined with Simha's equation for non-spherical particles, reveals aspect ratio of ~27. The presence of low concentration CNC in aqueous solutions of PVA-SbQ (6 wt.%) shows Newtonian behavior, with visible deviations arising at concentrations around 1.5 wt.%, showing non-linear behavior with yield stresses. This was attributed to the percolation network formed by CNC's, confirmed using van Gorp-Palmen and Cole-Cole plots often used as signatures for identification of a rheological percolation threshold. Finally, PVA-SbQ photo crosslinked using UV exposure at 10 mW/cm^2 for 3600 s in the presence of CNC's reveal shifts in G' and G'' crossover as well as final elastic modulus (G'), which shows a sharp increase at 1.4 wt.% estimated as the rheological percolation concentration. The final increase in moduli using 2.5 wt.% CNC was approximately 131% confirming the reinforcing effect of CNC's.

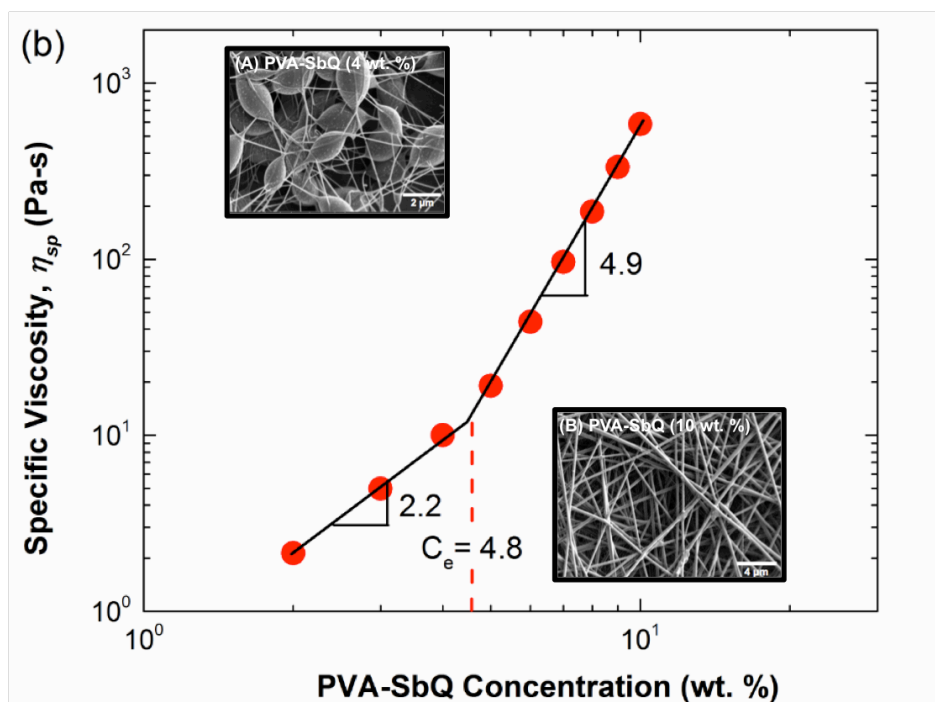
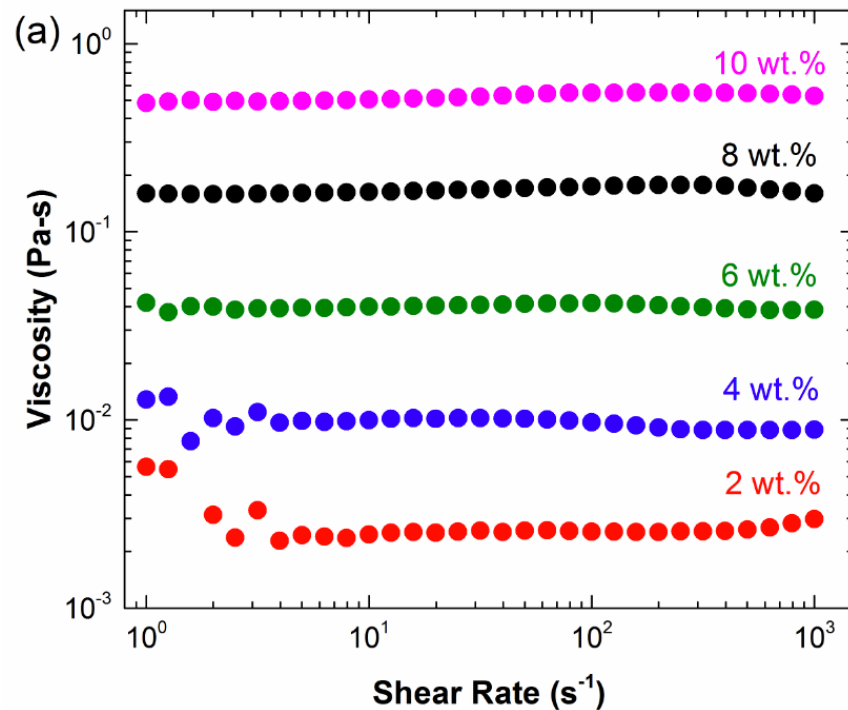


Figure 3.1 (a) Steady shear viscosity of neat PVA-SbQ at different concentrations, and (b) specific viscosity of PVA-SbQ at different concentrations used to estimate entanglement concentration.

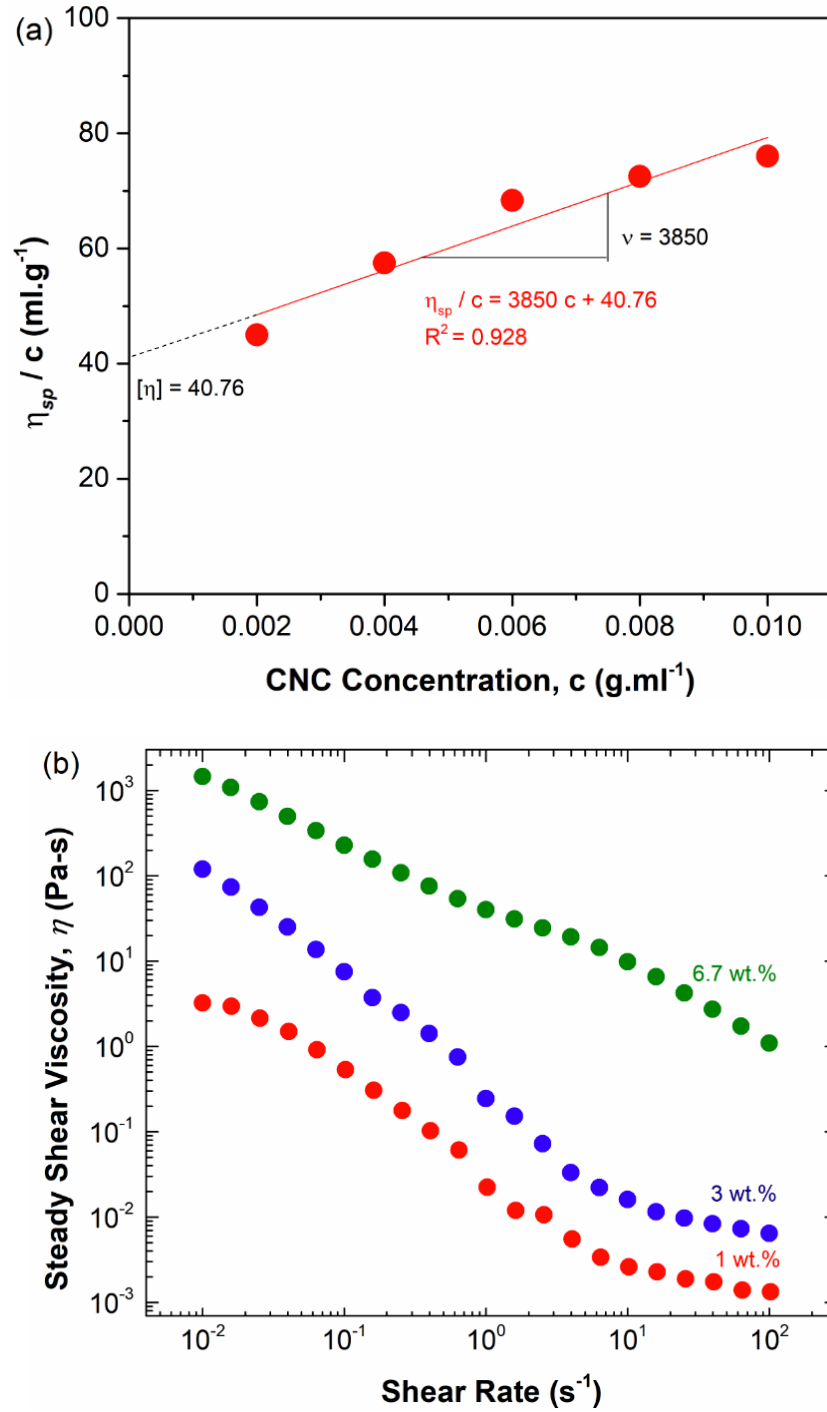


Figure 3.2 (a) Huggins plot showing specific viscosity vs. CNC concentration to determine aspect ratio of cellulose nanocrystals (using this method the aspect ratio of CNC is ~24), and (b) steady shear viscosity of cellulose nanocrystals at different concentrations

Table 3-1 Hydrodynamic size, zeta potential and conductivity of 0.1 wt.% and 0.5 wt. % CNC suspension in water and 100 μm PVA-SbQ Solution. Dispersions were prepared using bath sonication for 1 hour.

		CNC (0.1 wt. %)		CNC (0.5 wt. %)	
		Dispersed In		Dispersed In	
		DI Water	PVA-SbQ	DI Water	PVA-SbQ
Size	(nm)	90.7 \pm 0.4	348.7 \pm 6.2	69.8 \pm 0.7	149.7 \pm 1.7
	PDI	0.27 \pm 0.01	0.49 \pm 0.02	0.54 \pm 0.01	0.4 \pm 0.01
Zeta Potential	(mV)	-42.8 \pm 2.2	22.2 \pm 1.6	-53.6 \pm 4.9	-33.5 \pm 0.3
Mobility	(V)	-3.4 \pm 0.2	-1.7 \pm 0.1	4.2 \pm 0.4	2.6 \pm 0.03
Conductivity	mS /cm	0.04 \pm 0.002	0.08 \pm 0.002	0.08 \pm 0.002	0.13 \pm 0.005

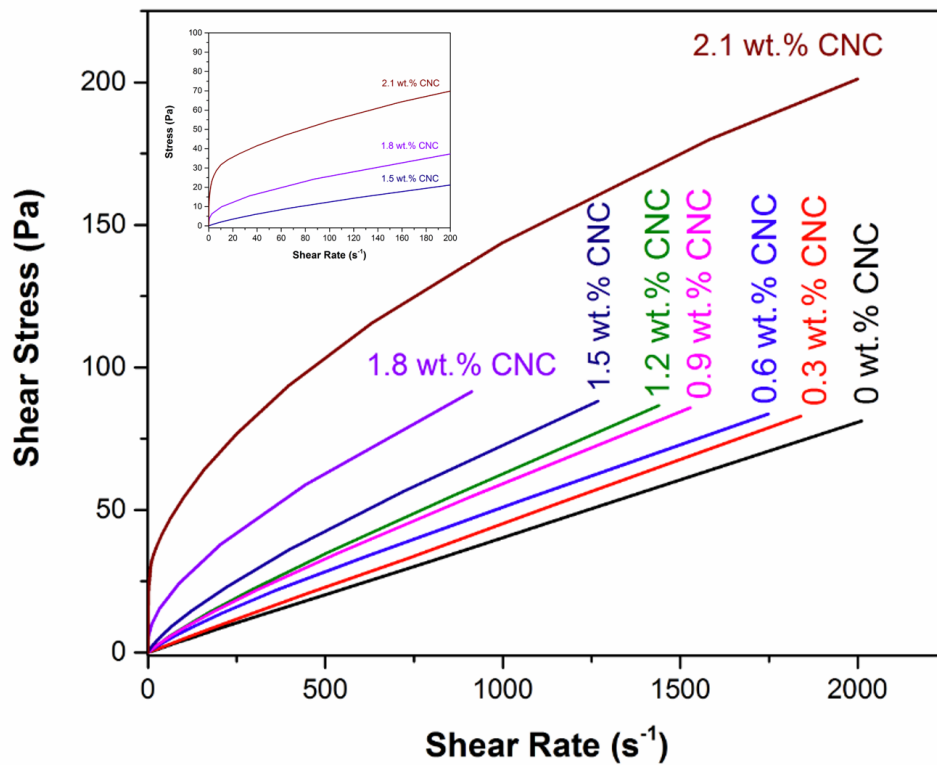


Figure 3.3 Shear stress as a function of shear rate for PVA-SbQ (6 wt. %) with different CNC concentration between 0 wt. % and 2.1 wt. % (for 0.3 wt. % increments).

Table 3-2 Herschel-Bulkley parameters (yield stress, consistency index and flow-behavior index) of PVA-SbQ (6 wt. %) containing different amounts of CNC.

CNC (wt. %)	τ_0 (Pa)	K (Pa.sⁿ)	n	R²
0	0.06	0.04	0.998	0.999
0.3	0.06	0.05	0.987	0.999
0.6	0.01	0.14	0.859	0.999
0.9	0.02	0.16	0.862	0.999
1.2	0.02	0.17	0.852	0.999
1.5	0.05	0.36	0.771	0.999
1.8	1.14	1.81	0.572	0.997
2.1	8.61	5.88	0.455	0.992

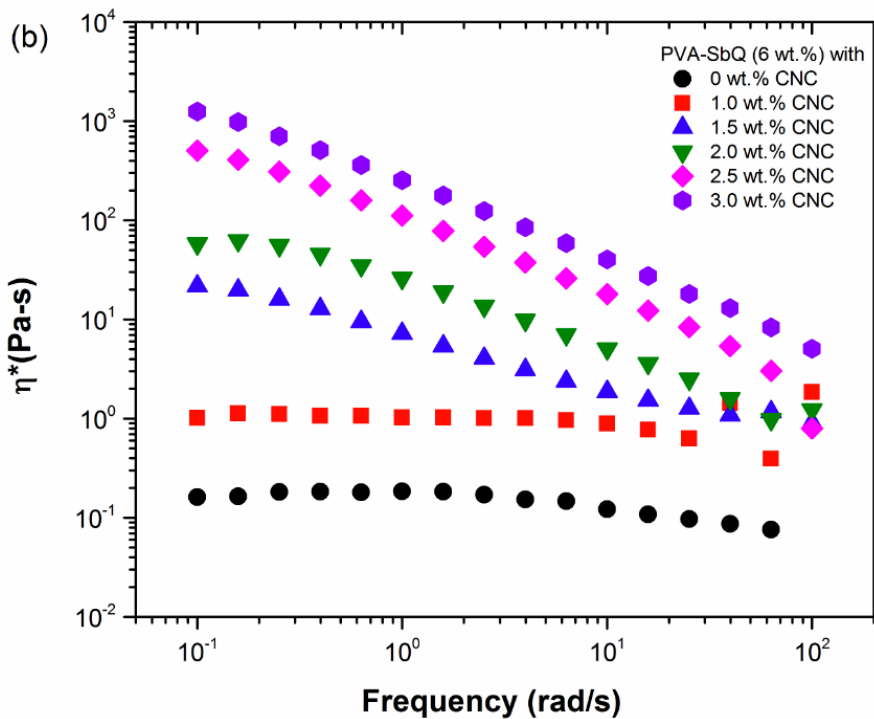
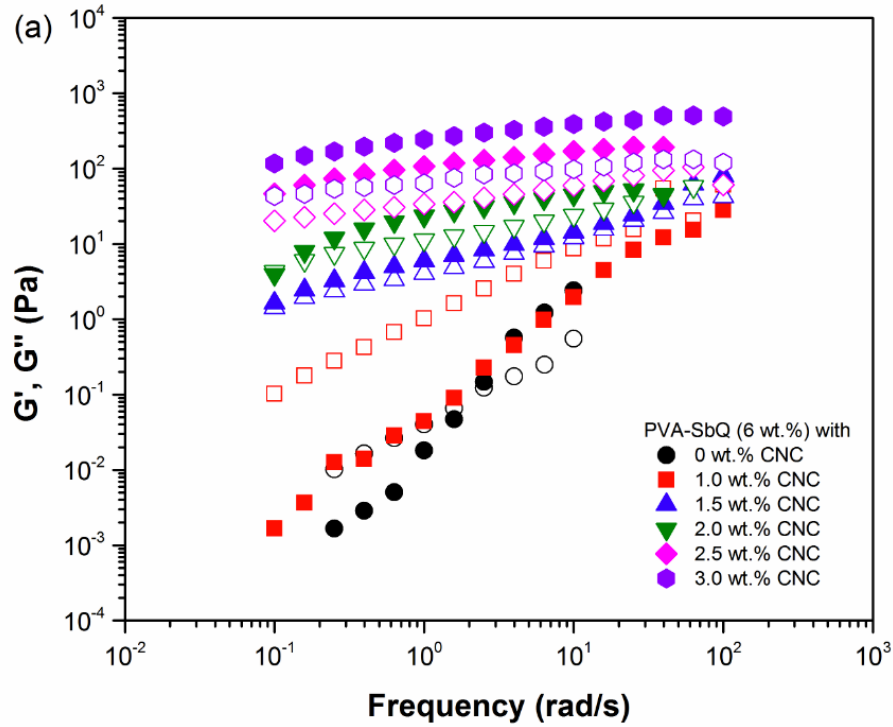


Figure 3.4 (a) Storage and loss modulus (G' and G'') and (b) complex viscosity vs. frequency, for neat PVA-SbQ and PVA-SbQ containing CNC's up to 3 wt.% using stress of 1 Pa.

Table 3-3 Slopes of G' and complex viscosity and relaxation exponent for neat PVA-SbQ and PVA-SbQ with CNC's at different concentrations.

CNC (wt. %)	Slope of G'	Slope of η^*	n	R^2
0	2.02	-0.14	-	0.999
1.0	1.43	-0.03	-	0.999
1.5	0.50	-0.50	0.49	0.999
2.0	0.37	-0.65	0.35	0.999
2.5	0.23	-0.85	0.15	0.995
3.0	0.21	-0.79	0.21	0.992

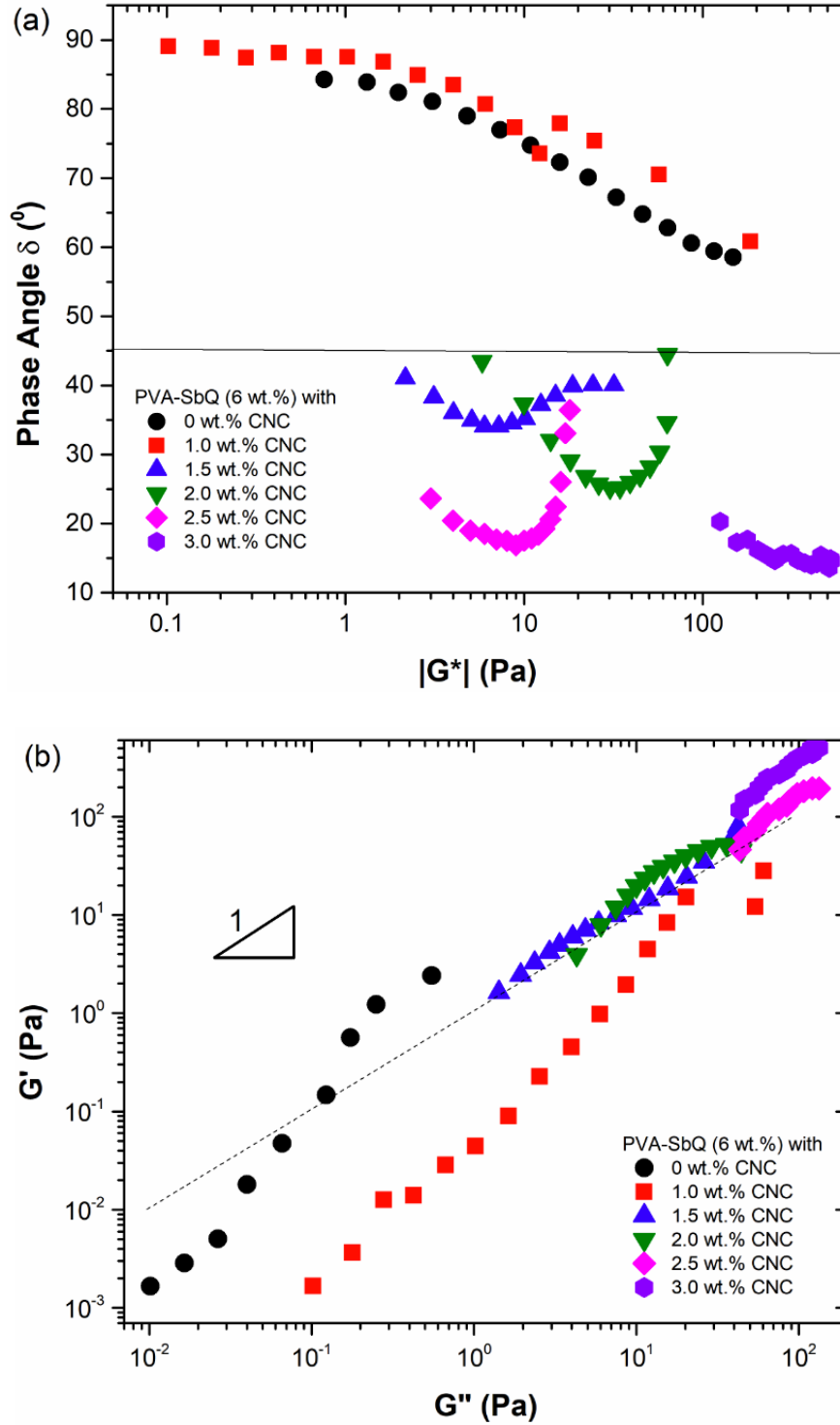


Figure 3.5 (a) van Gurp-Palmen plot (δ vs. $|G^*|$), and (b) Cole-Cole plot (G' vs. G'') for aqueous PVA-SbQ with varying CNC's used to observe percolation behavior.

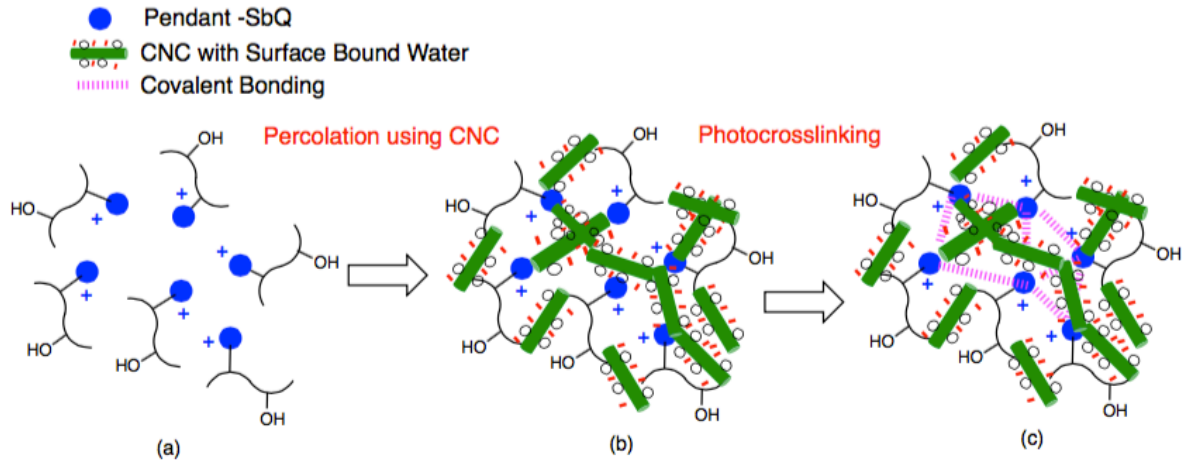


Figure 3.6 The design principle used to modulate mechanical strength via network formation using cellulose nanocrystals. Percolated network was first achieved by adding negatively charged CNC and further crosslinked using UV exposure to obtain densely interconnected structure.

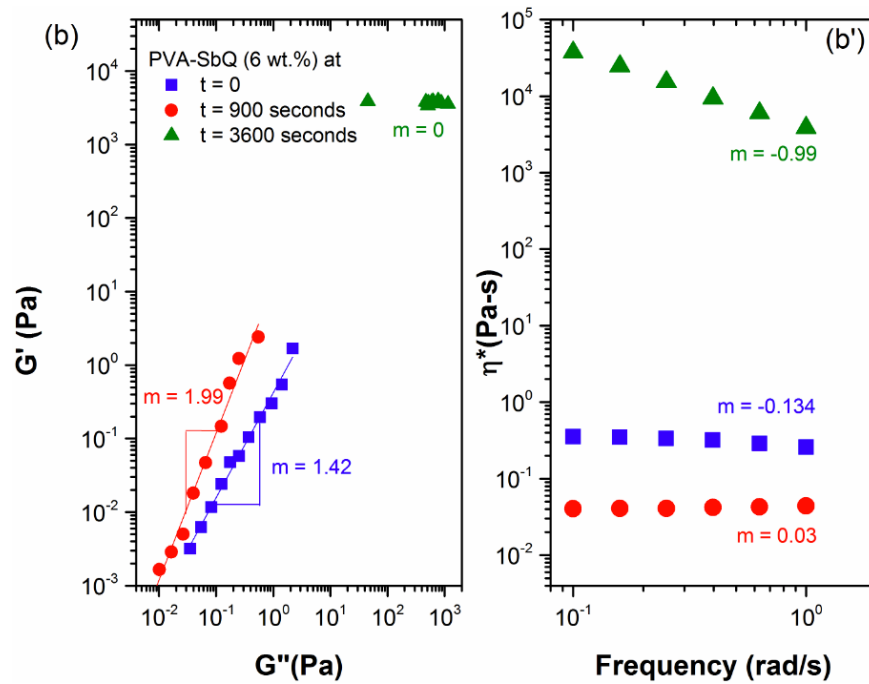
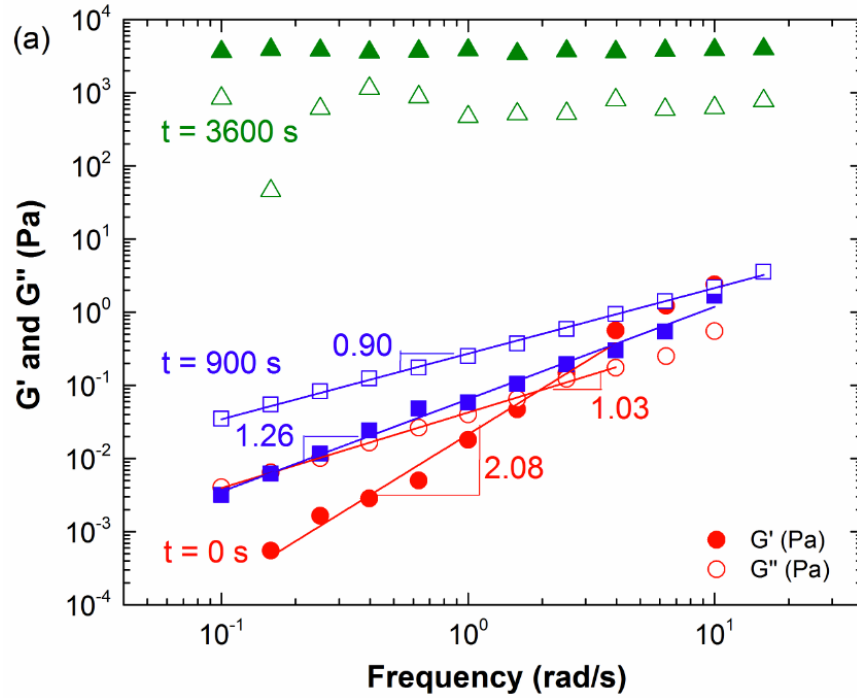


Figure 3.7 (a) Frequency sweep for PVA-SbQ (6 wt. %) using UV intensity of 10 W/cm², and (b) changes in slope (G' vs. G'') and complex viscosity as a function of frequency after different exposure times ($t = 0$ seconds, $t = 900$ seconds and $t = 3600$ seconds).

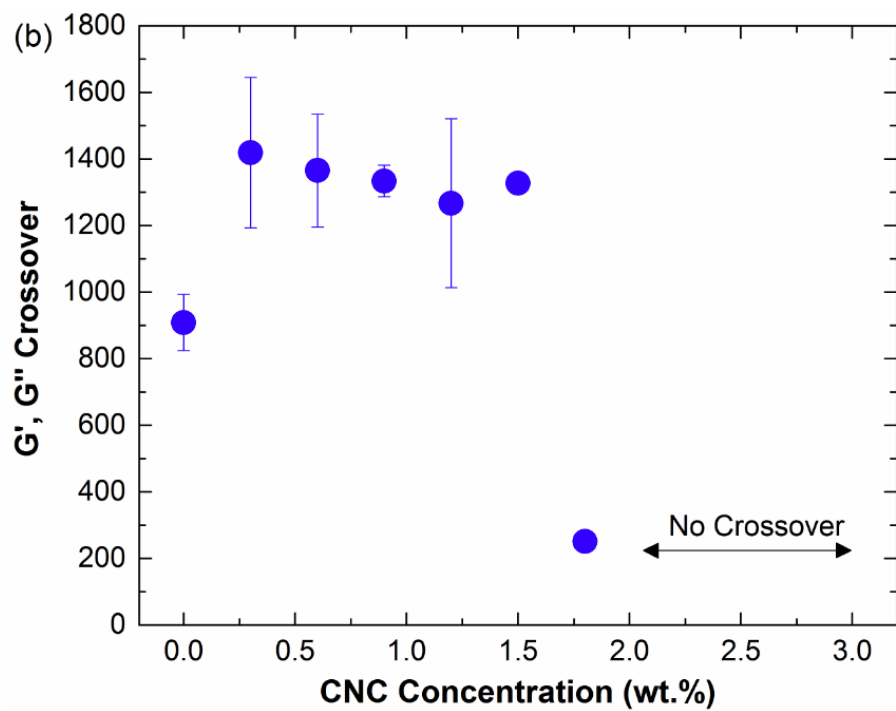
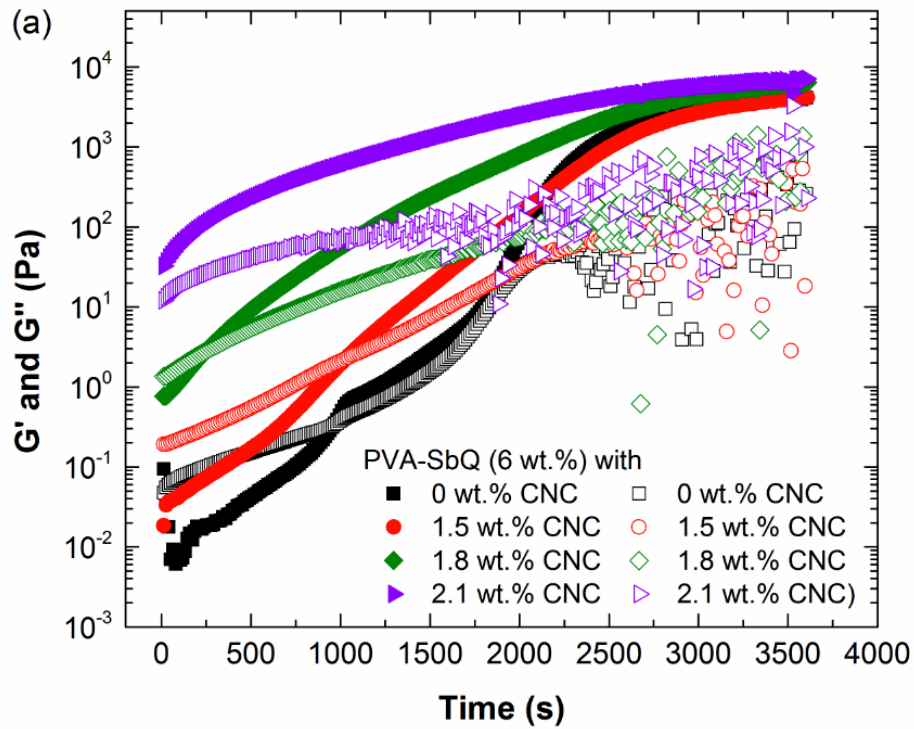


Figure 3.8 (a) Time sweeps for PVA-SbQ (6 wt. %) using UV intensity of 10 W/cm^2 , and (b) G' , G'' crossover for different CNC concentrations.

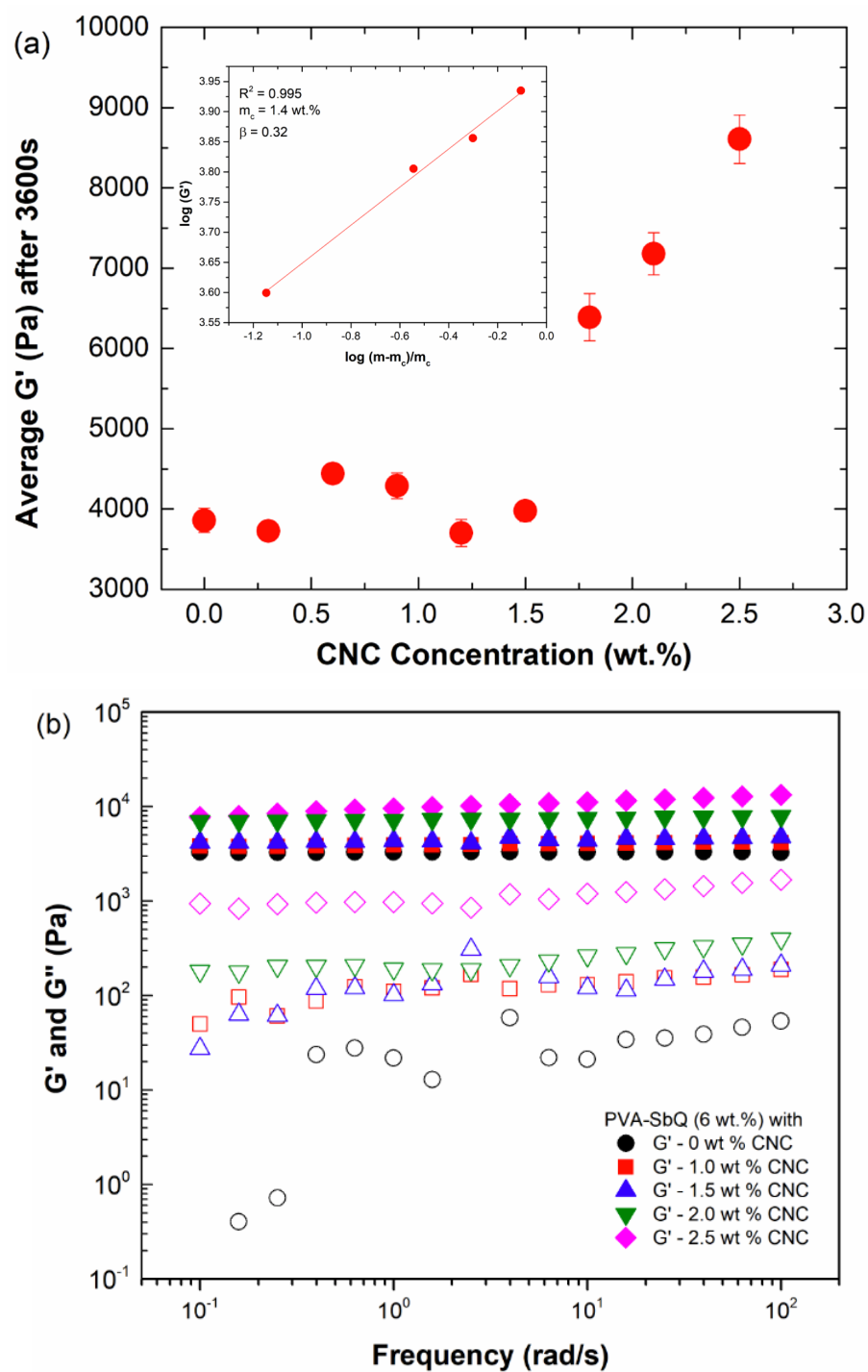


Figure 3.9 (a) Average storage modulus of PVA-SbQ (6 wt. %) for different CNC concentrations (wt. %), and (b) frequency sweep of PVA-SbQ (6 wt. %) with different CNC contents after UV exposure for 1 h at 10 mW/cm².

3.6 References

- (1) Kim, C. L.; Kim, D. E. Durability and Self-Healing Effects of Hydrogel Coatings with Respect to Contact Condition. *Sci. Rep.* **2017**, *7* (1), 1–11.
- (2) Somani, K. P.; Kansara, S. S.; Patel, N. K.; Rakshit, A. K. Castor Oil Based Polyurethane Adhesives for Wood-to-Wood Bonding. *Int. J. Adhes. Adhes.* **2003**, *23* (4), 269–275.
- (3) Valmikinathan, C. M.; Mukhatyar, V. J.; Jain, A.; Karumbaiah, L.; Dasari, M.; Bellamkonda, R. V. Photocrosslinkable Chitosan Based Hydrogels for Neural Tissue Engineering. *Soft Matter* **2012**, *8* (6), 1964–1976.
- (4) Saraiva, S. M.; Miguel, S. P.; Ribeiro, M. P.; Coutinho, P.; Correia, I. J. Synthesis and Characterization of a Photocrosslinkable Chitosan–gelatin Hydrogel Aimed for Tissue Regeneration. *RSC Adv.* **2015**, *5* (78), 63478–63488.
- (5) Kumar, S.; Hofmann, M.; Steinmann, B.; Foster, E. J.; Weder, C. Reinforcement of Stereolithographic Resins for Rapid Prototyping with Cellulose Nanocrystals. *ACS Appl. Mater. Interfaces* **2012**, *4* (10), 5399–5407.
- (6) Ouyang, L.; Highley, C. B.; Rodell, C. B.; Sun, W.; Burdick, J. A. 3D Printing of Shear-Thinning Hyaluronic Acid Hydrogels with Secondary Cross-Linking. *ACS Biomater. Sci. Eng.* **2016**, *2* (10), 1743–1751.
- (7) Markstedt, K.; Escalante, A.; Toriz, G.; Gatenholm, P. Biomimetic Inks Based on Cellulose Nanofibrils and Cross-Linkable Xylans for 3D Printing. *ACS Appl. Mater. Interfaces* **2017**, *9* (46), 40878–40886.
- (8) Piras, C. C.; Fernández-Prieto, S.; De Borggraeve, W. M. Nanocellulosic Materials as Bioinks for 3D Bioprinting. *Biomater. Sci.* **2017**, *5* (10), 1988–1992.
- (9) Valentin, T. M.; Leggett, S. E.; Chen, P.-Y.; Sodhi, J. K.; Stephens, L. H.; McClintock, H. D.; Sim, J. Y.; Wong, I. Y. Stereolithographic Printing of Ionically-Crosslinked Alginate Hydrogels for Degradable Biomaterials and Microfluidics. *Lab*

Chip **2017**, *17*, 3474–3488.

- (10) Jiang, S.; Liu, S.; Feng, W. PVA Hydrogel Properties for Biomedical Application. *J. Mech. Behav. Biomed. Mater.* **2011**, *4* (7), 1228–1233.
- (11) Kamoun, E. A.; Chen, X.; Mohy Eldin, M. S.; Kenawy, E. R. S. Crosslinked Poly(vinyl Alcohol) Hydrogels for Wound Dressing Applications: A Review of Remarkably Blended Polymers. *Arab. J. Chem.* **2015**, *8* (1), 1–14.
- (12) Park, J. H.; Bae, Y. H. Hydrogels Based on Poly (Ethylene Oxide) and Poly (Tetramethylene Oxide) or Poly (Dimethyl Siloxane). II . Physical Properties and Bacterial Adhesion. **2002**.
- (13) Yang, J.; Shi, F. K.; Gong, C.; Xie, X. M. Dual Cross-Linked Networks Hydrogels with Unique Swelling Behavior and High Mechanical Strength: Based on Silica Nanoparticle and Hydrophobic Association. *J. Colloid Interface Sci.* **2012**, *381* (1), 107–115.
- (14) Zhong, M.; Liu, Y.-T.; Liu, X.-Y.; Shi, F.-K.; Zhang, L.-Q.; Zhu, M.-F.; Xie, X.-M. Dually Cross-Linked Single Network Poly(acrylic Acid) Hydrogels with Superior Mechanical Properties and Water Absorbency. *Soft Matter* **2016**, *12* (24), 5420–5428.
- (15) Zhong, M.; Shi, F. K.; Liu, Y. T.; Liu, X. Y.; Xie, X. M. Tough Superabsorbent Poly(acrylic Acid) Nanocomposite Physical Hydrogels Fabricated by a Dually Cross-Linked Single Network Strategy. *Chinese Chem. Lett.* **2016**, *27* (3), 312–316.
- (16) Sannino, A.; Demitri, C.; Madaghiele, M. Biodegradable Cellulose-Based Hydrogels: Design and Applications. *Materials (Basel)*. **2009**, *2* (2), 353–373.
- (17) Chang, C.; Zhang, L. Cellulose-Based Hydrogels: Present Status and Application Prospects. *Carbohydr. Polym.* **2011**, *84* (1), 40–53.
- (18) Bhattarai, N.; Gunn, J.; Zhang, M. Chitosan-Based Hydrogels for Controlled, Localized Drug Delivery. *Adv. Drug Deliv. Rev.* **2010**, *62* (1), 83–99.
- (19) Augst, A. D.; Kong, H. J.; Mooney, D. J. Alginate Hydrogels as Biomaterials.

Macromol. Biosci. **2006**, *6* (8), 623–633.

- (20) Ahmed, E. M. Hydrogel: Preparation, Characterization, and Applications: A Review. *J. Adv. Res.* **2015**, *6* (2), 105–121.
- (21) Higham, A. K.; Bonino, C. A.; Raghavan, S. R.; Khan, S. A. Photo-Activated Ionic Gelation of Alginate Hydrogel: Real-Time Rheological Monitoring of the Two-Step Crosslinking Mechanism. *Soft Matter* **2014**, *10* (27), 4990–5002.
- (22) Bonino, C. A.; Samorezov, J. E.; Jeon, O.; Alsberg, E.; Khan, S. A. Real-Time in Situ Rheology of Alginate Hydrogel Photocrosslinking. *Soft Matter* **2011**, *7* (24), 11510.
- (23) Ichimura, K.; Watanabe, S. Preparation and Characteristics of Photocrosslinkable Poly(vinyl Alcohol). *J. Polym. Sci. Polym. Chem. Ed.* **1982**, *20* (6), 1419–1432.
- (24) Ichimura, K. Photocrosslinking Behavior of Poly (Vinyl Alcohol)s with Pendent Styrylpyridinium or Styrylquinolinium Groups. *Makromol. Chem.* **1987**, *188*, 2973–2982.
- (25) Azide, N. W. H. Photopolymer Side Groups Consisting and Sensitizer of PVA. **1995**, *8* (1), 29–36.
- (26) Hasegawa, M.; Kawanobe, J. Water Resistance of Photosensitive Poly (Vinyl Alcohol) Films. **2001**, *14*, 293–294.
- (27) Ichimura, K.; Iwata, S.; Mochizuki, S.; Ohmi, M.; Adachi, D. Revisit to the Photocrosslinking Behavior of PVA-SbQ as a Water-Soluble Photopolymer with Anomalously Low Contents of Quaterized Stilbazol Side Chains. *J. Polym. Sci. Part A Polym. Chem.* **2012**, *50* (19), 4094–4102.
- (28) Ichimura, K. The Reproducibility and Reliability of UV–vis Higher-Order Derivative Spectroscopy for Quantitative Analysis of Spectral Changes. *Bull. Chem. Soc. Jpn.* **2017**, *90* (4), 411–418.
- (29) Bai, H.; Xu, J.; Zhang, Y.; Liu, X.; Rojas, O. J. Dynamics of Cyclodimerization and Viscoelasticity of Photo-Crosslinkable PVA. *J. Polym. Sci. Part B Polym. Phys.* **2015**,

53 (5), 345–355.

- (30) Ichimura, K.; Watanabe, S. Immobilization of Enzymes With Use of Photosensitive Polymers Bearing Stilbazolium Groups. *Chem. Lett.* **1978**, *18* (11), 1289–1292.
- (31) Ichimura, K. A Convenient Photochemical Method to Immobilize Enzymes. *J. Polym. Sci. Polym. Chem. Ed.* **1984**, *22* (11), 2817–2828.
- (32) Hertzberg, S.; Moen, E.; Vogelsang, C.; Østgaard, K. Mixed Photo-Cross-Linked Polyvinyl Alcohol and Calcium-Alginate Gels for Cell Entrapment. *Appl. Microbiol. Biotechnol.* **1995**, *43* (1), 10–17.
- (33) Bai, H.; Sun, Y.; Xu, J.; Dong, W.; Liu, X. Rheological and Structural Characterization of HA/PVA-SbQ Composites Film-Forming Solutions and Resulting Films as Affected by UV Irradiation Time. *Carbohydr. Polym.* **2015**, *115*, 422–431.
- (34) Yang, J.; Han, C. R.; Zhang, X. M.; Xu, F.; Sun, R. C. Cellulose Nanocrystals Mechanical Reinforcement in Composite Hydrogels with Multiple Cross-Links: Correlations between Dissipation Properties and Deformation Mechanisms. *Macromolecules* **2014**, *47* (12), 4077–4086.
- (35) Yang, J.; Han, C.; Xu, F.; Sun, R. Simple Approach to Reinforce Hydrogels with Cellulose Nanocrystals. *Nanoscale* **2014**, *6* (11), 5934.
- (36) Yang, D.; Peng, X.; Zhong, L.; Cao, X.; Chen, W.; Wang, S.; Liu, C.; Sun, R. Fabrication of a Highly Elastic Nanocomposite Hydrogel by Surface Modification of Cellulose Nanocrystals. *RSC Adv.* **2015**, *5* (18), 13878–13885.
- (37) Yang, J.; Han, C. Mechanically Viscoelastic Properties of Cellulose Nanocrystals Skeleton Reinforced Hierarchical Composite Hydrogels. *ACS Appl. Mater. Interfaces* **2016**, *8* (38), 25621–25630.
- (38) Zhang, T.; Zuo, T.; Hu, D.; Chang, C. Dual Physically Cross-Linked Nanocomposite Hydrogels Reinforced by Tunicate Cellulose Nanocrystals with High Toughness and Good Self-Recoverability. *ACS Appl. Mater. Interfaces* **2017**, *9* (28), 24230–24237.

- (39) Dragan, E. S. Design and Applications of Interpenetrating Polymer Network Hydrogels. A Review. *Chem. Eng. J.* **2014**, *243*, 572–590.
- (40) Matricardi, P.; Di Meo, C.; Coviello, T.; Hennink, W. E.; Alhaique, F. Interpenetrating Polymer Networks Polysaccharide Hydrogels for Drug Delivery and Tissue Engineering. *Adv. Drug Deliv. Rev.* **2013**, *65* (9), 1172–1187.
- (41) Boluk, Y.; Zhao, L.; Incani, V. Dispersions of Nanocrystalline Cellulose in Aqueous Polymer Solutions: Structure Formation of Colloidal Rods. *Langmuir* **2012**, *28* (14), 6114–6123.
- (42) Hu, Z.; Cranston, E. D.; Ng, R.; Pelton, R. Tuning Cellulose Nanocrystal Gelation with Polysaccharides and Surfactants. *Langmuir* **2014**, *30* (10), 2684–2692.
- (43) Bardet, R.; Belgacem, N.; Bras, J. Flexibility and Color Monitoring of Cellulose Nanocrystal Iridescent Solid Films Using Anionic or Neutral Polymers. *ACS Appl. Mater. Interfaces* **2015**, *7* (7), 4010–4018.
- (44) Reid, M. S.; Villalobos, M.; Cranston, E. D. The Role of Hydrogen Bonding in Non-Ionic Polymer Adsorption to Cellulose Nanocrystals and Silica Colloids. *Curr. Opin. Colloid Interface Sci.* **2017**, *29*, 76–82.
- (45) Oguzlu, H.; Boluk, Y. Interactions between Cellulose Nanocrystals and Anionic and Neutral Polymers in Aqueous Solutions. *Cellulose* **2017**, *24* (1), 131–146.
- (46) Guo, C.; Zhou, L.; Lv, J. Effects of Expandable Graphite and Modified Ammonium Polyphosphate on the Flame-Retardant and Mechanical Properties of Wood Flour-Polypropylene Composites. *Polym. Polym. Compos.* **2013**, *21* (7), 449–456.
- (47) Ghimici, L.; Bercea, M.; Dragan, E. S. Rheological Behavior of Some Cationic Polyelectrolytes. *J. Macromol. Sci. Part B* **2009**, *48* (5), 1011–1024.
- (48) McKee, M. G.; Hunley, M. T.; Layman, J. M.; Long, T. E. Solution Rheological Behavior and Electrospinning of Cationic Polyelectrolytes. *Macromolecules* **2006**, *39* (2), 575–583.

- (49) Krause, W. E.; Bellomo, E. G.; Colby, R. H. Rheology of Sodium Hyaluronate under Physiological Conditions. *Biomacromolecules* **2001**, *2* (1), 65–69.
- (50) Borins, C. D.; Colby, H. R. Rheology of Sulfonated Polystyrene Solutions. *Macromolecules* **1998**, *31*, 5746–5755.
- (51) Dobrynin, a V; Colby, R. H.; Rubinstein, M. Scaling Theory of Polyelectrolyte Solutions. *Macromolecules* **1995**, *28* (6), 1859–1871.
- (52) Chang, H.; Luo, J.; Bakhtiary Davijani, A. A.; Chien, A. T.; Wang, P. H.; Liu, H. C.; Kumar, S. Individually Dispersed Wood-Based Cellulose Nanocrystals. *ACS Appl. Mater. Interfaces* **2016**, *8* (9), 5768–5771.
- (53) Li, M.-C.; Wu, Q.; Song, K.; Lee, S.; Qing, Y.; Wu, Y. Cellulose Nanoparticles: Structure–Morphology–Rheology Relationships. *ACS Sustain. Chem. Eng.* **2015**, *3* (5), 821–832.
- (54) Genovese, D. B. Shear Rheology of Hard-Sphere, Dispersed, and Aggregated Suspensions, and Filler-Matrix Composites. *Adv. Colloid Interface Sci.* **2012**, *171–172*, 1–16.
- (55) Wierenga, A. M.; Philipse, A. P. Low-Shear Viscosity of Isotropic Dispersions of (Brownian) Rods and Fibres; a Review of Theory and Experiments. *Colloids Surfaces A Physicochem. Eng. Asp.* **1998**, *137* (1–3), 355–372.
- (56) Ureña-Benavides, E. E.; Ao, G.; Davis, V. A.; Kitchens, C. L. Rheology and Phase Behavior of Lyotropic Cellulose Nanocrystal Suspensions. *Macromolecules* **2011**, *44* (22), 8990–8998.
- (57) Shafiei-Sabet, S.; Hamad, W. Y.; Hatzikiriakos, S. G. Rheology of Nanocrystalline Cellulose Aqueous Suspensions. *Langmuir* **2012**, *28* (49), 17124–17133.
- (58) Zhang, Q.; Fang, F.; Zhao, X.; Li, Y.; Zhu, M.; Chen, D. Use of Dynamic Rheological Behavior to Estimate the Dispersion of Carbon Nanotubes in Carbon Nanotube/Polymer Composites. *J. Phys. Chem. B* **2008**, *112* (40), 12606–12611.

- (59) Valentino, O.; Sarno, M.; Rainone, N. G.; Nobile, M. R.; Ciambelli, P.; Neitzert, H. C.; Simon, G. P. Influence of the Polymer Structure and Nanotube Concentration on the Conductivity and Rheological Properties of polyethylene/CNT Composites. *Phys. E Low-Dimensional Syst. Nanostructures* **2008**, *40* (7), 2440–2445.
- (60) Pötschke, P.; Abdel-Goad, M.; Alig, I.; Dudkin, S.; Lellinger, D. Rheological and Dielectrical Characterization of Melt Mixed Polycarbonate-Multiwalled Carbon Nanotube Composites. *Polymer (Guildf)*. **2004**, *45* (26), 8863–8870.
- (61) Pötschke, P.; Fornes, T. D.; Paul, D. R. Rheological Behavior of Multiwalled Carbon Nanotube / Polycarbonate Composites. *Polymer (Guildf)*. **2002**, *43*, 3247–3255.
- (62) Bagheriasl, D.; Carreau, P. J.; Riedl, B.; Dubois, C.; Hamad, W. Y. Shear Rheology of Polylactide (PLA)–cellulose Nanocrystal (CNC) Nanocomposites. *Cellulose* **2016**, *23* (3), 1885–1897.
- (63) Kamal, M. R.; Khoshkava, V. Effect of Cellulose Nanocrystals (CNC) on Rheological and Mechanical Properties and Crystallization Behavior of PLA/CNC Nanocomposites. *Carbohydr. Polym.* **2015**, *123*, 105–114.
- (64) Joshi, M.; Butola, B. S.; Simon, G.; Kukaleva, N. Rheological and Viscoelastic Behavior of HDPE/Octamethyl-POSS Nanocomposites. *Macromolecules* **2006**, *39* (5), 1839–1849.
- (65) Wu, D.; Wu, L.; Sun, Y.; Zhang, M. Rheological Properties and Crystallization Behavior of Multi-Walled Carbon Nanotube/ Poly(e-Caprolactone) Composites. *J. Polym. Sci. Part B Polym. Phys.* **2007**, *45*, 3137–3147.
- (66) Marcovich, N. E.; Auad, M. L.; Bellesi, N. E.; Nutt, S. R.; Aranguren, M. I. Cellulose Micro/nanocrystals Reinforced Polyurethane. *J. Mater. Res.* **2006**, *21* (4), 870–881.
- (67) Chambon, F.; Winter, H. H. Linear Viscoelasticity at the Gel Point of a Crosslinking PDMS with Imbalanced Stoichiometry. *Soc. Rheol.* **1987**, *31* (8), 683–697.
- (68) Winter, H. H.; Chambon, F. Analysis of Linear Viscoelasticity of a Crosslinking

Polymer at the Gel Point. *Journal of Rheology*. 1986, pp 367–382.

- (69) Chin, S. J.; Vempati, S.; Dawson, P.; Knite, M.; Linarts, A.; Ozols, K.; McNally, T. Electrical Conduction and Rheological Behaviour of Composites of Poly(ϵ -Caprolactone) and MWCNTs. *Polym. (United Kingdom)* **2015**, *58*, 209–221.
- (70) Hassanabadi, H. M.; Wilhelm, M.; Rodrigue, D. A Rheological Criterion to Determine the Percolation Threshold in Polymer Nano-Composites. *Rheol. Acta* **2014**, *53* (10–11), 869–882.

Chapter 4 Nanodiamond-Reinforced Electrospun Fibers: Understanding the Role of Interfacial Interactions on Mechanical Properties

4.1 Abstract

Macroscopic property reinforcements using nanodiamonds (ND's) in polymer-nanodiamond composites (PNC) have been extensively studied. However, not much is known about the relationship between polymer-ND interfacial energy parameters, polymer-ND interactions and final mechanical properties in ND-reinforced electrospun fibers. In this work, surface-energy dependent parameters such as wettability, work of spreading, and work of dispersion-aggregation transition of ND's were used to derive a criterion for dispersion (D_c) as a hypothesized predictor of polymer-ND interactions and final tensile strength in electrospun poly (vinyl) alcohol (PVA), polyacrylonitrile (PAN), and polystyrene (PS). We found that shifts in glass transition temperature (ΔT_g), used as a measure of polymer-ND interactions, showed a direct correlation with D_c in the order of PVA > PS > PAN regardless of amorphous or semi-crystalline nature of the polymer. However, the final tensile strength showed a direct correlation with D_c and ΔT_g for semi-crystalline polymers only, with amorphous polystyrene showing maximum reinforcement contrary to predictions made by ΔT_g , suggesting the additional role of polymer morphology to final tensile strength. The findings of this study could offer additional insight into the design of interfaces for polymer-ND fiber composites.

4.2 Introduction

Since their discovery by the Soviet Union in 1960's, and renewed interest in early 2000's,¹ nanodiamonds (ND's) have emerged as a new type of carbon-based nanomaterial with potential for wide-ranging applications in bioimaging,²⁻⁷ chromatography,⁸⁻¹⁰ coatings and composites,¹¹ drug delivery,¹²⁻¹⁶ electrochemistry,¹⁷⁻²¹ and tribology.²²⁻²⁵ Detonation synthesis using an explosive mixture of trinitrotoluene (TNT) and hexogen (RDX) in a negative oxygen condition is used in the large-scale and low-cost production of commercial ND's.²⁶ The resulting product of a detonation event is a diamond core containing graphitic carbon and soot that require further purification. Acid-based oxidizing systems and air-based oxidizing treatments oxidize non-diamond or graphitic carbon, resulting in ultrafine particles with a diamond core containing carbon-oxygen functionality in its outer periphery.²⁷⁻³¹ This method of detonation synthesis produces ND's with particle size of roughly 4-10 nm with narrow size distribution, spherical surface morphology, and strong agglomeration potential, in sharp contrast to methods employing high-pressure and high-temperature which yields ND's less than 100 nm with broad size distribution, faceted morphology and low agglomeration potential.^{32,33}

After decades of work dedicated toward synthesis, purification, and isolation of ND's, researchers have implemented them in numerous applications. Several emerging studies pointing toward low cytotoxicity of ND's, in addition to their properties such as small particle size and dispersibility in water, have spurred their use as drug delivery vehicles, presenting itself as a viable alternative to other carbon-based materials with known toxicity.³⁴ Simple and cheap ways to produce continuously and homogeneously fluorescent ND's,

combined with the stability of N-V defect on ND surface, has opened new avenues for ND's as biomarkers for use in biomedicine, replacing traditional markers beset with problems of photoblinking and photobleaching.²⁻⁷ ND's have also been used as anti-friction agents or lubricant additives and has shown to impart resistance to wear and tear of sliding surfaces.²³⁻²⁵ In addition, the exceptional diamond-like hardness, combined with its small particle size, has instigated research in ND-based polymer fibers and coatings.¹¹

Despite these useful properties, however, ND's are composed of core aggregates consisting of bridging interparticle bonds that are very difficult to disintegrate. For applications requiring well-controlled single digit particle size such as in the fabrication of composites using ND's as reinforcing agents, such aggregates pose significant difficulties during processing. Realizing the need to find ways to overcome this problem, researchers have reported different strategies to disintegrate these tight cores using heat treatment and oxidizing the confined graphitic layers,^{35,36} ultrasound and high-pressure pulse,³⁷ bead-assisted milling techniques using ceramic, zirconia or silica-based beads as milling agents.^{32,33,38-40} Most recently, particle size reduction without contamination using salt-assisted ultrasonic deaggregation was reported, opening up opportunities for applications that require small particle size such as in the fabrication of polymer-ND based composites.⁴¹ Several implementations of ND-based composites processed in various polymers such as poly (vinyl) alcohol (PVA),⁴²⁻⁴⁴ poly (methyl) methacrylate (PMMA),^{45,46} poly (L-lactic) acid (PLLA),⁴⁷⁻⁴⁹ polyacrylonitrile (PAN),⁵⁰ and polyethylene (PE)^{51,52} using solution casting, in-situ polymerization, melt compounding, compression molding, and

electrospinning have reported remarkable increase in properties such as elastic modulus, tensile strength, elongation at break, toughness, hardness and glass transition temperature.

Despite a large number of studies on ND-based composites successfully showing its reinforcing potential, correlation of bulk mechanical properties such as tensile strength to interfacial energy between polymer and ND, however, is non-existent. Central to the need for understanding the interfacial energetics of ND-based composites is the unknown effect of variations in the source of ND's subjected to various purification steps, resulting in subtle variations in particle size and functionality, which manifests into different extents of reinforcing even within the same polymer matrix under identical processing conditions. Realizing that fundamental understanding of interfacial energy parameters of commercial ND's can aid in the development of a standardized method, allowing successful engineering of ND-based composites, we present an approach that relies on using surface energy of polymer and ND to understand the role of interfacial energy parameters on polymer-ND interactions, measured using shifts in glass transition temperature (T_g) and the final tensile properties. Using different semi- crystalline and amorphous host polymers with varying polarities – polyvinyl alcohol (PVA), polyacrylonitrile (PAN) and polystyrene (PS) - we examine the role of wettability, work of spreading and work associated with the aggregation-dispersion transition on polymer-ND interactions and tensile strength of electrospun polymer-ND composite fibers. Fundamental understanding of interfacial energy parameters could provide a critical path forward in the design of successful strategies to create ND-based composites with reinforced properties.

4.3 Materials and Methods

4.3.1 Materials

Poly (vinyl alcohol) (PVA) under trade name of MW 10-98 (molecular weight ~61kDa, 98% hydrolyzed, Sigma Aldrich), polyacrylonitrile (PAN) (molecular weight ~150,000 g/mol, Scientific Polymer Products, NY) and polystyrene (PS) (typical M_w 230,000 and M_n 140,000, Sigma Aldrich) was used as received. Detonation nanodiamond (DND) functionalized with carboxylic acid groups (0.6 wt. % ash content, zeta potential -45 mV) with high colloidal stability in water was purchased from Adamas Nanotechnologies Brilliant Diamond Solutions (Raleigh, NC, USA) and used without further purification. Dimethylsulfoxide (anhydrous, >99%, Sigma Aldrich), dimethylformamide (anhydrous, 99.8%, Sigma Aldrich), dimethylacetamide (anhydrous, 99.8%, Sigma Aldrich), acetonitrile (anhydrous, 99.8%, Sigma Aldrich), acrylonitrile (> 99% contains 35-45 ppm monomethyl ether hydroquinone as inhibitor), acetone (AR, >99.5%, Sigma Aldrich), methanol (anhydrous, 99.8%, Sigma Aldrich), ethanol (99.8%, Sigma Aldrich), chloroform (anhydrous, >99%, Sigma Aldrich), methylene chloride (for high resolution gas chromatography, Fisher Scientific), 1-methyl-2-pyrrolidinone (99% ACS Reagent, Sigma Aldrich), tetrahydrofuran (minimum 99%, Sigma Aldrich), toluene, hexane (for HPLC >95%, Sigma Aldrich), cyclohexane (anhydrous, 99.5%, Sigma Aldrich), ethyl acetate (Certified ACS, Fisher Scientific), acetic anhydride (99% ACS,), sodium hydroxide (NaOH, 1.0 M, Fluka) (and sodium chloride (NaCl) (99+% A.C.S Reagent, Sigma Aldrich) were purchased and used as received.

4.3.2 Nanodiamond Dispersion and Ultrasonic Deaggregation

Carboxylated nanodiamond (c-ND) dispersions (1 wt.%) in different solvents were prepared using sonication for 1 hour using an ultrasonic bath (Fisher Scientific, 2.8 L). c-ND used for nanocomposite fabrication was obtained using salt-assisted ultrasonic deaggregation (SAUD) technique following procedures reported by Turcheniuk *et al.* with minor modifications.⁴¹ Briefly, c-ND (0.25 g) was added to sodium chloride (10 g) followed by deionized water (5 ml) in a scintillation vial. The contents were subjected to ultrasonication under ice-bath to prevent water evaporation using Branson S-450 digital sonifier (power 400W, amplitude 30% and duty cycle 50%) using 1/8” tapered microtip and flat tip for 100 minutes. Thereafter, the contents were emptied in centrifuge tubes and washed with water (2 x 50 ml) and centrifuged at 4000 rpm for 10 minutes (Centrifuge 5702, Eppendorf). The supernatant was discarded and c-ND particles were re-suspended in water and centrifuged second time at 12000 rpm for 1 hour. The supernatant was discarded and the particles were dried in air for 3 days. Dry de-aggregated c-ND will be referred to as SAUD c-ND for characterization and any reference to c-ND hereon refers to SAUD c-ND.

4.3.3 Electrospinning Polymers with Nanodiamonds

PVA, PAN and PS nanofibers with different c-ND loadings (0.1 wt. %, 0.5 wt. %, 1 wt. % and 2 wt. %) were fabricated using electrospinning setup consisting of a stationary collector. Polymer/c-ND solutions were sonicated for 15 minutes prior to loading in a syringe with a needle attachment (0.3 mm diameter). The syringe was loaded in syringe pump (Model No. 2345) that controlled the flow rate between 0.5-1 ml per hour. A high voltage supply power (Model No. 1721) was used to impart voltage between 15-25 kV at the needle

tip. The fibers were collected in an aluminum foil wrapped on grounded stationary collector plate placed 10-15 cm away from the needle tip. The experiments were carried out at room temperature (20-25°C) and relative humidity between 20-40%. The fibers were collected post spinning and placed in a vacuum oven for 3 hour to remove moisture and then placed in a desiccator with silica gels.

4.3.4 Characterization

Particle size and zeta potential of c-ND and SAUD c-ND were obtained using a zeta potential analyzer (Zeta2000, Malvern Instruments, U.S.A.) equipped with a 4.0 mW He-Ne laser ($\lambda=633$ nm). Dynamic light scattering (DLS) measurements were carried out on dispersions (0.1 wt.% and 1.0 wt.%) loaded onto dip-cell at room temperature. Dispersions of c-ND at 0.1 wt.% and 1.0 wt.% were diluted using 1mM NaCl solution and reported zeta potential was determined from an average of 5 measurements. To determine surface carboxylic group acid content, conductometric titration was performed using procedures employed for TEMPO-oxidized cellulose containing carboxylic acids groups.⁵³ Briefly, c-ND (3 wt. %) was dispersed in 100 ml water and initial pH was recorded. Hydrochloric (0.1 M), sodium chloride (10 mM) was added to protonate c-ND. 0.04 M of NaOH was used and the volume of NaOH and pH were recorded. The amount of carboxylic acid (mmol/g) on the surface was determined using $n = c \times v / m$, where n is number of moles of carboxylic acid groups, c is concentration of NaOH (mol/L), v is volume of NaOH (mL) and m is mass of c-ND (g). FTIR analysis of composition of surface groups on raw ND and c-ND was performed using Thermo Nicolet iN10 infrared microscope. Approximately, 1 mg of nanodiamond was mixed with 300 mg potassium bromide (KBr) to form a pellet. The spectra

were collected using a 2 cm resolution and 64 continuous scans. The surface elemental composition of ND's was analyzed using XPS. Data were obtained on Specs XPS using Mg source with an energy of 1253.6 eV. XPSPeak41 was used to calibrate C1s spectrum to 285.0 eV, determine peak areas and to calculate the elemental composition. The surface energy of c-ND was calculated using Washburn equation using dynamic contact angle analyzer (Cahn, U.S.A). Approximately 1 g of c-ND particles were packed in 4.9 mm glass tubing with a rigid porous base and left overnight to saturate in the vapor of test liquid. Thereafter, wicking experiments were performed using different probe solvents (hexane, diiodomethane, dimethylformamide, ethylene glycol and water). Increase in weight due to rising liquid was followed until a stable weight gain was achieved after ~10-15 minutes. Reported values of surface energies were obtained using an average of five independent measurements. The effect of c-ND loadings on the morphology of polymer fibers was studied using field emission scanning electron microscopy (FEI Verios 460L). Samples were cut from nanofiber mats and fixed on a carbon tape mounted on a stub before applying a gold-palladium (Au-Pd) coating of ~7 nm using a sputter-coating unit. Imaging of coated fibers was done using an accelerating voltage of 5 kV; current between 50 pA to 200 pA and a working distance of 6 mm. Cross-section images were obtained using tilt angles between 20°-30°. Thermal properties of c-ND and polymer fiber c-ND composites were characterized using differential scanning calorimeter (DSC) (Q2000, TA Instruments, USA). A heating rate of 10°C per min was used under nitrogen flow from ~40°C to 300°C. Thermal degradation of fiber composites was investigated using TGA (Q200, Texas Instruments, USA) under helium flow rate of 100 mL/min. Approximately 10 mg of sample was placed in a platinum pan and was heated to

110°C at 20°C/min. After isothermal heating at 110°C for 30 minutes, a scan rate of 5°C/min was used to further heat the sample from 110°C to 900°C. The samples were then cooled back to room temperature. Tensile testing of nanofiber specimens to obtain stress-strain curves were carried out at room temperature on a dynamic mechanical analyzer (RSA-G2, TA Instruments, USA) with extension rates between 0.15 mm/min to 0.30 mm/min depending on the polymer. Thick nanofiber mats cut into rectangular strips 15 mm in length, 5 mm in width, and a similar thickness between 0.60 mm to 0.70 mm were loaded with gauge gap of 5 mm. All reported values are average of at least five measurements.

4.4 Results and Discussion

4.4.1 Dispersion of Nanodiamond in Different Solvents

Carboxylated nanodiamond (c-ND) was dispersed in 18 different solvents with different dispersive, polar and hydrogen-bonding components of Hildebrand solubility parameters - water, dimethylsulfoxide (DMSO), dimethylformamide (DMF), dimethylacetamide (DMAc) acetonitrile, acrylonitrile, acetone, methanol, ethanol, chloroform, dichloromethane (DCM), N-methyl-2-pyrrolidone (NMP), tetrahydrofuran (THF), toluene, hexane, cyclohexane, ethyl acetate and acetic anhydride (see Table C.1 for solvent properties). Figure C.1 shows representative images of dispersions of c-ND in different solvents immediately post sonication, after 1 day and after 10 days. Dispersions after 10 days were labeled as stable such as those in water, DMF, and DMAc; moderately stable such as in acetone, methanol, and ethanol; less stable in acrylonitrile and acetonitrile and unstable in solvents such as THF and hexane based on visual differences in color of the colloidal suspension, with dispersions in water labeled as the most stable. To understand the

dispersion behavior, dispersion maps for different components of solubility parameter was plotted as shown in Figure C.2 (a)-(c). As shown in Figure C.2a, which relates dispersion state to dispersive component and polar component of solvent solubility parameter, c-ND dispersions were unstable until a critical polarity is reached ($\delta_p \sim 7 \text{ MPa}^{1/2}$ for the solvents used in this study), and is independent of the dispersive component of the solubility parameter of the solvents, δ_d , which varies between $14.7 \text{ MPa}^{1/2}$ to $18.4 \text{ MPa}^{1/2}$. This indicates negligible contributions of non-polar nature of solvent to stabilization of c-ND. Despite the polarity, however, c-ND formed unstable dispersions in DMSO. To probe the potential influence of hydrogen bonding component of the solubility parameter of the solvent (δ_h), dispersion state was related to hydrogen bonding component and polar component of solvent solubility parameter in Figure C.2b. As such, hydrogen-bonding parameter had no direct correlation with the dispersion behavior. Previous work on the rheology of ND's in mineral oil further corroborates the influence of polarity in final ND dispersions.⁵⁴ The polarity of a solvent aided in the dissociation of surface carboxylic acid groups into corresponding ions, increasing the conductivity and pH and further electrostatically stabilizing the system. Figure C.2c showed no correlation between hydrogen bonding ability and dispersive nature of the solvent, strongly indicating the influence of solvent polarity in forming stable c-ND dispersions.

4.4.2 Characterization of c-ND (as is) vs. SAUD c-ND

The stability of dispersions of c-ND in water was tested using DLS. The dispersions are opaque and brown, suggesting the presence of particles with sizes capable of scattering light (see Figure C.3). The dispersions were left to settle for 10 days and particle size and

visual appearance were reported. The c-ND particles in the dispersions aggregate over time, with visible particle settling at the bottom of the vial; however, the particle size remains unchanged within the sample suggesting stable dispersion. In contrast to dispersions containing 0.1 wt. % c-ND with particle size ~90 nm, dispersions containing 1 wt. % c-ND showed more visible aggregation and higher particle size ~100 nm. Polymer-ND fiber composites made with ~100 nm c-ND formed visible aggregates at 2 wt.% loading and no reinforcement in mechanical properties, hence smaller particle size was achieved using salt-assisted ultrasonic deaggregation (SAUD) using procedures reported earlier with minor modifications.⁴¹ Briefly, c-ND was mixed with NaCl and water and ultrasonicated using a flat tip and a microtip. The particle size recovered after drying c-ND was considerably lower than c-ND and is referred to as SAUD c-ND. The flat tip sonication resulted in a smaller particle size compared to those achieved with microtip (Figure C.4), which could be attributed to the difference in energy imparted by tips. After recovering SAUD c-ND, surface characterization was performed using FTIR, XPS and conductometric titration to ascertain any changes in surface functionality. FTIR spectrum in Figure 4.1a for c-ND and SAUD c-ND showed no changes, with both c-ND and SAUD c-ND showing a broad peak between 3000 cm^{-1} and 3700 cm^{-1} due to -OH stretching and additional peaks at 1625 cm^{-1} due to -OH bending groups. The peaks at 1730 cm^{-1} were due to the presence of C=O stretching arising due to carboxylic acid groups on the surface. XPS survey scans in Figure 4.1b shows c-ND to be predominantly carbon (86.7%), with some oxygen (13.3%) due to the presence of surface acid groups. After deaggregation, SAUD c-ND had similar atomic content – 84.3 % carbon and 12.9% oxygen. A trace amount of sodium (~1.7%) due to the presence of salt and

nitrogen (~1.2%) was seen. The amount of carboxylic acid present in SAUD c-ND was approximately ~0.05 mmol/g compared to 0.06 mmol/g for c-ND, obtained using conductometric titration data in Figure C.5, suggesting minor changes in surface functionality. Slight reduction in carboxylic acid content could be due to trace sodium ions, which is also reflected in zeta potential of c-ND (-53.3 mV) and SAUD c-ND (-48.8 mV). The difference could be a result of a modest amount of Na⁺ interacting with free carboxylic acid groups. Any reference to c-ND from here on refers to SAUD c-ND.

4.4.3 Nanodiamond Surface Energy

In the determination of surface free energy of a solid (in this case c-ND), the experimental inaccessibility of energetics associated with the solid-vapor interface (γ_{SV}) and solid-liquid interface (γ_{SL}) in Young's equation has spurred development of methods to measure them indirectly. A unifying theory for determination of γ_{SV} and γ_{SL} do not exist; however, pioneering work by Zisman and Fowkes,^{55,56} further extended by Owens-Wendt, and van Oss are well-accepted approaches.^{57,58} Such approaches rely on measurements of contact angle on solid surfaces using solvents with different dispersive and polar surface energies. The two most important but competing theoretical models include theory of surface tension components (STC) pioneered by Fowkes and EOS (equation of state) approach based on macroscopic thermodynamics proposed by Neumann.⁵⁹⁻⁶¹ While both these approaches require measurement of contact angles on solid surfaces, theory of STC relies on resolving γ_{SL} into contributions from dispersive and polar intermolecular forces, making γ_{SL} a function of type and magnitude of intermolecular forces (van der Waal's, hydrogen bonding, electrostatics) operating between interfaces, compared to EQS that eliminates the

components and identifies γ_{SL} as a function of total surface tension of solid and liquid phases, i.e. $\gamma_{SL} = f(\gamma_{SV}, \gamma_{LV})$. This allows a simultaneous solution of Young's equation combined with model equations to determine the two unknowns (γ_{SL}) and (γ_{SV}).⁵⁹ Although Neumann has shown the existence of identical contact angles on the solid surface of liquids with same total liquid surface tension, and independence of magnitude of dispersive components,⁶⁰ Graf *et al.* demonstrated the failure of EOS approach in Langmuir wetting configuration.⁶² The reader is directed to previous work describing limitations of EOS approach.⁶³ Therefore, among all the models present in literature, the Owens-Wendt (modified Fowkes) model, which requires equilibrium contact angle of probe liquids, was considered most appropriate for this work in the determination of surface energy of c-ND's.

The equilibrium contact angle of a probe liquid on a smooth, homogeneous solid c-ND surface is given by Young's equation as follows:

$$\gamma_L \cos\theta + \gamma_{L/ND} = \gamma_{ND} \quad (1)$$

where, γ is the surface energy of the probe liquid (γ_L), c-ND (γ_{ND}), liquid-ND interface ($\gamma_{L/ND}$) and θ is the equilibrium contact angle between the liquid phase and the solid phase (c-ND). Using STC theory, surface energy of liquid and c-ND is resolved into respective polar and dispersive components shown in equations (2) and (3)

$$\gamma_L = \gamma_L^d + \gamma_L^p \quad (2)$$

$$\gamma_{ND} = \gamma_{ND}^d + \gamma_{ND}^p \quad (3)$$

where, γ_L^d is the dispersive component of surface energy and γ_L^p is the polar component of surface energy of the liquid; γ_{ND}^d is the dispersive component of surface energy and γ_{ND}^p is

the polar component of surface energy of ND's. To calculate $\gamma_{L/ND}$, we invoke Dupree equation that results in equation (4), where $W_{L/ND}$ is the work of adhesion between liquid and c-ND.

$$\gamma_{L/ND} = \gamma_L + \gamma_{ND} - W_{L/ND} \quad (4)$$

Substitution of equation (4) in equation (1), combined with Fowkes equation based on the geometric mean allows calculation of work of adhesion between the wetting species and solid surfaces (liquid and c-ND or polymer and c-ND for composites) as shown in equation (5).

$$W_{L/ND} = \gamma_L(1 + \cos\theta) = 2 [\sqrt{\gamma_L^d \gamma_{ND}^d} + \sqrt{\gamma_L^p \gamma_{ND}^p}] \quad (5)$$

This can be further rearranged in the form of equation (6) typical of a straight line, where the square of the slope and intercept gives γ_{ND}^p and γ_{ND}^d respectively. Equation (6) requires wetting angles of probe liquids on the surface of c-ND's.

$$\frac{\gamma_L(1+\cos\theta)}{2\sqrt{\gamma_L^d}} = \sqrt{\gamma_{ND}^p} \left[\frac{\sqrt{\gamma_L^p}}{\sqrt{\gamma_L^d}} \right] + \sqrt{\gamma_{ND}^d} \quad (6)$$

However, accurate determination of surface energies using equilibrium contact angles of liquids on powder and porous materials is challenging. Several authors employed goniometer techniques such as sessile drop, captive bubble, or tilted plate, as well as Wilhelmy plate methods,⁶⁴⁻⁶⁷ on pellets and films to measure surface energies of graphene and cellulose nanocrystals powders. For example, Wang *et al.* and Kozbial *et al.* used graphene films prepared using filtration and chemical vapor deposition (CVD) graphene respectively, and obtained surface energies using Neumann and Fowkes model.^{68,69} Similarly, surface energies of cellulose nanocrystals pellets and spun-coated lignin films

were calculated using Owens-Wendt model.^{70,71} However, they are inaccurate due to surface roughness, inhomogeneity, liquid penetration in pores and swelling effects. Additional techniques such as gel trapping, inverse gas chromatography, and thin-layer wicking technique using Washburn and modified Washburn equation have been used previously for measuring contact angles on sub-micrometer silica particles, cellulose nanofibrils and commercial nanopowders of silica respectively.⁷²⁻⁷⁷ Barber *et al.* measured surface energy of carbon nanotubes by attaching them to atomic force microscopy cantilever and measuring the force between nanotubes and probe liquids.⁷⁸ Among these methods, thin-layer wicking technique based on measuring rates of liquid penetration into porous c-ND's loaded on a thin vertical column, combined with Washburn method in equation (7) was selected to calculate surface energy of ND's.

$$m^2 = \frac{C\rho^2}{\eta} \gamma_L \cos\theta(t) \quad (7)$$

Here, m is the mass of the liquid uptake at time t , C is the capillary factor within the powder packing, ρ is the density of the probe liquid, η is the viscosity of the probe liquid and γ_L is the surface energy of the probe liquid. The geometric factor C is obtained through wicking experiments using low surface energy probe liquid, such as hexane, that completely wets the particles. Mathematically, the wetting of solid particles by low surface energy liquid yields $\cos\theta$ of 1. Similar wicking experiments using three different probe liquids with known polar and dispersive energy – diiodomethane ($\gamma_d = 50.8 \text{ mJ/m}^2$ and $\gamma_p = 0 \text{ mJ/m}^2$), DMF ($\gamma_d = 25.2 \text{ mJ/m}^2$ and $\gamma_p = 11.3 \text{ mJ/m}^2$), and water ($\gamma_d = 21.8 \text{ mJ/m}^2$ and $\gamma_p = 51.0$) – was performed and surface energy components of SAUD c-ND's was determined using Owens-

Wendt plot. The contact angles on c-ND were $77.51^\circ \pm 2.73^\circ$ for water, $62.84 \pm 3.17^\circ$ for DMF and $45.60^\circ \pm 4.34^\circ$ for diiodomethane. c-ND is slightly hydrophilic as suggested by the wetting angle measurements obtained using Washburn method. This observation is in agreement with XPS results showing the presence of surface carboxylic groups resulting in its hydrophilicity. In the Owens-Wendt plot shown in Figure 4.2a, the slope of the line is related to the polar component of the surface energy of c-ND and the intercept is related to the dispersive component of the surface energy. The total surface energy of c-ND was determined to be $36.6 \pm 7.5 \text{ mJ/m}^2$, with a dispersive surface energy of $33.5 \pm 6.9 \text{ mJ/m}^2$ and polar surface energy of $3.1 \pm 2.9 \text{ mJ/m}^2$.

4.4.4 Theoretical Basis

The relatively low polar component compared to the dispersive component surface energy of SAUD c-ND's used in this work will significantly determine the overall performance of composites in terms of wetting of ND's on the polymer, polymer-ND adhesion strength and driving force for re-aggregation. This influence on polymer-ND interaction can be related to shifts in glass transition temperature and final mechanical properties of the resulting electrospun fiber composites. Stockelhuber *et al.* first studied the influence of surface energy of fillers such as carbon blacks, silica, organoclays and carbon nanotubes, and established thermodynamic predictors such as dispersibility, compatibility, and interfacial adhesion energies, as well as driving force for aggregation of filler, with different rubber polymers.⁷⁹ Natarajan *et al.* utilized the preceding work by Stockelhuber *et al.* and proposed a unifying hypothesis relating thermodynamic predictors to shifts in glass transition temperature, a property related to the polymer-filler interface.⁸⁰ We utilize these

concepts based on surface energy to calculate critical parameters important for ND-based composite fabrication. These parameters include polymer- ND compatibility, wettability, spreading coefficient, and work associated with the dispersion-aggregation transition. Combining these parameters together generates a parameter (D_c), which we use as the criterion for dispersion.

4.4.4.1 Compatibility of Nanodiamond with Polymer

The compatibility of ND in a polymer is obtained using the change in free energy of mixing ND's in a polymer, which is the difference between the interfacial energy of polymer-ND interface and the initial surface energy of ND surface as shown in equation (8).

$$\Delta G_{mix} = \gamma_{P/ND} - \gamma_{ND} = -\gamma_P \cos\theta \quad (8)$$

where, γ is the surface energy of the polymer (γ_P), and polymer-ND interface ($\gamma_{P/ND}$) and θ is the equilibrium contact angle between the polymer phase and the c-ND phase. Rearranging and combining with equation (4) and Fowkes model gives equation (9), in which $\Delta G < 0$ implies thermodynamic compatibility of ND with the polymer.

$$\Delta G_{mix} = \gamma_P - W_{P/ND} = \gamma_P - 2 \left[\sqrt{\gamma_P^d \gamma_{ND}^d} + \sqrt{\gamma_P^p \gamma_{ND}^p} \right] \quad (9)$$

where, γ_P^d is the dispersive component of surface energy and γ_P^p is the polar component of surface energy of the polymer and $W_{P/ND}$ is the work of adhesion between polymer and c-ND.

4.4.4.2 Wettability

A critical parameter required for c-ND's to make a good composite is its ability to wet the polymer. Assuming c-ND is the wetting species on the surface of the polymer, and using

combinations of Young and Dupree equations, we get equation (10).

$$\gamma_{ND}(1 + \cos\theta) = 2 \left[\sqrt{\gamma_P^d \gamma_{ND}^d} + \sqrt{\gamma_P^p \gamma_{ND}^p} \right] \quad (10)$$

Re-arranging equation (10) results in equation (11), which shows the effect of polymer-ND interaction (work of adhesion) and ND-ND interaction (work of cohesion) on the wettability of ND on the polymer surface. The ratio of work of adhesion and cohesion is defined as the wettability that determines the extent to which ND's wet the polymer surface.

$$\cos\theta = -1 + 2 \frac{\left[\sqrt{\gamma_P^d \gamma_{ND}^d} + \sqrt{\gamma_P^p \gamma_{ND}^p} \right]}{\left[\sqrt{\gamma_{ND}^d \gamma_{ND}^d} + \sqrt{\gamma_{ND}^p \gamma_{ND}^p} \right]} = -1 + 2 \frac{W_{P/ND}}{W_{ND/ND}} \quad (11)$$

4.4.4.3 Work of Spreading Polymer on Nanodiamonds

The equilibrium wetting of the ND-surface by a polymer is governed by the work of spreading shown in equation (12). If the work of spreading is greater than zero ($W_s > 0$), the polymer droplet wets the ND surface, and when $W_s < 0$, polymer droplets with well-defined contact angle are formed.

$$W_s = W_{P/ND} - W_{PP} \quad (12)$$

Combined with Dupree equation, and Fowkes model we obtain equation (13),

$$W_s = 2 \left[\sqrt{\gamma_P^d \gamma_{ND}^d} + \sqrt{\gamma_P^p \gamma_{ND}^p} \right] - 2 \left[\sqrt{\gamma_P^d \gamma_P^d} + \sqrt{\gamma_P^p \gamma_P^p} \right] \quad (13)$$

4.4.4.4 Work Associated with Dispersion-Aggregation Transition ($\Delta W_{DIS-AGG}$)

To understand how ND aggregation is influenced by the presence of surrounding polymer, we define two distinct states of ND's – well dispersed and aggregated. The

idealized model assumes ND's to be quasi-spherical and each sphere denoting a cluster of smaller particles as well as polymers representing spherical blobs. This allows us to define work associated with the dispersion-aggregation transition ($\Delta W_{DIS-AGG}$) as the difference between work of aggregation (W_{AGG}) and work of dispersion (W_{DIS}). For interaction of two ND units with N surrounding blobs (P), the total work associated with dispersion can be written as Equation 14, where $W_{P/ND}$ denotes work associated with the polymer-ND interaction.

$$W_{DIS} = -2N (W_{P/ND}) \quad (14)$$

Once the system reaches an aggregated state over time with two ND's approaching together, displacing n polymer blobs in the process, the total work associated with aggregation can be written as Equation 15, where W_{PP} denotes work associated with polymer-polymer interaction, and $W_{ND/ND}$ denotes work associated with ND-ND interaction.

$$W_{AGG} = -2 (N - n) W_{P/ND} - n W_{PP} - n W_{ND/ND} \quad (15)$$

Therefore, the work associated with the dispersion-aggregation transition ($\Delta W_{DIS-AGG}$) can be calculated as the difference between equation (15) and equation (14), which yields equation (16) and (17). To calculate $\Delta W_{DIS-AGG}$ associated with the particular polymer, W_{PP} , $W_{P/ND}$ and $W_{ND/ND}$ are first determined using combinations of Young's equation, Dupree equation and surface energy models available in literature discussed earlier.

$$\Delta W_{DIS=AGG} = -2 (N - n) W_{P/ND} - n W_{PP} - n W_{ND/ND} - (-2N W_{P/ND}) \quad (16)$$

$$\Delta W_{DIS=AGG} = n (W_{PP} + W_{ND/ND} - 2 W_{P/ND}) \quad (17)$$

The interfacial energetics associated with the aggregated state (γ_{P-ND}) can be taken as the sum of the energetics of creation of polymer interface (γ_P) and ND interface (γ_{ND})

followed by adhesion of polymer-ND interface ($W_{P/ND}$). Mathematically, this can be captured using the Dupree equation as shown in equation (18). Combining this equation with Young's equation shown in equation 1, results in equations (19) and (20), which is used to calculate work associated with polymer-polymer, polymer-ND and ND-ND interactions.

$$\gamma_{P/ND} = \frac{1}{2}W_{PP} + \frac{1}{2}W_{ND/ND} - W_{P/ND} = \gamma_P + \gamma_{ND} - W_{P/ND} \quad (18)$$

$$\gamma_P \cos\theta + \gamma_{P/ND} = \gamma_{ND} \quad (19)$$

$$W_{P/ND} = \gamma_P(1 + \cos\theta) \quad (20)$$

Equation (20) necessitates equilibrium contact angle of polymer on ND surface. Since direct measurements of contact angle of polymer on the surface of ND is not feasible, we invoked Fowkes model for surface energies, where, γ_P^d is the dispersive component and γ_P^p is the polar component of polymer surface energy, resulting in equation (21).

$$\Delta W_{DIS-AGG} = 2 \left[\sqrt{\gamma_P^d} - \sqrt{\gamma_{ND}^d} \right]^2 + 2 \left[\sqrt{\gamma_P^p} - \sqrt{\gamma_{ND}^p} \right]^2 \quad (21)$$

4.4.4.5 Criterion for Dispersion of Nanodiamonds in Polymers

An important implication of equation (17) is that the work associated with dispersion-aggregation transition has to be minimized ($\Delta W_{DIS-AGG} < 0$) for complete dispersion of ND in the polymer. As such, the following condition has to be satisfied

$$(W_{PP} + W_{ND/ND} - 2W_{P/ND}) < 0$$

We further define a criterion for dispersion (D_c) as shown in equations (22) and (23).

$$D_c = W_{P/ND} - \frac{1}{2}(W_{PP} + W_{ND/ND}) \quad (22)$$

$$D_c = 2 \left[\sqrt{\gamma_P^d \gamma_{ND}^d} + \sqrt{\gamma_P^p \gamma_{ND}^p} \right] - (\gamma_P^d + \gamma_P^p) - (\gamma_{ND}^d + \gamma_{ND}^p) \quad (23)$$

Therefore, a positive D_c implies complete dispersion of ND's in the polymer matrix since polymer-ND interactions overcome combinations of polymer-polymer and ND-ND interaction, and negative D_c implies incomplete dispersion of ND's in the polymer matrix since polymer-polymer and ND-ND interactions overcome the effect of polymer-ND interactions.

We begin by evaluating the compatibility of c-ND with different polymers using change in free energies associated with mixing c-ND into the polymers. Equation (9), combined with the surface energies of polymers available in literature (see Table C.2) and surface energy of c-ND's derived using Owens-Wendt model shown in Figure 4.2a, is used to calculate thermodynamic energy of mixing to compare compatibility of ND's in two semi-crystalline polymers (PVA and PAN) and amorphous PS. It was found that introducing c-ND's into these polymers leads to negative free energies of mixing, the effect being most pronounced for PVA and least for PAN. As shown in Figure 4.2b, thermodynamics favors the formation of c-ND-based polymer composites for PVA, PAN and PS as evident from negative ΔG_{mix} values of -36.2 mJ/m^2 , -32.3 mJ/m^2 and -35.5 mJ/m^2 respectively, making c-ND's compatible with all polymers used in this study.

In addition to compatibility, good dispersion of c-ND within the polymer plays a crucial role in enhancing polymer-ND interactions relative to ND-ND interactions. These interactions between polymer-ND and ND-ND can be quantitatively assessed by work of adhesion between polymer-ND, and work of cohesion between ND-ND. The relative ratio between work of adhesion to work of cohesion referred as the wettability is a quantitative measure of c-ND's preference to wet the polymer surface, assuming ND's is the wetting

species. The work of adhesion for PVA, PAN, and PS corresponds to 80.1 mJ/m², 81.9 mJ/m² and 77.5 mJ/m² respectively as shown in Figure 4.2b. For each of these polymers, the work of adhesion exceeds the work of cohesion between ND's, which is 73.2 mJ/m². This means wettability is greater than 1 for all polymers - 1.09 for PVA, 1.12 for PAN and 1.06 for PS. Note that wettability greater than 1 implies values for $\cos\theta$ greater than 1, which is not physically realizable, but nonetheless, implies a fully wetted surface and θ of 0°. This implies that c-ND's prefer to wet the surface of all polymers.

Once c-ND's wet the polymer surface, polymers ideally have to spread across the c-ND surface if polymer-ND interactions dominate. The energies involved in this process of polymers spreading across c-ND are captured using work of spreading (W_s). Complete wetting of polymer on c-ND results in positive W_s , whereas partial wetting of polymer on c-ND results in negative W_s . The work of spreading shown in Figure 4.3a and tabulated in Table 4.1 are negative for all polymer combinations. This suggests that wetting of the c-ND surface by the polymer is an unfavorable process, a direct consequence of mismatch in surface energies. PVA has a negative W_s of -7.7 mJ/m², compared to -17.4 mJ/m² for PAN and -6.6 mJ/m² for PS. This implies that the ability of polymers to wet the c-ND surface increases in the order of PAN < PVA < PS. Therefore, initially c-ND likes to wet the surface, but polymers do not like to spread on the surface. The phenomenon of c-ND wetting the polymer, and polymer spreading across the ND-surface takes place initially upon addition of c-ND into the polymer. However, over time c-ND may show an affinity to itself more than the polymer, causing the system to move to an aggregated state. Indeed, the driving force for this transition to take place is captured by ($\Delta W_{DIS-AGG}$). The mathematical formulation based

on equation 17 implies that the driving force of re-aggregation pronounced for systems that have disparate surface energies, i.e. the more mismatch in dispersive and polar surface energy components of polymer relative to the filler, the higher the driving force for aggregation. As shown in Figure 4.3a, the driving force of c-ND aggregation is considerably higher for PAN compared to PS and PVA. c-ND in PVA has a driving force of 0.88 mJ/m^2 , which is the lowest among the polymers, possibly due to the presence of hydrogen bonding with the polymer. To that end, c-ND aggregation should be more pronounced in PAN due to higher deviation in surface energies, especially the polar component which is 14.7 mJ/m^2 relative to polar component of nanodiamond of only 3.1 mJ/m^2 . The disparity in polarity contributes in large part to higher driving force for aggregation in the order $\text{PVA} < \text{PS} < \text{PAN}$. In the above discussion, however, there is no correlation between wettability, spreading coefficient and work associated with dispersion-aggregation transition. The simultaneous effect of all these mechanisms taking place from the initial dispersed state to the final aggregated state, therefore, can be captured using D_c , the criterion for dispersion. As shown in Figure 4.3b, D_c for PVA, PAN and PS is -0.4 mJ/m^2 , -4.3 mJ/m^2 and -1.2 mJ/m^2 respectively. This implies that ND composites in PVA are favorable relative to PS and least favorable for PAN. Note that a negative value of D_c imposes limitations in polymer-ND interactions, suggesting that the system leans towards aggregated state. This is particularly true for fillers without tailored surface functionalization.

4.4.5 Effect of Nanodiamond on Glass Transition Temperature of Polymer Fiber

Composites

In the presence of nanofillers, polymers may undergo changes in interphase properties due to favorable polymer-filler interactions that aid in the reinforcement of mechanical, thermal, or electrical properties and thus improve polymer functionality. Most specifically, polymer mobility can be altered in the presence of polymer-filler interactions, resulting in either depression or enhancement of polymer mobility due to attractive or repulsive polymer-filler interactions respectively. By measuring shifts in glass transition temperature (T_g), nanofiller-induced perturbation in polymer mobility can be captured experimentally, with positive and negative shifts in T_g implying an attractive or repulsive interaction between polymer-filler respectively. Ramanathan *et al.* reported increments in T_g of over 40°C for PAN and ~30°C for PMMA using functionalized graphene sheets at 1 wt.% and 0.05 wt.% respectively, with modulus and tensile strength showing similar trends.⁸¹ Experiments by Chen *et al.* using PS-grafted nanoparticles in PS observed T_g dependence on grafting density and ratio of matrix to grafted polymer molecular weight.⁸² Additional studies using graphene in PMMA matrix, which show enhancement in T_g have further corroborated the use of such measurements as a measure of strength of polymer-filler interaction.⁸³ This study, therefore, utilize the shifts in T_g of polymer composites measured using DSC to quantitatively infer the presence of attractive or repulsive interfacial interactions between polymer and c-ND. Figure 4.4a shows the effect of c-ND loadings on T_g on PVA, PAN and PS used in this study, and Figure 4.4b shows deviations of T_g from the pure polymer, ΔT_g , derived using the same data. Table 4.2 shows quantitative results including T_g obtained using DSC for the polymers and

their composites with c-ND. Reported values of T_g represent inflection points extracted from DSC isotherms. Representative images of electrospun fiber composites are shown in Figure C.6 and the conditions of electrospinning are shown in Table C.3.

Pure PVA nanofibers exhibit T_g of $78.3^\circ\text{C} \pm 0.4^\circ\text{C}$, which is very close to values reported in the literature. Incorporating c-ND into PVA nanofibers causes a positive shift in T_g for all c-ND loadings up to 2 wt. % used in this study. The inclusion of very low amounts of c-ND (0.1 wt.%) results in a modest positive shift to $79.5^\circ\text{C} \pm 0.5^\circ\text{C}$, an increase in $1.2^\circ\text{C} \pm 0.3^\circ\text{C}$ in comparison to pure PVA. Addition of c-ND up to 1 wt. % shows an increasing trend, with maximum positive shift occurring at 1 wt. %. The largest shift to $82.6^\circ\text{C} \pm 1.3^\circ\text{C}$, which is a $4.3 \pm 0.5^\circ\text{C}$ increase in T_g was observed at 1 wt.% loading. This result points to the fact that increasing amounts of c-ND hinders the mobility of PVA chains, possibly due to favorable interactions between $-\text{OH}$ group on PVA backbone with $-\text{COOH}$ groups on c-ND surface. Thus, the increase in T_g of composite fibers relative to pure implies presence of strong favorable interfacial interactions between the two phases. Upon further addition of c-ND to 2 wt. %, positive shifts are maintained; however, ΔT_g starts to saturate. A positive ΔT_g of $4.1 \pm 0.5^\circ\text{C}$, which is higher than T_g of pure PVA but less than that for 1 wt. % loading, is observed at 2 wt. % loading. The saturation could be an influence of particle crowding which favors interaction of c-ND with its neighbors, diminishing the likelihood of favorable interactions with polymer causing T_g to saturate. Similar analysis is extended to PS composite fibers to understand the role of c-ND. Similar trends were observed when c-ND is loaded into PS matrix, with loadings up to 2 wt. % causing positive ΔT_g . However, in contrast to PVA, increase in T_g for PS composite fibers did not saturate even up to maximum loading of 2 wt.

% . Furthermore, the magnitude of ΔT_g for PS is significantly smaller than that of PVA. The addition of 0.5 wt. % c-ND resulted in a modest increase of $0.7^\circ\text{C} \pm 0.1^\circ\text{C}$ from $103.6^\circ\text{C} \pm 0.1^\circ\text{C}$ to $104.3^\circ\text{C} \pm 0.1^\circ\text{C}$ which could be well within standard errors of the instrument. However, the shift in ΔT_g corresponds to $0.97^\circ\text{C} \pm 0.2^\circ\text{C}$ and $1.97^\circ\text{C} \pm 0.2^\circ\text{C}$ at loadings of 1 wt. % and 2 wt. % c-ND respectively, which are statistically significant. The upper limit of c-ND loading was capped to study reinforcement properties at low loadings. The reported values suggest some influence of c-ND on the mobility of PS. The smaller positive shift in ΔT_g for PS ($\sim 2^\circ\text{C}$) compared to that of PVA ($\sim 4^\circ\text{C}$) could be a result of weaker hydrophobic interactions relative to hydrogen bonding interactions. While hydrophobic interactions do retard the polymer mobility, it does so to a much lesser extent than hydrogen bonding interactions. In contrast to PVA, however, at higher loadings of 2 wt. %, ΔT_g does not saturate. This could be explained using the micron-sized PS fibers and amorphous nature of PS compared to PVA nanofibers, where more particles can be accommodated without necessarily exerting an influence on the neighboring particles or hindering crystallinity. Finally, the effect of c-ND loading on T_g was also monitored for PAN c-ND nanofiber composites. Pure PAN has a T_g of $100.5^\circ\text{C} \pm 0.1^\circ\text{C}$. In contrast to both PVA and PS, however, PAN does not show T_g increments at loadings less than 1 wt.%, but shows a maximum change of $1.1^\circ\text{C} \pm 0.3^\circ\text{C}$ at that loading. Further increase in c-ND loading results in a negative shift of $-1.1^\circ\text{C} \pm 0.2^\circ\text{C}$ in ΔT_g suggesting an unfavorable repulsive interaction between PAN nanofiber and c-ND. The maximum positive shifts in T_g ($\Delta T_{g, \text{max}}$) align well with predictions made by D_c as shown in Figure 4.5. Higher values of D_c result in greater

shifts in T_g ($^{\circ}\text{C}$) in the order PVA > PS > PAN, suggesting a correlation between adhesion parameters and ΔT_g .

4.4.6 Correlation between Glass Transition Temperature and Tensile Strength

The correlation between maximum shifts in T_g ($\Delta T_{g, \text{max}}$) with increasing D_c , which indicates a reduction of polymer mobility on c-ND surface and favorable polymer-ND interactions, and tensile strength is studied using stress-strain graphs of polymer-ND fiber specimens with different c-ND loadings. Figure C.7 shows stress-strain graphs of PVA nanofibers and with different c-ND loadings up to 2 wt. %. The average values of tensile strength and elongation at break extracted from stress-strain graphs are tabulated in Table 4.3. As shown in Figure C.7, PVA nanofibers undergo elastic deformation for low strains (< 5%), and the addition of c-ND increases the stiffness of the polymer captured by the elastic modulus. After elastic deformation, the nanofibers start to yield and undergo further elongation, which results in fiber alignment, followed by fiber rupture. Incorporation of 0.5 wt.% c-ND results in an increase of tensile strength from 2.97 ± 0.10 MPa to 4.46 ± 0.42 MPa corresponding to an increase of 50.2%, which further increases at a loading of 1 wt.% to 4.64 ± 0.08 MPa corresponding to an increase in 56.3% relative to PVA nanofibers. At much higher loadings up to 2 wt. %, however, the tensile strength goes down to 3.48 ± 0.13 MPa, resulting in the least gain in tensile strength of 17.3%. Despite the increase in tensile strength, increase in c-ND loadings reduces elongation at break, with a maximum reduction of ~65% seen for 2 wt. % loadings. This could be a consequence of c-ND particles hindering the semi-crystalline structure of PVA. Indeed, the crystallinity of PVA, obtained using DSC, decreases with c-ND loadings (see Figure C.8).

Similar analysis is repeated for PAN and PS (see Figures C.9 and C.10). Stress-strain curves for PS with different c-ND loadings show initial elastic deformation in the low-strain region (0-5 MPa) and immediate yielding without fiber elongation observed for PVA nanofibers at higher stress. The tensile strength in the range of 0.38-1.08 MPa for PS is much lower than that of PVA ranging between 2.97-3.48 MPa. Much weaker PS nanofibers, therefore, shows prolonged yielding since they are softer relative to PVA and does not yield immediately. Compared to pure PS nanofibers, the maximum tensile strength of c-ND increases by ~180% for 2 wt. % loading. This enhancement in tensile strength, much higher than those in PVA, could be a result of efficient stress transfer in PS due to its amorphous nature compared to PVA. In addition, very low elongation (10.4 %) of PS nanofibers is slightly improved with 0.5 wt. % c-ND, but the addition of 2 wt. % c-ND increases elongation at break to by ~90%. The same analysis is repeated for PAN, with stress-strain curves very similar to that of PS. The tensile strength of PAN nanofibers between 1.74 MPa and 0.98 MPa is much higher than that of PS but still lower than that of PVA. Unlike the increase in tensile strength seen for PVA and PS, the addition of c-ND results in the reduction of tensile strength in PAN. The initial tensile strength of PAN nanofibers of 1.74 ± 0.07 MPa decreased by ~27% with c-ND loadings of 1 wt.%, possibly due to weaker interfacial strength in PAN compared to PVA and PS.

High polymer-filler interfacial strength, a consequence of good interfacial bonding, dictate stress transfers efficiency in nanocomposites. Therefore, some of the most important mechanical properties such as tensile strength, elastic modulus, elongation at break, and fracture toughness of nanocomposites are governed by the interfacial strength between the

polymer matrix and the reinforcing phase. Unlike in fiber-based composites, for which fiber pullout technique is used to measure interfacial strengths experimentally, direct and precise measurements of the interfacial strength are difficult for ND-based composites, necessitating the use of models that can be fit to experimental data to extract interaction parameters. Several models in the literature, with assumptions of zero polymer-filler interfacial adhesion, and very strong matrix-filler interfacial adhesion have been used to predict the strength of composite materials. In particular, an empirical model shown in equation 24, consisting of an interaction parameter (B) characterizing the interfacial interaction, thickness and strength of composites is used to fit the experimental data.

$$\sigma_c = \sigma_p \left[\frac{1-\phi_F}{1+2.5\phi_F} \right] \exp(B\phi_F) \quad (24)$$

In equation 24, σ_c is the tensile strength of the composite, σ_p is the tensile strength of the polymer, ϕ_F is the volume fraction of the filler and B is the strength of interfacial interaction or capacity of stress transfer related to thickness and area of interphase.^{84,85} The first term physically represents a decrease in cross-section area for stress-transfer due to the addition of reinforcing phase and the second term accounts for the increase in strength of nanocomposites due to interfacial adhesion between the polymer and reinforcing phase. The normalized tensile strength as a function of c-ND volume fraction for PVA, PAN and PS are shown in Figure 4.6a. It can be seen that PVA and PS have higher tensile strength while PAN have lower tensile strength than the pure polymer with the addition of c-ND. The most significant improvement in tensile strength is seen in the order of PS > PVA > PAN. The inclusion of very low amounts of c-ND (0.5 wt.%, 0.16 vol.%) in PVA results in a positive

shift in the normalized tensile strength to 1.50, with maximum tensile strength increase of 56% occurring at 1 wt.% (0.32 vol.) as shown in Table 4.4. This trend mimics trends shown in shifts in T_g , which showed maximum positive shift (ΔT_g) of 4.3°C at 1 wt. % loading, establishing a correlation between tensile strength and shifts in T_g . However, increase in c-ND loading to 2 wt. % results in normalized tensile strength of 1.17, which is lower than that at 1 wt. % loading, but still higher than the pure PVA. This shows that tensile strength of the composite fibers starts to decrease at loadings higher than 1 wt. %. At high loadings, the interactions between PVA and c-ND is saturated as predicted by shifts in T_g , and further additions will have negligible influence on polymer-filler interactions.

In sharp contrast to increase in tensile strengths upon addition of c-ND in PVA, PAN shows no tensile strength reinforcements as shown by normalized values of tensile strength, which are all less than unity at any c-ND loading. At maximum loadings of 2 wt. %, PAN shows an approximate reduction of 44% in tensile strength, suggesting negative effects of c-ND. Correlating this to shifts in T_g , we find that PAN did not interact well with c-ND and no significant enhancement was seen. In addition, the interaction parameter of 2.2 for PAN is less than that for PVA and is purely dominated by a decrease in cross-section area due to the addition of fillers, suggesting that interfacial adhesion is negligible (Figure 4.6b). This is a direct consequence of mismatch in surface energies, which enhances driving force of aggregation of c-ND in PAN, thereby showing detrimental effects on the final composite tensile strength. The dependence of c-ND loading on normalized tensile strength as well as the interaction parameter for PS is significantly different from that of PVA. For PS, the increase in tensile strength occurs at even low contents and the trend does not reverse at high

loadings unlike those seen in PVA. The addition of 0.5 wt. % c-ND on PS results in a 52% increase in tensile strength, which goes up to 250% for 1.0 wt. % and 284% for 2.0 wt. % respectively. The interaction parameter of 4.8 for PS is higher compared to 3.2 for PVA.

4.5 Conclusions

Development of nanocomposites with enhanced properties necessitates the use of model filler as well as fundamental understanding of polymer-filler interactions at the nanoscale. Nanodiamonds (ND's) have emerged as a novel class of nanofillers, however, the propensity of ND's to aggregate in solution as well as in polymers presents significant challenges during processing of ND-based fibers composites. As such, understanding the interfacial energetics associated with polymer-ND composites to promote dispersion and enhance ND-polymer wetting at the nanoscale is an essential prerequisite in designing polymer-ND composite fibers with reinforced mechanical properties. In this work, we studied the aggregation behavior of carboxylated-ND (c-ND) in various solvents and polymers with varying polarities. Dispersion of c-ND in 18 different solvents revealed a dependence on the polar component of solvent solubility parameter, with stable to moderately stable dispersions observed in solvents with polar component of the solubility parameter of $\sim 7 \text{ MPa}^{1/2}$. The c-ND's $\sim 100 \text{ nm}$ in size were de-aggregated into smaller particles using salt-assisted ultrasonic deaggregation (SAUD), with a flat tip and microtip giving c-ND's with a primary particle size of $\sim 20\text{-}30 \text{ nm}$ and $\sim 60 \text{ nm}$ respectively. Wicking technique, combined with Washburn equation, was used to calculate surface energy of c-ND of $33.5 \pm 6.9 \text{ mJ/m}^2$ for dispersive component and $3.1 \pm 2.9 \text{ mJ/m}^2$ for polar component.

c-ND between 20-30 nm were used to make electrospun fiber composites in two semi-crystalline polymers poly(vinyl alcohol) (PVA) and polyacrylonitrile (PAN) and amorphous polystyrene (PS). Different parameters such as wettability, work of spreading, and work of dispersion-aggregation transition, calculation using the surface energy of c-ND and polymers, were used to derive a criterion for dispersion (D_c) as a predictor of final tensile properties of polymer-ND fiber composites. We found that shifts in glass transition temperature (ΔT_g), used as a measure of polymer-ND interactions, showed a direct correlation with D_c in the order of PVA > PS > PAN. However, the final tensile strength showed a direct correlation with D_c and ΔT_g for semi-crystalline polymers only, with amorphous polystyrene showing maximum reinforcement contrary to predictions made by ΔT_g , suggesting contributions of crystallinity to final tensile strength. The findings of this study could offer additional insight into the design of interfaces for polymer-ND fiber composites.

4.6 Acknowledgement

The author acknowledges the financial support from the Nonwovens Institute (NWI) at North Carolina State University, Raleigh, NC.

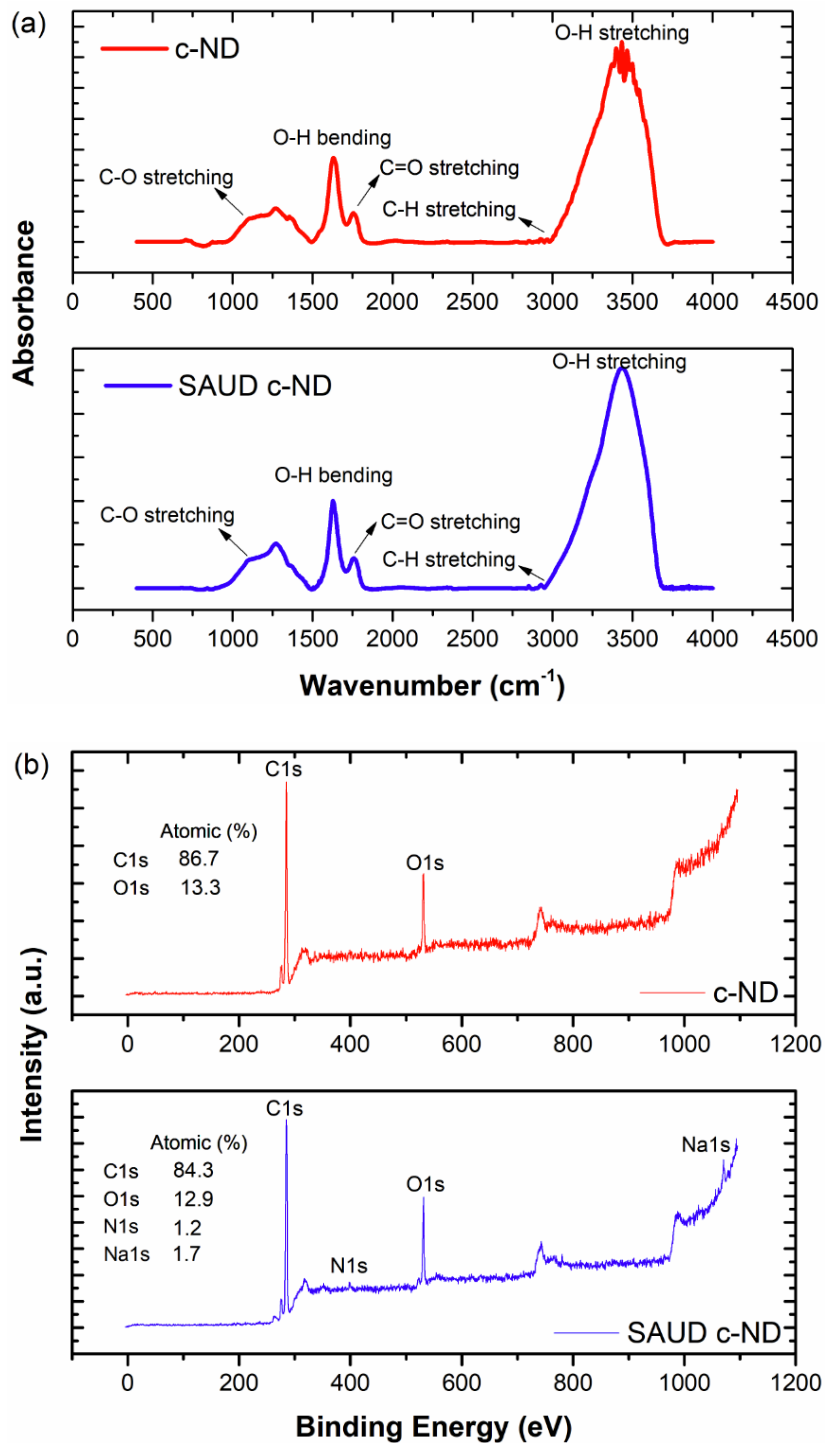


Figure 4.1 (a) FTIR spectrum and (b) XPS scan for c-ND and SAUD c-ND showing changes in surface composition after deaggregation. SAUD c-ND shows minor amounts of sodium (Na) and nitrogen (N).

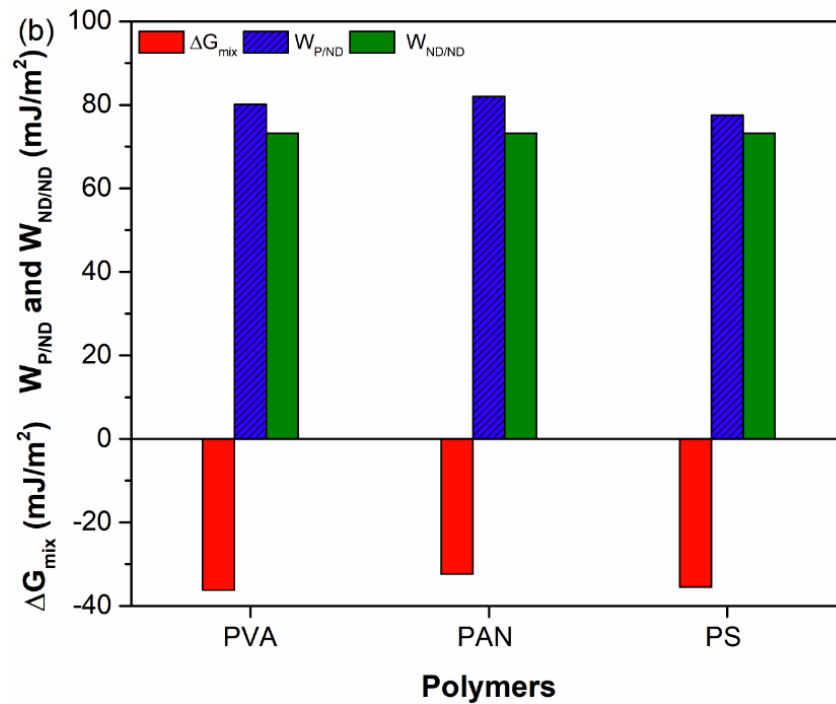
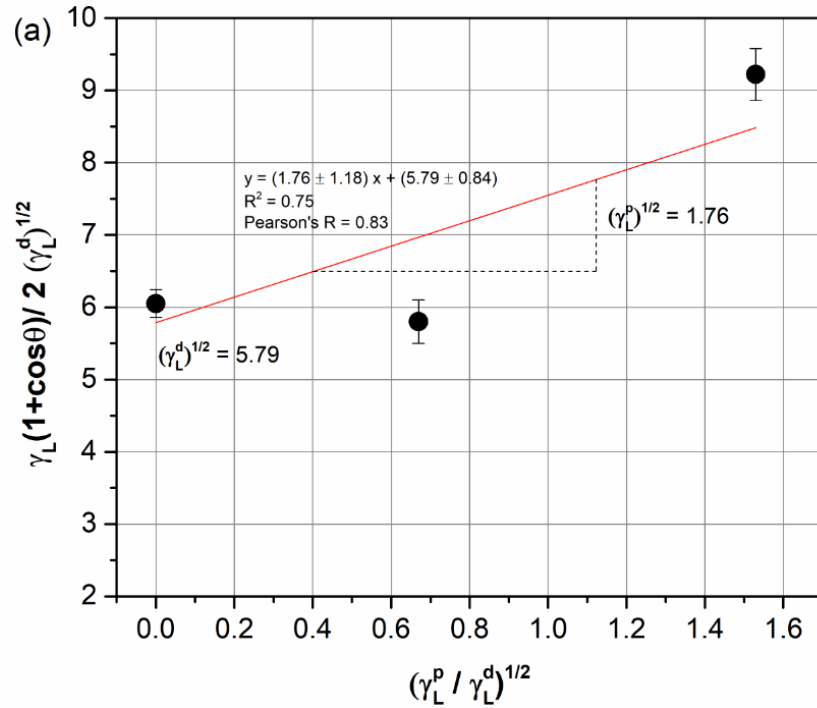


Figure 4.2 (a) Owens-Wendt plot used to calculate the surface energy of c-ND, and (b) ΔG_{mix} , work of adhesion ($W_{P/ND}$), and work of cohesion ($W_{ND/ND}$) for c-ND mixed in two semi-crystalline polymers (PVA, PAN) and amorphous polymer (PS).

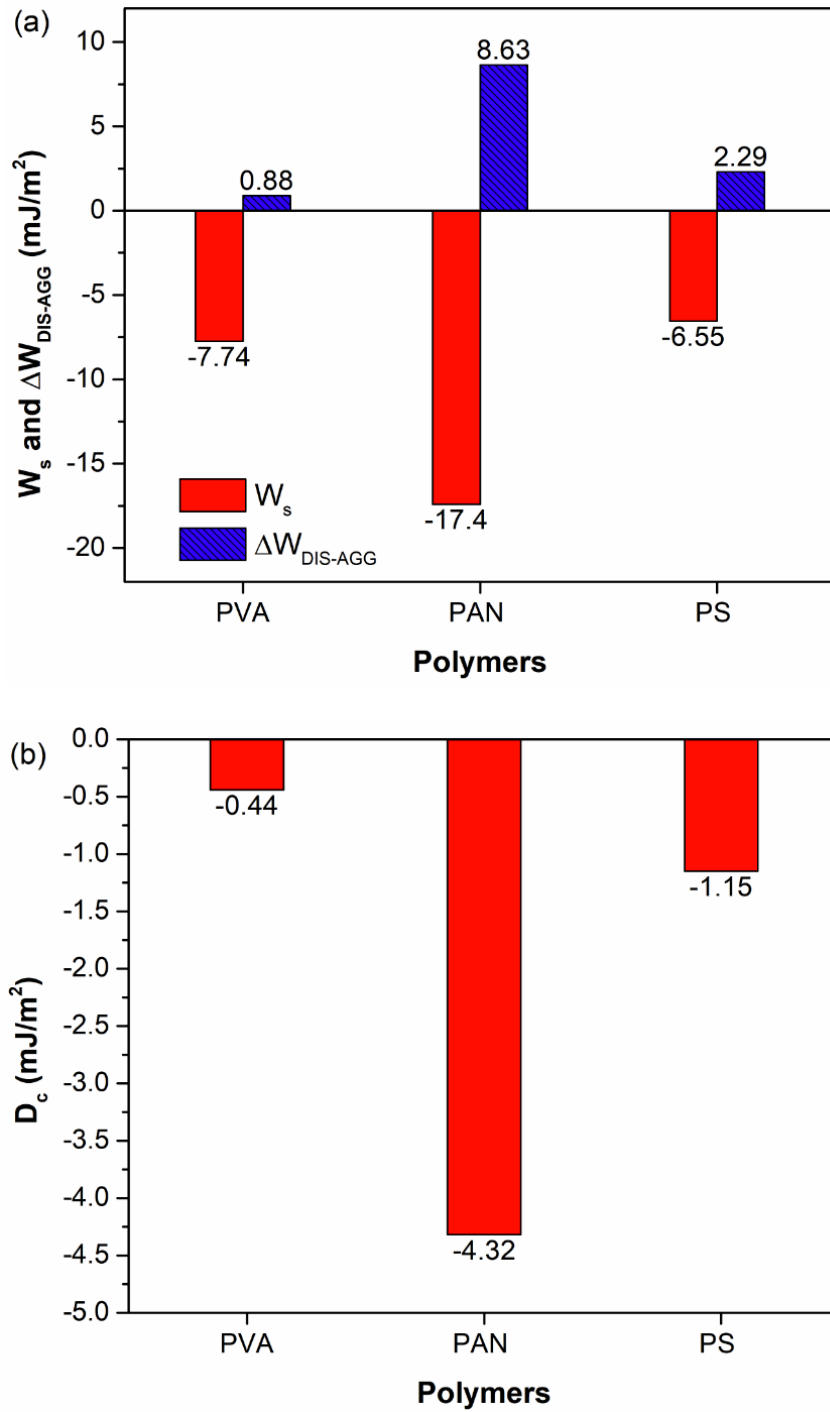


Figure 4.3 (a) Work of spreading, work of dispersion-aggregation transition, and (b) dispersion criterion for c-ND in PVA, PAN and PS derived using surface energies.

Table 4-1 Summary of relevant adhesion parameters in understanding dispersion-aggregation behavior of ND's in different polymers extracted from data shown in Figure 4.2 and 4.3

Polymers	ΔG_{mix} (mJ/m ²)	$W_{\text{P/ND}}$ (mJ/m ²)	$W_{\text{ND/ND}}$ (mJ/m ²)	$W_{\text{P/ND}} / W_{\text{ND/ND}}$	W_s (mJ/m ²)	$\Delta W_{\text{DIS-AGG}}$ (mJ/m ²)	D_c (mJ/m ²)
PVA	-36.2	80.1	73.2	1.09	-7.7	0.88	-0.4
PAN	-32.3	81.9	73.2	1.12	-17.4	2.29	-4.3
PS	-35.5	77.5	73.2	1.06	-6.6	8.63	-1.2

ΔG_{mix} : Gibbs energy of mixing c-ND in polymers

$W_{\text{P/ND}}$: work of polymer-ND interaction (work of adhesion)

$W_{\text{ND/ND}}$: work of ND-ND interaction (work of cohesion)

$W_{\text{P/ND}} / W_{\text{ND/ND}}$: wettability

W_s : work of spreading

$\Delta W_{\text{DIS-AGG}}$: work of dispersion-aggregation transition (driving force)

D_c : dispersion criterion

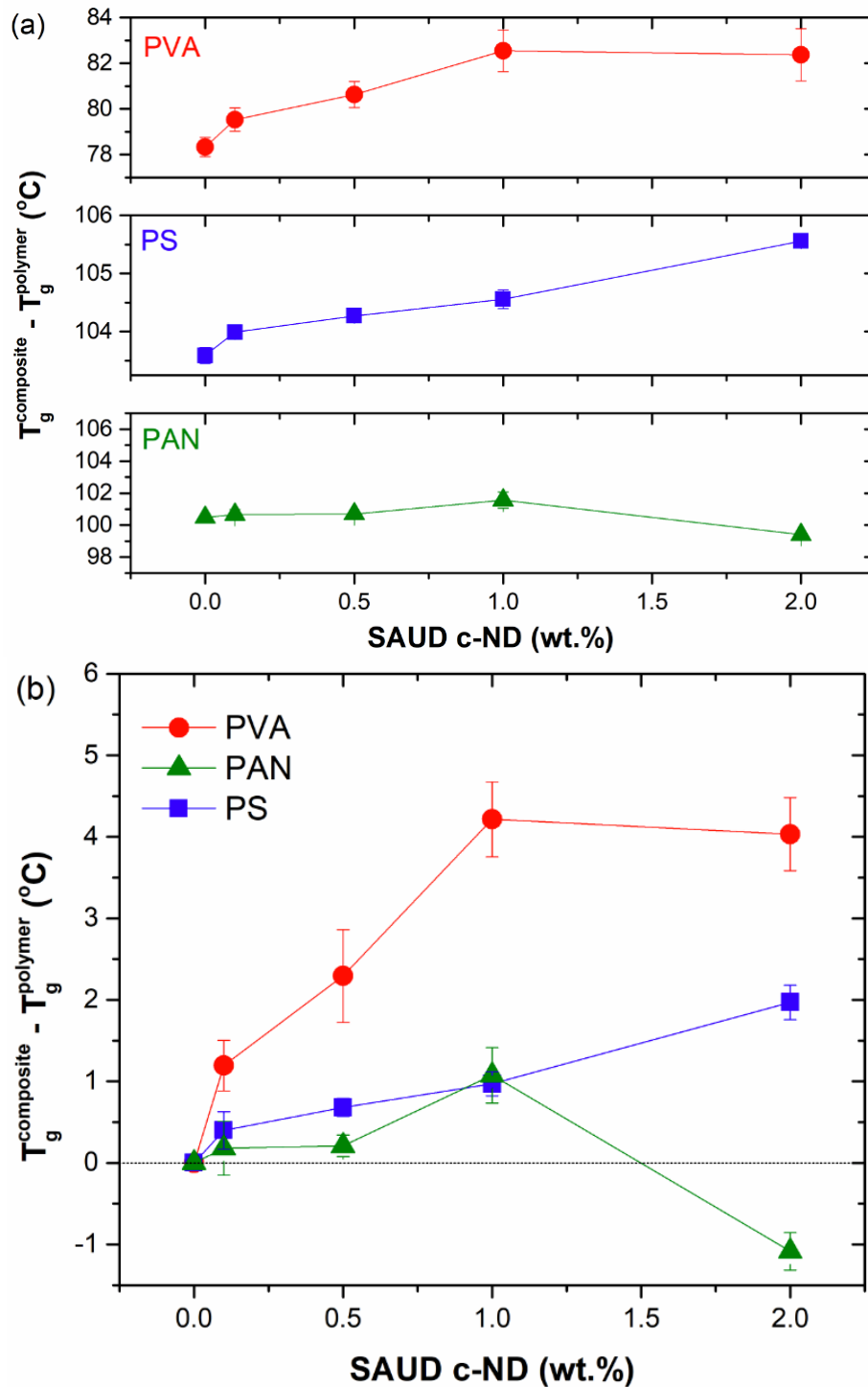


Figure 4.4 (a) The effect of c-ND loadings on glass transition temperature (T_g) of PVA, PAN and PS electrospun fibers, and (b) the change in glass transition temperature (ΔT_g) post c-ND addition relative to nanofibers without c-ND.

Table 4-2 Glass transition temperature (T_g) and relative shift in glass transition temperature (ΔT_g) of electrospun polymer fibers with varying c-ND loadings

	PVA	
ND (wt. %)	T_g ($^{\circ}\text{C}$)	ΔT_g ($^{\circ}\text{C}$)
0	78.3 ± 0.4	-
0.1	79.5 ± 0.5	1.2 ± 0.3
0.5	80.6 ± 0.6	2.3 ± 0.6
1.0	82.6 ± 1.3	4.3 ± 0.5
2.0	82.4 ± 1.1	4.1 ± 0.5

	PAN	
ND (wt. %)	T_g ($^{\circ}\text{C}$)	ΔT_g ($^{\circ}\text{C}$)
0	100.5 ± 0.1	-
0.1	100.7 ± 0.3	0.2 ± 0.3
0.5	100.7 ± 0.1	0.2 ± 0.1
1.0	101.6 ± 0.5	1.1 ± 0.3
2.0	99.4 ± 0.2	-1.1 ± 0.2

	PS	
ND (wt. %)	T_g ($^{\circ}\text{C}$)	ΔT_g ($^{\circ}\text{C}$)
0	103.6 ± 0.1	-
0.1	104.0 ± 0.1	0.4 ± 0.2
0.5	104.3 ± 0.1	0.7 ± 0.1
1.0	104.6 ± 0.2	0.97 ± 0.2
2.0	105.6 ± 0.1	1.98 ± 0.2

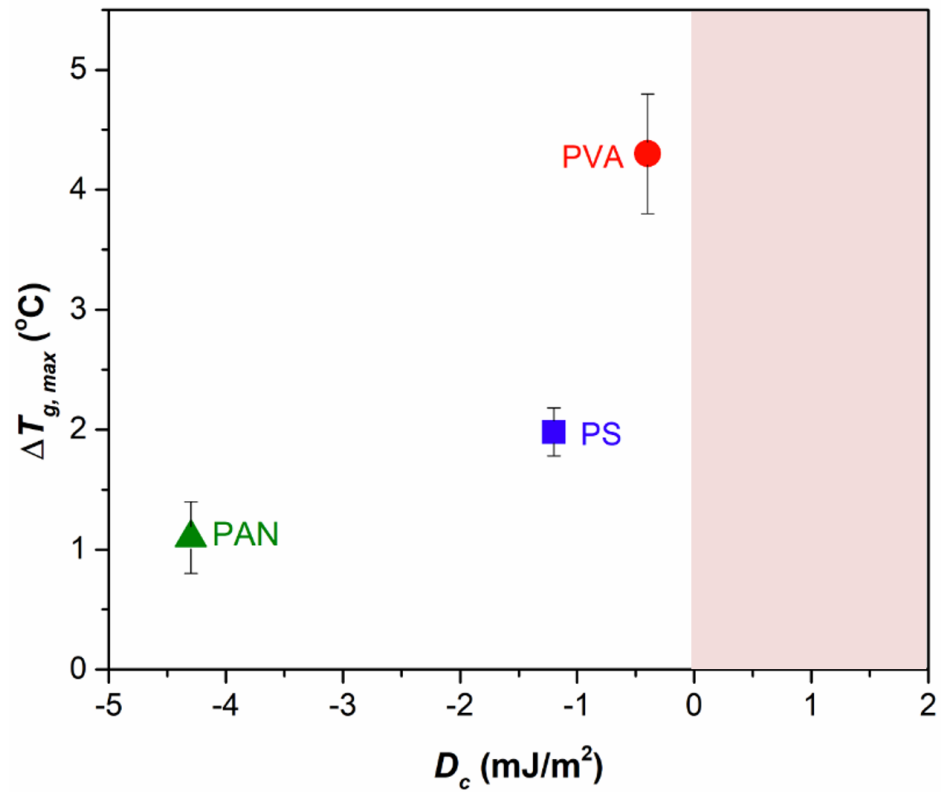


Figure 4.5 Plot showing maximum change in glass transition temperature of electrospun fibers containing c-ND as a function of criteria for dispersion (D_c). Higher values of (D_c) result in greater shifts in T_g (°C) in the order PVA > PS > PAN.

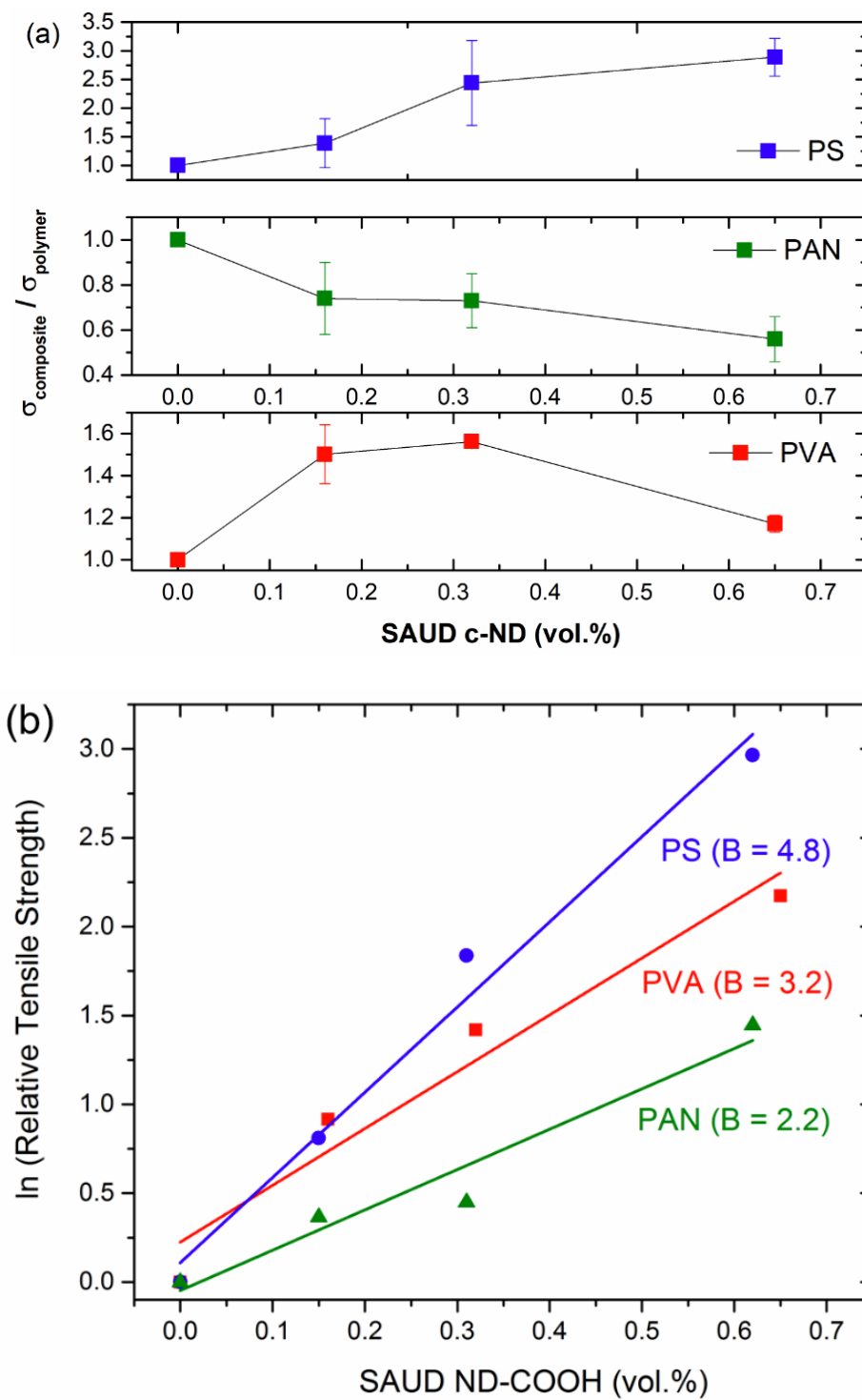


Figure 4.6 (a) Normalized tensile strength as a function of SAUD c-ND loadings (vol. %) and (b) adhesion parameter (B) as a function of SAUD c-ND loadings derived by fitting experimental data to Pukanszky model.

Table 4-3 Tensile strength (σ) and elongation at break (ϵ) of polymer nanofibers with different c-ND loadings, obtained using stress-strain data shown in Figures C.7-C.9.

	PVA	
ND (wt. %)	σ (MPa)	ϵ (%)
0	2.97 ± 0.10	126.2 ± 19.4
0.5	4.46 ± 0.42	99.3 ± 8.6
1.0	4.64 ± 0.08	77.1 ± 12.1
2.0	3.48 ± 0.13	44.8 ± 6.3

	PAN	
ND (wt. %)	σ (MPa)	ϵ (%)
0	1.74 ± 0.07	18.9 ± 6.4
0.5	1.28 ± 0.29	13.9 ± 5.1
1.0	1.27 ± 0.20	9.42 ± 2.1
2.0	0.98 ± 0.18	9.37 ± 0.6

	PS	
ND (wt. %)	σ (MPa)	ϵ (%)
0	0.38 ± 0.13	10.4 ± 6.1
0.5	0.58 ± 0.12	18.0 ± 6.6
1.0	0.95 ± 0.35	17.3 ± 2.6
2.0	1.08 ± 0.13	19.7 ± 3.7

Table 4-4 Shifts in glass transition temperature (ΔT_g), normalized tensile strength and Pukanszky interaction parameter of polymer nanofibers with different c-ND loadings.

PVA			
ND (wt. %)	ΔT_g (oC)	σ_c / σ_m	B
0	0	1	3.2
0.5	2.3 ± 0.6	1.50	
1	4.3 ± 0.5	1.56	
2	4.1 ± 0.5	1.17	

PAN			
ND (wt. %)	ΔT_g (oC)	σ_c / σ_m	B
0	0	1	2.2
0.5	0.2 ± 0.3	0.74	
1	1.1 ± 0.1	0.73	
2	-1.1 ± 0.3	0.56	

PS			
ND (wt. %)	ΔT_g (oC)	σ_c / σ_m	B
0	0	1	4.8
0.5	0.7 ± 0.1	1.52	
1	0.97 ± 0.2	2.5	
2	1.98 ± 0.2	2.84	

4.7 References

1. Danilenko, V. V. On the history of the discovery of nanodiamond synthesis. *Phys. Solid State* **46**, 595–599 (2004).
2. Hsiao, W. W. W., Hui, Y. Y., Tsai, P. C. & Chang, H. C. Fluorescent Nanodiamond: A Versatile Tool for Long-Term Cell Tracking, Super-Resolution Imaging, and Nanoscale Temperature Sensing. *Acc. Chem. Res.* **49**, 400–407 (2016).
3. Hui, Y. Y., Cheng, C.-L. & Chang, H.-C. Nanodiamonds for optical bioimaging. *J. Phys. D. Appl. Phys.* **43**, 374021 (2010).
4. Boudou, J.-P. *et al.* High yield fabrication of fluorescent nanodiamonds. *Nanotechnology* **20**, 235602 (2009).
5. Chang, Y.-R. *et al.* Mass production and dynamic imaging of fluorescent nanodiamonds. *Nat. Nanotechnol.* **3**, 284–288 (2008).
6. Fu, C.-C. *et al.* Characterization and application of single fluorescent nanodiamonds as cellular biomarkers. *Proc. Natl. Acad. Sci. U. S. A.* **104**, 727–32 (2007).
7. Shu-Jung Yu, †, Ming-Wei Kang, †, Huan-Cheng Chang, *, †, ‡, Kuan-Ming Chen, § and Yu§, Y.-C. Bright Fluorescent Nanodiamonds: No Photobleaching and Low Cytotoxicity. 17604–17605 (2005). doi:10.1021/JA0567081
8. Xue, Z., Vinci, J. C. & Colón, L. A. Nanodiamond-Decorated Silica Spheres as a Chromatographic Material. *ACS Appl. Mater. Interfaces* **8**, 4149–4157 (2016).
9. Saini, G. *et al.* Core - Shell Diamond as a Support for Solid-Phase Extraction and High-Performance Liquid Chromatography. **82**, 4448–4456 (2010).
10. Spitsyn, B. V. *et al.* The physical-chemical study of detonation nanodiamond application in adsorption and chromatography. *Diam. Relat. Mater.* **19**, 123–127

(2010).

11. Behler, K. D. *et al.* Nanodiamond-polymer composite fibers and coatings. *ACS Nano* **3**, 363–369 (2009).
12. Mochalin, V. N., Pentecost, A., Li, X. & Neitzel, I. Adsorption of Drugs on Nanodiamond : Towards Development of a Drug Delivery Platform Adsorption of Drugs on Nanodiamond : Towards Development of a Drug Delivery Platform. (2013). doi:10.1021/mp400213z
13. Chow, E. K. *et al.* Nanodiamond Therapeutic Delivery Agents Mediate Enhanced Chemoresistant Tumor Treatment. *Sci. Transl. Med.* **3**, 73ra21-73ra21 (2011).
14. Zhang, X. Q. *et al.* Multimodal nanodiamond drug delivery carriers for selective targeting, imaging, and enhanced chemotherapeutic efficacy. *Adv. Mater.* **23**, 4770–4775 (2011).
15. Liu, K.-K. *et al.* Covalent linkage of nanodiamond-paclitaxel for drug delivery and cancer therapy. *Nanotechnology* **21**, 315106 (2010).
16. Huang, H., Pierstorff, E., Osawa, E. & Ho, D. Active nanodiamond hydrogels for chemotherapeutic delivery. *Nano Lett.* **7**, 3305–3314 (2007).
17. Kausar, A., Ashraf, R. & Siddiq, M. Polymer/Nanodiamond Composites in Li-Ion Batteries: A Review. *Polym. Plast. Technol. Eng.* **53**, 550–563 (2014).
18. Kovalenko, I., Bucknall, D. G. & Yushin, G. Detonation nanodiamond and onion-like-carbon-embedded polyaniline for supercapacitors. *Adv. Funct. Mater.* **20**, 3979–3986 (2010).
19. Zang, J. B., Wang, Y. H., Zhao, S. Z., Bian, L. Y. & Lu, J. Electrochemical properties of nanodiamond powder electrodes. *Diam. Relat. Mater.* **16**, 16–20 (2007).

20. Portet, C., Yushin, G. & Gogotsi, Y. Electrochemical performance of carbon onions, nanodiamonds, carbon black and multiwalled nanotubes in electrical double layer capacitors. *Carbon N. Y.* **45**, 2511–2518 (2007).
21. Ferreira, N. G. *et al.* Nanodiamond films growth on porous silicon substrates for electrochemical applications. *Diam. Relat. Mater.* **14**, 441–445 (2005).
22. Ivanov, M. & Shenderova, O. Nanodiamond-based nanolubricants for motor oils. *Curr. Opin. Solid State Mater. Sci.* **21**, 17–24 (2017).
23. Elomaa, O., Oksanen, J., Hakala, T. J., Shenderova, O. & Koskinen, J. A comparison of tribological properties of evenly distributed and agglomerated diamond nanoparticles in lubricated high-load steel-steel contact. *Tribol. Int.* **71**, 62–68 (2014).
24. Elomaa, O. *et al.* Diamond nanoparticles in ethylene glycol lubrication on steel-steel high load contact. *Diam. Relat. Mater.* **34**, 89–94 (2013).
25. Chou, C. C. & Lee, S. H. Tribological behavior of nanodiamond-dispersed lubricants on carbon steels and aluminum alloy. *Wear* **269**, 757–762 (2010).
26. Dolmatov, V. Y., Veretennikova, M. V., Marchukov, V. A. & Sushchev, V. G. Currently available methods of industrial nanodiamond synthesis. *Phys. Solid State* **46**, 611–615 (2004).
27. Shenderova, O. *et al.* Surface chemistry and properties of ozone-purified detonation nanodiamonds. *J. Phys. Chem. C* **115**, 9827–9837 (2011).
28. Pichot, V. *et al.* An efficient purification method for detonation nanodiamonds. *Diam. Relat. Mater.* **17**, 13–22 (2008).
29. Petrov, I. *et al.* Detonation nanodiamonds simultaneously purified and modified by gas treatment. *Diam. Relat. Mater.* **16**, 2098–2103 (2007).

30. Osswald, S., Yushin, G., Mochalin, V., Kucheyev, S. O. & Gogotsi, Y. Control of sp²/sp³ carbon ratio and surface chemistry of nanodiamond powders by selective oxidation in air. *J. Am. Chem. Soc.* **128**, 11635–11642 (2006).
31. Kulakova, I. I. Surface chemistry of nanodiamonds. *Phys. Solid State* **46**, 636–643 (2004).
32. Krueger, A. & Boedeker, T. Deagglomeration and functionalisation of detonation nanodiamond with long alkyl chains. *Diam. Relat. Mater.* **17**, 1367–1370 (2008).
33. Krueger, A. *et al.* Deagglomeration and functionalisation of detonation diamond. *Phys. Status Solidi Appl. Mater. Sci.* **204**, 2881–2887 (2007).
34. Mochalin, V. N., Shenderova, O., Ho, D. & Gogotsi, Y. The properties and applications of nanodiamonds. *Nat. Nanotechnol.* **7**, 11–23 (2012).
35. Xu, X., Yu, Z., Zhu, Y. & Wang, B. Influence of surface modification adopting thermal treatments on dispersion of detonation nanodiamond. *J. Solid State Chem.* **178**, 688–693 (2005).
36. Xu, K. & Xue, Q. A New Method for Deaggregation of Nanodiamond from Explosive Detonation: Graphitization – Oxidation Method 1. *Phys. Solid State* **46**, 633–634 (2004).
37. Vul, A. Y. *et al.* Direct observation of isolated ultrananodimensional diamond clusters using atomic force microscopy. *Tech. Phys. Lett.* **32**, 561–563 (2006).
38. Osawa, E. Recent progress and perspectives in single-digit nanodiamond. *Diam. Relat. Mater.* **16**, 2018–2022 (2007).
39. Ozawa, M. *et al.* Preparation and behavior of brownish, clear nanodiamond colloids. *Adv. Mater.* **19**, 1201–1206 (2007).

40. Liang, Y., Ozawa, M. & Krueger, A. A general procedure to functionalize agglomerating nanoparticles demonstrated on nanodiamond. *ACS Nano* **3**, 2288–2296 (2009).
41. Turcheniuk, K., Trecuzzi, C., Deelepojananan, C. & Mochalin, V. N. Salt-Assisted Ultrasonic Deaggregation of Nanodiamond. *ACS Appl. Mater. Interfaces* **8**, 25461–25468 (2016).
42. Kurkin, T. S. *et al.* Structure of oriented fibers based on poly(vinyl alcohol) modified by detonation nanodiamonds. *Polym. Sci. - Ser. A* **50**, 43–50 (2008).
43. Maitra, U., Prasad, K. E., Ramamurty, U. & Rao, C. N. R. Mechanical properties of nanodiamond-reinforced polymer-matrix composites. *Solid State Commun.* **149**, 1693–1697 (2009).
44. Morimune, S., Kotera, M., Nishino, T., Goto, K. & Hata, K. Poly (vinyl alcohol) Nanocomposites with Nanodiamond. 4415–4421 (2011).
45. Protopapa, P., Kontonasaki, E., Bikiaris, D., Paraskevopoulos, K. M. & Koidis, P. Reinforcement of a PMMA resin for fixed interim prostheses with nanodiamonds. *Dent. Mater. J.* **30**, 222–231 (2011).
46. Jee, A. Y. & Lee, M. Mechanical properties of Polycarbonate and Poly(Methyl Methacrylate) Films Reinforced with Surface-Functionalized Nanodiamonds.pdf. (2011).
47. Zhao, Y. Q. *et al.* Nanodiamond/poly (lactic acid) nanocomposites: Effect of nanodiamond on structure and properties of poly (lactic acid). *Compos. Part B Eng.* **41**, 646–653 (2010).
48. Zhang, Q. *et al.* Fluorescent PLLA-nanodiamond composites for bone tissue engineering. *Biomaterials* **32**, 87–94 (2011).

49. Zhang, Q. *et al.* Mechanical properties and biomineralization of multifunctional nanodiamond-PLLA composites for bone tissue engineering. *Biomaterials* **33**, 5067–5075 (2012).
50. Branson, B. T., Seif, M. A., Davidson, J. L. & Lukehart, C. M. Fabrication and macro/nanoscale characterization of aggregated and highly de-aggregated nanodiamond/polyacrylonitrile composite thick films. *J. Mater. Chem.* **21**, 18832 (2011).
51. Jee, A. Y. & Lee, M. Thermal and mechanical properties of alkyl-functionalized nanodiamond composites. *Curr. Appl. Phys.* **11**, 1183–1187 (2011).
52. Roumeli, E. *et al.* Factors controlling the enhanced mechanical and thermal properties of nanodiamond-reinforced cross-linked high density polyethylene. *J. Phys. Chem. B* **118**, 11341–52 (2014).
53. Saito, T. & Isogai, A. TEMPO-mediated oxidation of native cellulose. The effect of oxidation conditions on chemical and crystal structures of the water-insoluble fractions. *Biomacromolecules* **5**, 1983–1989 (2004).
54. Burns, N. a., Naclerio, M. a., Khan, S. a., Shojaei, A. & Raghavan, S. R. Nanodiamond gels in nonpolar media: Colloidal and rheological properties. *J. Rheol. (N. Y. N. Y.)* **58**, 1599–1614 (2014).
55. Fox, H. W. & Zisman, W. A. The Spreading of Liquids on Low-Energy Surfaces. III. Hydrocarbon Surfaces. (1952).
56. Fowkes, F. M. Additivity of Intermolecular Forces At Interfaces. I. Determination of the Contribution To Surface and Interfacial Tensions of Dispersion Forces in Various Liquids¹. *J.phys.chem* **67**, 2538–2541 (1963).
57. Owens, D. K. & Wendt, R. C. Estimation of the surface free energy of polymers. *J.*

- Appl. Polym. Sci.* **13**, 1741–1747 (1969).
58. Van Oss, C. J., Good, R., Chaudhury, M. & Oss, C. Additive and nonadditive surface tension components and the interpretation of contact angles. *Langmuir* **4**, 884–891 (1988).
 59. Neumann, A. W., Good, R. J., Hope, C. J. & Sejpal, M. An equation-of-state approach to determine surface tensions of low-energy solids from contact angles. *J. Colloid Interface Sci.* **49**, 291–304 (1974).
 60. Spelt, J. K., Absolom, D. R. & Neumann, A. W. Solid surface tension: The Interpretation of Contact Angles by the Equation of State Approach and the Theory of Surface Tension Components. *Langmuir* **3**, 620–625 (1986).
 61. Spelt, J. K. & Neumann, a. W. Solid surface tension: the equation of state approach and the theory of surface tension components. Theoretical and conceptual considerations. *Langmuir* **3**, 588–591 (1987).
 62. Graf, K. & Riegler, H. Is there a general equation of state approach for interfacial tensions? *Langmuir* **16**, 5187–5191 (2000).
 63. Lee, L. H. Scope and limitations of the equation of state approach for interfacial tensions. *Langmuir* **9**, 1898–1905 (1993).
 64. Lander, L. M., Siewierski, L. M., Brittain, W. J. & Vogler, E. A. A systematic comparison of contact angle methods. *Langmuir* **9**, 2237–2239 (1993).
 65. Tretinnikov, O. N. & Ikada, Y. Dynamic Wetting and Contact Angle Hysteresis of Polymer Surfaces Studied with the Modified Wilhelmy Balance Method. *Langmuir* **10**, 1606–1614 (1994).
 66. Erbil, H. Y., McHale, G., Rowan, S. M. & Newton, M. I. Determination of the Receding Contact Angle of Sessile Drops on Polymer Surfaces by Evaporation.

Langmuir **15**, 7378–7385 (1999).

67. Bormashenko, E. *et al.* Contact angle hysteresis on polymer substrates established with various experimental techniques, its interpretation, and quantitative characterization. *Langmuir* **24**, 4020–4025 (2008).
68. Kozbial, A. *et al.* Study on the surface energy of graphene by contact angle measurements. *Langmuir* **30**, 8598–8606 (2014).
69. Wang, S., Zhang, Y., Abidi, N. & Cabrales, L. Wettability and surface free energy of graphene films. *Langmuir* **25**, 11078–11081 (2009).
70. Notley, S. M. & Norgren, M. Surface energy and wettability of spin-coated thin films of lignin isolated from wood. *Langmuir* **26**, 5484–5490 (2010).
71. Khoshkava, V. & Kamal, M. R. Effect of surface energy on dispersion and mechanical properties of polymer/nanocrystalline cellulose nanocomposites. *Biomacromolecules* **14**, 3155–3163 (2013).
72. Chibowski, E. & Holysz, L. Use of the Washburn Equation for Surface Free Energy Determination. *Langmuir* **8**, 710–716 (1992).
73. Ji, L. & Shi, B. A novel method for determining surface free energy of powders using Washburn's equation without calculating capillary factor and contact angle. *Powder Technol.* **271**, 88–92 (2015).
74. Paunov, V. N. Novel method for determining the three-phase contact angle of colloid particles adsorbed at air-water and oil-water interfaces. *Langmuir* **19**, 7970–7976 (2003).
75. Grimsey, I. M., Feeley, J. C. & York, P. Analysis of the surface energy of pharmaceutical powders by inverse gas chromatography. *J. Pharm. Sci.* **91**, 571–583 (2002).

76. Fox, D. M. *et al.* Simultaneously Tailoring Surface Energies and Thermal Stabilities of Cellulose Nanocrystals Using Ion Exchange: Effects on Polymer Composite Properties for Transportation, Infrastructure, and Renewable Energy Applications. *ACS Appl. Mater. Interfaces* **8**, 27270–27281 (2016).
77. Peng, Y., Gardner, D. J., Han, Y., Cai, Z. & Tshabalala, M. A. Influence of drying method on the surface energy of cellulose nanofibrils determined by inverse gas chromatography. *J. Colloid Interface Sci.* **405**, 85–95 (2013).
78. Barber, A. H., Cohen, S. R. & Daniel Wagner, H. Static and dynamic wetting measurements of single carbon nanotubes. *Phys. Rev. Lett.* **92**, 186103–1 (2004).
79. Stockelhuber, K. W., Das, A., Jurk, R. & Heinrich, G. Contribution of physico-chemical properties of interfaces on dispersibility, adhesion and flocculation of filler particles in rubber. *Polymer (Guildf)*. **51**, 1954–1963 (2010).
80. Natarajan, B., Li, Y., Deng, H., Brinson, L. C. & Schadler, L. S. Effect of interfacial energetics on dispersion and glass transition temperature in polymer nanocomposites. *Macromolecules* **46**, 2833–2841 (2013).
81. Ramanathan, T. *et al.* Functionalized graphene sheets for polymer nanocomposites. *Nat. Nanotechnol.* **3**, 327–331 (2008).
82. Chen, F. *et al.* Glass transition temperature of polymer-nanoparticle composites: Effect of polymer-particle interfacial energy. *Macromolecules* **46**, 4663–4669 (2013).
83. Liao, K. H., Aoyama, S., Abdala, A. A. & Macosko, C. Does graphene change T_g of nanocomposites? *Macromolecules* **47**, 8311–8319 (2014).
84. Zare, Y. ‘a’ interfacial parameter in Nicolais-Narkis model for yield strength of polymer particulate nanocomposites as a function of material and interphase properties. *J. Colloid Interface Sci.* **470**, 245–249 (2016).

85. Lazzeri, A. & Phuong, V. T. Dependence of the Pukánszky's interaction parameter B on the interface shear strength (IFSS) of nanofiller- and short fiber-reinforced polymer composites. *Compos. Sci. Technol.* **93**, 106–113 (2014).

Chapter 5 Conclusions and Future Outlook

5.1 Conclusions

In this dissertation, we successfully designed new multicomponent systems in the form of copolymers as surface coatings for protein capture, modulated gelation kinetics and mechanical strength of photocrosslinkable polymer via network formation using cellulose nanocrystals and investigated the interfacial aspects of polymeric systems consisting of nanodiamonds in electrospun fibers of either semi-crystalline or amorphous polymers with different surface energies to create fundamental knowledge on their structure-property-function relationships. The main conclusions of each chapter are as follows:

Chapter 2. Modification of model polyester thin films and nonwoven fabrics for protein immobilization is desirable in applications such as wastewater purification and biofiltration, yet challenging due to lack of reactive functional groups, thus limiting their possibility for protein binding. In this Chapter, polyester was successfully modified with trimethyl cellulose followed by vapor-phase acid-hydrolysis, which generated reactive hydroxyl groups. This facilitated grafting of random hydrophilic copolymers of poly (sodium vinyl benzene sulfonate-co-hydroxyethyl methacrylate) (poly(SVBS-co-HEMA)) using activator re-generated by electron transfer (ARGET) atom-transfer radical polymerization (ATRP). The copolymer architecture was studied for enhanced protein capture and release. It was found that PBT surfaces modified with the poly(SVBS-co-HEMA) adsorbed significant amounts of model proteins and a maximum binding was found for a copolymer with dominant HEMA composition (20% SVBS and 80% HEMA or 2:8 poly(SVBS-co-HEMA)). Such system was regenerated after protein adsorption by introducing electrolyte solutions, as

shown in quartz-crystal microgravimetry experiments that also unveiled details about the dynamics of adsorption (capture) and regeneration (protein release). The adsorption of representative proteins – lysozyme, fibrinogen and bovine serum albumin (BSA) – depended on the pH of the aqueous matrix, with fibrinogen and BSA adsorbing on the ‘wrong side’ of the isoelectric point under electrostatically repulsive conditions. Such adsorption behavior was interpreted in terms of the balance of protein-surface and protein-protein interactions. The modified polyester represents an attractive alternative for imparting protein-adsorption functionality toward advanced separations.

Chapter 3. Weak mechanical performance associated with photocrosslinkable polymer necessitates strategies to reinforce their mechanical properties. In this Chapter, a simple technique using cellulose nanocrystals (CNC’s) that induces favorable electrostatic interactions was used to modulate the crosslinking kinetics as well as to enhance the mechanical performance of aqueous photoactive polyvinyl alcohol derivative, poly (vinyl alcohol), N-methyl-4 (4’-formylstyryl) pyridinium methosulfate acetal (PVA-SbQ). The resulting changes in the rheological behavior of PVA-SbQ were studied before and after exposure to UV at a fixed intensity of 10 mW/cm². Steady-shear rheological measurements of PVA-SbQ showed characteristics similar to neutral polymers and entanglement at ~4.8 wt.%. Low concentration CNC rheology, combined with Simha’s equation for non-spherical particles, revealed an aspect ratio of ~27. The presence of low concentration CNC in aqueous solutions of PVA-SbQ (6 wt.%) showed Newtonian behavior, with visible deviations arising at concentrations around 1.5 wt.%, showing non-linear behavior with yield stresses as the interactions between PVA-SbQ and CNC present in dispersions prepared using simple

solution mixing facilitated network formation. The inclusion of CNC's above a critical threshold concentration between 1-1.5 wt.% formed a percolated CNC network before UV-exposure, further corroborated using Van Gorp Palmen and Cole-Cole plots used as signatures for percolation. The structure build-up after UV exposure studied using in-situ dynamic photo-crosslinking experiments revealed alterations in gelation kinetics and mechanical strength of neat systems. The crossover times of storage (G') and loss moduli (G'') increased with CNC's less than 1.5 wt.% but dramatically reduced above 1.5 wt.%. A steep jump in the storage modulus of fully-crosslinked networks representative of percolation with critical threshold concentration (~ 1.4 wt.%) as well as $\sim 131\%$ increase in storage modulus (G') at 2.5 wt.% CNC was observed. The results point to the existence of microstructural changes wherein the polymer-CNC interactions induced a percolated microstructure that allows efficient stress transfer. The induced percolation mechanism can be utilized in the design of photocrosslinkable systems for applications requiring mechanical reinforcement.

Chapter 4. Nanodiamonds (ND's) have emerged as a novel class of nanofillers, however, the propensity of ND's to aggregate in solution as well as in polymers presents significant challenges during processing of ND-based fibers composites. As such, understanding the interfacial energetics associated with polymer-ND composites to promote dispersion and enhance ND-polymer wetting at the nanoscale is an essential prerequisite in designing polymer-ND composite fibers with reinforced mechanical properties. While macroscopic property reinforcements using nanodiamonds (ND's) in polymer-nanodiamond composites (PNC) have been extensively studied, not much is known about the relationship

between polymer-ND interfacial energy parameters, polymer-ND interactions and final mechanical properties in ND-reinforced electrospun fibers. In this Chapter, surface-energy dependent parameters such as wettability, work of spreading, and work of dispersion-aggregation transition of ND's were used to derive a criterion for dispersion (D_c) as a hypothesized predictor of polymer-ND interactions and final tensile strength in electrospun poly (vinyl) alcohol (PVA), polyacrylonitrile (PAN), and polystyrene (PS). We found that shifts in glass transition temperature (ΔT_g), used as a measure of polymer-ND interactions, showed a direct correlation with D_c in the order of PVA > PS > PAN regardless of amorphous or semi-crystalline nature of the polymer. However, the final tensile strength showed a direct correlation with D_c and ΔT_g for semi-crystalline polymers only, with amorphous polystyrene showing maximum reinforcement contrary to predictions made by ΔT_g , suggesting the additional role of polymer morphology to final tensile strength. The findings of this study could offer additional insight into the design of interfaces for polymer-ND fiber composites.

5.2 Future Work and Recommendations

The following sections discuss some key ideas that can be explored as part of future work and highlight some limitations associated with current approaches if applicable. The recommendations can be used as a starting point for designing systems with better functionality.

5.2.1 Photoinduced Grafting of Copolymer on Nonwoven Fabrics

While successful implementation of a facile cellulose chemistry to impart protein capture functionality was demonstrated in Chapter 2, the proposed approach can be further

improved by using copolymers that make the system more versatile by using industrially scalable techniques, introducing ‘dry’ measurement techniques, and by establishing comparisons to benchmarks in the industry. The poly(SVBS-co-HEMA) copolymer shown in **Figure 2.1** was specifically designed to study protein adsorption using lysozyme as a model protein. The high isoelectric point of lysozyme (pH 11), which implies a net positive charge for pH values less than 11, facilitates adsorption on negatively charged surfaces due to favorable electrostatic conditions. However, this particular chemistry is not robust enough to ensure high adsorption capacity for proteins under unfavorable electrostatic conditions such as bovine serum albumin (BSA) at pH 7.4, which is used as the ‘gold standard’ in the industry for comparing different protein-capture systems. In addition, surface-initiated polymerization technique which is ‘grafting from’ technique utilized herein is not ideal to maximize protein adsorption since it forms surfaces with high grafting density, that eliminates primary and secondary modes of protein adsorption. Also, the polymerization technique is not scalable for industrial production primarily due to large amounts of copper involved in the atom transfer radical polymerization (ATRP) process. The limitations in the current approach, therefore, need to be addressed to develop nonwoven fabrics with high non-specific BSA capture efficiency using controllable surface chemistries involving scalable and robust grafting techniques capable of reducing time and cost of scale-up technology. Therefore, better chemistry and scalable approaches are necessary for the design of robust coatings for protein adsorption.

The most viable approach to tackling the problem is to devise a system that is capable of non-specific protein capture via ‘grafting to’ technique by using pre-made copolymers

capable of capturing proteins via electrostatic as well as hydrophobic interactions. The most suitable end functionalities that will impart electrostatic and hydrophobic properties necessary for protein adsorption are shown in Figure 5.1. The motivation for using sulfonated functionality (SO_3^-) in the form of (poly (3-sulfopropyl methacrylate) (3-PSPMA)) comes from results reported in Chapter 2 showing adsorption of ~ 10 mg lysozyme per gram of PBT nonwoven via electrostatic interactions. Similarly, the presence of a positive charge in the quaternary structure in quaternized poly (dimethylaminoethyl) methacrylate will facilitate adsorption of negatively charged protein such as BSA at pH 7.4. In addition, the presence of permanent charge in the system will make the system pH independent and highly versatile. Finally, the alkyl chain in poly (butyl methacrylate) (PBMA) will facilitate protein adsorption via hydrophobic interactions. Figure 5.2a shows proposed route of synthesis and grafting of copolymer onto nonwoven substrate. Free-radical copolymerization is used to make copolymers with varying compositions and attached to the substrate in the presence of benzophenone and UV light as shown in Figure 5.2b. Benzophenone in the presence of UV abstracts a hydrogen atom from the polymer as well as the substrate as shown in Figure 5.2c, forming a dense crosslinked network.¹

Some preliminary results on the synthesis and characterization of P(DMAEMA-co-BMA) copolymer, as well as on UV-induced surface grafting of copolymer using benzophenone on PBT nonwovens are reported.

5.2.1.1 Materials and Methods

PBT nonwoven with a basis weight of 20 g/m^2 manufactured using meltblown technology was provided by Nonwovens Institute (NCSU, Raleigh). 2-(Dimethylamino)

ethyl methacrylate (DMAEMA, containing 700-1000 ppm monomethyl ether hydroquinone as inhibitor, 98%) and butyl methacrylate (BMA, 99%, containing 10 ppm monomethyl ether hydroquinone as inhibitor) were purchased from Sigma-Aldrich (Allentown, PA). Inhibitors in the monomers, DMAEMA and BMA, were removed using a pre-packed inhibitor column removal purchased from Sigma Aldrich prior to use (Allentown, PA). 2,2'-Azobis (2-methylpropionitrile) (AIBN), Toluene (anhydrous, 99.8%), dimethylacetamide, tetrahydrofuran (anhydrous, >99.9%, inhibitor-free), dichloromethane (HPLC grade, 99.9%), methanol (anhydrous, 99.8%), petroleum ether, hexanes (anhydrous, 95%) and benzophenone were purchased from Sigma Aldrich and used as received.

A stock solution of AIBN was first prepared by dissolving re-crystallized AIBN (3.12 mg/ml) in toluene for 30 minutes. In a schlenk flask, thoroughly rinsed with acetone and dried in an oven, AIBN (620 μ l) was added followed by monomers DMAEMA (1.3 ml) and BMA (1.3 ml) to prepare 50:50 poly (BMA-co-DMAEMA). Following initiator and monomer addition, reaction solvent toluene was added to flask slowly washing the contents on the sides of the flask. Next, three freeze-pump-thaw cycles were performed to conduct the reaction in an inert atmosphere. In a typical cycle, the contents of the flask were immersed in liquid nitrogen until the contents were frozen, followed by pulling vacuum. The frozen contents of the flask were then immersed in a crystallization dish containing tap water until all the contents were completely thawed. Following three freeze-pump-thaw cycles, free-radical polymerization reaction was carried out for 20 hours at 75°C. At the end of 20 hours, the solvent was removed using Rotovap at 60°C and pressures <100 mbar, until most of the toluene was removed. The remaining viscous product with trace amounts of toluene was re-

dissolved in THF and the dissolved solution was added drop-wise to ~90 ml petroleum ether. Precipitation in petroleum ether resulted in a bright white-colored product, which was re-dissolved in minimum amounts of THF and precipitated again. The choice of product dissolution and precipitation solvent for homopolymers, and copolymers of BMA and DMAEMA are listed in Table 5.1.

Fourier-transform infrared spectroscopy (FTIR) spectra of poly (BMA), 1:1 poly (BMA-co-DMAEMA) and poly (DMAEMA) were performed using Thermo Nicolet iN10 infrared microscope operating in the range 4000-500 cm^{-1} range. Samples were prepared by mixing ~5 mg of polymer with ~495 mg potassium bromide (KBr) to form a pellet. The spectra were collected using a 2 cm resolution and 64 continuous scans. The surface elemental composition of the synthesized polymers was analyzed using XPS. Data were obtained on Specs XPS (AIF, NCSU) using Mg source with energy of 1253.6 eV, and XPSPeak41 was used to calibrate C1s spectrum to 285.0 eV, determine peak areas and to calculate the elemental composition. ^1H NMR spectra of polymers were recorded on a Varian Mercury 400 spectrometer equipped with 5mm Pulse-Field Gradient (PFG) auto-switchable 4-nuclei (^1H , ^{13}C , ^{19}F , ^{31}P), operating at 400 MHz. Samples were prepared by dissolving ~5 mg of polymers in 0.5 ml of deuterated solvent and chemical shifts were recorded in ppm.

PBT nonwoven fabrics were thoroughly rinsed with methanol and dried at 40°C before use. Then, the fabrics were cut into 1 cm by 1 cm and pre-weighed samples were dipped into a solution of methanol to increase wettability. Thereafter, the samples were immersed in 0.01 wt.% benzophenone (BP) solutions in toluene and completely soaked for 10 seconds followed by drying with nitrogen. Samples soaked in benzophenone were placed

in a petri dish and was exposed to UV light with a wavelength at 365 nm and intensity varying between 10-30 mW/cm². The distance between nonwoven samples and UV light was kept constant at around 5 mm, and the reaction was carried out for times ranging between 10-30 minutes. After the reaction, the nonwoven fabric was thoroughly rinsed in methanol to get rid of the unreacted polymer solution and allowed to dry in vacuum at 40° overnight. The nonwoven fabrics were then weighed to calculate the degree of copolymer grafting using the expression shown in Equation (1).

$$\text{Degree of Copolymer Grafting} = \left(\frac{W_f - W_i}{W_i} \right) \times 100 \% \quad (1)$$

Here, W_i is the initial weight of PBT nonwoven and W_f is the final weight of PBT nonwoven after co-polymer grafting.

The effect of benzophenone-induced polymer/copolymer attachment on the morphology of PBT nonwovens fabrics was studied using field emission scanning electron microscopy (FEI Verios 460L). Samples (1 cm by 1 cm) cut from polymer-grafted nonwoven mats and fixed on a carbon tape mounted on a stub before applying a gold-palladium (Au-Pd) coating of ~7 nm using a sputter-coating unit. Imaging of coated fabrics was done using an accelerating voltage of 5 kV and a working distance of 6 mm.

5.2.1.2 Results and Discussion

Homopolymers of PBMA and PDMAEMA and copolymers of 1:1 and 3:1 P(BMA-co-DMAEMA) were synthesized using free-radical copolymerization in toluene at 75°C. PBMA and PDMAEMA homopolymers were obtained by direct precipitation in cold methanol and hexanes respectively, and 1:1 P(BMA-co-DMAEMA) product was obtained after direct precipitation in cold petroleum ether. Precipitation solvents were chosen based on

visual appearance of the color of the precipitate. In the case of 3:1 P(BMA-co-DMAEMA), no suitable solvent was found that could precipitate the copolymer out of solution; therefore, any relevant characterization was performed in toluene solution (see Table 5.1). The functional groups on the synthesized polymer were characterized using FTIR as shown in Figure 5.3, which contains spectra of homopolymers PBMA, PDMAEMA and 1:1 copolymer of P(BMA-co-DMAEMA). For all polymers, well-defined bands at $\sim 1730\text{ cm}^{-1}$ attributed to the stretching of C=O groups, distinct bands between 1150 cm^{-1} to 1250 cm^{-1} due to C-O-C stretching, bands at $\sim 2997\text{ cm}^{-1}$ and 2950 cm^{-1} due to stretching vibration of C-H in CH_3 and CH_2 respectively, as well as adsorption bands between 3100 cm^{-1} to 3700 cm^{-1} and $\sim 1640\text{ cm}^{-1}$ attributed to stretching and bending vibrations of -OH bonds due to adsorbed moisture are visible. The two sharp bands at $\sim 2800\text{ cm}^{-1}$ and 2770 cm^{-1} due to the presence of -N(CH₃)₂ for PDMAEMA, which is absent from PBMA, clearly shows that the synthesized macromolecule is PDMAEMA. The distinct feature corresponding to -N(CH₃)₂ in PDMAEMA which is absent in PBMA, appears in the spectra for 1:1 P(BMA-co-DMAEMA), but at much lower intensity suggesting the presence of smaller amounts of DMAEMA in the copolymer.

The chemical structures of PBMA, PDMAEMA, and 1:1 P(BMA-co-DMAEMA) were also verified using ¹H NMR spectroscopy, which shows distinct proton signals due to unique proton environments along the polymer backbone as shown in Figure 5.4. The characteristic signal corresponding to (-O-CH₂) for PBMA, labeled H₂ is observed at 3.89 ppm, distinguishes itself from characteristic signal corresponding to (-O-CH₂) for PDMAEMA labeled H'₂ observed at 4.02 ppm. Both experimental chemical shifts for H₂

environments are close to the predicted theoretical shifts, which correspond to 4.0 ppm and 4.2 ppm for PBMA and PDMAEMA respectively. The characteristic peak separating PBMA and PDMAEMA, however, is proton labeled H_3 and H'_3 which is present in PDMAEMA at much higher chemical shifts (~ 2.54 ppm) compared to PBMA at 1.58 ppm. The signal corresponding to $(-CH_2)$ in PBMA at ~ 1.36 ppm (H_4) is also distinct relative to PDMAEMA with signals corresponding to $(-CH_3)$ occurring at 2.54 ppm. For homopolymer 1:1 P(BMA-co-DMAEMA), proton environments corresponding to PDMAEMA (H'_2 , H'_3 , and H'_4) missing in bulk PBMA, and proton environments corresponding to PBMA (H_2 , H_3 , and H_4) missing in bulk PDMAEMA, both appear suggesting the presence of both PBMA and PDMAEMA in the copolymer. In addition, the chemical composition of PBMA, PDMAEMA, 1:1 P(BMA-co-DMAEMA) and 3:1 (PBMA-co-DMAEMA) synthesized in this work was assessed by XPS. Survey scans for each polymer are shown in Figure 5.5, and theoretical values, calculated using the number of carbon, oxygen and nitrogen atoms on a repeat unit of a polymer backbone, and experimental values atomic content are listed in Table 5.2. Survey scans for all polymers reveal combinations of ionization peaks for carbon at 285 eV, nitrogen at 398 eV and oxygen at 531 eV and nitrogen. The corresponding atomic content for PBMA is 77.2 % carbon and 22.8 % oxygen, which compares very well to theoretical values. Similar conclusions are made for 1:1 P(BMA-co-DMAEMA) with 70.9 % carbon, 23.2 % oxygen and 4.5 % nitrogen, 3:1 P(BMA-co-DMAEMA) with 76.8 % carbon, 22.2 % oxygen and 1.05 % nitrogen, and PDMAEMA with 70.1 % carbon, 20.5 % oxygen and 2.9 % nitrogen obtained using XPS, closely matching theoretical predictions. All the evidence combined suggests successful synthesis of polymers and copolymers of interest for protein

adsorption.

Next, the synthesized polymers were grafted onto PBT nonwoven fabrics in the presence of benzophenone. Briefly, pre-cut and cleaned fabrics were immersed for 2 minutes in THF containing 100 mg/ml of the polymer of interest and 10 wt.% BP and were exposed to UV light with intensities ranging between 10-30 mW/cm² for 5 minutes. XPS spectra of pristine PBT and PBT grafted with copolymers shown in Figure 5.6 reveal changes in elemental composition relative to PBT after copolymer grafting. PBT shows carbon content of 74.2% and oxygen content of 25.8%, which is close to theoretical values corresponding to 75% for carbon and 25% for oxygen. Grafting of PBT with PBMA changes carbon content to 79.4% and oxygen content to 20.6%. The reduction in oxygen content is due to the presence of PBMA without oxygen-containing functionalities. Further grafting of PBT with 1:1 P(BMA-co-DMAEMA) showed the presence of 2.7% nitrogen due to the presence of PDMAEMA. The surface morphology of PBT nonwoven fabrics before and after grafting of PBMA and 1:1 P(BMA-co-DMAEMA) under different UV intensity was studied using SEM and representative images are shown in Figure 5.7. Neat PBT shows a uniform, smooth surface with an average diameter of 8.1 ± 1.4 microns, open pore structure, and fused fibers. After UV induced grafting of PBMA using UV intensity of 3 J/cm², the diameter increases to 8.6 ± 2.1 microns very similar to blank PBT; however, 'web' like layers of polymers between fibers were clearly visible instead of open porous structure suggesting some compromise in the porous structure. Further grafting the same concentration of BP/PBMA at higher UV intensity 9 J/cm² validated the formation of web-like morphology. Unlike grafting of PBMA at higher UV intensity, grafting of 1:1 P(BMA-co-DMAEMA) under same conditions did not

yield morphology with web-like structures, suggesting a difference in the extent of grafting of PBMA compared to 1:1 P(BMA-co-DMAEMA).

The dependence of the degree of grafting for PBMA and 1:1 P(BMA-co-DMAEMA) on the UV intensity corroborated film formation seen under SEM. As the UV intensity was increased from 3 to 9 J/cm², the degree of grafting increased from 25% to 50.3%, confirming that the web like formation was due to higher amounts of polymer grafted onto the surface. Similarly, the degree of grafting increased from 12% to 52% as UV intensity increased from 3 J/cm² to 18 J/cm² for 1:1 P(BMA-co-DMAEMA). This also confirms that higher intensity is required for 1:1 poly (BMA-co-DMAEMA) to achieve similar degrees of grafting of PBMA. However, the concentration needs to be optimized in order to protect the open structure of blank PBT nonwoven fabrics.

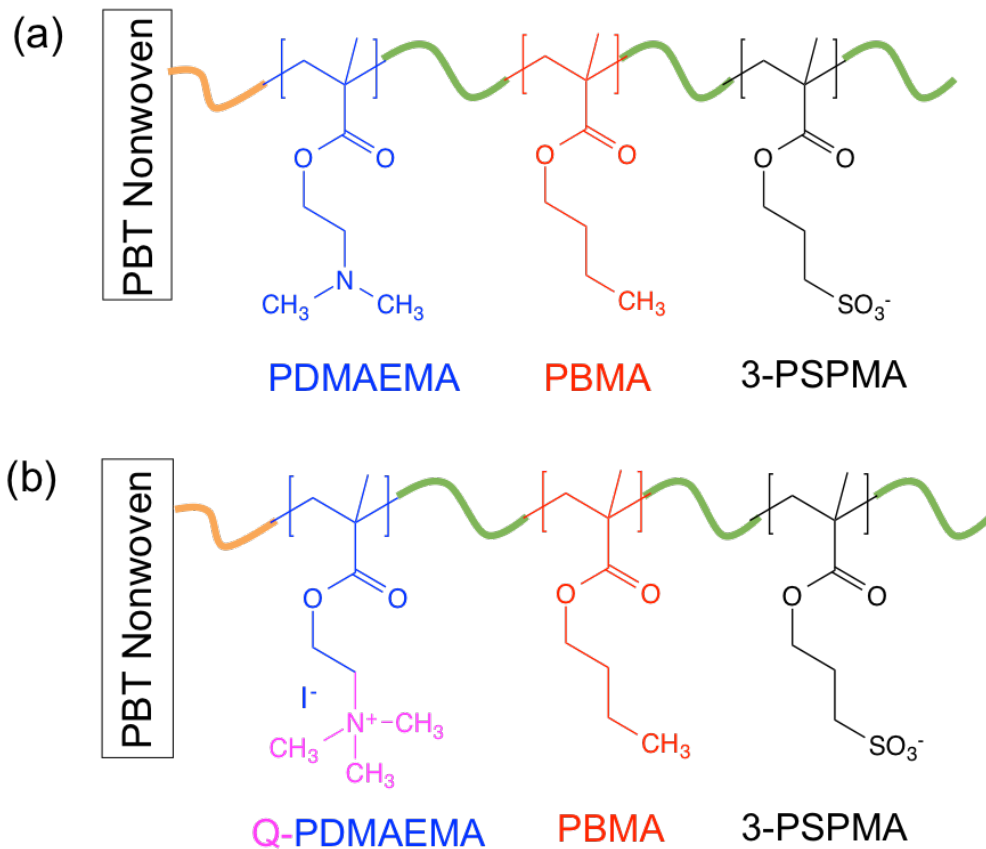


Figure 5.1 (a) Proposed chemistry for development of PBT nonwovens with high non-specific protein capture efficiency consisting of poly(2-dimethylaminoethyl methacrylate) (PDMAEMA), poly(butyl) methacrylate (PBMA) and poly(3-sulfopropyl) methacrylate, and (b) positively charged segment obtained after quaternization of PDMAEMA, which allows capture of proteins with negative charges.

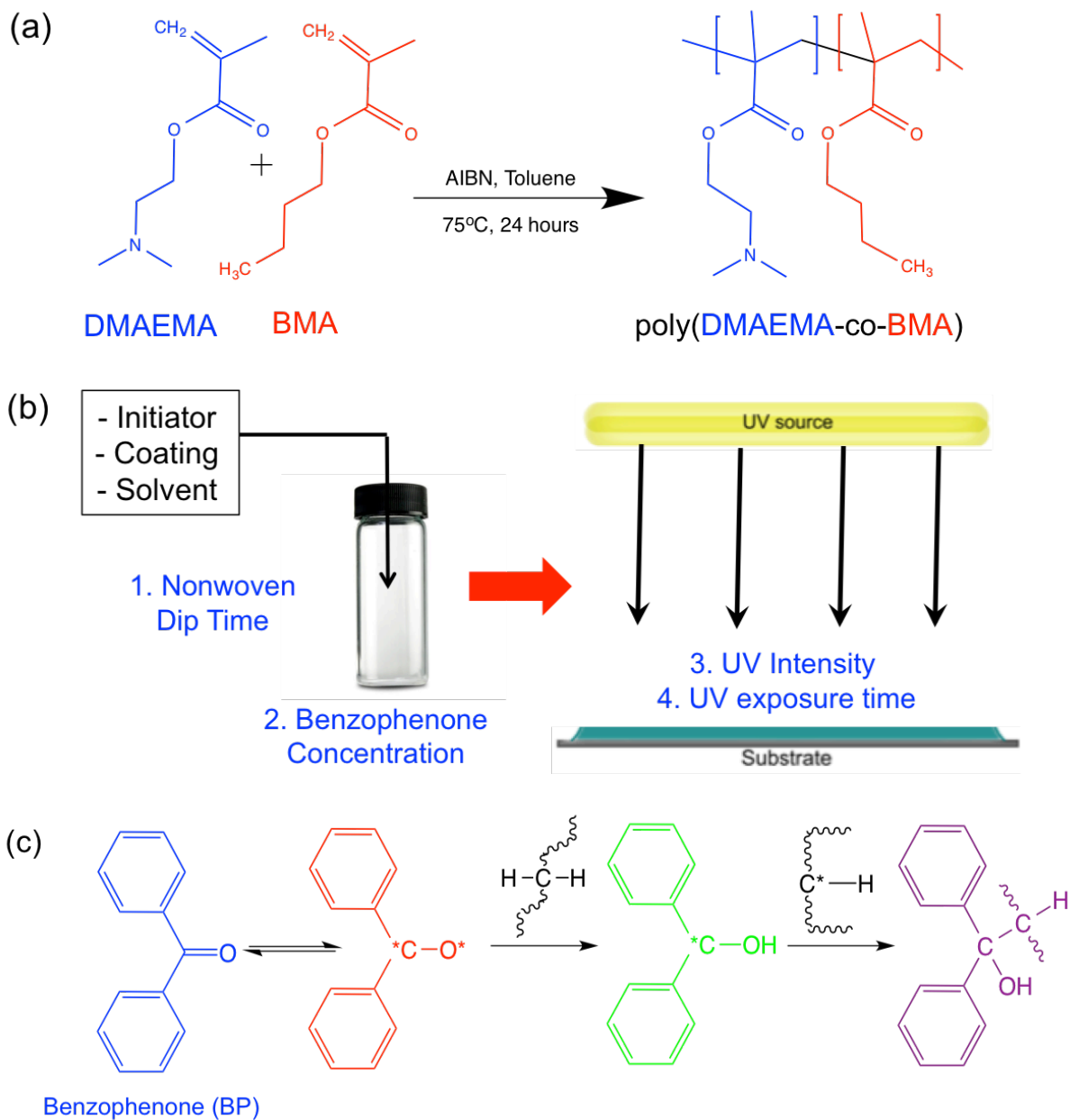


Figure 5.2 (a) Free-radical polymerization synthesis route for the fabrication of P(BMA-co-DMAEMA) copolymer using AIBN and suitable solvent at 75°C, (b) strategy for attachment of copolymer to nonwoven substrate using UV-induced crosslinking in the presence of benzophenone, and (c) mechanism of crosslinking in the presence of benzophenone, showing hydrogen abstraction from polymer and attachment to the substrate.

Table 5-1 Free-radical polymerization synthesis conditions for homopolymers and copolymers of poly (butylmethacrylate) (PBMA) and poly (dimethylaminoethyl) methacrylate (PDMAEMA) at 75°C

(Co) Polymers	Solvent	Dissolved In	Precipitated In
PBMA	Toluene	-	Cold methanol
1:1 P (BMA-co-DMAEMA)	Toluene	THF	Cold petroleum ether
3:1 P (BMA-co-DMAEMA)	Toluene	Toluene	Recovered as solution
PDMAEMA	DMAc*	Dichloromethane	Hexanes

*DMAc – dimethylacetamide

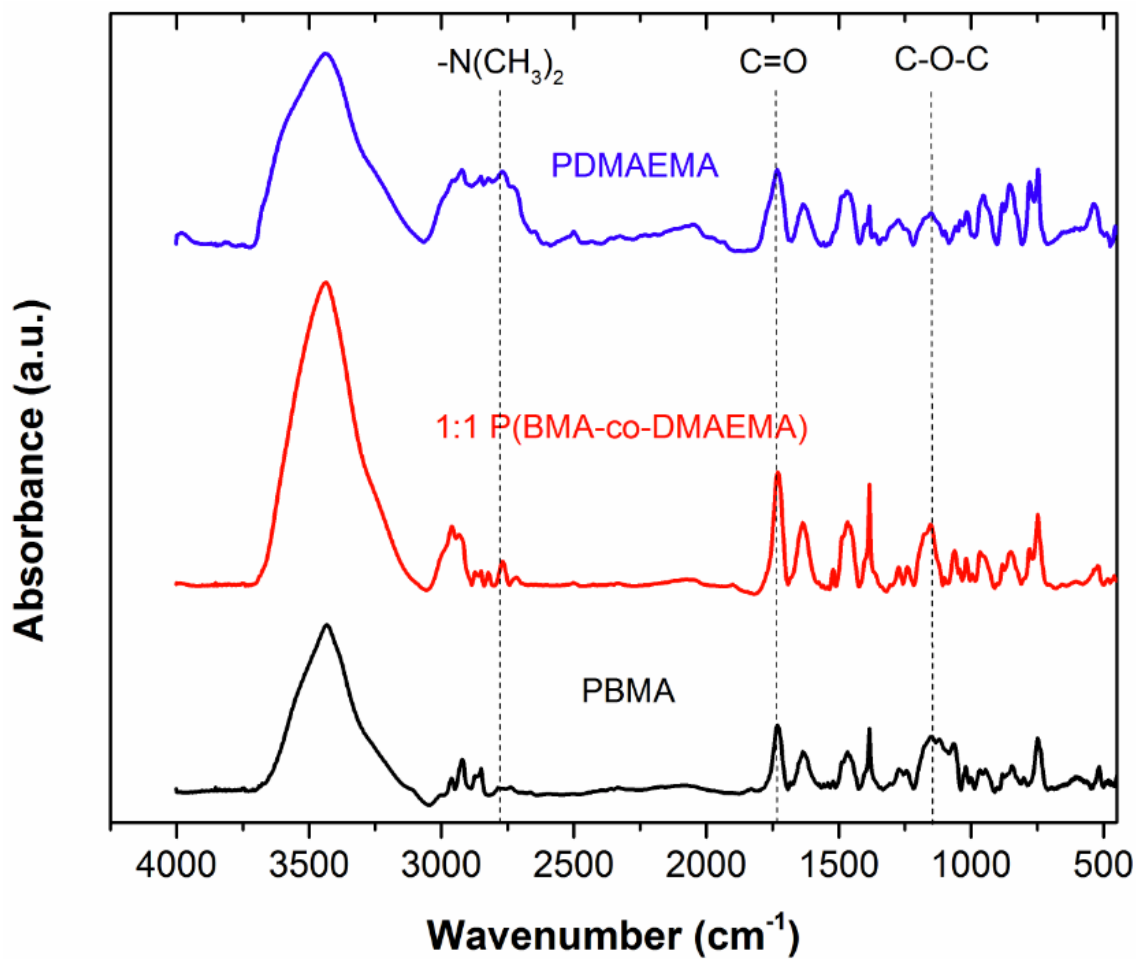


Figure 5.3 FTIR-spectra of homopolymers of PBMA, PDMAEMA and 1:1 P (BMA-co-DMAEMA) synthesized using free-radical copolymerization.

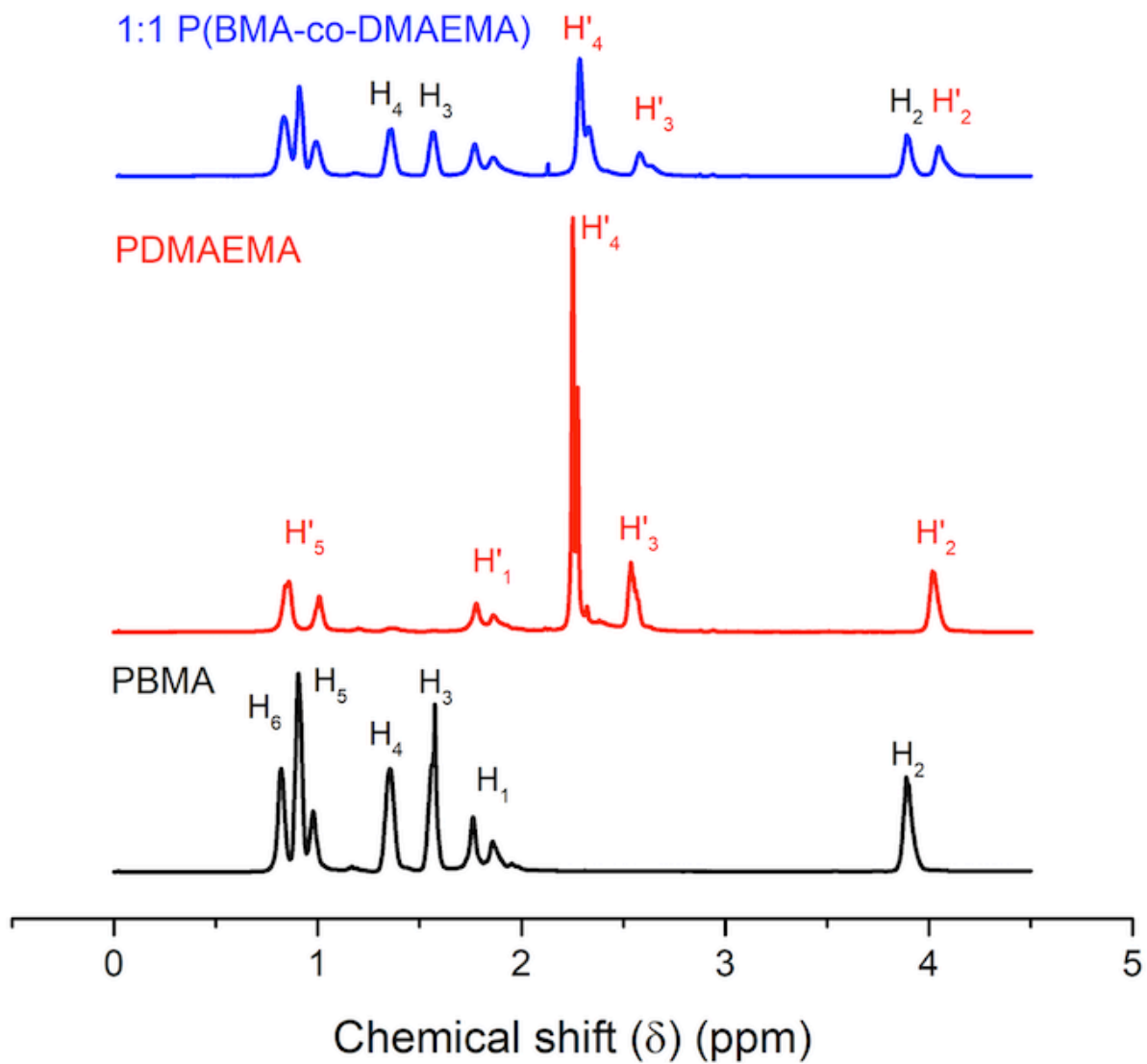


Figure 5.4 Comparison of NMR spectra of homopolymer of PBMA, PDMAEMA and 1:1 (theoretical ratio) P (BMA-co-DMAEMA) synthesized using free-radical copolymerization.

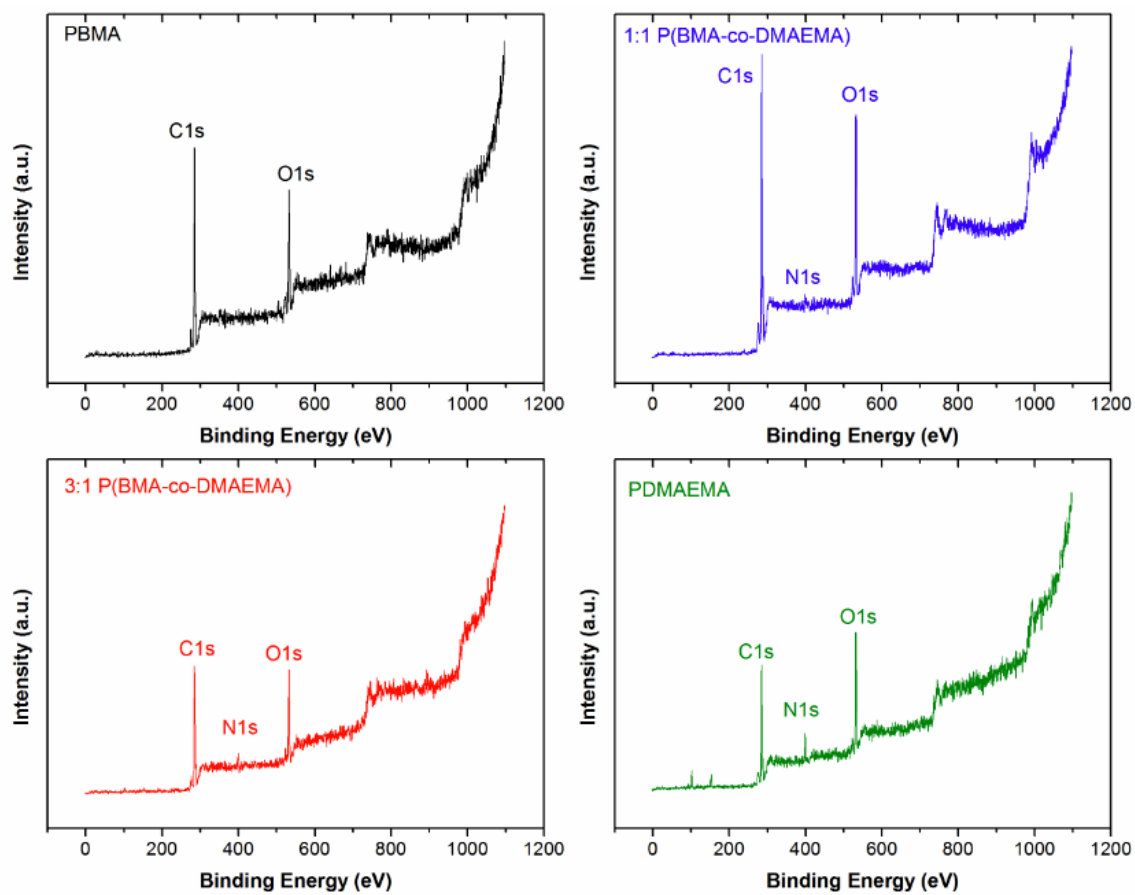


Figure 5.5 XPS-spectra of homopolymer of PBMA, PDMAEMA, 1:1 and 3:1 P(BMA-co-DMAEMA) synthesized using free-radical copolymerization.

Table 5-2 Theoretical and experimental atomic content (%) for homopolymers of PBMA and PDMAEMA, and copolymers with 1:1 and 3:1 P(BMA-co-DMAEMA).

Polymer	Theoretical Value (%)			Experimental Value (%)		
	C	O	N	C	O	N
PBMA	75	25	-	77.2	22.8	-
1:1	71.1	23.7	5.2	70.9	23.2	4.5
3:1	72.2	24.3	2.7	76.8	22.2	1.05
PDMAEMA	67.6	22.5	9.9	60.1	20.5	2.9

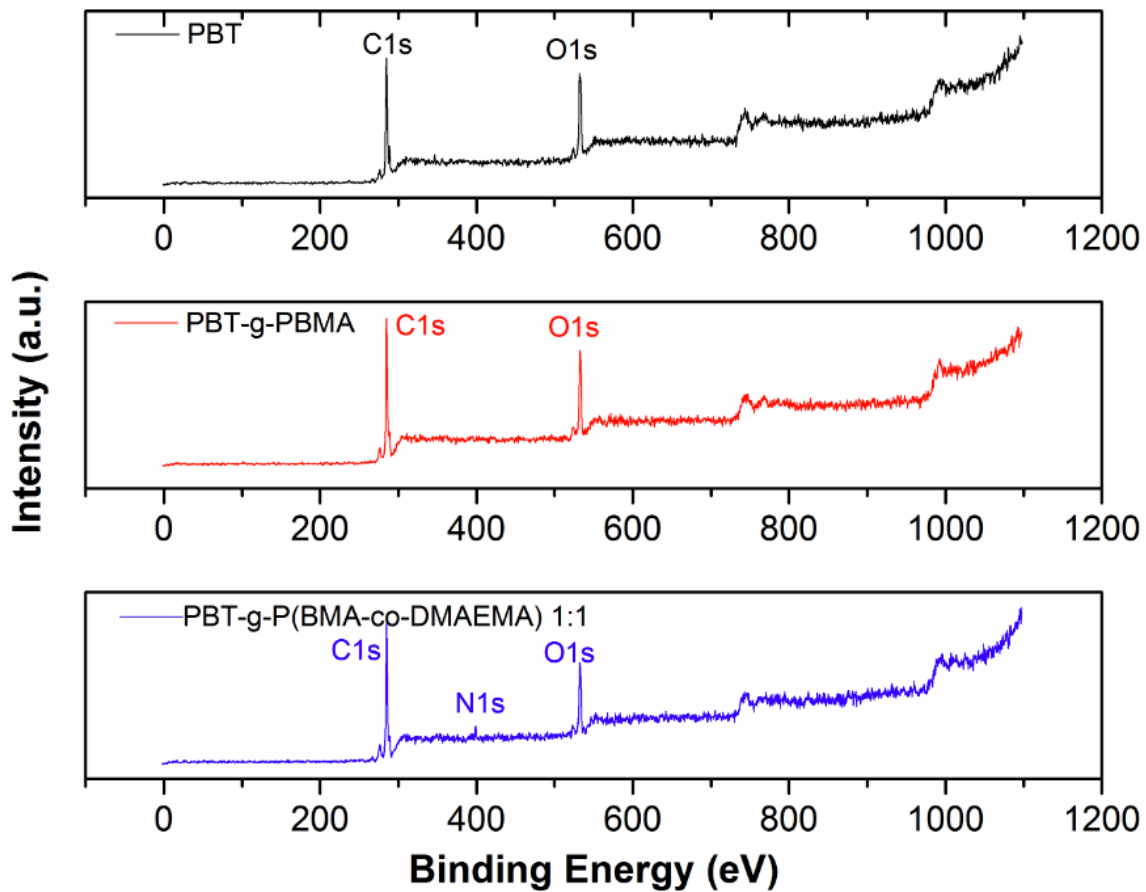


Figure 5.6 XPS-spectra of neat PBT nonwoven fabric (20 g/m² basis weight) and fabric grafted with PBMA and 1:1 P(BMA-co-DMAEMA) showing successful attachment of copolymer using UV crosslinking in the presence of benzophenone.

Table 5-3 Element content (%) of carbon, nitrogen and oxygen for PBT nonwoven fabric (as is) and nonwoven fabrics grafted with PBMA and 1:1 P(BMA-co-DMAEMA).

Substrate (Nonwoven)	C (%)	O (%)	N (%)
PBT	74.2	25.8	-
PBT-g-PBMA	79.4	20.6	-
PBT-g-P (BMA-co-DMAEMA) 1:1	78.7	18.7	2.7

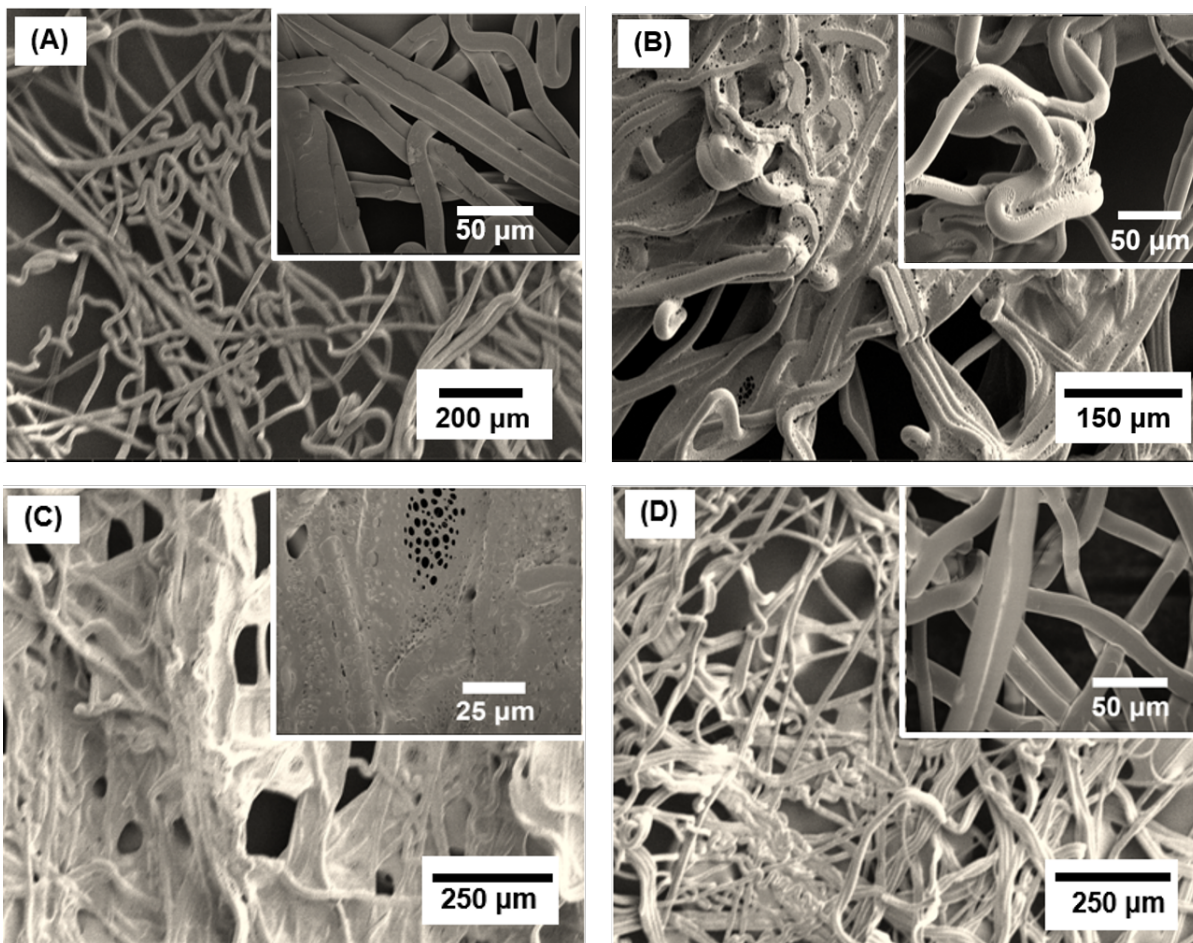


Figure 5.7 SEM images showing morphology of (A) neat PBT nonwoven fabrics, (B) grafted with PBMA using UV intensity of 3 J/cm^2 , (C) grafted with PBMA using UV intensity of 9 J/cm^2 , and (D) grafted with 1:1 P(BMA-co-DMAEMA) using UV intensity of 9 J/cm^2 .

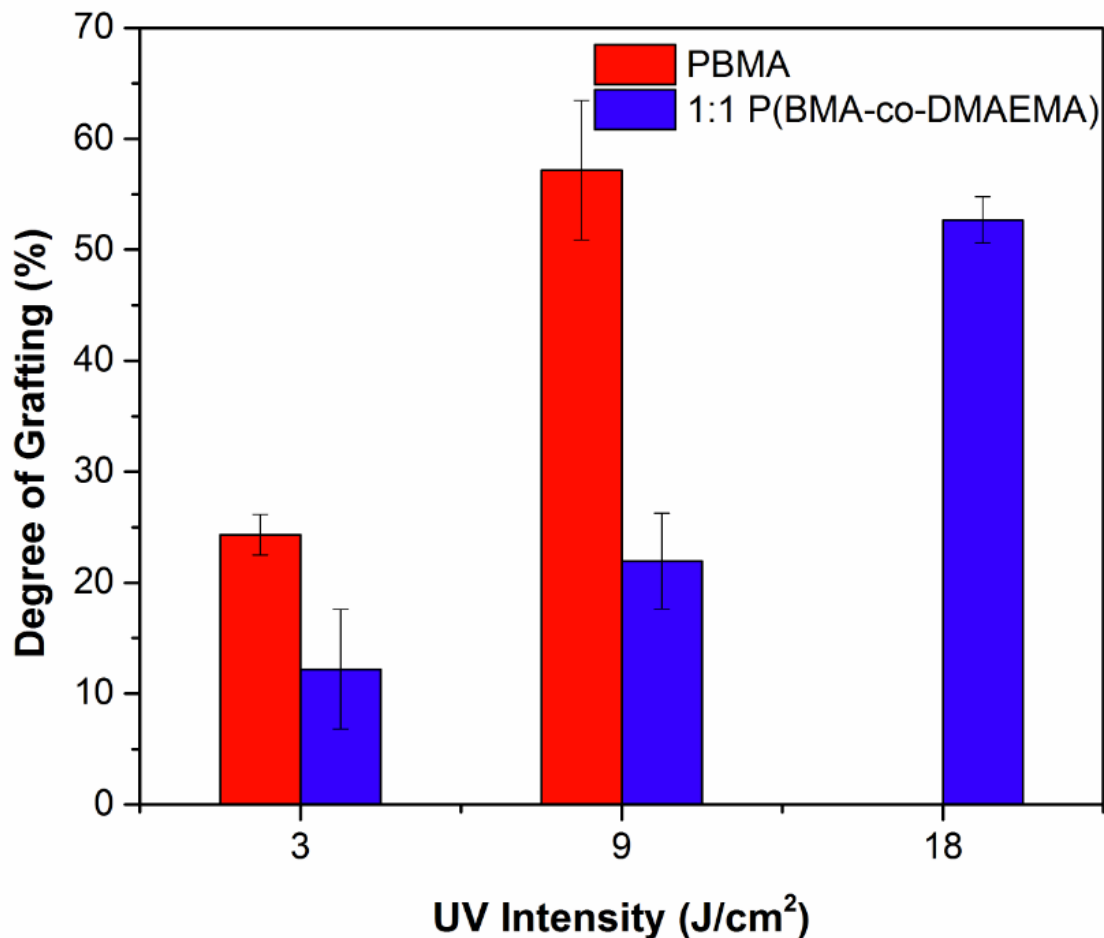


Figure 5.8 Degree of grafting of PBMA and 1:1 P(BMA-co-DMAEMA) on PBT nonwoven fabric. PBT nonwoven fabric (20 g/m²) was immersed in THF containing 100 mg/ml of polymer of interest and 10 wt.% benzophenone, and samples exposed to UV 10-30 mW/cm² for 5 minutes. Samples were then rinsed in THF overnight to dissolve unreacted polymer and benzophenone, followed by rinsing in water and drying in oven to constant weight.

5.2.2 Modulating Gelation Kinetics and Mechanical Strength of PVA-SbQ

Some key recommendations to improve the current experimental work reported in Chapter 3 to modulate the gelation kinetics and mechanical strength using cellulose nanocrystals are:

- Chapter 3 focused primarily on modulating the gelation kinetics and mechanical strength using native CNC's without appropriate functionalization. To create better compatibility with the photocrosslinkable polymer (PVA-SbQ), CNC's can be functionalized using PVA-SbQ or poly (vinyl alcohol) PVA, which might lead to better dispersion and higher reinforcement. In addition, high intensity ultrasonication could be used to achieve better dispersion of CNC's.
- While the CNC's used are commercially available and have been characterized in the previous literature, further characterization of length scales of CNC's can be performed using atomic force microscopy (AFM), and transmission electron microscopy (TEM) to compare the aspect ratio obtained using rheology.
- There is no direct evidence suggestion any adsorption of PVA-SbQ on the surface of CNC's. The extent of and rate of adsorption of PVA-SbQ on CNC's can, therefore, be studied using quartz-crystal microbalance (QCM). This allows us to quantify how much PVA-SbQ gets adsorbed onto CNC if any.
- The presence of hydrophobic and electrostatic interactions between PVA-SbQ and CNC can be confirmed using isothermal calorimetry (ITC) studies.
- Additional stress relaxation experiments can be done to probe the effect on the microstructure and its potential for recovery.

5.2.3 Nanodiamond-Reinforced Electrospun Fibers

Some key recommendations to improve the current experimental work reported in Chapter 4 to understand the dispersion state of ND's in different solvents and the structure-property-function relationship of nanodiamond based polymer composites are:

- In the study of nanodiamond dispersions in different solvents, the maximum concentration that can be dispersed in any solvent can be quantitatively measured using UV absorbance, as nanodiamonds are known to absorb UV. This allows accurate calculations of maximum concentration of nanodiamonds (C_{\max}) that can be dispersed in any solvent. C_{\max} can be further correlated with different components of solvent solubility parameter.
- The precise mechanism for nanodiamond deaggregation can be further explored since the use of a flat tip and microtip played a significant role in the size of nanodiamonds obtained after de-aggregation.
- Several other charged moieties such as polyelectrolytes or surfactants could be used in the deaggregation process to explore other milling agents that might be suitable for deaggregation.
- For the polymer-ND composites, additional studies need to be done using amorphous polymers such as poly(methyl) methacrylate to prove the hypothesis that nanodiamonds indeed form better composites with amorphous polymers.
- One of the most important limitations of this work is the accuracy of the nanodiamond surface energy measurements. To improve the accuracy, highly

sensitive and advanced analytical instruments such as inverse gas chromatography (IGC) can be used to calculate surface energy of nanodiamonds.

- Nanodiamonds can be functionalized with the matrix polymer for better compatibilization and subsequent reduction in aggregation behavior. For example, carboxylated nanodiamonds can be modified with PVA to form composites in PVA. By activating the carboxylic acid groups using carbodiimide chemistry, PVA can be successfully attached to the nanodiamonds.
- To understand fundamental aspects of nanodiamond aggregation and its effect on glass transition temperature and mechanical properties, the composites can be studied in thin films instead of nanofibers.
- To measure the interaction forces between nanodiamonds and polymers of interest, surface force apparatus or atomic force microscopy (AFM) can be utilized. AFM tip can be modified using thiol-terminated polymers creating well-defined polymer brushes and their interaction forces with nanodiamonds can be measured.

5.3 References

1. Pandiyarajan, C. K. & Genzer, J. Effect of Network Density in Surface-Anchored Poly(N-isopropylacrylamide) Hydrogels on Adsorption of Fibrinogen. *Langmuir* **33**, 1974–1983 (2017).

APPENDICES

Appendix A Supplemental Information for Chapter 2

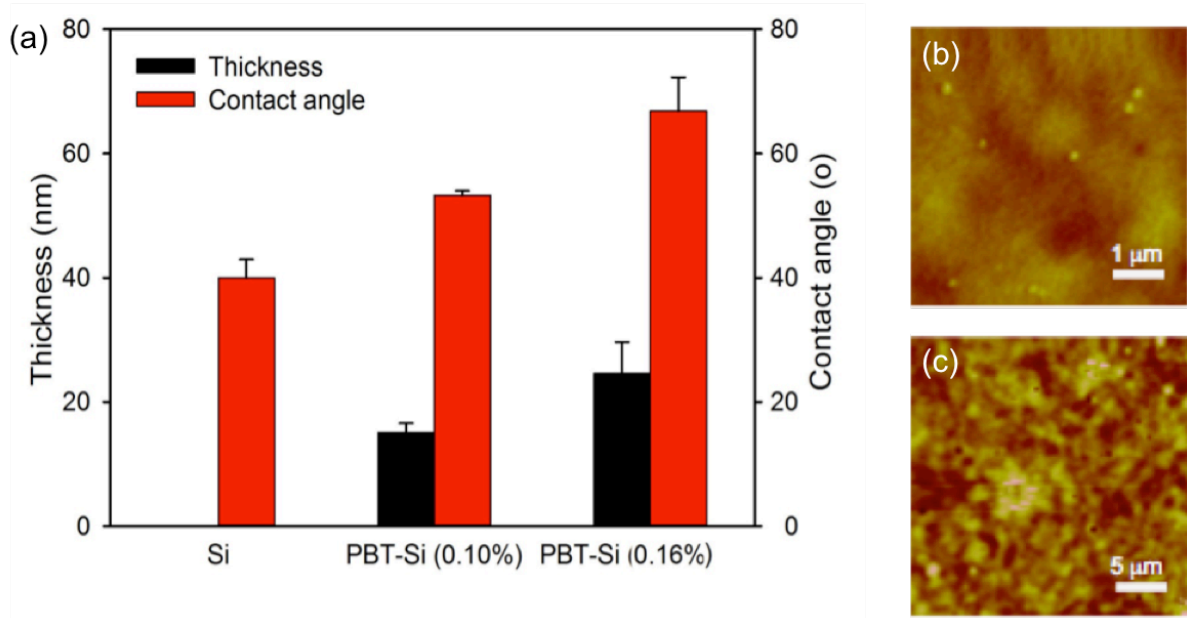


Figure A.1 Spin-coating PBT thin films onto silicon substrate using different PBT concentrations (0.10 wt.% and 0.16 wt.%) in 1,1,1,3,3,3-hexafluoro-2-propanol (HFIP) - (left) thickness and corresponding contact angles for the PBT-coated surfaces, and (right) AFM images of spin-coated surface.

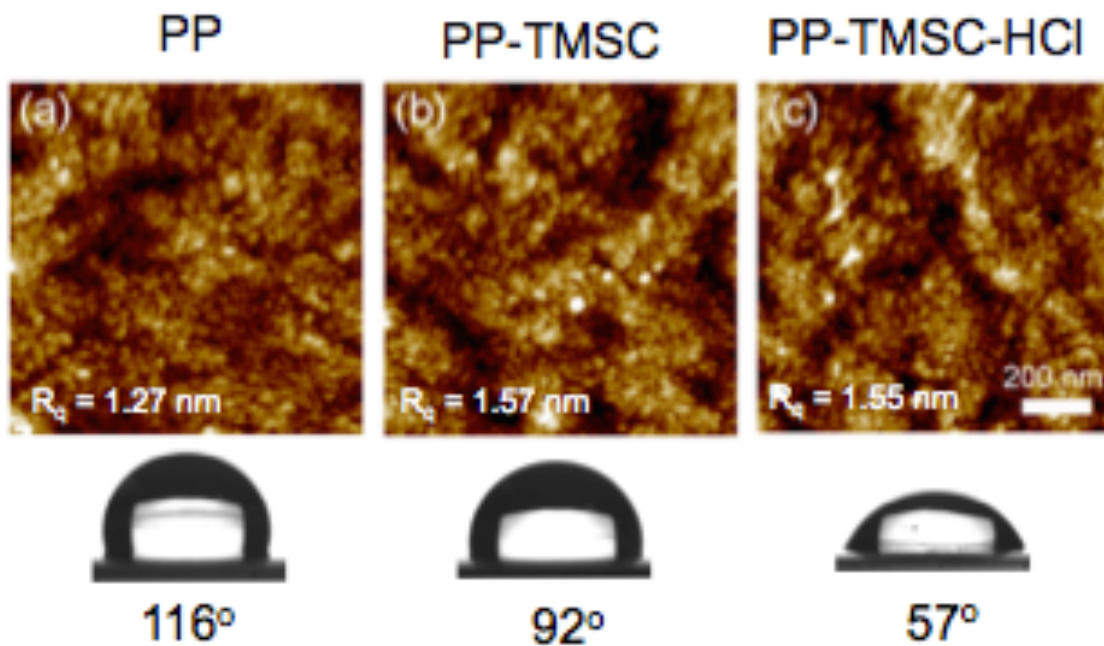


Figure A.2 AFM images of PP thin films on silicon substrate and corresponding changes in contact angle upon using TMSC as an anchoring layer and subsequent acid hydrolysis.

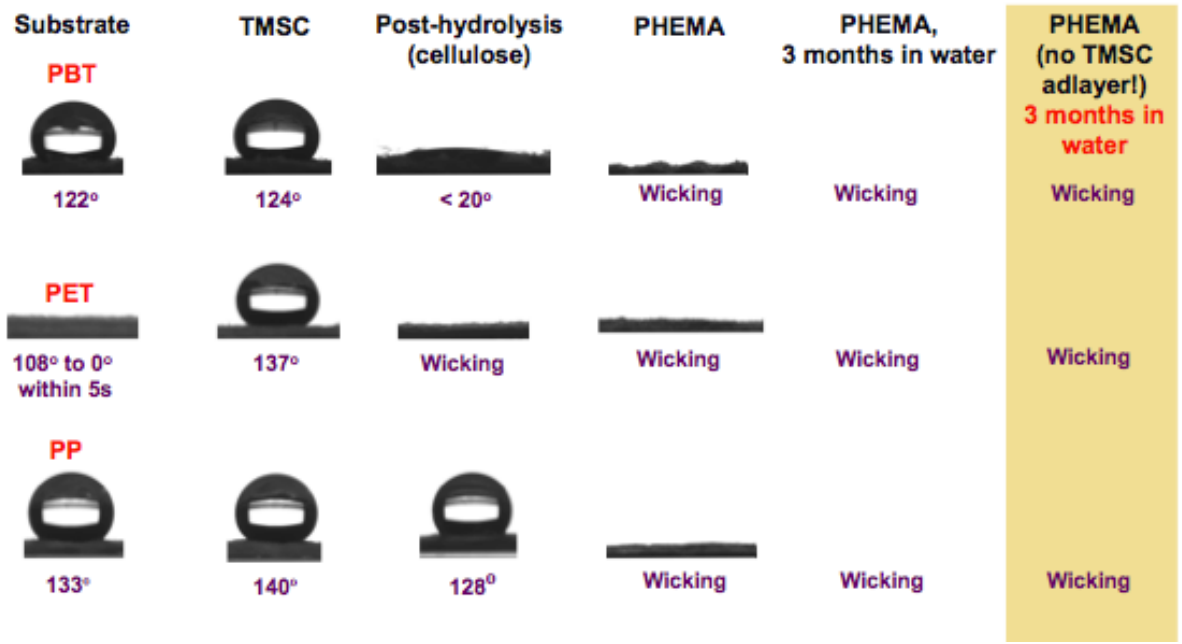


Figure A.3 (a) The effect of surface modification on apparent contact angle for different nonwoven fabrics (PBT, PET and PP). Grafting of pure poly (HEMA) creates super hydrophilic nonwovens that are stable for 3 months in water.

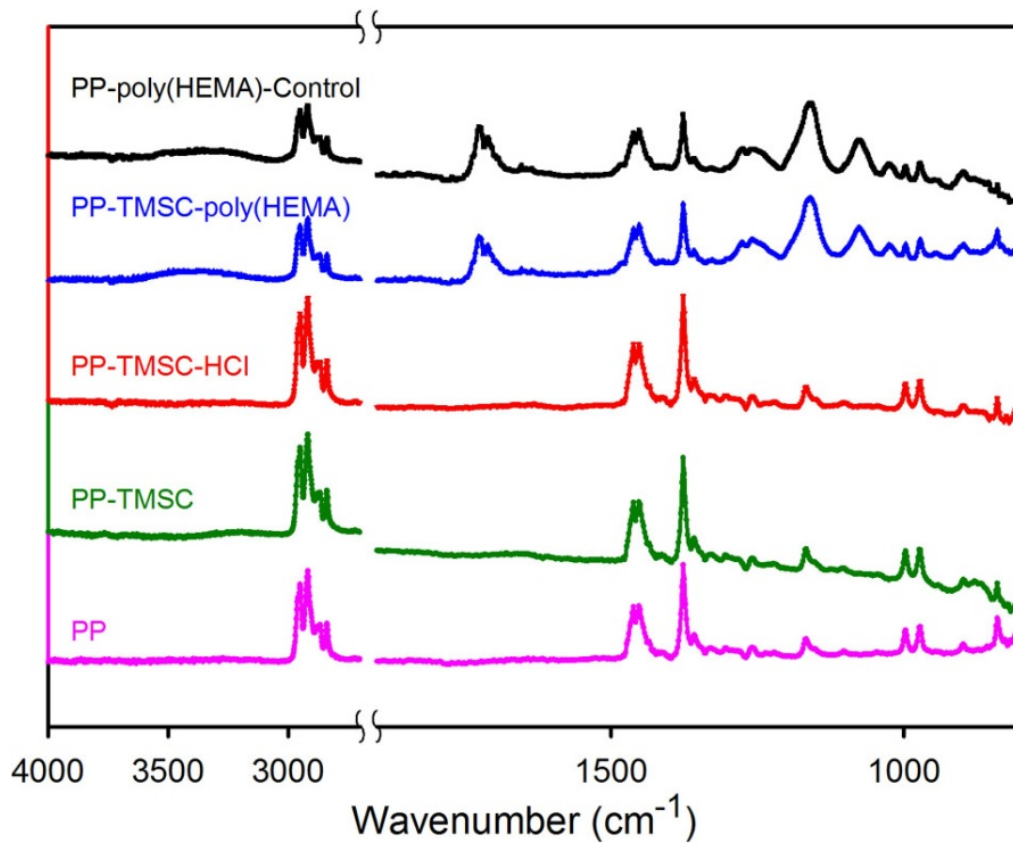


Figure A.4 FTIR spectra of polypropylene nonwoven fabric after different surface modification steps. The grafting of pure poly (HEMA) was confirmed by peak at $\sim 1730 \text{ cm}^{-1}$ indicative of strong C=O stretching vibration.

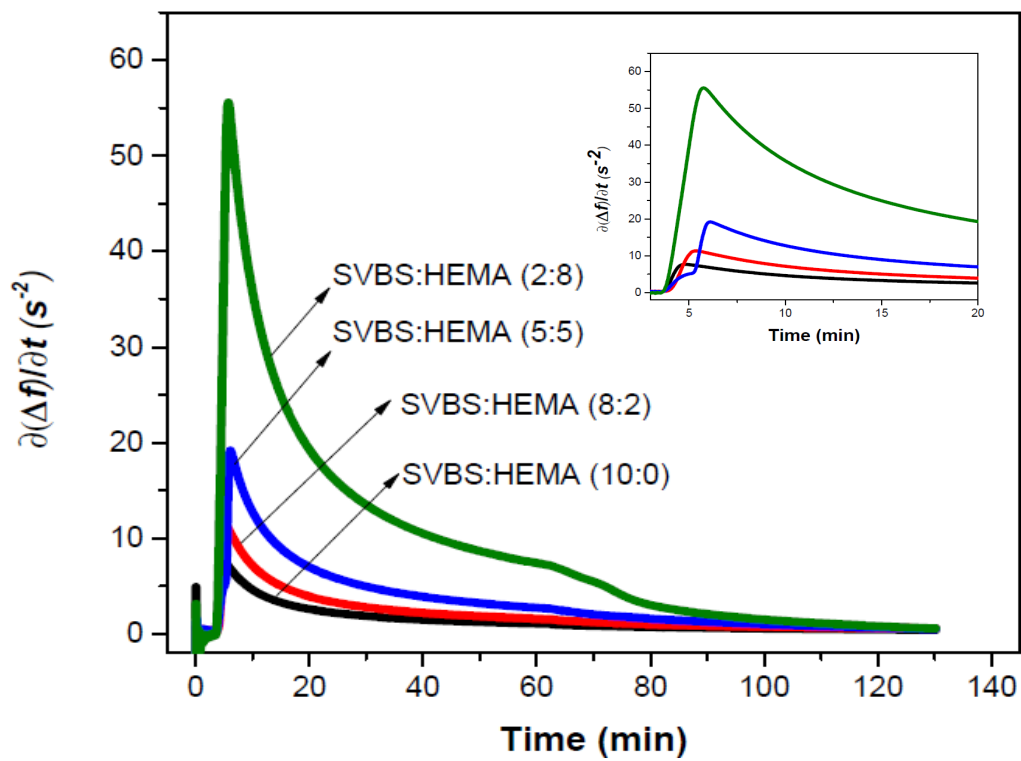


Figure A.5 First derivative of frequency changes for different surfaces showing rate of lysozyme adsorption on different poly (SVBS-co-HEMA) surfaces.

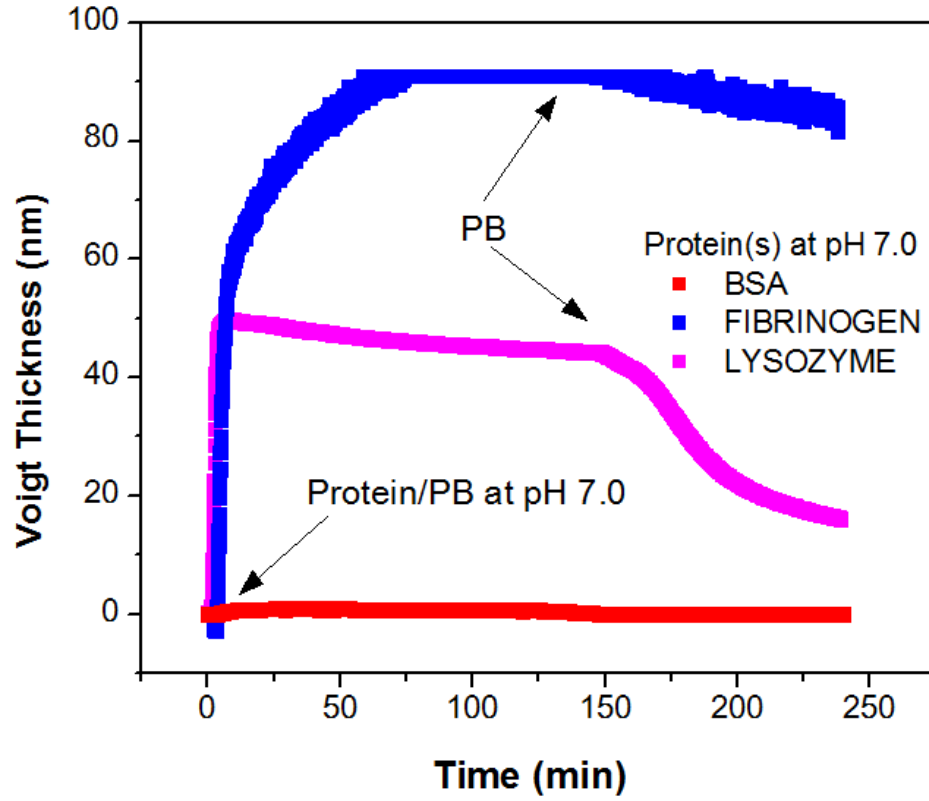


Figure A.6 Thickness of protein layer (1 mg/ml in PB at pH 7.0) adsorbed on the surface of 2:8 poly (SVBS-co-HEMA) calculated using Voigt model.

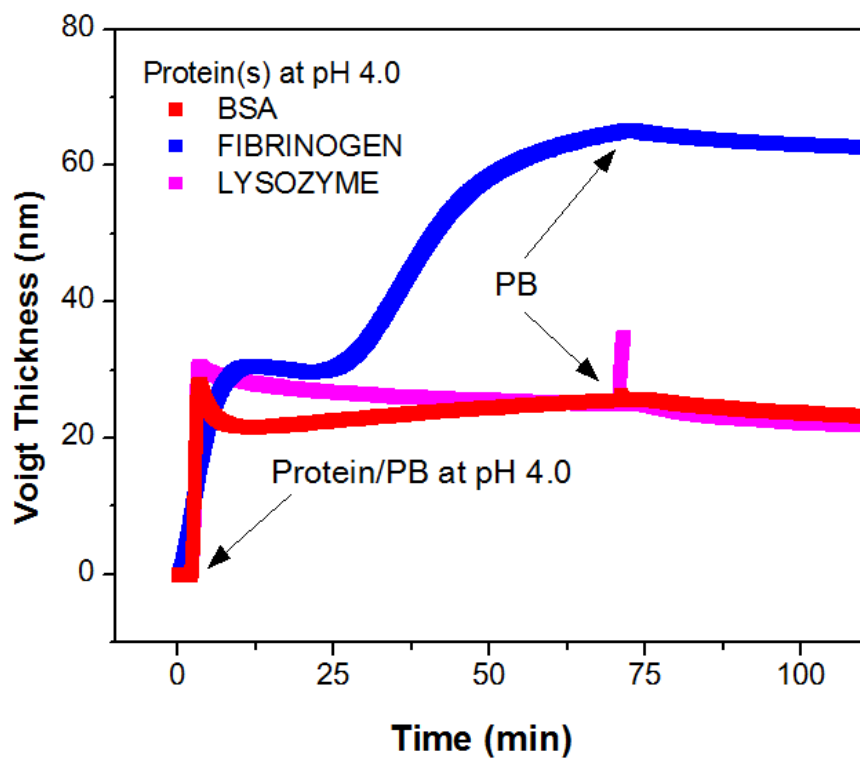


Figure A.7 Thickness of protein layer (1 mg/ml in PB at pH 4.0) adsorbed on the surface of 2:8 poly (SVBS-co-HEMA) calculated using Voigt model.

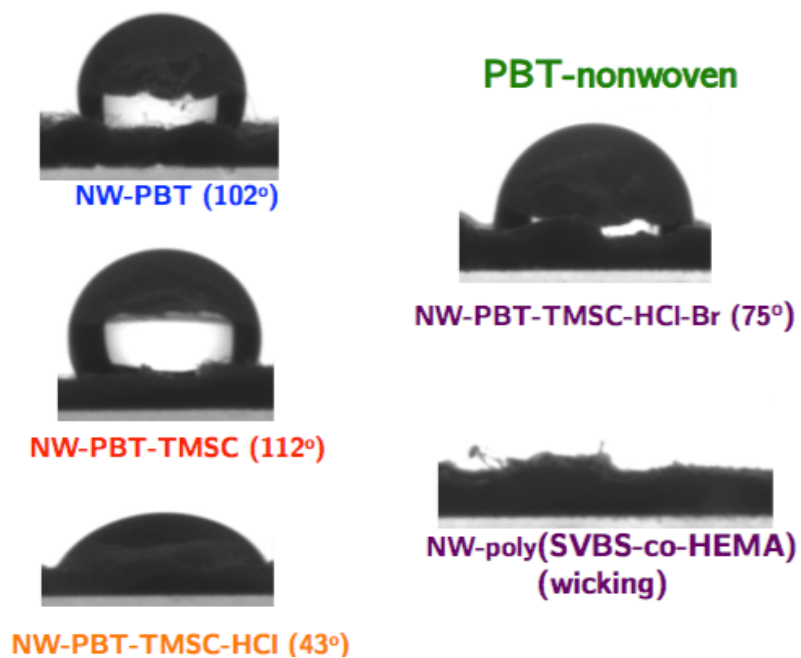


Figure A.8 Changes in apparent wettability of PBT nonwoven fabric in different steps of surface modification. Grafting of 2:8 poly (SVBS-co-HEMA) completely wicks the surface.

Appendix B Supplemental Information for Chapter 3

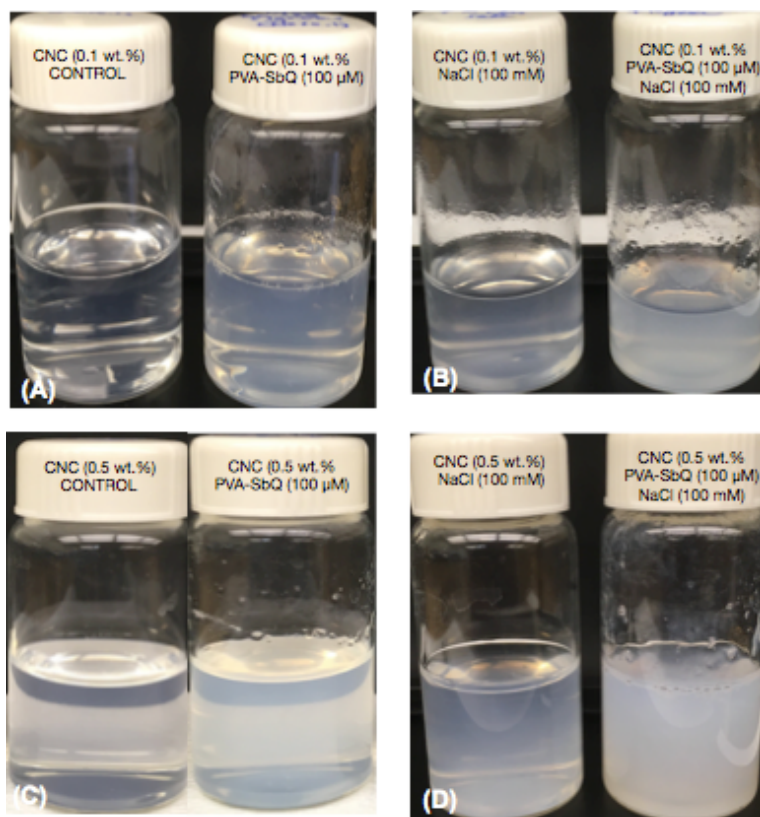


Figure B.1 Representative digital images of (A) CNC (0.1 wt.%) and CNC (0.1 wt.%) with PVA-SbQ (100 μ M), (B) CNC (0.1 wt.%) with NaCl (100 mM, 5.84 mg/ml) and CNC (0.1 wt.%) with PVA-SbQ (100 μ M) / NaCl (100 mM, 5.84 mg/ml); (C) CNC (0.5 wt.%) and CNC (0.5 wt.%) with PVA-SbQ (100 μ M) and (D) CNC (0.5 wt.%) with NaCl (100 mM, 5.84 mg/ml) and CNC (0.5 wt.%) with PVA-SbQ (100 μ M) / NaCl (100 mM, 5.84 mg/ml). All CNC suspensions shown above were prepared using bath sonication for 1 hour. CNC dispersion turns cloudy upon addition of PVA-SbQ as well as sodium chloride. CNC dispersions containing PVA-SbQ show some aggregation whereas dispersions containing both PVA-SbQ and sodium chloride show intense aggregation.

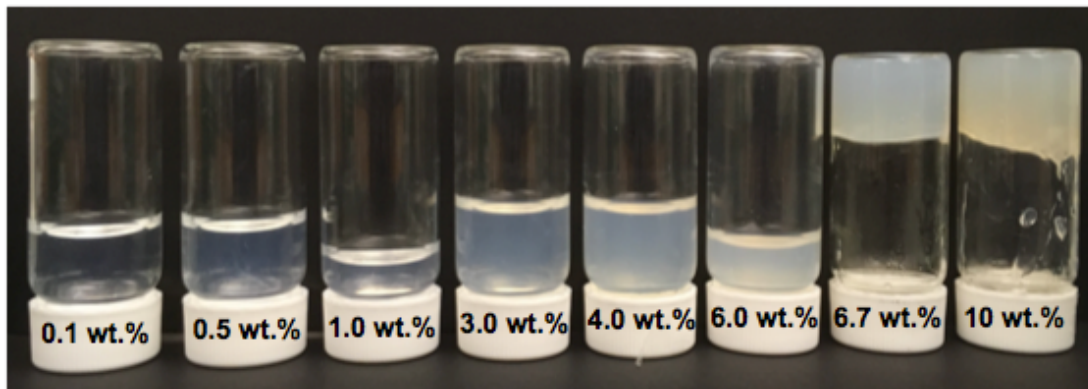


Figure B.2 Representative digital images of CNC's at different weight percent dispersed in water after sonication for 4 hours (Branson 1510). Concentrations below 6 wt. % show solution-like behavior whereas concentrations above 6 wt. % show gel-like behavior.

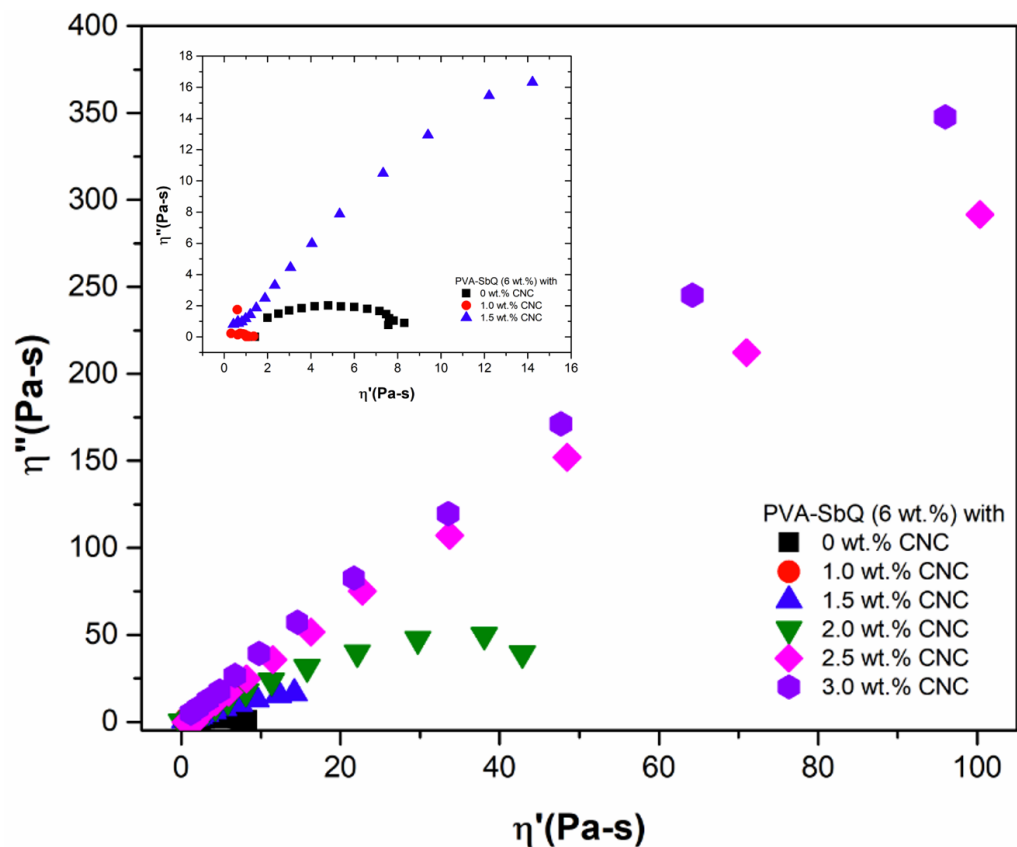


Figure B.3 Cole-Cole plot showing the relationship between real (η') and imaginary parts of complex viscosity (η'') for PVA-SbQ with different CNC concentrations. The inset shows data for neat PVA-SbQ, and PVA-SbQ with 0.5 wt. % and 1 wt. % CNC not visible in the original plot.

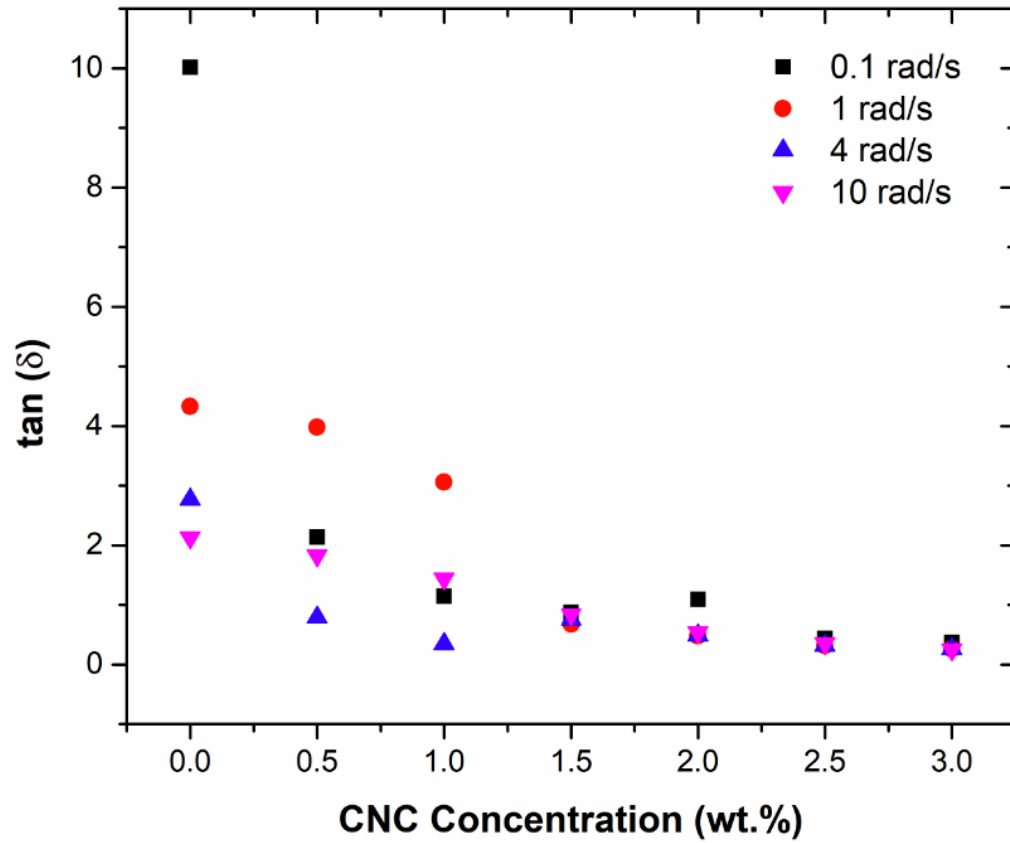


Figure B.4 Determination of gel-point concentration using frequency independence of $\tan \delta$ based on Winter-Chambon criterion.

Appendix C Supplemental Information for Chapter 4

Table C-1 Solubility parameters of different solvents used to disperse nanodiamonds

Solvent	δ_d (MPa ^{1/2})	δ_p (MPa ^{1/2})	δ_h (MPa ^{1/2})
Water	15.5	16.0	42.3
DMSO	18.4	16.4	10.2
DMF	17.4	13.7	11.3
Dimethylacetamide	16.8	11.5	10.2
Acetonitrile	15.3	18.0	6.1
Acrylonitrile	16.0	12.8	0.8
Acetone	15.5	10.4	7.0
Methanol	15.1	12.3	22.3
Ethanol	14.7	12.3	22.3
Dichloromethane	18.2	6.30	6.1
Chloroform	17.8	3.10	5.7
N-methyl-2-pyrrolidone	18.0	12.3	7.2
Tetrahydrofuran (THF)	16.8	5.70	8.0
Toluene	18.0	1.40	2.0
Hexane	14.9	0	0
Cyclohexane	16.8	0	0.2
Ethyl Acetate	15.8	5.3	7.2
Acetic Anhydride	16.0	11.7	10.2

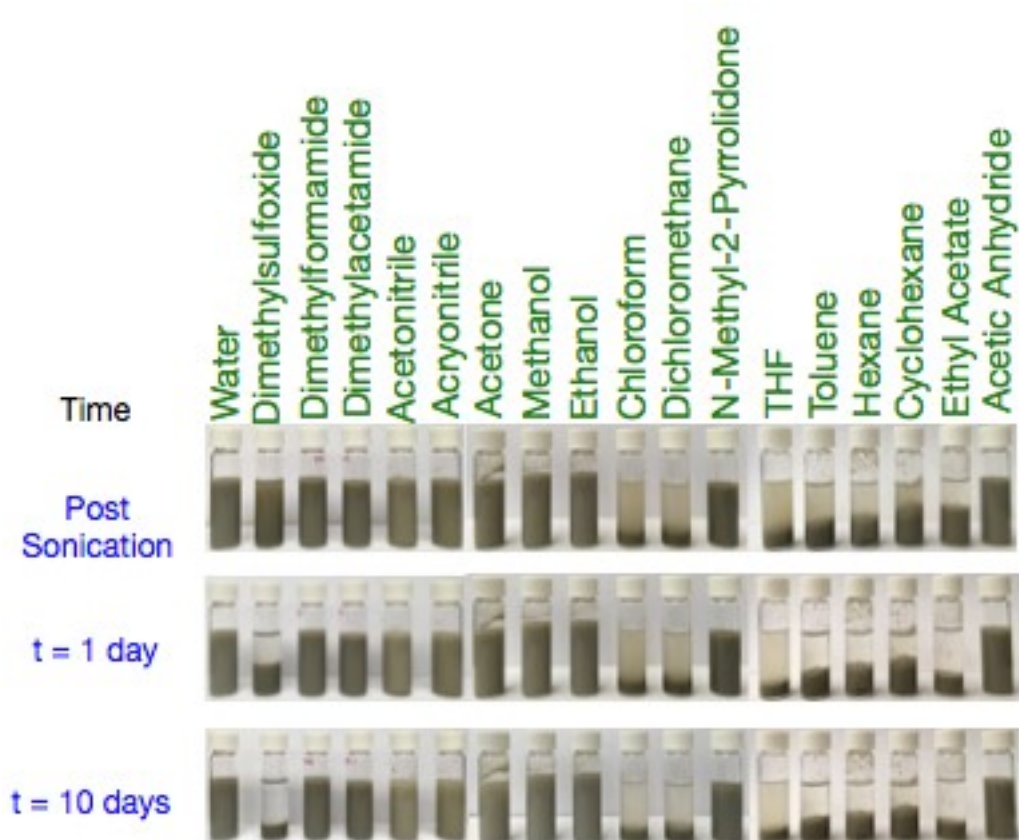


Figure C.1 Dispersion of carboxylated nanodiamonds (c-ND) in 18 different solvents immediately post-sonication, after 1 day and 10 days. Dispersion stability was labeled stable, moderately stable, less stable and unstable based on the visual differences in color of colloidal solution - most stable in water, DMF, and DMAc; moderately stable in acetone, methanol, and ethanol; less stable in acrylonitrile and acetonitrile; and unstable in DMSO.

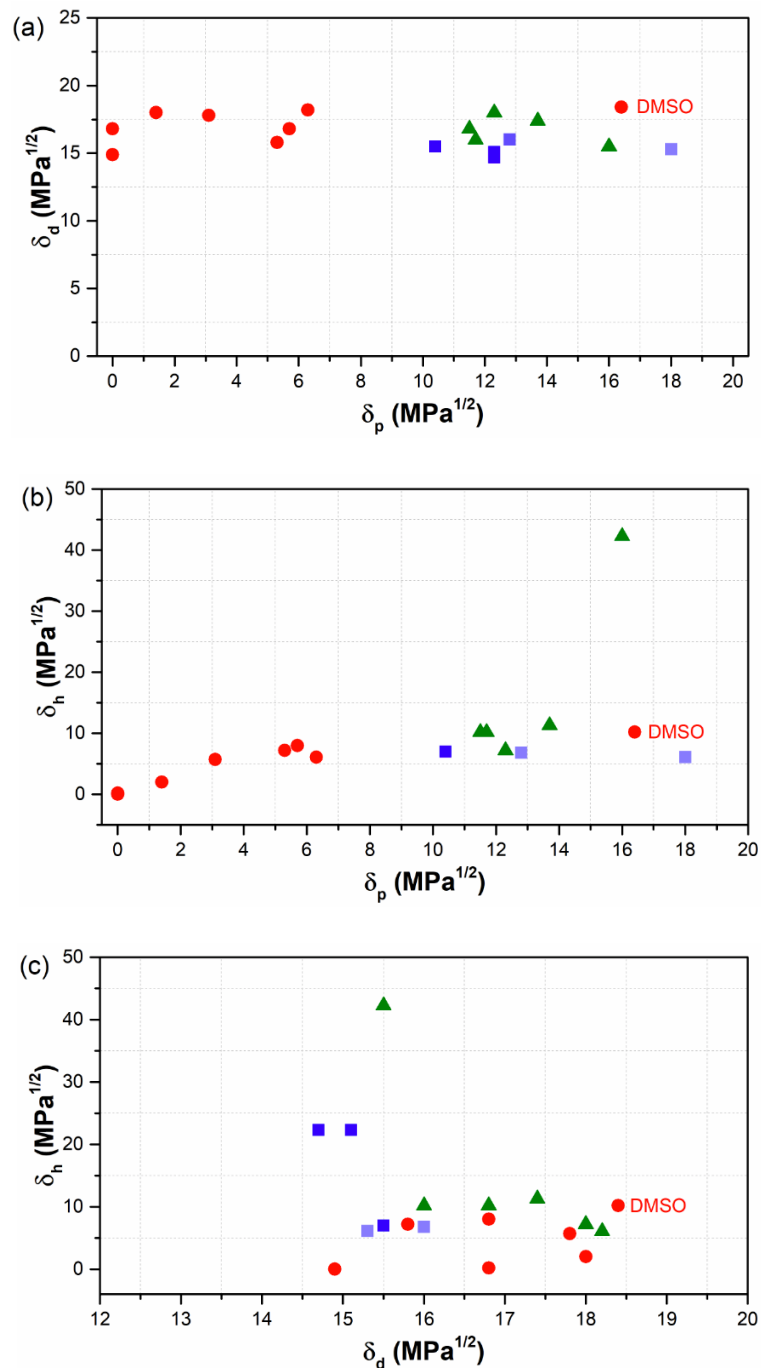


Figure C.2 Dispersion map for c-ND dispersed in different solvents, showing stable dispersions (triangles), moderately stable dispersions (squares), less stable dispersions (light squares) and unstable dispersions (circles) - (a) dispersive solubility parameter vs. polar solubility parameter (b) hydrogen bonding solubility parameter vs. polar solubility parameter and (c) hydrogen bonding solubility vs. dispersive solubility parameter.

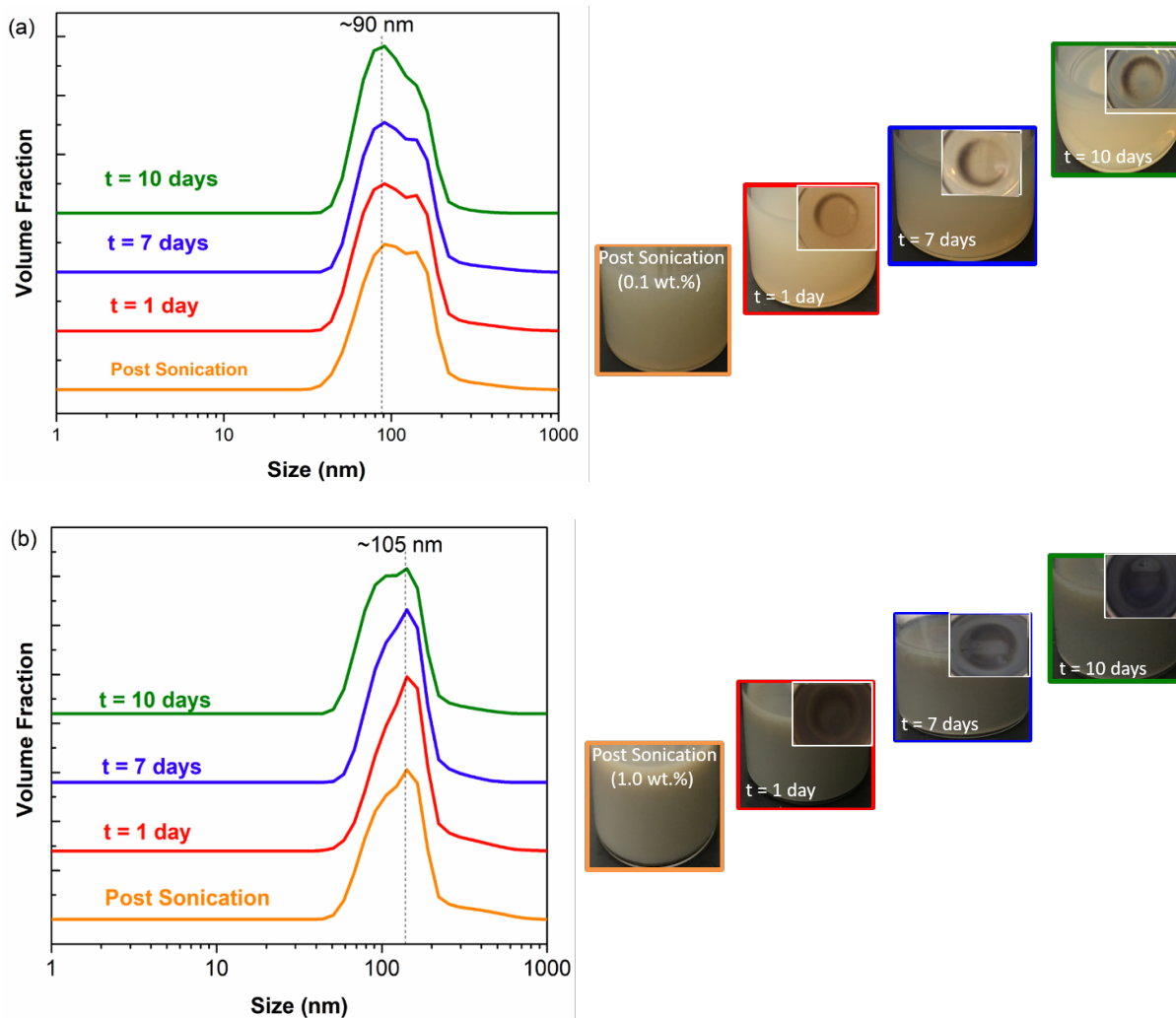


Figure C.3 Particle size distribution for (a) ND-COOH (0.1 wt. %) and (b) ND-COOH (1.0 wt. %) post sonication and after 1 day, 7 days and 10 days. Digital images show ND-COOH at different times after initial sonication. Inset shows particle settling at the bottom of the vial.

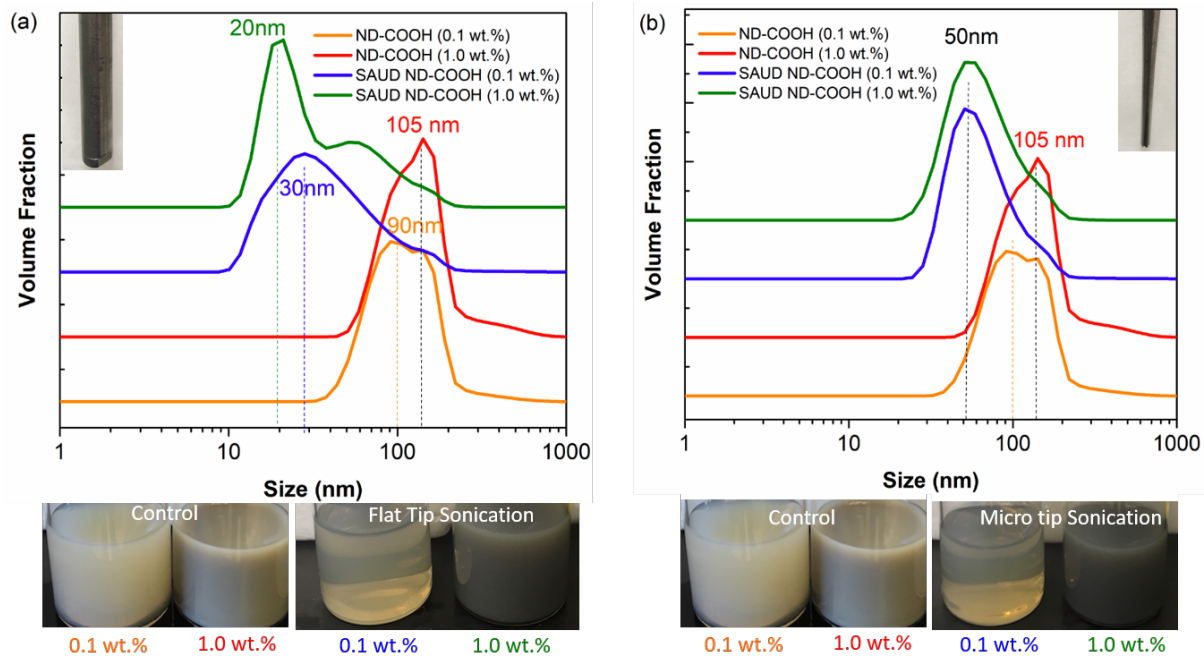


Figure C.4 Salt-Assisted Ultrasonic Deaggregation (SAUD) technique was employed to obtain c-ND (labeled ND-COOH in the plot) with smaller particle size. Branson Sonifier S-450 with a flat tip (a) and micro tip (b) was used for ultrasonic deaggregation. DLS measurements were obtained for c-ND (as-received) and SAUD c-ND for 0.1 wt. % and 1.0 wt. % using refractive index of 1.427 and viscosity of 0.899 mPa-s. The data shown above are an average of 5 measurements.

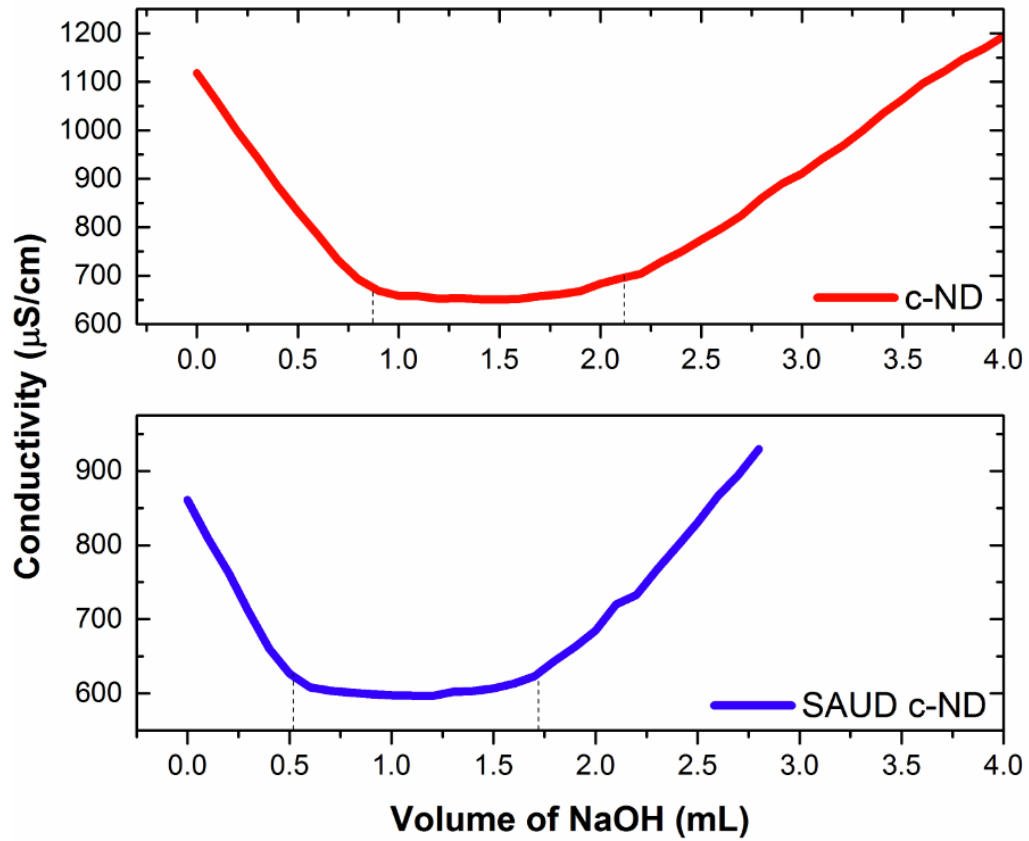


Figure C.5 Conductometric titration curves for c-ND and SAUD c-ND showing similar amounts of surface carboxylic acid groups, confirming no significant functionality changes upon deaggregation.

Table C-2 Dispersive and polar components of total surface energy of polymers

Polymers	γ^d (MPa ^{1/2})	γ^p (MPa ^{1/2})	γ^t (MPa ^{1/2})
Poly (vinyl) Alcohol	38.8	5.1	43.9
Polyacrylonitrile	35.0	14.7	49.7
Polystyrene	41.2	0.8	42

Table C-3 Electrospinning conditions for PVA (MW 10-98, 15 wt.%) in water, PAN (8 wt.%) in DMF and PS (30 wt.%) in DMF and with different SAUD c-ND loadings (0.1 wt.%, 0.5 wt.%, 1.0 wt.% and 2.0 wt.%)

Polymers	Voltage (kV)	DCD (cm)	Flow Rate (ml/h)	Temperature (°C)	Humidity (%)
PVA (15 wt. %)	20	15	0.5	23-25	25-40
PVA (15 wt. %) + SAUD-ND (0.1 wt. %)	20	15	0.5	23-25	25-40
PVA (15 wt. %) + SAUD-ND (0.5 wt. %)	20	15	0.5	23-25	25-40
PVA (15 wt. %) + SAUD-ND (1.0 wt. %)	25	15	0.5	23-25	25-40
PVA (15 wt. %) + SAUD-ND (2.0 wt. %)	25	15	0.3*	23-25	25-40

	Voltage (kV)	DCD (cm)	Flow Rate (ml/h)	Temperature (°C)	Humidity (%)
PS (30 wt. %)	15	15	0.5	23-25	25-40
PS (30 wt. %) + SAUD-ND (0.1 wt. %)	15.6	15	0.5	23.4	36
PS (30 wt. %) + SAUD-ND (0.5 wt. %)	15.2	15	0.5	23.6	44
PS (30 wt. %) + SAUD-ND (1.0 wt. %)	17.5	15	0.5	22.6	38-43
PS (30 wt. %) + SAUD-ND (2.0 wt. %)	17.4	15	0.5	24	41

	Voltage (kV)	DCD (cm)	Flow Rate (ml/h)	Temperature (°C)	Humidity (%)
PAN (8 wt. %)	15	10	1	23-25	25-40
PAN (8 wt. %) + SAUD-ND (0.1 wt. %)	15	10	1	23-25	25-40
PAN (8 wt. %) + SAUD-ND (0.5 wt. %)	15	10	1	23-25	25-40
PAN (8 wt. %) + SAUD-ND (1.0 wt. %)	15	10	1	23-25	25-40
PAN (8 wt. %) + SAUD-ND (2.0 wt. %)	15-16.5	10	1	23-25	25-40

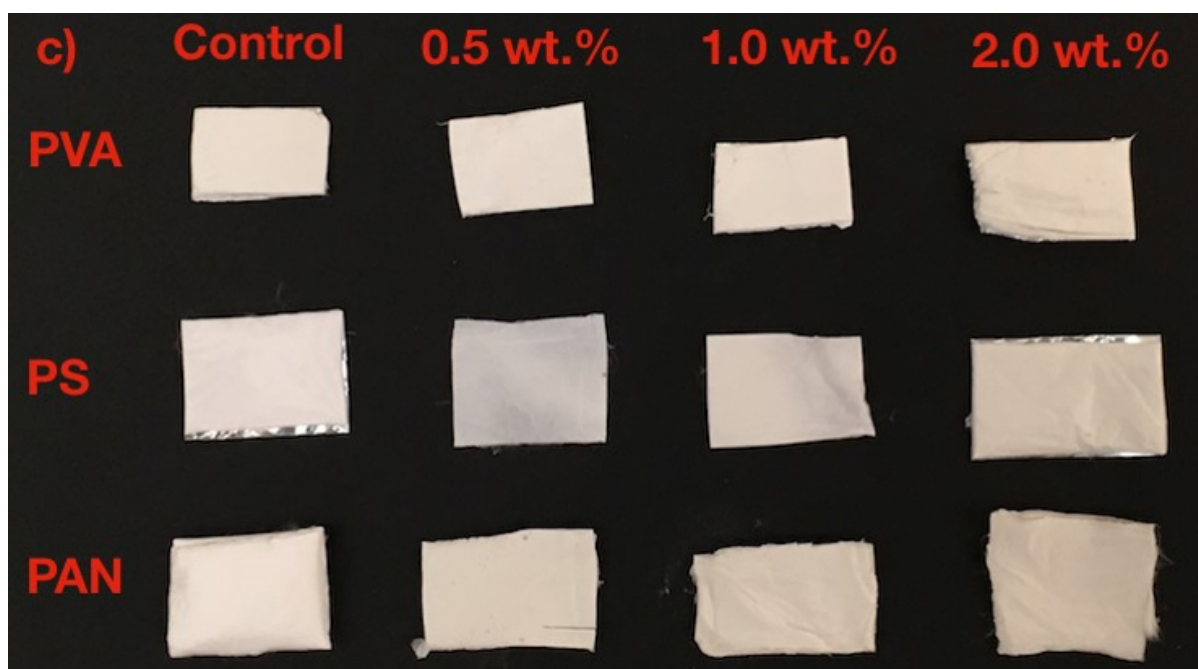
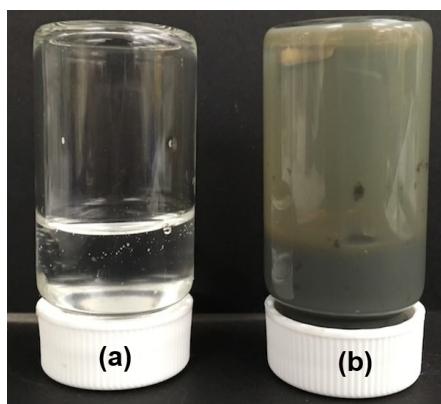


Figure C.6 Electrospinning solution containing (a) polyvinyl alcohol (MW 10-98, 15 wt. %), and (b) polyvinyl alcohol (MW 10-98, 15 wt. %) with SAUD c-ND (2 wt. %) showing the effect of SAUD c-ND on appearance of solution. Electrospun fiber mats are shown in (c) showing the effect of c-ND on color of electrospun mats indicative of aggregation.

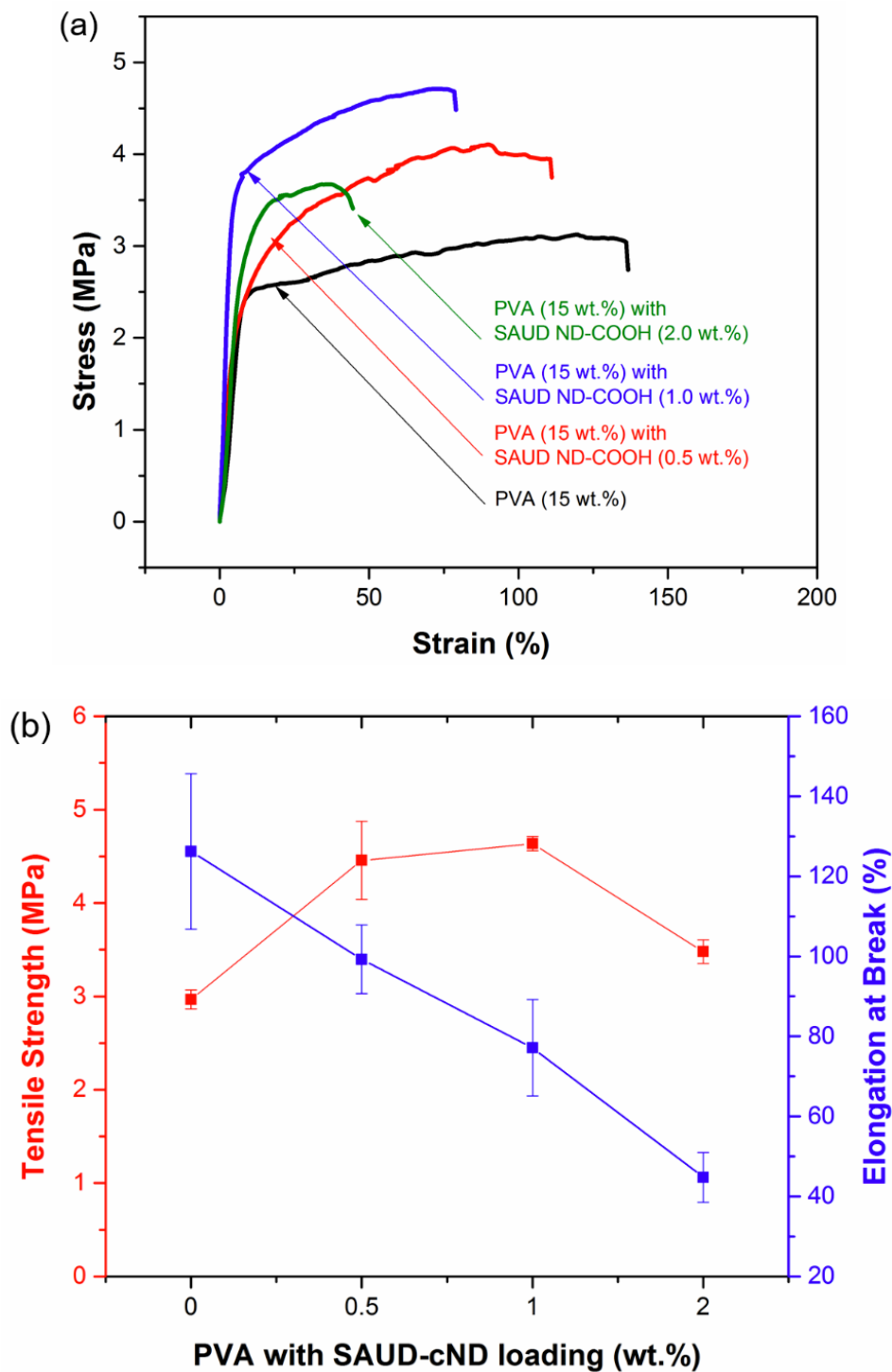


Figure C.7 (a) Stress-strain plot for poly(vinyl alcohol) (PVA) nanofibers with different SAUD c-ND loadings between 0.1 wt.% to 2 wt.% and (b) tensile strength and elongation at break at different SAUD c-ND extracted from data in (a).

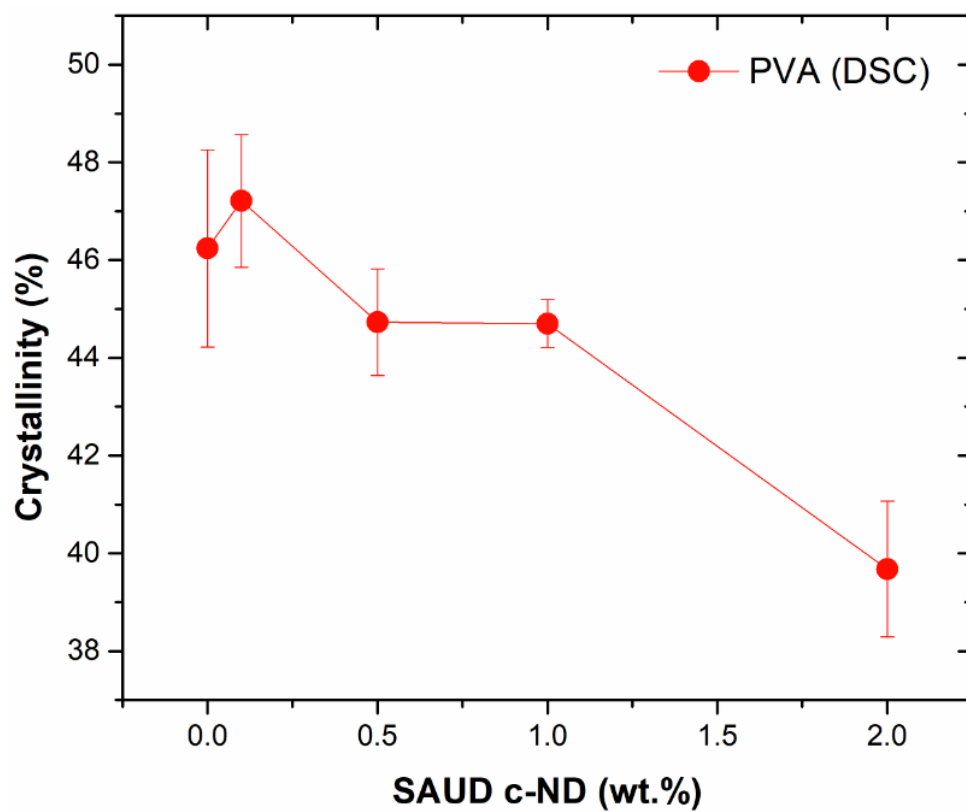


Figure C.8 The effect of ND's on crystallinity of PVA nanofibers calculated using DSC.

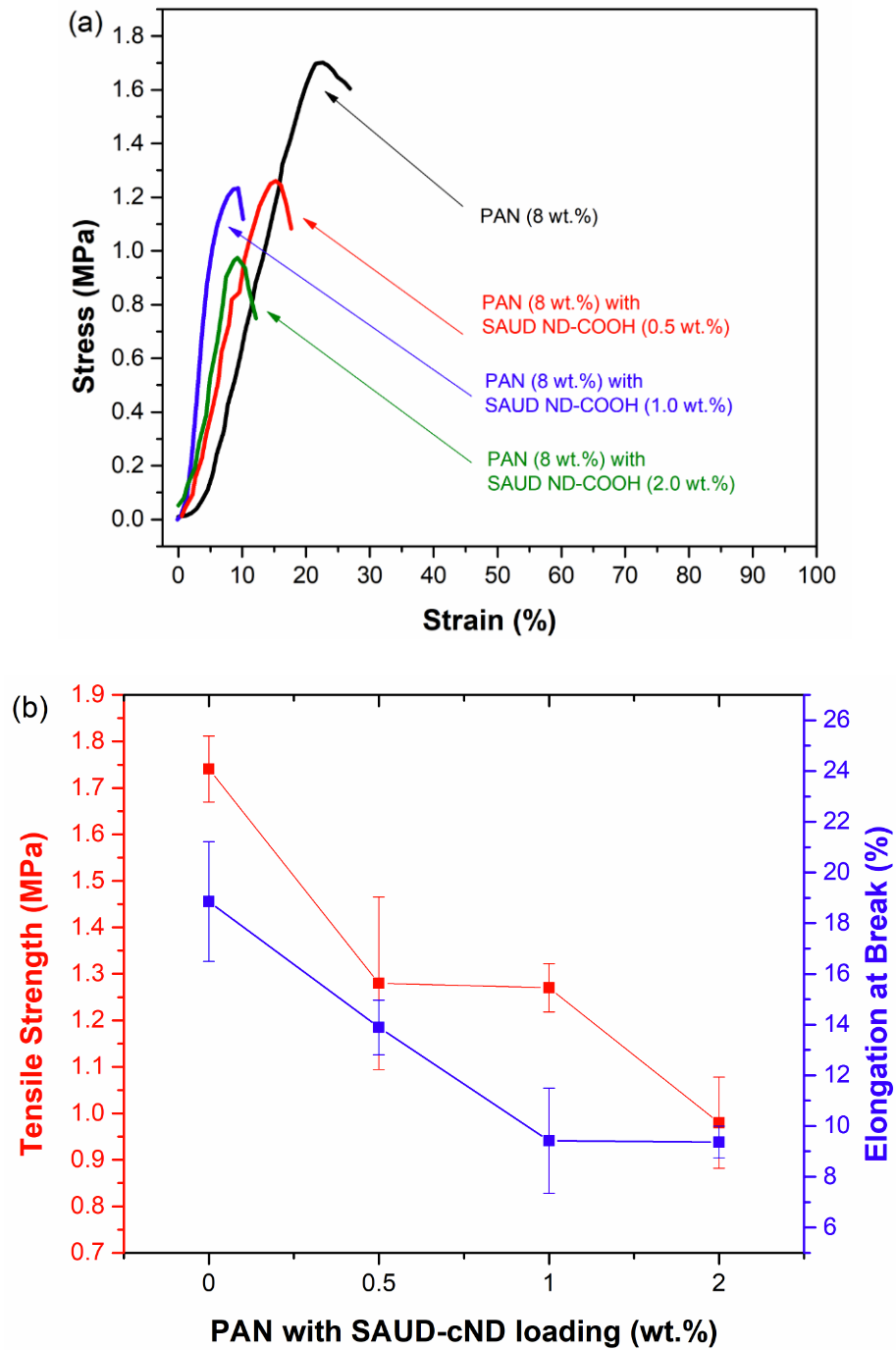


Figure C.9 (a) Stress-strain plot for polyacrylonitrile (PAN) nanofibers with different SAUD c-ND loadings between 0.1 wt.% to 2 wt.% and (b) tensile strength and elongation at break at different SAUD c-ND extracted from data in (a).

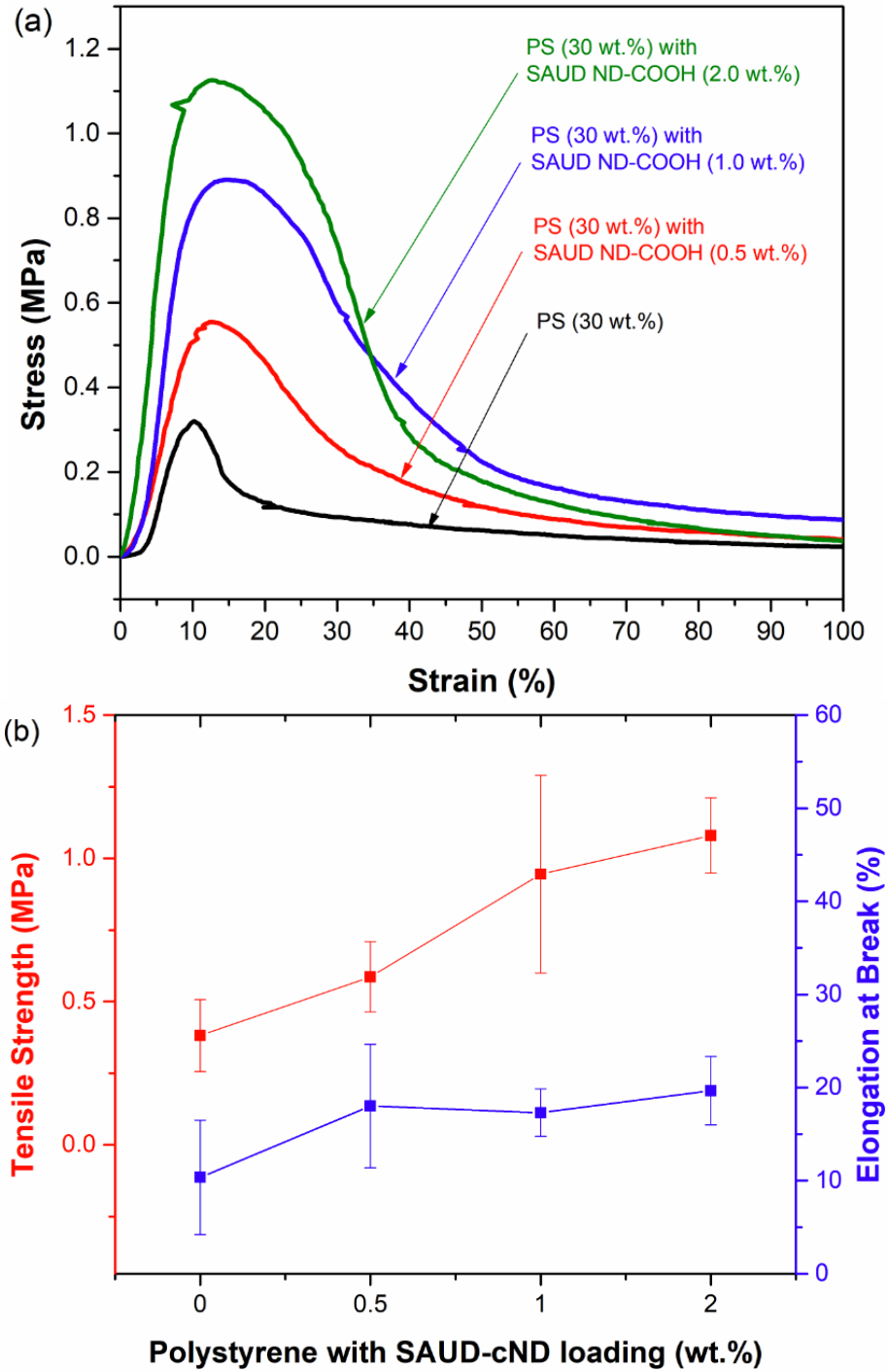


Figure C.10 Stress-strain plot for polystyrene (PS) nanofibers with different SAUD c-ND loadings between 0.1 wt.% to 2 wt.% and (b) tensile strength and elongation at break at different SAUD c-ND extracted from data in (a).

Morphology of Polymer-ND Composite Nanofibers

Fiber mats of PVA, PAN, and PS containing c-ND were obtained after electrospinning homogenous mixtures of polymer and c-ND dispersions in water (for PVA) and DMF (for PAN and PS). By increasing the concentration of each polymer, bead-free uniform fibers with smooth surfaces were first obtained at 15 wt. % for PVA, 8 wt. % for PAN and 30 wt. % for PS. The concentration of c-ND in polymers was then varied to obtain nanofibers with c-ND loadings between 0.1 wt. % to 2 wt. %. Figure C.11 shows typical SEM image of electrospun fiber mats with and without c-ND's. For the case of c-ND loaded fibers, representative images at the maximum loading of 2 wt. % are shown. PVA solution at 15 wt. % yielded bead-free fibers with a diameter of 187.9 ± 55 nm. Similarly, fibers containing c-ND at 0.1 wt. % and 0.5 wt. % yielded homogeneous fibers at the same voltage, since no considerable increase in viscosity was seen. However, higher voltages were necessary for c-ND loadings of 1 wt. % and 2 wt. % to get uniform, bead-free (see Table C.3 for experimental parameters), possibly due to interactions between PVA and ND. Similarly, higher voltages were used to spin higher c-ND loadings in PS relative to PS fibers, but c-ND loaded PAN fibers were electrospun at voltages similar to PAN. The inclusion of 2 wt. % ND resulted in uniform PVA nanofibers with an average diameter of 360 ± 111 nm, significantly higher compared to c-ND-free nanofibers. Similar trends in diameter increase were seen for both PS and PAN, with diameters increasing from 1.7 ± 0.3 μm to 2.7 ± 0.7 μm for PS and 346 ± 69 nm to 430 ± 168 nm for PAN. In addition, a simple morphological analysis carried out on samples also indicates qualitative differences in the distribution of c-ND within the fibers. Note that quantification of cluster sizes using SEM is extremely

difficult, nonetheless, aggregation phenomena are observable. c-ND's appear as visible aggregates at 2 wt.% loading for PVA and PAN, and appears as white patches for PS, due to its nanometer size on a micron-sized fiber. The aggregates on PAN suggest that dispersions may not be homogeneously dispersed. Figure C.12 shows cross-section images also reveal the presence of ND's within the fibers. Figure C.13 shows TEM images of electrospun fibers of PVA, PS and PAN containing 2 wt. % c-ND. While quantitative information such as size and number density of aggregates cannot be obtained, qualitative differences suggest aggregation behavior in the order of PVA > PS > PAN as predicted by the criterion of dispersion (D_c).

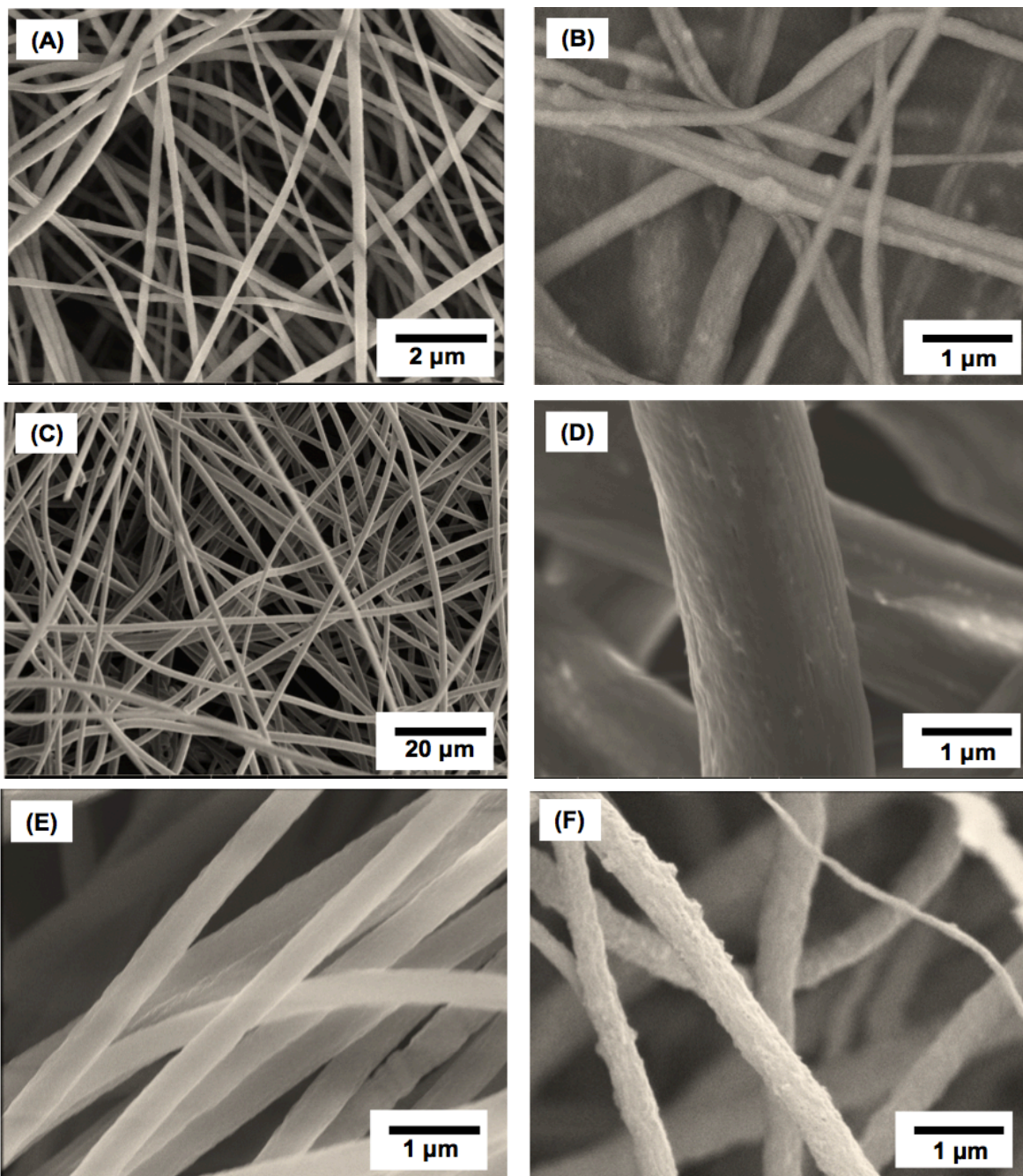


Figure C.11 (a-f) SEM images of electrospun fibers containing ND: (a) PVA (15 wt. %) and (b) PVA (15 wt.%) with SAUD c-ND (2 wt.%); (c) PS (30 wt.%) and (d) PS (30 wt.%) with SAUD c-ND (2 wt.%); (e) PAN (8 wt.%) and (f) PAN (8 wt.%) with SAUD c-ND (2 wt.%). Uniform nanofibers were produced at different polymer concentrations. Electrospinning conditions are shown in Table C.3.

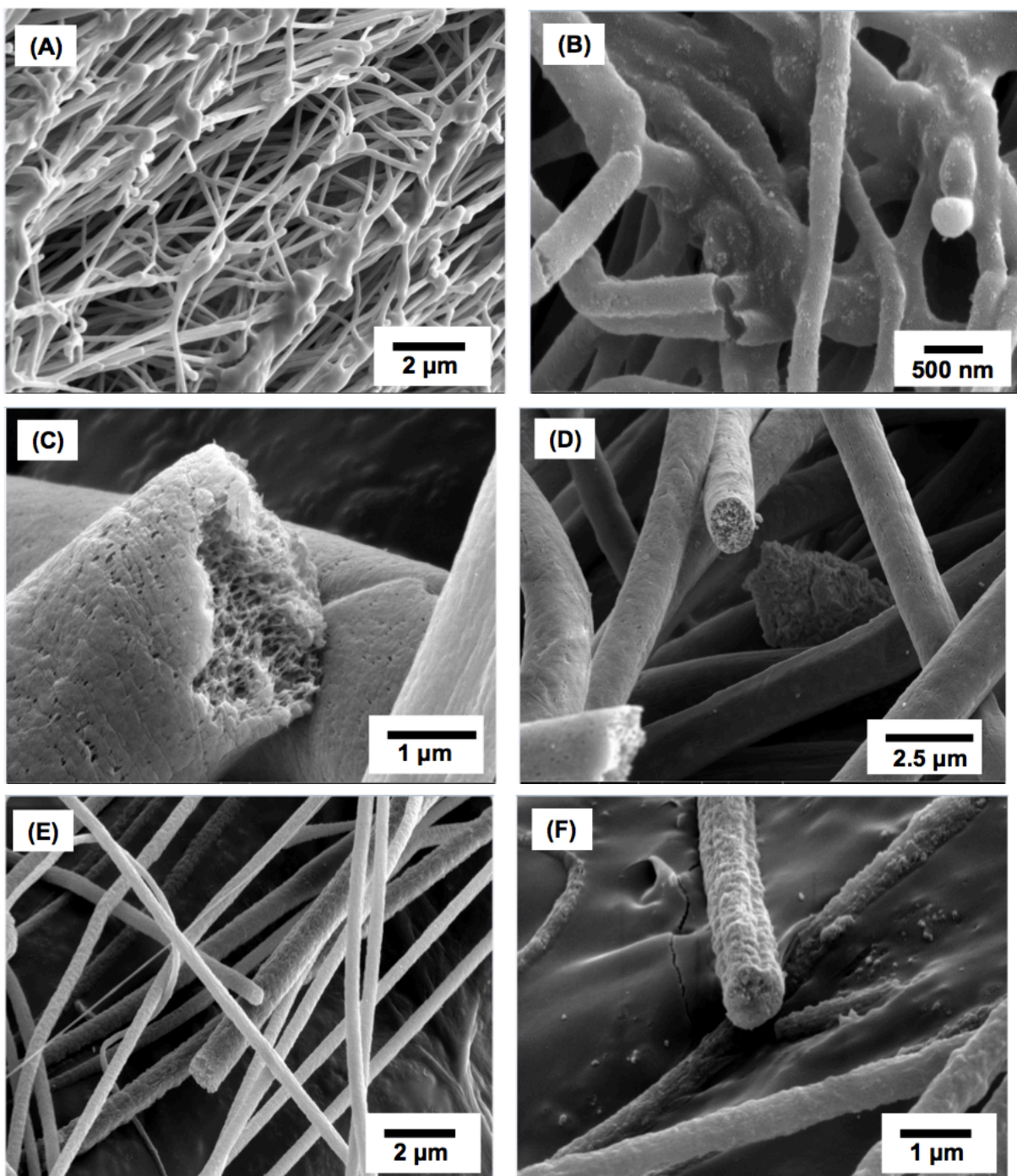


Figure C.12 (a-f) Cross-section images of electrospun fiber composites containing SAUD c-ND: (a) PVA (15 wt.%) and (b) PVA (15 wt.%) with SAUD c-ND (2 wt.%); (c) PS (30 wt.%) and (d) PS (30 wt.%) with SAUD c-ND (2 wt.%); (e) PAN (8 wt.%) and (f) PAN (8 wt.%) with SAUD c-ND (2 wt.%). Uniform nanofibers were produced at these polymer concentrations.

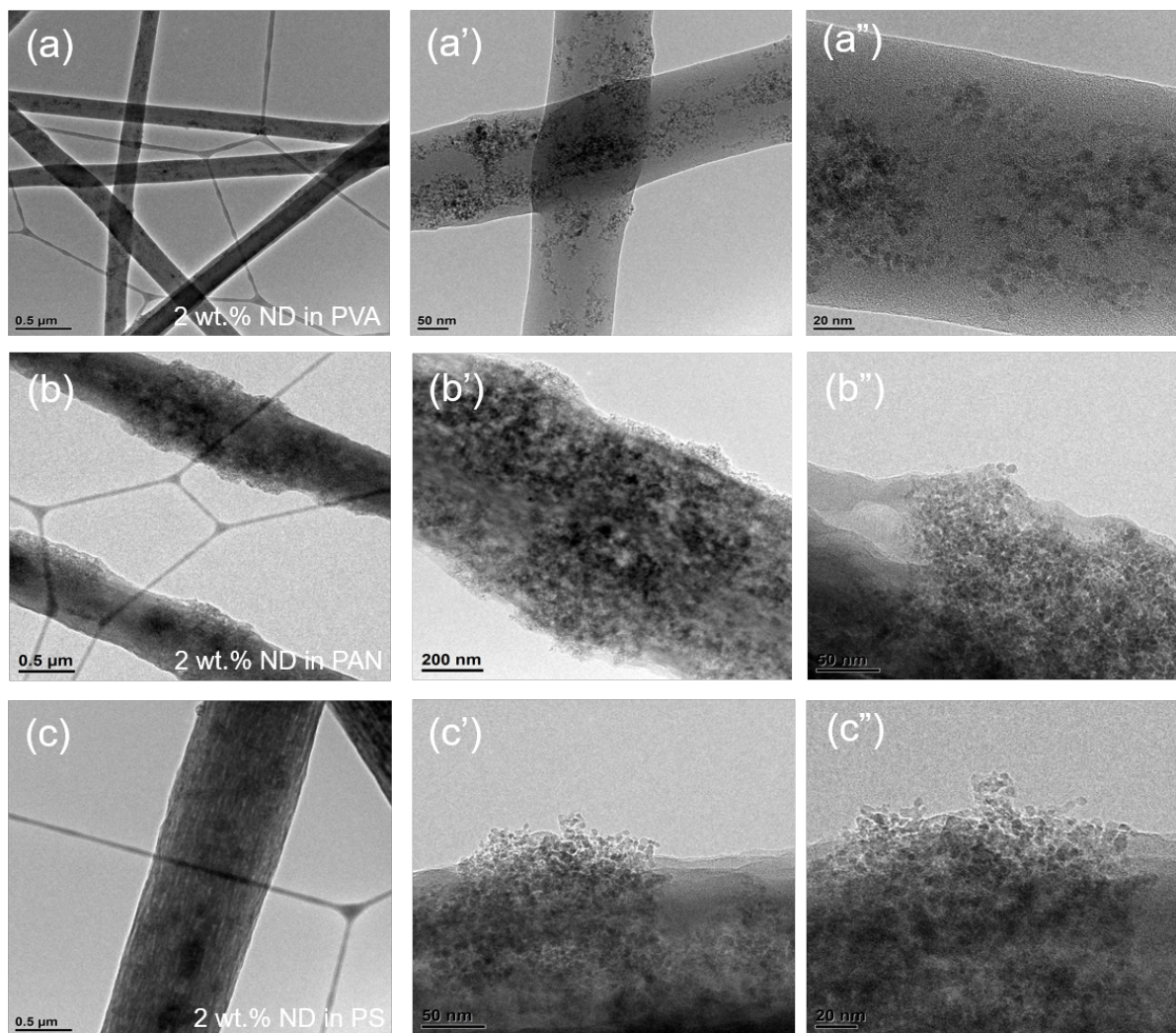


Figure C.13 Morphology of electrospun fibers showing aggregation behavior of ND's in (a) PVA, (b) PAN and (c) PS. Figures (a', b',c') and (a'', b'', c'') shown images at different magnifications.

Thermal Stability of Polymer-ND Fiber Composites

TGA thermograms for weight loss and their first-order derivatives reveal temperatures for maximum weight loss (T_{\max}), decomposition temperatures (T_d), and residual weight for c-ND and c-ND loaded polymers (PVA, PS, and PAN). TGA was performed under a nitrogen environment to prevent any mass loss due to c-ND oxidation. Figure C.14a shows very high thermal stability up to 700°C for c-ND in PVA, resulting in only ~10% of weight loss. The addition of c-ND at 0.1 and 0.5 wt. % shows negligible changes in T_d of ~225°C as well as residual weight for PVA. At higher loadings of 1 wt. % and 2 wt. % c-ND, the increase in T_d becomes more pronounced and results in higher residual weight. Thermograms for the first-order derivative show three distinct regimes in the range between 200-400°C, with maximum weight loss temperatures for PVA nanofibers at 260°C (beginning of pyrolysis), followed by 300°C and 360°C (Figure C.14b). Table C.4 shows different transition temperatures obtained from TGA.

The production of carbon nanofibers from PAN precursors typically involves three steps: stabilization using oxygen through cyclization and dehydrogenation reactions at 200-300°C to form a stable ladder structure that can be processed at high temperature, carbonization at high temperature (~1000°C) under inert gas to facilitate removal of non-carbon contents, and graphitization at 2000°C. TGA thermograms for PAN as shown in Figure C.15 performed from 40°C to 800°C reveal four distinct stages of weight loss, with initial loss starting at temperatures less than 150°C, then further loss between 250°C to 350°C followed by loss between 350°C to 425°C, finally showing a monotonous drop in weight up to 800°C with a total weight loss of 72%. ~8.5 wt. % loss pure PAN nanofiber at

temperatures less than 150°C is due to the removal of surface-bound water and residual solvents. However, the composite fibers show lower weight loss in this region - 4.5% loss at 0.1 wt.%, 3.75% loss at 0.5 wt.%, 3.5 % loss at 1.0 wt.% and 4.25% loss at 2.0 wt.%. The initial onset of degradation, which occurs at 268°C for PAN nanofibers, increases with the addition of c-ND with a maximum increase of ~22°C occurring at 2 wt.% loading and lower weight loss, suggesting enhanced stability after ND addition. However, it appears the cyclization temperature increase from 273.4°C to 294.2°C, and the presence of ND's retards the release of reaction products. Compared to pure PAN which showed a total loss of 72% at 800°C, only 65% and 54% loss in weight was observed for PAN containing ND's at 1 wt.% and 2 wt.% respectively, further showing increased stability of nanofibers in the presence of ND's.

Weight loss and corresponding derivative curves for PS between 300-350°C shown in Figure C.16 reveal the effect of c-ND on PS nanofibers. The onset of polymer degradation is significantly retarded by the presence of c-ND with increments of 20°C upon addition of 2 wt.% c-ND from ~350°C for pure PS to ~370°C for PS loaded with c-ND (2 wt.%). The derivative weight loss shows that upon addition of c-ND, maximum weight loss shifts to a higher temperature and the kinetics of degradation is significantly altered. For control PS, the maximum weight loss occurs at 382.5°C, which shifts to 390°C for c-ND loading of 0.1 wt. % c-ND with negligible changes in the kinetics of degradation. Further increasing c-ND loading to 0.5 wt. %, shifts temperatures to 398°C with some retarded kinetics. This effect of c-ND is significantly pronounced for 1 and 2 wt. % c-ND loadings, considerably shifting to

higher temperatures and dampening the rate of weight loss. There was a significant enhancement in the thermal degradation temperature after incorporation of c-ND.

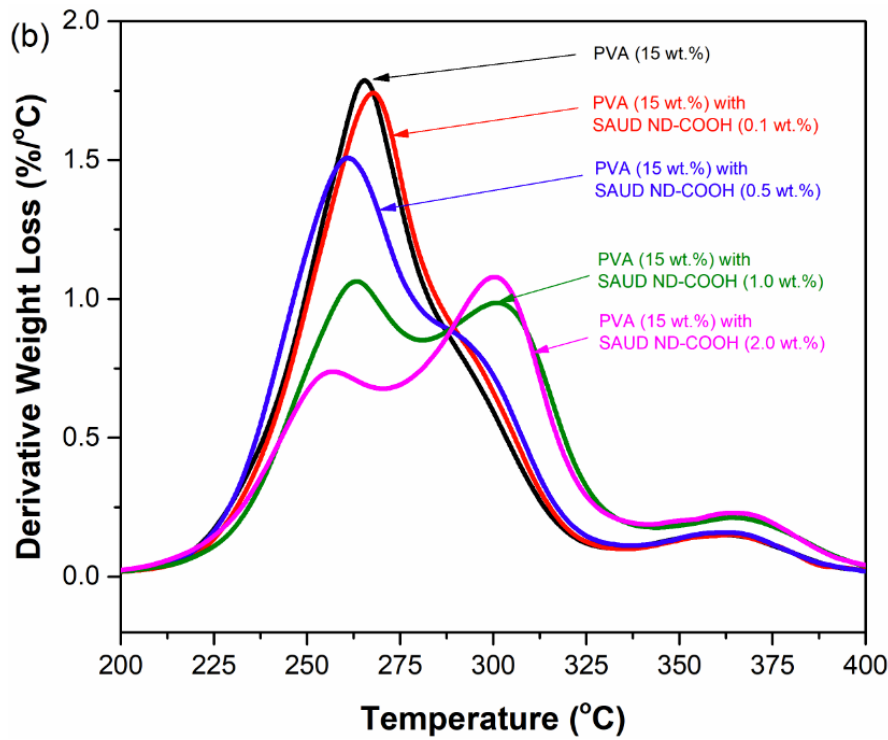
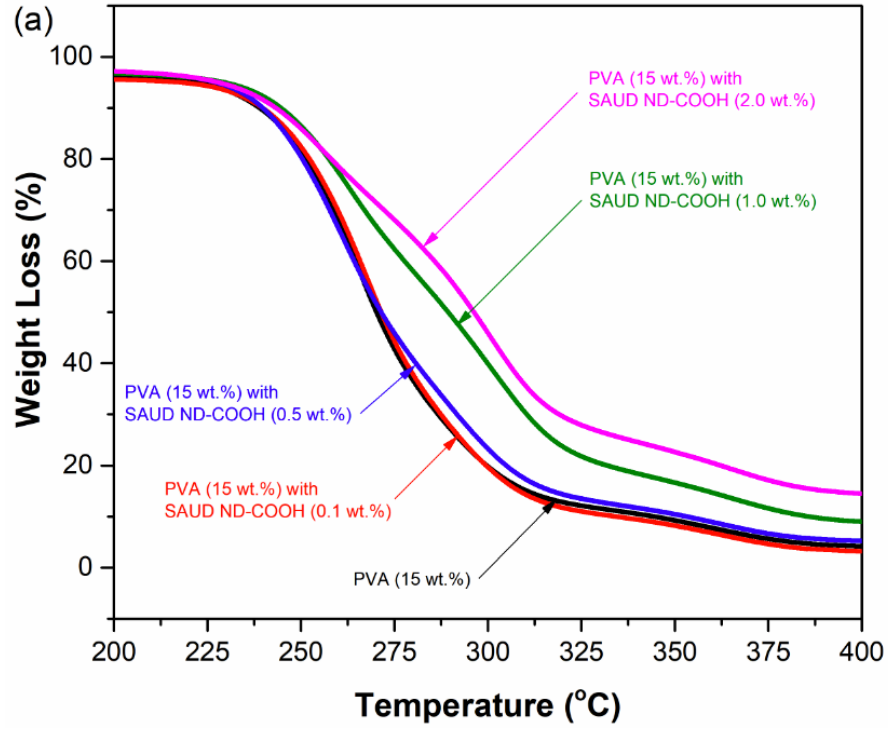


Figure C.14 (a) Weight loss (%) and (b) derivative weight loss of PVA nanofibers with different SAUD c-ND loadings between 0.1 wt.% and 2.0 wt.%.

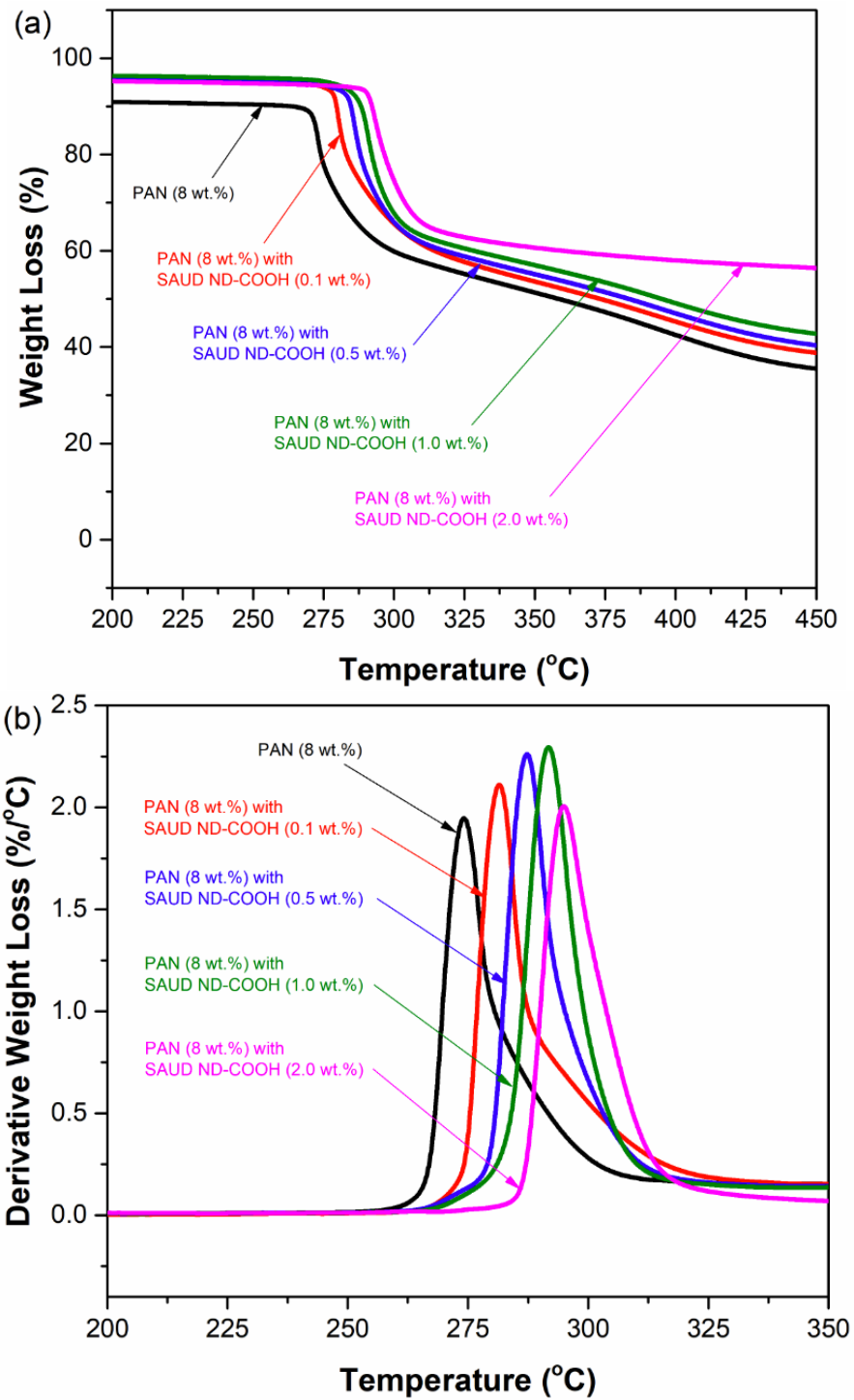


Figure C.15 (a) Weight loss (%) and (b) derivative weight loss of PAN nanofibers with different SAUD c-ND loadings between 0.1 wt.% and 2.0 wt.%.

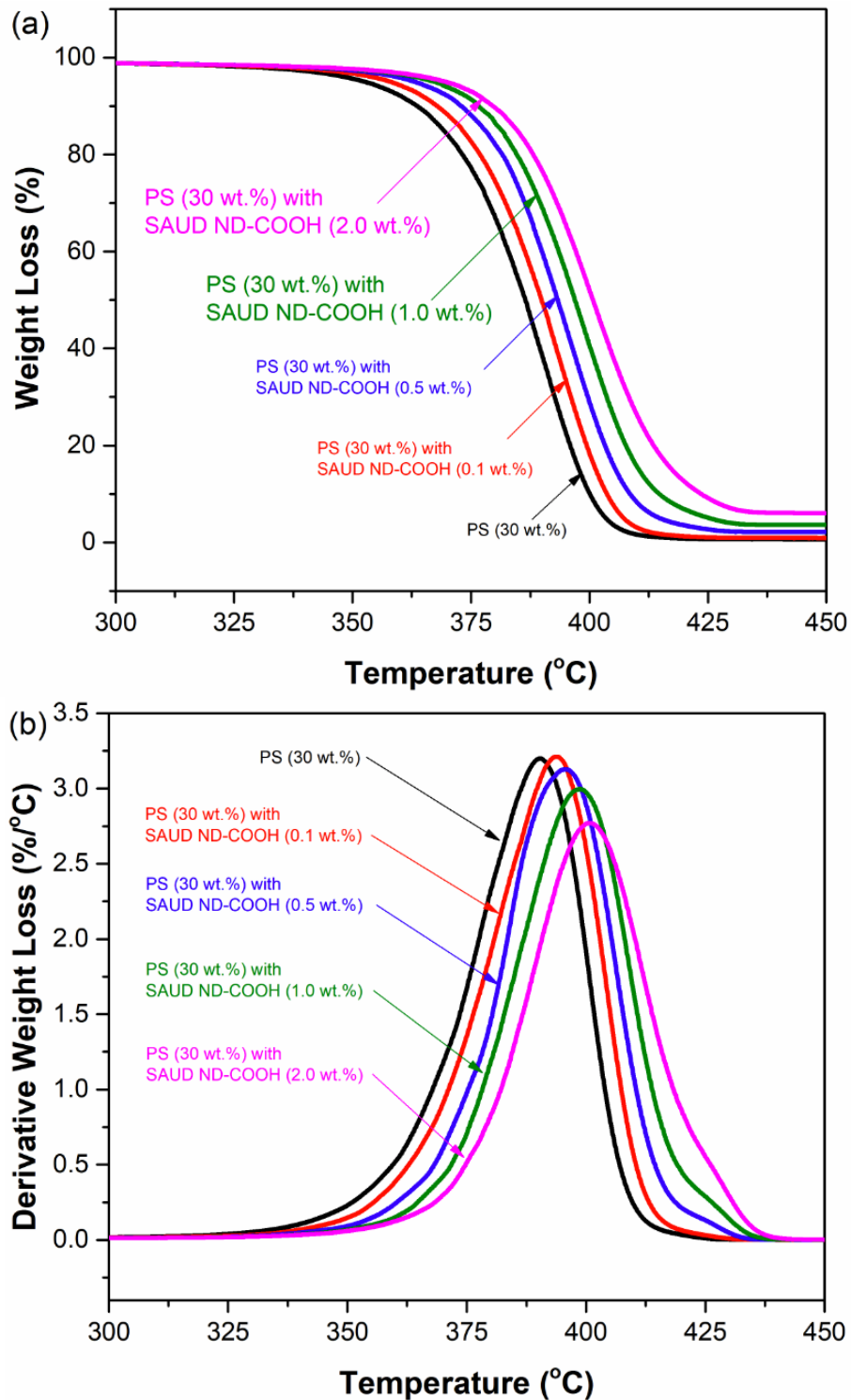


Figure C.16 (a) Weight loss (%) and (b) derivative weight loss of PS nanofibers with different SAUD c-ND loadings between 0.1 wt.% and 2.0 wt.%.

Table C-4 Parameters extracted from TGA graph of polymer-ND fiber composites showing decomposition temperature (T_d) and temperatures of maximum weight loss (T_{max}).

ND (wt. %)	PVA			
	T_d ($^{\circ}\text{C}$)	$T_{max, 1}$ ($^{\circ}\text{C}$)	$T_{max, 2}$ ($^{\circ}\text{C}$)	$T_{max, 3}$ ($^{\circ}\text{C}$)
0	231.3	265.8	-	363.8
0.1	238.2	267.5	-	362.7
0.5	231.5	260.9	-	363.2
1.0	239.1	262.9	299.7	365.8
2.0	233.4	257.2	299.7	365.9

ND (wt. %)	PAN		
	T_d ($^{\circ}\text{C}$)	$T_{max, 1}$ ($^{\circ}\text{C}$)	$T_{max, 2}$ ($^{\circ}\text{C}$)
0	268	273.4	405.4
0.1	277.1	281.3	399.6
0.5	280.2	287.7	401.8
1.0	281.2	292.0	397.5
2.0	289.9	294.2	-

ND (wt. %)	PS	
	T_d ($^{\circ}\text{C}$)	T_{max} ($^{\circ}\text{C}$)
0	349.8	389.6
0.1	360.3	392.8
0.5	364.1	395.5
1.0	370.3	398.7
2.0	367.2	400.9